

**EXPLORATION OF METFORMIN EFFECT OVER OXALIPLATIN
ANTINEOPLASIC PROPERTIES IN MKN45, KATOIII AND HS746T GASTRIC
CANCER CELL LINES *IN VITRO* AND OVER OXALIPLATIN INDUCED RAT
PAINFUL SENSORY NEUROPATHY *IN VIVO*.**

EXPLORACIÓN DEL EFECTO DE METFORMINA SOBRE LAS PROPIEDADES
ANTINEOPLÁSICAS DEL OXALIPLATINO EN LAS LINEAS CELULARES DE
CANCER GÁSTRICO MKN45, KATOIII Y HS746T *IN VITRO* Y SOBRE LA
NEUROPATÍA SENSORIAL DOLOROSA INDUCIDA POR EL OXALIPLATINO EN
RATAS *IN VIVO*.

Tesis entregada a la Pontificia Universidad Católica de Chile en cumplimiento
parcial de los requisitos para optar al Grado de Doctor en Ciencias Biológicas con
mención en Ciencias Fisiológicas por:

WASHINGTON NICOLÁS MARTÍNEZ ALARCÓN.

Director de la tesis Dr. Felipe Court Goldsmith

Codirector de la tesis Dr. Felipe Barros Olmedo

En septiembre de 2018

2. DOCTORAL THESIS APPROVAL CERTIFICATE

3. DEDICATORIA

(tr. DEDICATION).

Dedico agradecidamente esta tesis doctoral a la memoria indeleble de mi abuela Lucila del Carmen Araya Durán, que me dio la lección más grande de tesón al disponerse como estudiante para aprender a escribir después de los 90 años, a mi madre Carmen Rosa Alarcón Araya una mujer formidable e infinitamente superior a mí en lucidez, y a la familia Alarcón, porque sin el pan y el amor que me han entregado a lo largo de mi vida nada de lo que yo pudiera producir de bueno en este mundo habría sido posible y porque este avance en el desarrollo de los integrantes de nuestra familia corresponde al proceso que ellos han sostenido durante tres generaciones.

Dedico además esta tesis doctoral, a todos los marginados y desposeídos de Chile que llevan en su interior la semilla de superación y búsqueda del progreso del hombre y que, al aceptarme como uno de ellos, han dejado en mí la estampa moral y dignidad que poseemos todos los que hemos sido excluidos por nacimiento del canon social y que nos hemos atrevido a producir una cultura propia desde la nada. Especialmente a los habitantes de la gloriosa Población San Gregorio de la comuna de La Granja en Santiago de Chile.

Y a todo aquel que crea que el acceso a la educación, información y difusión científica son un

Derecho Humano Universal. Por ustedes lo hice.

4. AGRADECIMIENTOS

(tr. ACKNOWLEDGMENTS).

Agradezco especialmente al Dr. Felipe Court Goldsmith como tutor de mi tesis doctoral, por todo el apoyo profesional y humano brindado durante los años que hemos trabajado juntos, en este y otros proyectos. Especialmente, por confiar en mí y ayudar a desarrollarme intelectualmente, considerando mis virtudes y defectos. Además, por imprimir en mí aptitudes que espero le llenen de orgullo en el futuro.

Por otra parte, agradezco también al Dr. Felipe Barros Olmedo, como cotutor de mi tesis doctoral, su invaluable guía profesional y humana en los momentos de trabajo científico arduo y en las situaciones difíciles que enfrenté durante el desarrollo de este proyecto.

Además, por todo el apoyo, afecto y retroalimentación científica, esta tesis doctoral no habría sido posible sin los generosos aportes de las siguientes personas: Dra. Eileen Collyer, Dra. Rosario Villegas, Dra. Claudia Muñoz, Dra. Maritza Oñate Valenzuela, Dra. Tamara Sotelo Hitschfeld, Dra. Claudia Pissani Alvear, Dra. Margarita Calvo, Dra. Dominique Lemaitre Mujica, Dr. Diego Hernández Trejo, Dr. Sebastián Barrientos Baeza, Dr. Jaime Álvarez Marín, Dr. Alejandro San Martín, Dr. Ignacio Fernández Moncada, Dr. Rodrigo Lerchundi Monje, Dr. Felipe Baeza Lehnert, Dr. Sebastián Jara y Dr. Sebastián Ceballo Charpentier.

Por las mismas razones también, a los profesionales: Bruno Nervi Nattero, Alejandra Catenaccio Jovaní, Mónica Pérez Vicent, Cheryg Chávez Vega, Micaela Ricca, Dinka Ivulic, Richard Broekhuizen, Francisca Julio Kalajzić, Francisco Yáñez Vargas, Massiel Salazar, Gonzalo Martínez Riquelme, Manuel Alarcón Araya, y Álvaro Sánchez.

En ellos, agradezco también a todos los profesionales científicos, administrativos y auxiliares de la Pontificia Universidad Católica de Chile en Santiago y a los del Centro de Estudios Científicos en Valdivia que me acogieron y me facilitaron siempre en lo cotidiano y lo fundamental de este proceso. Especialmente, a los integrantes del programa de Doctorado en Ciencias Biológicas mención Ciencias Fisiológicas de la Pontificia Universidad Católica de Chile.

Además, es necesario agradecer el rol fundamental de las herramientas de acceso directo a la literatura científica en la realización de esta tesis, opción sin la cual la calidad del marco teórico y el análisis de los resultados que se realizó habrían sido inferiores. Con especial gratitud a la neurocientífica Alexandra Elbakyan por el proyecto Sci-Hub.

Finalmente, a los vitales financiamientos de la Facultad de Ciencias Biológicas de la Pontificia Universidad Católica de Chile a través de la Beca de Ayudante e Instructor Becario y de la Comisión Nacional de Investigación Científica y Tecnológica (CONICYT) del Gobierno de Chile a través de las Becas de Asistencia a cursos y eventos cortos, la Beca de Doctorado Nacional y Beca de Extensión del Doctorado, que han permitido la ejecución de esta tesis doctoral.

5. CONTENT INDEX.

1. THESIS TITLE (p.1).
2. DOCTORAL THESIS APPROVAL CERTIFICATE (p.2).
3. DEDICATORIA (p.3).
4. AGRADECIMIENTOS (pp. 4-5)
5. CONTENT INDEX (pp. 6-11).
6. FIGURES AND TABLES INDEX (pp.12-15).
7. ABBREVIATIONS AND ACRONYMS LIST (pp.16-20).
8. RESUMEN (pp.21-22).
9. ABSTRACT (pp. 23-24).
10. INTRODUCTION (pp. 25-48).
 - 10.1 Neuronal Fibers for Pain Perception (pp. 25-34).
 - 10.2 Pathology and Clinical Implications of Chemotherapy Induced Peripheral Neuropathy (pp. 35-36).
 - 10.3 Oxaliplatin Induced Peripheral Neuropathy (pp. 37-44).
 - 10.4 Metformin Role in Cancer and Neurodegeneration (pp..45-47).
 - 10.5 Hypothesis (p.48).
 - 10.6. General Objective (p.48).
 - 10.7. Specific Objectives (p.48).

10.7.1 Specific Objective N°1 (p.48).

10.7.2 Specific Objective N°2 (p.48).

10.7.3 Specific Objective N°3 (p.48).

11. MATERIALS (pp.49-57).

11.1 Culture Media and General Reactives (pp.49-52).

11.2 Markers, Reporters and Antibodies (pp.53-54).

11.3 Drugs and Treatments (p.54).

11.4 Plastic Materials, Surgical Instruments and Medical Supplies (pp.55-56).

11.5 Specialized Hardware, Devices and Equipment (pp.56-57).

11.6 Software (p.57).

12. METHODS (pp. 58-77).

12.1 Animal Housing and Handling (p.58).

12.2 OIPN Animal Model and Metformin Treatment (pp.58-62).

12.3 Axotomy Protocol (p.63).

12.4 Histology Procedures (pp.63-64).

12.5 Quantification and Analysis of Immunofluorescences (pp.64-68).

12.5.1 Table N°1. Primary Antibodies Dilutions (p.66).

12.5.2 Table N°2. Secondary Antibodies Dilutions (p.67).

12.5.3 Table N°3. Markers Dilutions (p.68).

12.6 Assessment of Mechanical Allodynia (Von Frey Test) (pp. 69-70).

12.7 Assessment of Cold Allodynia (Acetone Test) (p.70).

12.8 Assessment of Thermal Hypoalgesia (Hargreaves Test) (pp.70-71).

12.9 Blood Collection and Analysis (p.71).

12.10 Cell Lines Culture, Treatments and Assays (pp.74-75).

12.11 *In vitro* Determination of Axonal Degeneration (pp.76-77).

12.12 Statistical Analysis (p.77).

13. RESULTS (pp. 76-109).

13.1 Oxaliplatin Antineoplastic Effect After Cotreatment with Metformin *In vitro* Cellular Models of Gastric Cancer (pp.78-82).

13.2 Metformin Effect over Oxaliplatin Chemotherapy Induced Peripheral Neuropathy (pp. 83-101).

13.2.1 Inhibitory Effect of Metformin Over Oxaliplatin Induced Axonal Degeneration *In Vitro* (pp. 83-84)

13.2.2 A New Regime of Chemotherapy Administration in the Context of a Murine Model of Oxaliplatin Induced Peripheral Neuropathy (pp.85-86).

13.2.3 Metformin Inhibits Oxaliplatin Induced Intraepidermal Nerve Fibers Degeneration (pp.87-88).

13.2.4 Effect of Oxaliplatin and Metformin Treatment over Axonal Integrity *In vivo* (pp. 89-90).

13.2.5 Effect of Metformin and Oxaliplatin Treatment over Sensory Neurons Cell Bodies Numbers and Expression of Cellular Stress Markers (pp. 91-96).

13.2.6 Oxaliplatin Induced Astrocyte Activation in the Spinal Cord Is Inhibited by Metformin Cotreatment (pp. 97-101).

13.3 Metformin Effect over Oxaliplatin Induced Sensory Impairment (pp. 102-110).

13.3.1 Metformin Inhibits Oxaliplatin Induced Acute Mechanical Allodynia (pp.103-105).

13.3.2 Metformin Reverses Oxaliplatin Induced Chronic Thermal Hypoalgesia in Response to Heat (pp. 106-108).

13.3.3 Metformin inhibits Oxaliplatin Induced Chronic Thermal Allodynia in Response to Cold (pp.109-110).

13.4 Effect of Oxaliplatin and Metformin over Glycaemia, Weight and White Blood Cells Counting (pp. 111-114).

14. DISCUSSION (pp. 115-139).

14.1 Relevance of the Exploration of the Effect of Metformin over Oxaliplatin Induced Peripheral Neuropathy in the Context of Other Platinum Derivative Toxicities (pp. 115-117).

14.2 Metformin and Oxaliplatin Antineoplastic Effect over Gastric Cancer (pp. 117-121).

14.3 Use of Metformin as a Treatment Against Oxaliplatin Induced Peripheral Neuropathy: Morphological and Cytological Changes in Sensory Circuits (pp. 121-133).

14.4 Use of Metformin as a Treatment Against Oxaliplatin Induced Peripheral Neuropathy: Sensory Symptoms (pp. 134- 139).

15. CONCLUSIONS (pp.140-141).

16. BIBLIOGRAPHY (pp. 142-187).

17. ADDENDUM PREFACE (p.188)

18. RESUMEN DEL ADDENDUM (tr. ADDENDUM ABSTRACT) (p. 189).

19. ADDENDUM ABSTRACT (p. 190)

20. ADDENDUM INTRODUCTION (pp. 191-195).

21. ADDENDUM MATERIALS (pp. 196-202).

21.1 Addendum Culture Media and General Reactives (pp. 196-199).

21.2 Addendum Plastic Materials, Surgical Instruments and Medical Supplies (pp. 199-200).

21.3 Addendum Drugs and Treatments (p. 200).

21.4 Addendum Markers, Reporters and Antibodies (p. 201).

21.5 Addendum Energetic Metabolism Nanosensors (adenoviral vectors) (p. 202).

21.6 Addendum Specialized Hardware, Devices and Equipment (p. 202).

21.7 Addendum Software (p. 202).

22. ADDENDUM METHODS (pp. 203-219).

22.1 Addendum Animal Housing (p. 203).

22.2 Addendum Dorsal Root Ganglia Culture and Infection (pp. 203-204).

22.3 Addendum Immunofluorescence (p. 204-205).

22.4 Glut2 and MCT1 or MCT2 Qualitative Expression and Distribution in DRG Neurons (p. 205).

22.5 Addendum Table 1. Addendum Primary and Secondary Antibodies Dilutions (p. 206).

22.6 *In vitro* Determination of Depolarization Induced Cytosolic Calcium Dynamics (pp. 207-208).

22.7 *In vitro* Determination of Mitochondrial Pyruvate Consumption Rate in Neurons (pp. 208-213).

22.8 *In vitro* Determination of Glycolytic Rate in Neurons (pp. 214-218).

22.9 Addendum Statistical Analysis (p. 219).

23. ADDENDUM RESULTS (pp. 200-240).

23.1 Glucose and Pyruvate Transporters Distribution in Soma and Axons of Disaggregated

DRG Neurons (pp.220-223).

23.2 Cytosolic Calcium Dynamics After High K⁺ or Electrical Stimulation Depolarization Induction in Soma and Axons of Disaggregated DRG Neurons (pp. 224-229).

23.3 Pyronic and FLII12Pglu600 mΔ6 Expression in Disaggregated DRG Neurons (p. 230).

23.4 Mitochondrial Pyruvate Consumption Rates in Soma and Axons of Disaggregated DRG Neurons (pp. 231-247).

23.5 Glycolytic Rates in Soma and Axons of Disaggregated DRG Neurons (pp. 248-260).

24. ADDENDUM DISCUSSION (pp. 261-281).

24.1 Glucose and Pyruvate Transporters Distribution in Soma and Axons of Disaggregated DRG Neurons (pp. 262-264).

24.2 Spontaneous Cytosolic Calcium Spikes and Regulation of Cytosolic Calcium After Depolarization in Soma and Axons of Disaggregated DRG Neurons (pp. 265-267).

24.3 Mitochondrial Pyruvate Consumption Rates in Disaggregated DRG Neurons (pp. 268-271).

24.4 Glycolytic Rates in Soma and Axons of Disaggregated DRG Neurons (pp. 272-281).

25. ADDENDUM CONCLUSION (p.282).

26. ADDENDUM BIBLIOGRAPHY (pp. 283-293).

6. FIGURES AND TABLES INDEX.

- Figure N°1. Pain Sensory Afferent Pathways and Pain Sensitization (p. 34).
- Figure N°2. Scheme of Oxaliplatin and Metformin Administration Regime (p. 62).
- Figure N°3. Schemes of the Sensory Testing Procedures (pp. 72-73).
- Figure N°4. MKN45, KatoIII and HS746T Gastric Cancer Cell Lines Basal Viability (p. 79).
- Figure N°5. Oxaliplatin and Metformin Effect over Viability of Cancer Cells (p.81).
- Figure N°6. Metformin Effect over Survival of Cancer Cells and Antineoplastic Effect of Oxaliplatin (p. 82).
- Figure N°7. Effect of Metformin over Oxaliplatin Induced Axonal Degeneration *In Vitro* (p.87).
- Figure N°8. Effect of Metformin over Oxaliplatin Induced Intraepidermal Nerve Fiber (IENF) Degeneration (p. 88).
- Figure N°9. Effect of Metformin and Oxaliplatin Cotreatment over Axonal Density (p. 90).
- Figure N°10. Effect of Oxaliplatin and Metformin Cotreatment over Sensory Peptidergic and Non-peptidergic Neurons Populations at Sensory DRG (pp. 93-94).
- Figure N°11. Effect of Oxaliplatin and Metformin over ATF3 Nuclear localization

(pp.95-96).

- Figure N°12. Effect of Oxaliplatin and Metformin Cotreatment Over Sensory Peptidergic and Non-peptidergic Neurons Terminals at L4, L5 and L6 Spinal Cord Region Dorsal Horn (p.99).
- Figure N°13. Effect of Oxaliplatin and Metformin Cotreatment over Astrocyte Reactivity at Spinal Cord (pp. 100-101).
- Figure N°14. Effect of Oxaliplatin and Metformin Cotreatment over Mean Threshold Withdrawal Response to Touch (p.101).
- Figure N°15. Effect of Oxaliplatin and Metformin Cotreatment over Withdrawal Response Latency to Heat (p.105).
- Figure N°16. Effect of Oxaliplatin and Metformin Cotreatment over Withdrawal Response to Cold Duration (p.110).
- Figure N°17. Effect of Oxaliplatin and Metformin Cotreatment over Relevant Physiological Parameters in the Context of Chemotherapy (pp. 113-114).
- Figure N°18. Graphical Abstract. (pp.141)
- Table N°1. Primary Antibodies Dilutions (p.66).
- Table N°2. Secondary Antibodies Dilutions (p.67).
- Table N°3. Markers Dilutions (p.68).
- Addendum Table 1. Addendum Primary and Secondary Antibodies Dilutions (p. 206).
- Addendum Figure N°1. Measurement of Mitochondrial Pyruvate Consumption Rate (pp. 212-213).
- Addendum Figure N°2. Measurement of Glycolytic Rate (pp. 217-218).

- Addendum Figure N°3. Glucose Transporter 2 (Glut2) Cellular Distribution in Dorsal Root Ganglia Neurons (p.221).
- Addendum Figure N°4. Monocarboxylate Transporter 1 (MCT1) Cellular Distribution in Dorsal Root Ganglia Neurons (p.222).
- Addendum Figure N°5. Monocarboxylate Transporter 2 (MCT2) Cellular Distribution in Dorsal Root Ganglia Neurons (p.223).
- Addendum Figure N°6. Calcium Dynamics after High K^+ or Electrical Field Stimulation (pp. 227-229).
- Addendum Figure N°7. Pyronic Fluorescence Intensity in Disaggregated DRG Neurons Soma during MCTs Inhibition (pp. 233-234).
- Addendum Figure N°8. Pyronic FRET Efficiency in Disaggregated DRG Neurons Soma during MCTs Inhibition (pp. 235-236).
- Addendum Figure N°9. Mitochondrial Pyruvate Consumption Rate in Soma of Disaggregated DRG Neurons (pp. 237-239).
- Addendum Figure N°10. Pyronic Fluorescence Intensity in Disaggregated DRG Neurons Axons during MCTs Inhibition (pp. 240-241).
- Addendum Figure N°11. Pyronic FRET Efficiency in Disaggregated DRG Neurons Axons during MCTs Inhibition (pp. 242-243).
- Addendum Figure N°12. Mitochondrial Pyruvate Consumption Rate in Axons of Disaggregated DRG Neurons (pp. 244-246).
- Addendum Figure N°13. Mitochondrial Pyruvate Consumption Rate in Soma and Axons of Disaggregated DRG Neurons (p. 247).
- Addendum Figure N°14. FLII12Pglu600 mΔ6 Fluorescence Intensity in

Disaggregated DRG Neurons Soma during Glucose Transport Inhibition (pp. 250-251).

- Addendum Figure N°15. Glycolytic Rate in Soma of Disaggregated DRG Neurons (pp. 252-254).
- Addendum Figure N°16. FLII12Pglu600 mΔ6 Fluorescence Intensity in Disaggregated DRG Neurons Axons during Glucose Transport Inhibition (pp. 255-256).
- Addendum Figure N°17. Glycolytic Rate in Axons of Disaggregated DRG Neurons (pp. 257-259).
- Addendum Figure N°18. Glycolytic Rate in Soma and Axons of Disaggregated DRG Neurons (p. 260).

7. ABBREVIATIONS AND ACRONYMS LIST.

- ACS: American Chemical Society
- AD: Axonal Degeneration; Degeneración Axonal (Spanish)
- ANLS: Astrocyte-Neuron Lactate Shuttle
- Approx.: Approximately
- AR: MCTs inhibitor AR-C155858
- ASCO: American Society of Clinical Oncology
- ATF3: Activating Transcription Factor
- ATP: Adenosine Triphosphate
- AU: Arbitrary Units
- Axot: Axotomy
- BMV: Brain Microvessels
- Cat.No.: Catalogue Number
- CFP: Citrine Fluorescent Protein
- CGRP: Calcitonin Gene Related Peptide
- CID: Chemotherapy Induced Diarrhea
- CIPN: Chemotherapy Induced Peripheral Neuropathy; Neuropatía Periférica Inducida por Quimioterapia (Spanish)
- CONICYT: Comisión Nacional de Investigación Científica y Tecnológica

- CRC: Colorectal Cancer
- CytoB: Cytochalasin B
- DAPI: 4', 6-Diamidino-2-Phenylindole, Dihydrochloride
- DMEM: Dulbecco's Modified Eagle Medium
- DNA: Deoxyribonucleic Acid
- DRG: Dorsal Root Ganglia Neurons
- EM: Electron Microscopy
- ETC: Electron Transport Chain
- F: Fluorescence
- FDA: United States Government Food and Drugs Administration.
- F₀: Initial Fluorescence
- F₁: First filial generation of offspring of distinctly different parental types
- FBS: Fetal Bovine Serum
- Fluo-4: Cytosolic calcium reporter Fluo-4 acetoxymethyl (AM)
- fMRI: Functional Magnetic Resonance Imaging
- FRET: Fluorescence Resonance Energy Transfer
- GFAP: Glial Fibrillary Acidic Protein
- Gluc: Glucose
- Glut: Glucose Transporter
- HS746T: *Homo Sapiens* gastric carcinoma cells from stomach epithelial fibroblast
- Hz: Hertz
- i.p.: Intraperitoneally
- i.v.: Intravenous

- IB4: Isolectin GS-IB₄ from *Griffonia simplicifolia*, biotin-XX Conjugate
- Iba1: Ionized calcium-binding adapter molecule 1.
- IC50: Half Maximal Inhibitory Concentration.
- IF: Immunofluorescence.
- IgG (H+L): Heavy and Light chains of Immunoglobulin G.
- IHC: Immunohistochemistry
- IP: Immunoprecipitation
- ISO: International Standard Organization.
- K⁺: Potassium
- Kato III: *Homo sapiens* gastric carcinoma cells derived from metastatic sites in pleural effusion, supraclavicular, axillary lymph nodes and Douglas *cul de sac*.
- K_D: Dissociation Constant
- KRH: Krebs Ringer Hepes Buffer
- L1; L2: Laminae 1 and Laminae 2 from spinal cord dorsal horn.
- L4, L5 and L6: Lumbar 4, Lumbar 5 and Lumbar 6 spinal cord segment.
- Lac: Lactate
- MCT: Monocarboxylate Transporter
- MEM: Modified Eagle Medium.
- Met: 1, 1-Dimethylbiguanide Hydrochloride; metformin; metformina (Spanish)
- MKN45: *Homo sapiens* gastric adenocarcinoma cells.
- ms: milliseconds
- mTFP: Monomeric Teal Fluorescence Protein
- MTT: 3- [4, 5-dimethylthiazol--2-yl]-2, 5-diphenyl tetrazolium bromide.

- NF-H: Neurofilament Heavy chain.
- OCT: Optimum Cutting Temperature formulation of water soluble glycol and resins.
- OCTN: Organic Cation Transporter.
- OD: Optical Density.
- OIPN: Oxaliplatin Induced Peripheral Neuropathy; Neuropatía Periférica Inducida por Oxaliplatino.
- ON: Over Night.
- Oxal: Oxaliplatin; oxaliplatino (Spanish)
- Oxal+Met: Oxaliplatin and Metformin.
- PB: Phosphate Buffer.
- PBS: Phosphate Buffered Salinum pH 7, 2-7, 4.
- PET: Positron Emission Transport
- PFA: Paraformaldehyde solution 4% in PBS.
- PGP 9, 5: Permeability Glycoprotein 9, 5.
- Pir: Pyruvate; Piruvato (spanish)
- PPP: Pentose Phosphate Pathway
- Reag. Ph. euR.: Reagent (specification as per) European Pharmacopoeia.
- ROI: Region Of Interest
- RPMI: Roswell Park Memorial Institute Medium.
- RT: Room Temperature.
- TCA: Tricarboxylic Acid Cycle
- TMRM: Tetramethyl rhodamine, Methyl Ester, Perchlorate.

- tr.: Translation from Spanish to English.
- TRP channels: Transient Receptor Potential generating channels
- V: Volts
- VDCC: Voltage Dependent Calcium Channels
- WB: Western Blot.
- YFP: Yellow Fluorescent Protein
- Δ : Delta

8. RESUMEN.

(tr. ABSTRACT)

La neuropatía periférica inducida por quimioterapia (CIPN) es una patología que se presenta como un efecto adverso que limita la dosis de ciertos tratamientos anticáncer y afecta la calidad de vida a largo plazo por inducción de discapacidad permanente o transitoria. Las quimioterapias inducen principalmente degeneración axonal (AD), degeneración de fibras intraepidermales (IENFD) y activación glial en los circuitos sensoriales centrales. En ese contexto, hiperexcitabilidad y descargas ectópicas se han relacionado con síntomas sensoriales tales como diestesia, parestesia y alodinia. Estos síntomas a menudo llevan a una suspensión anticipada de la quimioterapia, lo cual reduce la expectativa de vida de manera significativa. Actualmente, no existen tratamientos efectivos contra la CIPN.

Esta tesis explora pruebas de concepto para sugerir a la droga antidiabética metformina como un blanco experimental de investigaciones futuras, con el objetivo de desarrollar un potencial tratamiento contra la CIPN. El efecto de metformina fue estudiado en un modelo de neuropatía periférica inducida por oxaliplatino (OIPN), el cual se caracteriza por la toxicidad del oxaliplatino sobre las neuronas sensoriales del ganglio de la raíz dorsal (DRG). Considerando que la toxicidad de las quimioterapias ocurre en el contexto de un tratamiento anticáncer, evaluamos primero el rol de la metformina sobre el efecto antineoplásico del oxaliplatino. Para esto, determinamos supervivencia celular en tres líneas celulares diferentes de cáncer gástrico (células MKN45, HS746T y KatoIII), bajo diversas concentraciones de oxaliplatino y metformina en cotratamiento. En todas las líneas celulares estudiadas, encontramos que la reducción significativa de la supervivencia celular inducida por oxaliplatino no fue modificada por el cotratamiento con metformina. Este resultado sugiere que la metformina no interfiere con el efecto antineoplásico del oxaliplatino. Luego, exploramos el efecto de metformina sobre la toxicidad inducida por oxaliplatino en los DRG y la función sensorial. Para esto, se les administró metformina a ratas que estaban desarrollando neuropatía periférica inducida por oxaliplatino (OIPN) y se estudiaron marcadores histológicos de degeneración en las ramas centrales y periféricas del DRG después de evaluar el desempeño de la función sensitiva durante el tiempo de progresión de la OIPN. Específicamente, se exploró la degeneración de neuronas peptidérgicas y no peptidérgicas -a lo largo de las ramas centrales y periféricas de neuronas en L4, L5 y L6 -en las IENF, el nervio ciático, los ganglios de la raíz dorsal (soma) y los terminales en la médula espinal. Adicionalmente, se exploró la activación de los astrocitos en la médula espinal. En este contexto, metformina inhibió significativamente la degeneración de las IENF y la activación de los astrocitos en la médula espinal. Además, el tratamiento con oxaliplatino indujo una significativa disminución en el umbral de respuesta aversiva al estímulo táctil y en la latencia de respuesta aversiva frente a la estimulación por calor. Además, el tratamiento con oxaliplatino también indujo un significativo aumento de la duración de la respuesta aversiva al estímulo frío. Sorpresivamente, el cotratamiento con

metformina a ratas tratadas con oxaliplatino mantuvo el desempeño de la función sensitiva en niveles control. Considerando todo esto, dichos resultados sugieren que la metformina protege de la OIPN. Finalmente, ensayamos periódicamente los niveles de glóbulos blancos, glicemia y peso, con el objetivo de evaluar los efectos de nuestros tratamientos sobre variables fisiológicas relevantes. Los niveles de todas estas variables permanecieron en rangos fisiológicos bajo todos los tratamientos y a lo largo de todo el estudio. Estos resultados sugieren que nuestro modelo experimental es resolutivo en un marco fisiológico en ratas. Considerando esto, el régimen de administración, los dosajes y los resultados presentados en esta tesis podrían potencialmente ser extrapolables a los del contexto clínico.

En conclusión, este grupo de resultados proveen un set fundamental de pruebas de conceptos para un tratamiento potencial contra la CIPN basándose en la administración de la metformina. Sin embargo, se requiere de investigación adicional para determinar los mecanismos celulares y moleculares detrás del ubicuo efecto protector de la metformina contra la toxicidad del oxaliplatino sobre los circuitos del dolor y la consecuente mantención de la función sensitiva en el contexto de la OIPN. Adicionalmente, son necesarios estudios de gran escala para extrapolar estos descubrimientos al contexto del tratamiento de la CIPN en humanos.

9. ABSTRACT.

Chemotherapy induced peripheral neuropathy (CIPN) is a pathological condition presented as a dose-limiting adverse effect of certain cancer treatments that affects long term quality of life by induction of transient or permanent disability. Chemotherapeutics induce axonal degeneration (AD), intraepidermal nerve fibers degeneration (IENFD) and glial activation at the central sensory circuits. There, chemotherapy induced hyperexcitability and ectopic discharges have been associated with sensory symptoms such as dysesthesia, paraesthesia and allodynia. Those CIPN symptoms often lead to an early suspension of chemotherapy that significantly reduces life expectancy. Unfortunately, there are no effective treatments for CIPN.

This thesis explores proof of concepts to suggest the anti-diabetic drug metformin for further research as an experimental target to develop a potential treatment for CIPN. The effect of metformin was assayed in a model of oxaliplatin induced peripheral neuropathy (OIPN), which is characterized by oxaliplatin toxicity over dorsal root ganglia (DRG) sensory neurons. Considering that chemotherapy toxicity occurs in the context of an anticancer treatment, we first evaluated the role of metformin over the antineoplastic effect of oxaliplatin. To this goal, we determined cell survival of three different gastric cell lines (MKN45, HS746T and KatoIII cells) under several concentrations of oxaliplatin and metformin cotreatment. In all studied gastric cancer cell lines, we found that the significant reduction of cell survival induced by oxaliplatin was unaffected by metformin cotreatment. This result suggests that metformin does not interfere with the antineoplastic effect of oxaliplatin. Then, we explored the effect of metformin over oxaliplatin induced toxicity over sensory neurons at DRG and sensory function. To this goal, metformin was administered to rats undergoing oxaliplatin induced peripheral neuropathy (OIPN) and histological markers of degeneration along central and peripheral branches of DRG were determined after sensory function performance testing along the time of OIPN progression. Specifically, degeneration of peptidergic and non peptidergic neurons was explored along the peripheral and central branches of L4, L5 and L6 sensory neurons at IENF, sciatic nerve, dorsal root ganglia (soma) and spinal cord terminals. Additionally, activation of astrocytes was explored also at the spinal cord. In this context, metformin significantly inhibited oxaliplatin induced degeneration of IENF and activation of astrocytes in the spinal cord. Furthermore, oxaliplatin treatment induced a significant decrease threshold of the withdrawal response for mechanical stimulus and in the withdrawal latency response to heat stimulus. Additionally, oxaliplatin treatment also induced a significant increase in the withdrawal response duration to cold. Surprisingly, metformin cotreatment to rats treated with oxaliplatin maintained the sensory function performance at control levels. Altogether, these results suggest that metformin protects against OIPN. Finally, white blood cells, glycaemia and weight levels were

periodically assayed to evaluate the effects of our treatments over relevant physiological variables. The levels of all these variables remained in physiological ranges under all the treatments along the study. Those results suggest that our experimental model is resolute in a physiological framework in rats. Considering this, the administration regime, dosage and outcomes presented in this thesis could be potentially extrapolated to the clinical context.

In conclusion, this group of findings provide a fundamental set of proof of concepts to a potential treatment against CIPN based on metformin administration. However, further research is needed to determine the cellular and molecular mechanism behind the ubiquitous protective effect of metformin against the toxicity of oxaliplatin over pain fibers and consequent maintenance of the sensory function in the context of OIPN. Additionally, large scale studies are needed to extrapolate these findings to the context of CIPN treatment in humans.

10. INTRODUCTION.

10.1 Neuronal Fibers for Pain Perception.

Nerve fibers of the peripheral nervous system sense heat, cold, chemical and mechanical noxious stimuli (Kuner, 2010) [Figure N°1]. Anatomically, nerve cell bodies of sensory neurons at the peripheral nervous system are organized in a cluster (ganglia) at the dorsal root of spinal nerves (DRG). This group of peripheral sensory nerves is composed by pseudounipolar neurons that have peripheral sensory terminals at the skin and central terminals at the laminae I and II of the dorsal horn in the spinal cord [Figure N°1].

DRG neurons have been categorized by several criteria, including: the size of their cell body, degree of myelination, electrophysiological properties, peripheral innervation of sensory organs, central projection in the spinal cord, and gene expression profiles (Abraira and Ginty, 2013; Basbaum *et al.*, 2010; Lallemand and Ernfors, 2012). Considering all these criteria, DRG are composed by four widely accepted neuron categories: large diameter, thickly myelinated proprioceptive neurons; large diameter, myelinated A β low-threshold mechanoreceptors that mediate touch; medium sized, lightly myelinated A δ nociceptive neurons and small diameter, unmyelinated C nociceptive neurons that detect noxious stimuli including pain, itch, and temperature (Basbaum *et al.*, 2009) [Figure N°1].

Peripheral branches of DRG neurons have highly specialized free nerve endings known as Intraepidermal Nerve Fibers (IENF) [Figure N°1]. These nerve endings are in direct contact with the epidermis and mediate the transduction of several noxious stimuli through morphological adaptations and membrane receptors located at protrusions (Han, et al., 2013; Imamachi, *et al.*, 2009; Liu, *et al.*, 2009; Zylka, *et al.*, 2005). Importantly, membrane receptors that mediate sensory function at the IENF have a high degree of specialization for noxious stimuli (Owens and Lumpkin., 2014).

In the peripheral branches of DRG neurons, noxious stimuli applied to the skin deform the nerve endings or directly stimulate their membrane receptors (Woolf and Ma, 2007; Owens and Lumpkin., 2014). Consequently, ionic permeability of the transducer membrane receptors at the nerve endings changes in response to stimulation. Then, these changes in permeability generate a depolarizing current in the nerve endings (Purves, *et al.*, 2001; Owens and Lumpkin., 2014; Han., et al., 2013; Imamachi, *et al.*, 2009; Liu, *et al.*, 2009; Zylka, *et al.*, 2005). Specifically, noxious stimuli are transduced to electrical signals by transient receptor potential generating channels (TRP channels) or purinergic channels. In response to electrical, thermal, chemical or mechanical stimulation over IENF terminals, those transducer membrane receptor channels undergo conformational changes that modulate their ionic permeability inducing a depolarizing current. Consequently, these depolarizing signals are amplified by nearby sodium channels at DRG sensory neurons (Denk et al., 2014; Todd, 2010) [Figure N°1]. As a result, action potentials propagate retrogradely from the IENF through the peripheral axonal shaft to the central branches terminals of DRG sensory neurons at the laminae I and II in the dorsal horn of the spinal cord (Kuner, 2010; Denk *et al.*, 2014; Todd,

2010) [Figure N°1].

This overall process, in which the energy of a stimulus is converted into an electrical signal in the sensory neuron, is the critical first step in all sensory processing (Purves *et al.*, 2001; Owens and Lumpkin., 2014; Han et al., 2013; Imamachi *et al.*, 2009; Liu et al., 2009; Zylka *et al.*, 2005).

The quality of the noxious stimulus (i.e., what it represents and where is it coming from) is determined by the downstream signaling of the specialized receptors and by the synaptic relay that each DRG neuron subtype has at the spinal cord (David and Lumpkin., 2014; Rice and Albrecht, 2008; Gardner and Johnson, 2013). Furthermore, the intensity of each noxious stimulus is determined by the discharge frequencies triggered by the membrane receptors at the DRG neurons (Owens and Lumpkin., 2014; Rice and Albrecht, 2008; Gardner and Johnson, 2013).

In response to noxious stimulation, DRG sensory neurons also release signaling molecules (neuropeptides) and inflammatory mediators at their free nerve endings. In this context, based on the release of neuropeptides (e.g.: substance P), DRG sensory neurons are classified as peptidergic or non peptidergic (Owens and Lumpkin., 2014; Rice and Albrecht, 2008; Gardner and Johnson, 2013). At the skin, those signals participate in the integration between sensory reception at IENF and skin functions. In brief, neuropeptides fine-tune cutaneous immune response and promote skin maintenance and repair. Specifically, neuropeptides regulate keratinocyte proliferation/migration, immunocyte infiltration, dendritic cell activation and cutaneous neurogenic activation through a complex interaction of activating and inhibitory signaling at those target cells at the skin (Peters *et al.*, 2006). Those activating and inhibitory

neuropeptide functions in coordination with regulatory proteases keep the central stress-response, the peripheral cytokine production, and the local neurogenic inflammatory response in a balance (Peters *et al.*, 2006; Owens and Lumpkin., 2014; Rice and Albrecht, 2008; Gardner and Johnson, 2013).

At the spinal cord, glutamatergic synapses signalize to second order neurons of the central nervous system. In this process, noxious stimuli are processed and integrated before transmission to higher pathways of the CNS with distinct projections sites in the brain (Kuner, 2010; Gold and Gebhart, 2016). Specifically, lateral spinothalamic tracts transmit noxious sensory inputs to the lateral thalamus where sensory and discriminative aspects are processed (Kuner, 2010; Gold and Gebhart, 2016; Whalley, 2015; Colleoni and Sacerdote, 2010). In parallel, spinobrachial and spinothalamic tracts transmit noxious inputs to limbic system and the medial thalamus where emotional and aversive responses are generated [Figure N°1] (Kuner, 2010; Colleoni and Sacerdote, 2010; Whalley, 2015; Berger *et al.*, 2011).

Pain is a distressing experience associated with actual or potential tissue damage with sensory, emotional, cognitive and social components (Williams ^{and} Craig, 2016). This experience is a complex function of the nervous system that involves the interplay of peripheral and central sensory circuits. In brief, pain perception is processed at the cortex and accordingly, signals are transmitted to the motor tracts of the spinal cord to execute withdrawal from the pain source (Kuner, 2010; Gold and Gebhart, 2016) [Figure N°1].

Withdrawal of the limb from noxious stimuli (e.g.: heat, cold, touch) is executed through a flexion reflex that receives converging inputs from cutaneous receptors, spinal cord interneurons and upper motor neurons pathways. This flexion reflex stimulates rapid changes in muscular contraction at the limbs (Purves *et al.*, 2001; Owens and Lumpkin., 2014; Rice and Albrecht, 2008; Gardner and Johnson, 2013). Currently, the functional dynamics between those flexor reflex regulating inputs are still under research (Kuner, 2010; Gold and Gebhart, 2016). However, there is a consensus that descending pathways modulate a reflex arc between sensory neurons and motor neurons connected by interneurons at the spinal cord (Purves *et al.*, 2001; Owens and Lumpkin., 2014; Rice and Albrecht, 2008; Gardner and Johnson, 2013; Kuner, 2010; Gold and Gebhart, 2016). The activity of this complex circuitry promotes a fast excitation of flexor muscles and a reciprocal inhibition of extensor muscles at the limb in response to a noxious stimulus. Additionally, to promote postural support during the withdrawal reflex, the flexor muscles are inhibited, and the extensor muscles are excited in the contralateral limb to the noxious stimulus (Purves *et al.*, 2001).

The physiological role of pain is to protect tissues from further damage after a noxious stimulus. To achieve this, sensory neurons signalize to nociceptive pathways at the CNS until pain is so unpleasant that it cannot be ignored, and the withdrawal response is executed. Accordingly, noxious stimulation changes and pain is reduced or discontinued (Woolf and Ma, 2007). Under physiological conditions, the quality and intensity of this nociceptive pain is proportional to the noxious stimulus (Torres *et al.*, 2006). More importantly, nociceptive pain persists only during the presence of the noxious stimulus (Torres *et al.*, 2006). Consequently, dysfunctions of nociception and pain responses are pathological (Cox *et al.*, 2006; Indo,

2001).

Notably, it is widely known that pain could also be elicited because of the pathophysiological changes induced in the CNS or PNS by mechanical trauma, chemotherapy toxicity, viral infections, tumor invasion, ischemia or diabetes (Colleoni and Sacerdote, 2010; Boland *et al.*, 2014; Dworkin *et al.* 2003, Woolf and Mannion, 1999). In this respect, several studies have found abnormal sensory thresholds, ectopic impulse generation, conduction slowing, aberrant connectivity, neuronal loss, and glial scarring observed during neurodegeneration of CNS or PNS correlate with the onset or chronification of neuropathic pain in mammals (Howe *et al.*, 1977; Treede *et al.*, 1992; Pak *et al.*, 2018; Torres *et al.*, 2006; Basbaum and Woolf, 2009; Gold and Gebhart , 2016; Thacker *et al.*, 2007). Based on this, it has become widely accepted that several neurodegenerative conditions could lead to a persistent neuropathic pain. Under those conditions, the quality, intensity and duration of pain becomes inconsistent with the presence of a noxious stimuli.

Interestingly, several authors have reported an increase in membrane excitability (sensitization) of PNS and CNS neurons in the context of neurodegeneration at murine and human models (Urban and Gebhart, 1999; Treede *et al.*, 1992; Koltzenburg *et al.*, 1994; Basbaum and Woolf, 2009; Costigan *et al.*, 2009). In the PNS, sensitization has been related with an increase in the production, transport, and membrane insertion of sensory transducer channels and voltage-gated ion channels at the peripheral branches of DRG neurons (Treede *et al.*, 1992; Koltzenburg *et al.*, 1994; Basbaum and Woolf, 2009; Costigan *et al.*, 2009). In this context, it has been described that importin-dependent retrograde signaling mediated by

RasGTPase (Yudin *et al.*, 2008) activates significant transcriptional changes (2236 transcripts) at the soma of axotomized DRG neurons, including altered regulation of ion channels (Costigan *et al.*, 2002) and their accessory subunits (Pertin *et al.*, 2005). It has been proposed that master regulators such as the transcription factors Sox11, c-Jun, and ATF3 orchestrate those transcriptional changes at DRG neurons after injury (Seijffers *et al.*, 2007). Additionally, it has been also found that DRGs axonal gene translation modulate the synthesis of local effectors after injury (Jimenez-Diaz *et al.*, 2008). Interestingly, authors have proposed that transcriptional changes after injury promote an increase sodium and TRP channel currents through posttranslational changes mediated by cytokines and growth factors (Jin & Gereau 2006; Zhu & Oxford 2007). Concomitantly, it has been suggested that these pathological patterns of sensory channels expression induce a significant decrease in the threshold for activation of DRG neurons. Specifically, upregulation of voltage gated sodium channels Nav1.8, Nav 1.7 and Nav 1.3 has been functionally related to neuropathic pain after nerve injury using pharmacological inhibition or gene knockdown with antisense oligonucleotides (Hains *et al.*, 2003; Dong *et al.*, 2007, Ekberg *et al.*, 2006, Gold *et al.*, 2003, Jarvis *et al.*, 2007, Joshi *et al.*, 2006, Roza *et al.*, 2003; Hoyt *et al.*, 2007, Schmalhofer *et al.*, 2008). Furthermore, the hyperpolarization-activated cyclic nucleotide-modulated channel (HCN), also generates ectopic activity in DRG neurons after nerve injury (Luo *et al.*, 2007).

Under those conditions, noxious stimuli induce an increased pain response (hyperalgesia) (Fields *et al.*, 1998). [Figure N°1]. Interestingly, authors have reported a significant reduction of hyperalgesia associated with peripheral sensitization after antiinflammatory treatments in murine models (Kim *et al.*, 2006; Dworkin *et al.*, 2003; McMahon *et al.*, 2005; Thacker *et al.*, 2007). Considering this, accumulating evidence suggests that immune cells may play a central

role in the PNS related neuropathic pain.

On the other hand, sensitization at the CNS involves a significant increase in neurotransmitters release from DRG neurons central branches terminals at the spinal cord (Urban and Gebhart, 1999). For example, it has been shown that mechanical injury at the sciatic nerve induces neuropathic pain through activation of NMDA channels that are silent under physiological conditions at the postsynaptic sensory transmission neurons of the spinal cord (Inquimbert *et al.*, 2018; Campbell and Meyer *et al.*, 2006; Baba *et al.*, 2000; Aiyer *et al.*, 2018). Consequently, synapses between DRG neurons and postsynaptic sensory transmission neurons at the spinal cord strengthen after nerve injury. These altered transmission dynamics of the CNS nociceptive circuitry in the context of neurodegeneration exacerbate the responses to noxious stimuli (hyperalgesia). In addition, it has been reported that complete sciatic nerve transection, chronic constriction injury, or spared nerve injury also promote a decrease in the inhibitory postsynaptic currents from GABAergic interneurons at the spinal cord (Michaelis *et al.*, 1999; Moore *et al.*, 2002; Polgár *et al.*, 2005; Polgár and Todd, 2008). Consequently, spinal cord projection neurons depolarization threshold decreases. Furthermore, increased activity in spinal cord projection neurons induced by peripheral nerve damage leads to allodynia (pain in response to noxious stimulus that normally do not produce it) (Polgár and Todd, 2008; Keller *et al.*, 2007; Torsney and MacDermott, 2006) [Figure N°1].

Finally, it has been shown that neurodegenerative conditions are characterized by a significant accumulation of activated astrocytes and microglia around the terminals of central branches of

sensory DRG neurons at the dorsal horn of the spinal cord in mammals (Peng *et al.*, 2016; Gwak *et al.*, 2017; Ji *et al.*, 2013; Wen, *et al.*, 2011). Concomitantly, central sensitization after nerve injury has been related with microglial release cytokines such as TNF- α , interleukin-1 β and interleukin 6 at the spinal cord (Zhang, *et al.*, 2007). Furthermore, injection of activated brain microglia into cerebrospinal fluid (CSF) of the spinal cord reproduces neuropathic pain observed after nerve injury (Yao *et al.*, 2016). Considering this, glial activation during neurodegeneration may be enough to induce neuropathic pain.

Altogether, after the induction of pain in the context of a neurodegenerative condition, pathophysiological changes in the CNS and PNS contribute to the establishment of a chronic neuropathic pain. In this context, it is relevant to emphasize that it has been vastly demonstrated that sensory dysfunctions could outlast the progression of the neurodegenerative condition that originated them, and thus neuropathic pain could persist even if the underlying pathology is successfully treated (Basbaum and Jessell, 2000). As we mentioned before, this neuropathic pain could arise as hyperalgesia, when a stimulus that normally induces pain produces an exacerbated response, or even allodynia, when pain arises in response to a stimulus that normally does not induces it (Jensen and Finnerup, 2014) [Figure N°1].

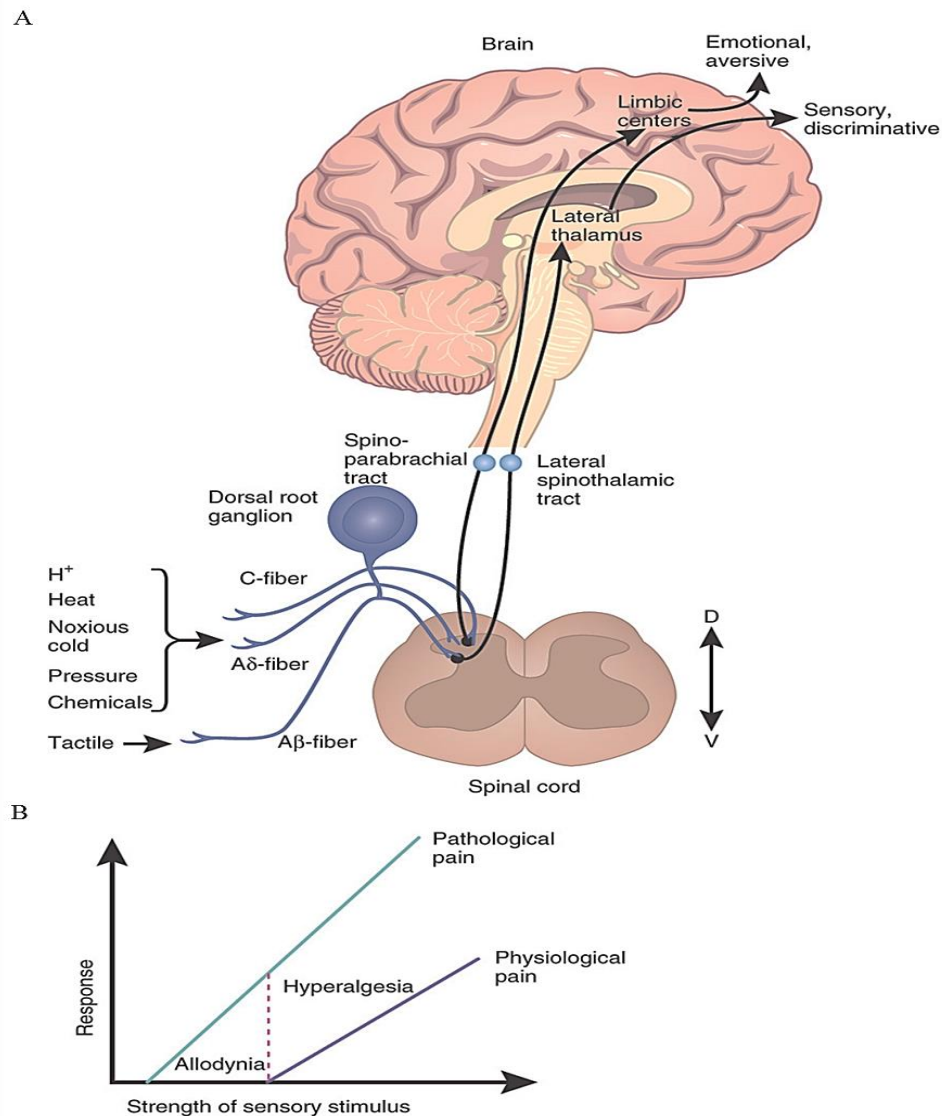


FIGURE N°1. Pain Sensory Afferent Pathways and Pain Sensitization. (A) Scheme showing major afferent sensory pathways involved in pain generation. Sensory receptors transduce Touch (Tactile), Heat, Cold and other stimuli at intraepidermal nerve fibers (IENF) in peripheral branch sensory tracts terminals to retrograde transmission. C, A β and A δ fibers are associated with receptors for specific stimuli. Sensory signal is retrogradely transmitted through peripheral and central branches of sensory dorsal root ganglia until synapses at the dorsal horn of spinal cord with spinothalamic and parabrachial pathways. Consequently, sensory information is processed at limbic centers and thalamus respectively, for sensory emotional response and discrimination components of pain. (B) Sensitization of sensory response induces pathological pain. Allodynia (pain due to a stimulus that does not usually provoke pain) and hyperalgesia (increased pain from a stimulus that usually provokes pain) manifest as pathological pain under several conditions including CIPN.

(Authorized reproduction from Kuner, 2010)

10.2 Pathology and Clinical Implications of Chemotherapy Induced Peripheral Neuropathy.

Chemotherapy induced peripheral neuropathy (CIPN) is primarily a sensory, rather than motor neuropathy, and involves morphofunctional anomalies in sensory circuits (Mohty *et al.*, 2010). More specifically, common findings during CIPN include degeneration of intraepidermal nerve fibers (IENFD), axonal degeneration (AD), ATF3 nuclear localization at DRGs, focal demyelination and inflammation at both PNS and CNS (Pachman *et. al*, 2014; Argyriou *et. al*, 2014; Wolf *et. al*, 2008; Bennett, *et al.*, 2011). Furthermore, reduction in the amplitude of nerve action potential has been also reported in sensory axons of the peripheral nervous system during CIPN (Leandri *et al.*, 2012). Additionally, some reports suggest that toxicity of chemotherapy affects terminals of the central branches of sensory dorsal root ganglia at the spinal cord (Han and Smith, 2013). Despite the very recent reports of chemotherapeutics toxicity over CNS, current terminology (i.e.: CIPN; OIPN) still refers only to peripheral neuropathy induced by chemotherapeutics. Due to the lack of consensus over the relevance of chemotherapy induced maladaptative changes at the CNS on the chemotherapy induced neuropathy pathology there is not a current wider terminology on the field. Based on this, this thesis uses the acronym CIPN (or OIPN) to referring also to CNS phenotypes in response to chemotherapy.

Moreover, the morphofunctional anomalies in sensory circuitry observed during CIPN have been related with clinical manifestations such as neuropathic pain, paresthesia, hyperalgesia, tingling, allodynia, numbness and vibratory sensation (Stubblefield *et al.*, 2009; Argyriou *et*

al., 2014). In this respect, it has been suggested that clinical manifestations of CIPN involve abnormal gain in sensory function or a loss of sensory function or even a complex combination of the former ones (Stubblefield *et al.*, 2009; Argyriou *et. al.*, 2014). Currently, it is unclear why some patients experience loss of sensory function while others experience augmented sensibility.

In anatomical terms, it has become widely accepted that CIPN related sensory dysfunction begins mainly at arms and legs (Cavaletti and Marmiroli, 2010). This sensory dysfunction pattern has been related with the dying back degeneration of larger sensory nerves that innervate limbs (Brown *et al.*, 2014).

Chemotherapy induced peripheral neuropathy (CIPN) is a major side effect on most of cancer therapies. This side effect limits the dose and duration of chemotherapies by affecting long term quality of life and is the main cause of anti-cancer treatment discontinuation because its symptoms often become too severe, debilitating or even life threatening (Bhatnagar *et al.*, 2014; Ferrier *et al.*, 2013; Seretny *et al.*, 2014). Interestingly, around a half of patients under chemotherapy receive drugs that are proven inductors of CIPN (McWhinney *et al.*, 2009). Specifically, vinca alkaloid derivatives and taxol, proteasome inhibitors, angiogenic inhibitors and platinum derivative agents-cisplatin, carboplatin, oxaliplatin-(Fehrenbacher, 2015). Unfortunately, there are no current clinical probes to predict predispositions to develop CIPN (Boyette-Davis *et al.*, 2013). Considering this, CIPN is a major clinical problem.

10.3 Oxaliplatin Induced Peripheral Neuropathy.

In this thesis we will focus on the toxicity of oxaliplatin, a third generation platinum derivative, over the peripheral sensory nervous system. Oxaliplatin is used in the adjuvant and palliative treatment for digestive tumours, especially colorectal and gastric cancer (Yothers *et al.*, 2011; Park and Chun, 2013). These types of cancers together affect between 1,400,000 and 952,000 people worldwide per year (Qureshi *et al.*, 2014). In this group, colo-rectal cancer (CRC) alone is the third most common cancer worldwide (American Cancer Society, 2009).

Oxaliplatin induced peripheral neuropathy (OIPN) is catalogued as a grade 3 manifestation in NCI-Common Terminology Criteria for Adverse Events, considering it as severe symptoms of neuropathy that limit everyday activities of daily living, and even a grade 4 manifestation, which indicates a life threatening neuropathy (U.S. Department of health and human services, 2009). Unfortunately, it has been reported that around 70-86% of patients treated with oxaliplatin have some degree of both acute and /or chronic neurological symptoms in the context of an oxaliplatin chemotherapy induced peripheral neuropathy (OIPN) (Ewertz *et al.*, 2015; Ibrahim *et al.*, 2004). This emphasizes the potential direct toxicity of oxaliplatin over nervous system cells during chemotherapeutic treatments.

In one hand, OIPN can present as acute distal paraesthesia's and thermal allodynia, which appear soon after oxaliplatin administration (Brzeziński, 2012a; Ling *et al.*, 2007). This syndrome is transient and reversible within hours, days or weeks (Grisold *et al.*, 2012;

Toyama *et al.*, 2013). OIPN has been associated with significant peripheral nerve hyperexcitability, which suggests an immediate pharmacologic rather than structural basis for acute symptoms (Webster, RG., *et al.*, 2005). In this respect, it has been suggested that the oxaliplatin-induced acute neurotoxicity is mediated by neural sodium channels dysfunction (Park *et al.*, 2000). More specifically, oxalate, a cytotoxic metabolite of platinum derivatives, chelates calcium and modifies the activity of neural calcium dependent sodium channels (Grolleau *et al.*, 2001). Furthermore, oxalate alters the intracellular divalent cation equilibrium impairing neuronal homeostasis (Gamelin *et al.*, 2002).

On the other hand, it has been proposed that a chronic manifestation of OIPN occurs in response to high cumulative doses and it is presented as a persistent sensory neuropathy (Kawashiri *et al.*, 2014). This persistent sensory neuropathy interferes with the normal activities of patients. More importantly, chronic manifestation of OIPN may lead to chemotherapy dose reduction or even cessation. Thereby limiting potential anti-cancer benefits and greatly impacting on patient survival. Unfortunately, several clinical studies indicate that a dose reduction or discontinuation occurs in more than 60% of oxaliplatin treatments due to chronic OIPN (Grisold *et al.*, 2012; Wolf *et al.*, 2008; Kannarkat *et al.*, 2007). Among them, 64% to 97% of patients still show chronic neurological symptoms after one year post last oxaliplatin administration. Even more, around 12% of patients experiences a serious chronic neuropathy that severely affects their quality of life (Grisold *et al.*, 2012; Wolf *et al.*, 2008; Kannarkat *et al.*, 2007).

The aforementioned effects of oxaliplatin over the nervous system are caused by the mechanism of toxicity of oxaliplatin that is the basis of its antineoplastic clinical use. In brief, after administration, oxaliplatin is converted into an aqueous form by non-enzymatic conversion in the physiological medium (Di Francesco *et al.*, 2002). The resulting molecular conformation promotes the interaction of oxaliplatin with nitrogen bases at nucleic acids and sulfhydryl groups of proteins (Di Francesco *et al.*, 2002). Concomitantly, it has been reported that the antineoplastic effect of oxaliplatin is specifically related with the formation of adducts with the DNA. This DNA binding property of oxaliplatin induces the arrest of DNA synthesis and repair processes during cell proliferation and consequently promotes cell death by apoptosis (Di Francesco *et al.*, 2002; Cascinu, 2002). Additionally, the interaction of oxaliplatin with proteins has been also related with cytotoxicity beyond the cell death promotion. Moreover, it has been suggested that the secondary effects of oxaliplatin are based on the same DNA and proteins interaction properties affecting also non-replicating cells (Di Francesco *et al.*, 2002; Cascinu, 2002). Altogether, in the context of chemotherapy, oxaliplatin neurotoxicity and antineoplastic effect would share cellular targets. This results in an extremely complex clinical scenario when trying to prevent the OIPN while treating cancer.

Considering the aforementioned, it is important to remember that the nervous system is protected by the permeability properties of its surrounding vasculature through barriers that regulate the passage of blood components into neural tissue. In one hand, Blood Brain Barrier (BBB) operates as a network of tight junctions and regulated nonspecific transcytosis at vessels endothelial cells that inhibits proteins and macromolecules passage to the CNS (Kodji *et al.*, 2016; Jacobs, 1976; Fullerton *et al.*, 2001; Kiernan, 1996). Also, a matrix of collagen,

laminin, and heparan sulfate at the luminal side of CNS capillaries contributes to the impermeability of the BBB to charged molecules of high molecular weight. In parallel, endothelial cells upregulate specific transport mechanism to supply particular proteins and nutrients and maintain homeostasis of the CNS (Kodji *et al.*, 2016; Jacobs, 1976; Fullerton *et al.*, 2001; Kiernan, 1996). On the other hand, peripheral nerves are protected by two selective structures that compose the Blood Nerve Barrier (BNB). First, PNS capillaries endothelia also have tight junctions that regulate the passage of molecules from the blood to peripheral nerves. Additionally, BNB permeability properties are also based on the enwrapment of the fascicles of peripheral axons by multiple layers of fibroblast derived cells (perineurium) (Kodji *et al.*, 2016; Jacobs, 1976; Fullerton *et al.*, 2001; Kiernan, 1996). This component of the BNB restricts the diffusion of ions and nutrients by tight junctions between fibroblast derived cells. Importantly, it has been reported that PNS capillary endothelia are considerably more permeable than in BBB, allowing the presence at the peripheral endoneurium of proteins that are completely excluded from CNS (Kodji *et al.*, 2016; Jacobs, 1976; Fullerton *et al.*, 2001; Kiernan, 1996). Even more, it has been also reported that ganglia of sensory neurons are surrounded by a perineurium that is fully permeable to macromolecules and extravasated proteins, while central and peripheral branches of these neurons are surrounded by BBB or BNB respectively (Jimenez-Andrade *et al.*, 2000; Kodji *et al.*, 2016; Kiernan, 1996). In this context, it has been proposed that the metabolic needs at the ganglia of sensory neurons are supplied by vessels with similar permeability than non-nervous tissues (Kodji *et al.*, 2016; Kiernan, 1996). Furthermore, the differential permeability between endothelial components BBB and BNB has been related with higher transport rates and less adherent tight junctions in the PNS (Kodji *et al.*, 2016; Jacobs, 1976; Fullerton *et al.*, 2001; Kiernan, 1996).

Interestingly, this differential permeability between CNS and PNS barriers is highly relevant to the analysis of OIPN pathophysiology considering that DRG neurons have central and peripheral branches that are exposed to permeabilities of either BBB or BNB respectively. Furthermore, this characteristic of DRG has been related with a susceptibility to neurodegeneration by preferential accumulation of toxic agents in comparison to neurons only surrounded by BBB (Jimenez-Andrade *et al.*, 2000; Kiernan, 1996; Screnci *et al.*, 2000).

Notably, BBB permeability to oxaliplatin has been studied scarcely. Despite this, it has been shown that the mean concentration of oxaliplatin in CSF is low and consequently, it has been suggested that BBB is highly impermeable to this drug (Jacobs *et al.*, 2005; Huang *et al.*, 2016). More specifically, it has been recently reported that platinum concentration peaks in CSF 30 min after intravenous administration of 5mg/Kg oxaliplatin in a model of non-human primates (Jacobs *et al.*, 2005). In the same study, the mean concentration ratio of oxaliplatin between CSF and plasma ultrafiltrate was 2 per cent. Furthermore, only 25% of that oxaliplatin measured in CSF of non-human primates was estimated as an active drug (Jacobs *et al.*, 2005). In this context, organic cationic transporters (OCTN1 and OCTN2) have been proposed as the major contributors of the oxaliplatin cytotoxicity (Zamboni *et al.*, 2002; Zhang *et al.*, 2006), although their presence on the plasma membranes of the BBB endothelial compartment is still under debate and the results seem to depend on the experimental models (Jacobs *et al.*, 2010; Wu *et al.*, 2015). However, it has been reported that OCTN1 and OCTN2 proteins are expressed in Brain Microvessels (BMV) cell lines from humans, rats (Wistar) and mice (C57BL/6) (Lin *et al.*, 2010). Interestingly, some authors have proposed that OCTNs

could participate in the efflux of drugs from CNS as unsaturated active efflux transporters (Sawchuk and Elmquist, 2000; Kusuhara and Sugiyama, 2005). Considering this, a potential efflux from BBB through OCTNs could be the mechanism underlying low concentration of oxaliplatin in CSF.

Up to date, most studies have focused on the penetration of oxaliplatin to the CNS immediately after a single administration rather than under repeated administration regimes (Jacobs *et al.*, 2005; Huang *et al.*, 2016). Thus, potential changes in BBB permeability after cumulative doses of oxaliplatin remain unexplored. Moreover, to our knowledge, oxaliplatin concentration in peripheral has never been estimated. However, as we mentioned before, it is assumed that BNB is considerably more permeable than BBB to oxaliplatin.

Beyond the potential role of permeability in oxaliplatin effect over the sensory circuitry, it has been extensively demonstrated that oxaliplatin intraperitoneal administration in murine models of chemotherapy induces several maladaptive phenotypes in both CNS neurons and glial cells (Renn *et al.*, 2011; Di Cesare Mannelli *et al.*, 2013; Di Cesare Mannelli *et al.*, 2014; Di Cesare Mannelli *et al.*, 2015). Specifically, it has been shown that every other day by one week administration of oxaliplatin induces significant IENFD in rats (Boyette-Davis *et al.*, 2011a; Toyama *et al.*, 2013). Furthermore, oxaliplatin treatment also induces swollen and vacuolated mitochondria in axons (Zheng *et al.*, 2011), axonal degeneration and demyelination at sciatic nerve of murine models (Han and Smith, 2013). Notably, it has been also established that direct administration of oxaliplatin at spinal cord (6,6 nM) significantly increases abnormal field potential firing activity in the dorsal horn of rats (Huang *et al.*, 2016). In correlation,

acute mechanical allodynia and thermal hyperalgesia was reported in the same study (Huang *et al.*, 2016). Furthermore, intraperitoneal administration of oxaliplatin doses extrapolated from human chemotherapeutics regimes significantly reduces the sensory nerve conduction velocity in sciatic nerves of Wistar rats *in vivo* (Cavaletti *et al.*, 2001). Altogether, these results suggest that the OIPN induced by the administration of oxaliplatin in the context of cancer treatment, could be related with the presence of oxaliplatin in CSF, affecting neural cells directly. Accordingly, the molecular identity responsible for oxaliplatin transport into DRG has been a highly relevant topic for OIPN studies. Overall, considering that platinum accumulation within DRG neurons has been proposed as the major determinant of oxaliplatin neurotoxicity as we mentioned earlier (Screnci *et al.*, 1997; Screnci *et al.*, 2000; Holmes *et al.*, 1998; Luo *et al.*, 1999; Ta *et al.*, 2006). Interestingly, oxaliplatin transporters OCTN1 and OCTN2 transport oxaliplatin and are expressed in soma of DRG neurons and mediate DRG oxaliplatin uptake *in vitro* (Jong *et al.*, 2011). To our knowledge, *in vivo* OCTNs presence in central or peripheral branches of the DRG neurons remains unexplored.

Furthermore, other maladaptive phenotypes in DRG neurons have been reported in the context of OIPN. For example, it has been suggested that DRG neurons of mice treated with oxaliplatin express significantly more cold transducers. Specifically, a significantly higher levels of TRPM8 after a single oxaliplatin dose has been reported (Han and Smith, 2013). Besides that, it is also known that administration of oxaliplatin induces a significant increase in ATF3 nuclear localization in rats (Kawashiri *et al.*, 2014; Renn *et al.*, 2011).

Morphological and cytological changes in pain circuitry changes after oxaliplatin treatment have been related to sensory impairment in mammals. Importantly, it has been vastly demonstrated that sensory dysfunctions studied in murine models are analogous to the sensory dysfunctions reported in patients (Koltzenburg *et al.*, 1994; Rowbotham and Fields, 1996; Mogil *et al.*, 1999). Specifically, oxaliplatin treatment induces a significant lower pain threshold in response to touch in mice (Toyama *et al.*, 2013). Furthermore, oxaliplatin also induces a sensitization to cold stimuli. Sensory tests of pain in response to cold report a longer withdrawal response after oxaliplatin treatment (Toyama *et al.*, 2013). Altogether, these morphofunctional changes in pain fibers reproduce the clinical manifestations of OIPN.

Finally, several strategies have been proposed to alleviate CIPN. Among them, coadministration of antioxidants (vitamin C, vitamin E, N-Acetylcysteine and glutathione) (Pace, 2003; Argyriou *et al.*, 2005; Cascinu, 2002; Lin *et al.*, 2006) adrenocorticotrophic hormone analogues (ORG 2766) (Van der Hoop *et al.*, 2014; Roberts *et al.*, 1998), calcium-magnesium infusions (Loprinzi *et al.*, 2014; Gamelin *et al.*, 2004), antiepileptic drugs like carbamazepine, gabapentin and glutamine (Lersch *et al.*, 2002; Wang *et al.*, 2007), amifostine (Penz *et al.*, 2001), and glutathione (Cascinu *et al.*, 2007). However, the ability of these compounds to relieve pain in CIPN pre-clinical models is modest or null. Concomitantly, meta-analysis of clinical trials for OIPN prevention report inconclusive results as determined using quantitative measures of neuropathy (Seretny *et al.*, 2014). Actually, the American Society for Clinical Oncology (ASCO) guidelines for prevention and management of chemotherapy-induced peripheral neuropathy states there are no agents recommended for the prevention of CIPN (Hershman *et al.*, 2014).

10.4 Metformin Role in Cancer and Neurodegeneration.

Metformin is an antidiabetic drug that was approved by FDA in 1995 to be used in the therapy of hyperglycaemia in humans (Potts and Lim., 2012). Currently, metformin is one of the most recommended medications worldwide (Goswami *et al.*, 2012).

The main systemic effect of metformin is reduction of glycaemia, by inducing activation of AMP activated protein kinase (AMPK) in hepatocytes, which modifies energy consumption by regulating carbohydrate and lipid metabolism through insulin signaling (Viollet *et al.*, 2012). AMPK activation by metformin also inhibits mitochondrial respiration by targeting mitochondrial complex I activity, which in turn activates mitochondrial β -oxidation (Viollet *et al.*, 2012; Mahmood *et al.*, 2013; Cho and Kieffer, 2011). Consequently, it increases the uptake and utilization of glucose by skeletal muscle and adipose tissues (Cho and Kieffer, 2011). Furthermore, systemic effects of metformin include increase the plasma glucagon-like peptide 1 (GLP-1) and gene expression of islet incretin receptor via peroxisome proliferator activated receptor- α (PPAR- α) (Viollet *et al.*, 2012; Mahmood *et al.*, 2013; Cho and Kieffer, 2011). Altogether, these effects of metformin lead to a decrease in the hepatic glucose production. After oral administration, metformin has a plasma elimination half-life of 6.2 hours and 90% is eliminated by the renal system (Lipska *et al.*, 2011). Importantly, the lowering of blood glucose levels by metformin is only observed in people with diabetes and insulin resistance but has no effect on healthy people, except those who have been subjected to prolonged fasting (Mahmood *et al.*, 2013).

In the last years, metformin treatment in patients with diabetes has been associated with a significantly lower incidence of cancer related mortality (Ateron *et al.*, 2010). In this context, meta-analysis of observational studies indicates a significant correlation between metformin treatment for type 2 diabetes and reduction in risk of liver, colorectal, pancreatic, gastric, esophagus and breast cancer (Lee *et al.*, 2011; Franciosi *et al.*, 2013).

Beyond the statistical correlation between metformin treatment and lower cancer mortality, it has been also suggested that metformin specifically enhances antineoplastic effects of certain chemotherapeutics. Interestingly, different *in vitro* studies have proposed that metformin may enhance the efficacy of anti-cancer treatments (Lin *et al.*, 2014; Honjo *et al.*, 2014; Qu *et al.*, 2014; Lau *et al.*, 2014). Specifically, it has been reported that metformin synergizes with the antineoplastic effects of Gemcitabine and Resveratrol separately in *in vitro* models of pancreatic cancer by significantly reducing tumor growth and inducing apoptosis of cancer cells (Shi *et al.*, 2016; Zhu *et al.*, 2016). Additionally, metformin also induces a decrease in proliferation of bile duct cancer cells (cholangiocarcinoma) in cotreatment with gemcitabine and cisplatin (Park *et al.*, 2015).

Notably, synergy between metformin treatment and chemotherapy also occurs *in vivo*. Recently, it has been reported that oral metformin administration significantly increases the survival of mice undergoing glioma, promoting apoptosis and formation of tumors induced by Temozolomide (Yu *et al.*, 2015). Finally, metformin also synergizes with oxaliplatin in the reduction of colon cancer tumors and angiogenesis in mice and consequently metformin significantly increases lifespan (Zaafar *et al.*, 2014). Altogether, these results suggest that

metformin is a potentially relevant coadjuvant of chemotherapeutics and emphasizes the need of further research on this topic.

On the other hand, neuroprotective effects of metformin started to be reported as a consequence of glycaemia regulation in the context of diabetes (Sharma *et.al*, 2012). However, in the last years, neuroprotection with metformin has been extended to other inductors of degeneration. In this respect, it has been reported that metformin *per se* significantly diminishes A β induced reduction of human neural stem cells by inhibition of apoptosis in an *in vitro* model of Alzheimer (Chiang *et al.*,2016). Furthermore, several independent studies have shown that metformin also inhibits 1-methyl-4-phenyl-1, 2, 3, 6-tetrahydropyridine (MPTP) and 3, 4-methylenedioxymethamphetamine (MDMA) induced degeneration of dopaminergic neurons at the *substantia nigra pars compacta* in murine models of Parkinson disease (Bayliss *et al.*, 2016; Francesca *et al.*, 2016; Lu *et al.*, 2016). Finally, neuroprotective effects of metformin extend beyond degeneration in response to chemo toxicity and also it has been reported that metformin significantly reduces neuronal apoptosis in a model of global cerebral ischemia in rats (Ashabi *et al.* 2014). Thus, metformin could potentially act as a neuroprotective drug in response to other inductors of degeneration in neurons.

Considering all the previously reported experimental evidences mentioned along this introduction, we aimed to determine whether metformin could exert neuroprotection in a model of oxaliplatin chemotherapy induced peripheral neuropathy (OIPN). To this goal we proposed the following hypothesis and experimental objectives.

10.5 Hypothesis:

Metformin inhibits painful neuropathy induced by the toxicity of oxaliplatin over dorsal root ganglia neurons and is innocuous for antineoplastic effects of oxaliplatin.

10.6. General Objective:

Explore the effect of metformin over an *in vitro* model of the antineoplastic properties of oxaliplatin and an *in vivo* model of rat painful neuropathic induced by oxaliplatin.

10.7. Specific Objectives:

10.7.1 Specific Objective N°1: Evaluate the survival of MKN45, Kato III and HS746T gastric cancer cell lines under oxaliplatin and/or metformin treatment *in vitro*.

10.7.2 Specific Objective N°2: Evaluate the degeneration of rat DRG neurons and astrocyte reactivity at spinal cord sensory DRG neurons relay laminae under oxaliplatin and/or metformin treatment *in vivo*.

10.7.3 Specific Objective N°3: Evaluate the mouse withdrawal response to thermal, cold and touch stimulation during oxaliplatin and/or metformin treatment *in vivo*.

11. MATERIALS.

11.1 Culture Media and General Reactives.

- 5-Fluoro-2'-deoxyuridine $\geq 98\%$ (Sigma-Aldrich Cat. No. 856657).
- Acetone for analysis, ACS standard (Merck-Millipore Cat. No. 100014).
- Aphidicolin from *Nigrospora sphaerica* $\geq 98\%$ (HPLC) (Sigma-Aldrich Cat. No. A0781).
- B27 Supplement 50X, serum free, cell culture grade (Thermo-Fisher Cat. No. 17504044).
- Cold Water Fish Skin Gelatin (Sigma-Aldrich, Cat. No. G704).
- Collagen I Rat Protein, Tail (Thermo-Fisher, Cat. No. A1048301).
- D-glucose, $C_6H_{12}O_6$, cell culture tested (Sigma-Aldrich, Cat. No. G7021).
- Dulbecco's Modified Eagle Medium (DMEM), ISO13485 standard (Thermo-Fisher Cat. No. 12491015).

- EDTA; Ethylenediaminetetraacetic acid anhydrous, crystalline, BioReagent, suitable for cell culture (Sigma-Aldrich, Cat. No. E6758).
- Ethanol, ACS, ISO, and Reag. Ph. Eur standards (Merck-Millipore, Cat. No. 1009832500).
- Fetal Bovine Serum (FBS) (Biological Industries Cat. No.04-001-1A) *was used for cell line cultures.*
- Fetal Bovine Serum (FBS), ISO13485 standard (Thermo-Fisher, Cat. No. 10437-028) *was used for primary dorsal root ganglia culture.*
- Fluoromont G (Electron Microscopy Sciences, Cat. No. 17984-25).
- Glycerol, BioReagent, suitable for cell culture, suitable for insect cell culture, suitable for electrophoresis, $\geq 99\%$ (GC) (Sigma-Aldrich, Cat. No. G2025).
- Glycine, for electrophoresis, $\geq 99\%$ (Sigma-Aldrich, Cat. No. G8898).
- Hydrochloric acid 37%, ACS, ISO, and Reag. Ph. Eur standards (Merck-Millipore, Cat. No. 100317).
- Isopropanolol, ACS, ISO, and Reag. Ph. Eur standards (Merck-Millipore, Cat. No.109634).
- L-glutamine 200 mM, animal origin free, ISO13485 standard (Thermo-

Fisher, Cat. No. 25030-081).

- Manganese Chloride Tetrahydrate ($\text{MnCl}_2 \times 4\text{H}_2\text{O}$) 99, 99% trace metal basis (Sigma-Aldrich, Cat. No. 203734).
- MEM Non-Essential Amino Acids, ISO13485 standard (Gibco Cat. No. 12492013).
- Methanol, ACS standard. (Merck-Millipore, Cat. No. 1070182511).
- Neurobasal Medium (NBS) Serum Free (Thermo-Fisher, Cat. No. 21203049).
- OCT (Sakura Finetek, Cat. No. 4583).
- Paraformaldehyde Powder 95% (Sigma-Aldrich, Cat. No. 158127).
- Penicillin-Streptomycin 100X 10,000 U/mL (Thermo-Fisher, Cat. No. 15140-122).
- Poly-L-lysine hydrobromide (PLL) molecular weight 30,000-70,000 (Sigma-Aldrich, Cat. No. P2636).
- Potassium chloride Molecular Biology Grade (Merck Millipore Cat. No. 7447407).
- RPMI Medium; Roswell Park Memorial Institute Medium, ISO13485 standard (Gibco Cat. No. 12633012).
- Sodium bicarbonate (NaHCO_3), ACS, ISO, and Reag. Ph. Eur

standards (Merck-Millipore, Cat. No. 1063290500).

- Sodium chloride (NaCl) ACS, ISO, and Reag. Ph. Eur standards (Merck-Millipore, Cat. No. 1064041000).
- Sodium hydroxide (NaOH) (Sigma-Aldrich, Cat. No. S5881).
- Sodium phosphate dibasic 99.95% trace metals basis (Sigma-Aldrich, Cat. No.255793).
- Sodium phosphate monobasic BioReagent, for molecular biology, anhydrous, $\geq 98\%$ (Sigma-Aldrich, Cat. No S3139).
- Sodium pyruvate 100 mM, ISO13485 standard (Gibco Cat. No. 11-360-070).
- Sucrose for molecular biology, $\geq 99.5\%$ (GC) (Sigma-Aldrich S0389).
- Triton-X-100 laboratory grade (Sigma-Aldrich, Cat. No. 234729).
- Trizma[®] base Primary Standard and Buffer, $\geq 99.9\%$ (titration), crystalline (Sigma-Aldrich Cat.No. T1503).
- Trypsin 2, 5 % 10X (Thermo-Fisher, Cat. No. 15090046).
- Vectashield antifade mounting medium (Vector Laboratories Cat. No.H-1000).

11.2 Markers, Reporters and Antibodies.

- DAPI; 4', 6-Diamidino-2-Phenylindole, Dihydrochloride (Thermo-Fisher, Cat. No. D1303).
- ExtrAvidin-FITC from *Streptomyces avidinii* (Sigma-Aldrich, Cat. No. E2761).
- Goat anti-mouse Alexa 488 igG (H+L) secondary antibody (Molecular Probes, Cat. No. A11029).
- Goat anti-rabbit Alexa 546 igG (H+L) secondary antibody (Molecular Probes, Cat. No. A-11035).
- Isolectin GS-IB₄ from *Griffonia simplicifolia*, biotin-XX Conjugate (Thermo Fisher, Cat. No. I21414).
- Mouse Anti- Activating Transcription Factor (ATF3), protein G purified (95% Approx.), Suitable for: WB, Dot Blot, ICC/IF, IHC-Fr (Abcam, Cat.No. ab58668).
- Mouse anti-Acetylated Tubulin primary antibody, 6-11B-1, monoclonal, purified from hybridoma cell culture, suitable for: WB, IF, IHC and EM. (Sigma-Aldrich, Cat. No. T7451).
- MTT 98%; 3- [4, 5-dimethylthiazol--2-yl]-2, 5-diphenyl tetrazolium bromide (Sigma-Aldrich, Cat. No.M2128).
- Rat Anti -PGP 9.5, 98% purity, suitable for WB, IHC and IF

(Ultraclone, Cat.No. Limited 31A).

- Rat Anti-Glial Fibrillary Acidic Protein (GFAP), suitable for IHC and IF (Dako, Cat.No. N1506).
- Rat Anti-Neurofilament 200 (NF-H), suitable for IHC, microarray and WB (Sigma-Aldrich, Cat.No. N4142).
- Tetramethylrhodamine, Methyl Ester, Perchlorate (TMRM) (Thermo-Fisher, Cat. No. T-668).

11.3 Drugs and Treatments.

- Metformin; 1, 1-Dimethylbiguanide Hydrochloride, 97% (Sigma-Aldrich, Cat. No. D150959).
- Oxaliplatin Ebewe Recalcine Pharma 5mg/mL (Recalcine Ebewe Pharma).
- Ringer-Lactate physiological serum (Fresenius-Kabi).

11.4 Plastic Materials, Surgical Instruments and Medical Supplies:

- 1, 5 mL Microcentrifuge tubes (SSI, Inc.).
- 12 mm coverslips (Marienfeld, Cat. No. 0111520).
- 15 mL FALCON conical centrifuge tube (Genexpress Cat. No. FC.352097).
- 24-well multiwell dishes (TrueLine, Cat. No. TR5002).
- 50 mL FALCON conical centrifuge tube (Genexpress Cat. No. FC.352098).
- 6-well multiwell dishes (TrueLine, Cat. No. TR5000).
- Bacteriologic culture plastic dishes (ISOLAB, Cat. No. 081.02.091).
- Economy Tweezers #5, 11cm, 0.4x0.45 (WPI, Cat. No. 501979).
- Falcon™ Cell strainer (Fisher Scientific, Cat. No. 08-771-2).
- Gillies Dissecting Forceps, 15.5cm, Straight, 1x2 teeth (WPI, Cat. No. 501266).
- Mini Dissecting Scissors, 8.5cm, Curved, Blunt Tips (WPI, Cat. No. 503668).
- Operating Scissors, 14cm, Blunt/Blunt, Curved (WPI, Cat. No.

501222).

- Operating Scissors, 16cm, Sharp/Sharp, Straight (WPI, Cat. No. 501225).
- Spring Scissors, 14cm, Round Hand les, straight, 6.5mm Blades (WPI, Cat. No. 14111).
- Syringe, 1mL with 25G 5/8 tuberculin needle, disposables (TCL Cat. No. JD-01T2516-SB by Nipro).
- Syringe, 5mL with 21X 1 ½ l/lock tip needle, disposable (TCL Cat. No. JD-05L2138-SB by Nipro).
- Tissue Forceps, 12.5cm long, Curved, 1x2 Teeth (WPI, Cat. No. 501216).
- Vannas Scissors, 8.5cm, Curved, 7mm Blades (WPI, Cat. No. 501232).

11.5 Specialized Hardware, Devices and Equipment:

- Basic CO2 Water Jacketed Incubator, Infrared (IR) Sensor, 6, 7 Cu. Ft. 220V (Shell Lab, Cat. No. 2406-2).
- BioTek EL800 microplate reader (BioTek instruments, Inc.).

- Blood Glucose Monitor SD Codefree Meter (SD Biosensor, Inc.).
- Blood Glucose Test Strips (SD Biosensor, Inc.).
- Carbon Dioxide 95% gas cylinder (AGA).
- Class II, Type B2 (Total Exhaust) Biosafety Cabinet (Labconco).
- Horiba ABX Micros 60 Hematology Analyzer (Horiba Ltd.).
- Olympus IX81-DSU microscope (Olympus).
- Orca-R2 camera (Hamamatsu, Cat. No. C10600-10B).
- Plantar Test Hargreaves Apparatus (Ugo Basile Cat. No. 37370).
- Semmes-Weinstein monofilaments for Touch Sensory Evaluation of Von Frey Test (Stoelting Co., Cat. No. 58011).

11.6 Software:

- Fiji (NIH).
- Graphpad Prism 6 (Graphpad Software)
- ImageJ 1.48v (NIH).
- Olympus Xcellence (Olympus).

12. METHODS.

12.1 Animal Housing and Handling.

Adult Sprague Dawley rats weighting 250g at the beginning of the experiment were purchased from Harlan Biosciences. Rats were housed on a 12h light/dark cycle with *ad libitum* food and water. Experiments with animals followed protocols approved by the NIH Institutional Animal Care and Use Committees and complied with National Institutes of Health guidelines (Pitts *et al.*, 2002). We report this study in compliance with the ARRIVE guidelines 63 for animal handling and housing (Kilkenny *et al.*, 2010).

12.2 OIPN Animal Model and Metformin Treatment.

We developed a model of OIPN where adult Sprague Dawley rats (250 grs) were injected intraperitoneally (i.p.) with oxaliplatin (4 mg/Kg i.p.) in two consecutive days for two times every week, for 4 weeks [Figure N°2]. Considering this regime, oxaliplatin total cumulative dose at 4 weeks was 32 mg/Kg per rat. This dosage is in the range of the clinical cumulative oxaliplatin dose causing chronic neuropathy (De Gramont *et al.*, 2000; Souglakos *et al.*, 2002). To our knowledge, this is the first time, these particular concentrations and dosage of metformin and oxaliplatin in cotreatment is used to explore the readouts we show on this

thesis. The selection of those experimental drug concentration and dosage was based on a comprehensive review of bibliography.

Current FDA standards recommend the use of the Reagan-Shaw method for extrapolation between human and animal doses in the context of preclinical studies (Reagan-Shaw *et al.*, 2008). This algorithm calculates the human extrapolated dose (HED) as the product of the animal dose multiplied by the ratio between animal ($K_{m_{animal}}$) and human ($K_{m_{human}}$) correction factors (Reagan-Shaw *et al.*, 2008).

$$\text{HED (mg / kg)} = \text{Animal dose (mg / kg)} \times [K_{m_{animal}} / K_{m_{human}}] \quad \text{Eq. (1)}$$

$K_{m_{animal}}$ and $K_{m_{human}}$ factors are determinate by the average body weight (kg) of a standard species organism divided by its body surface area (m²), which account for difference in metabolic rate, to convert doses between animals and humans (Nahir and Jacob, 2016).

$K_{m_{animal}} / K_{m_{human}}$ is considered constant (Reagan-Shaw *et al.*, 2008).

Metformin concentration used in our study (250 mg/kg) was chosen considering the absence of pathological side effects in middle ranges of dosage for diabetes mellitus treatment in human and murine models reviewed (Wilcock and Bailey, 1994; Beatriz, *et al.*, 2013; Hostalek, *et al.*, 2015). Human clinical dose of diabetes mellitus ranges from 500- 3000 oral mg/day for a 60 kg human. Furthermore, experimental range for the treatment of murine streptozotocin induced diabetes ranges from 50 to 300 mg/kg per day for 200g rats (Wilcock and Bailey, 1994; Beatriz, *et al.*, 2013; Hostalek, *et al.*, 2015). Using the Eq. (1) the HED of 250 mg/Kg per day metformin dose administered to rats in our study would be 1250 mg per

day for a 60 Kg adult human.

Oxaliplatin concentration used in our study (4mg/kg) was chosen considering previous reports of OIPN acute sensory symptoms in the lower cumulative doses and significant histological changes in the higher cumulative doses of OIPN murine models reviewed (Coriat, *et al.*, 2014; Park, *et al.*, 2015; Renn, *et al.*, 2011; Toyama, *et al.*, 2013). We found reports of murine models of OIPN at ranges from 1 to 48 mg/kg total cumulative dose (Coriat, *et al.*, 2014; Park, *et al.*, 2015; Renn, *et al.*, 2011; Toyama, *et al.*, 2013). OIPN has been reported in human clinical use of oxaliplatin at ranges from single 65 to 85 mg/m² administered by up to 12 cycles (Ahmet and Ray., 2014; Gamelin, *et al.*, 1998; Cho, *et al.*; 2006; Beijers, *et al.*, 2014). Using the Eq. (1) the HED of 32 mg/kg dose (total cumulative) administered to rats in our study would be 197 mg/m² total cumulative dose for a 60 kg adult human.

Rats in three groups were treated separately: metformin (Met; n=15), oxaliplatin (Oxal; n=15) and cotreatment of oxaliplatin and metformin (Oxal+Met; n=15). Metformin (250mg/Kg) was diluted in Ringer-Lactate Serum every time and administrated daily by four weeks of intraperitoneal injections. Oxaliplatin (4mg/Kg) was administered intraperitoneally two consecutive days every five days for four weeks. Cotreatment of metformin (250mg/Kg) and oxaliplatin (4mg/Kg) was administered intraperitoneally in the same fashion described for separated administration. Metformin injections were administered 6 hours before oxaliplatin injections in the days that corresponded to inject both drugs of the cotreatment (Oxal +Met) group. Rats with a common treatment were housed together with a maximum of 5 animals per box. All the *in vivo* studies were analysed by a blinded single observer.

To avoid bias from manipulation, from the total of 15 rats per treatment, 12 rats were used for sensory testing and the last 3 rats of the same treatment were used for blood extraction. On the other hand, histological analysis was performed over tissue extracted from all rats of each treatment.

Also, to prevent bias from stimulation, timeline was designed to avoid cold and heat stimulation on the same rat at the same day. Accordingly, touch and cold stimulation were performed in the same days with a 30 min delay between each stimulus, but heat stimulation was performed in alternate days.

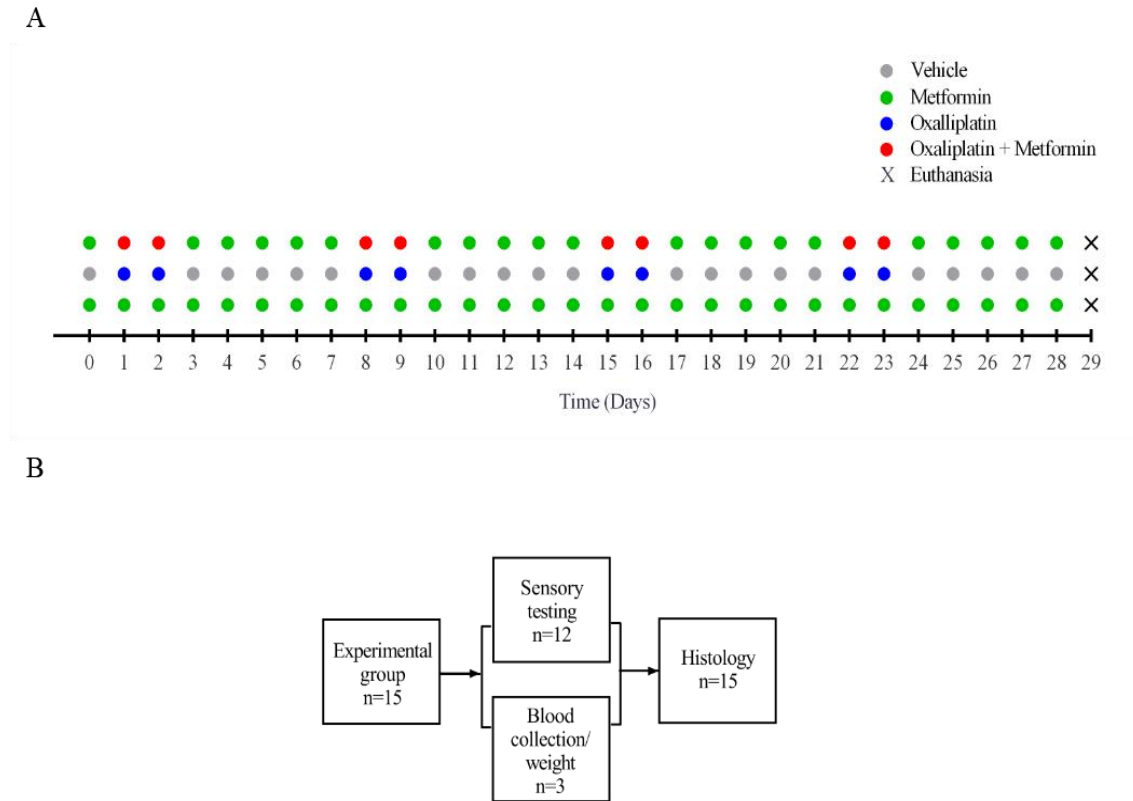


FIGURE N°2. Scheme of Oxaliplatin and Metformin Administration Regime and experimental groups samples organization. (A) Oxaliplatin (blue dots) was diluted in Ringer-Lactate serum (Vehicle) and 4mg/Kg were administered intraperitoneally (i.p) to 15 Sprague Dawley rats twice per week by four weeks. Ringer-Lactate volumes adjusted by weight were administered intraperitoneally (i.p) to Oxaliplatin group rats in the days the chemotherapy was not injected. Metformin (green dots) was freshly diluted in Ringer-Lactate serum (Vehicle) and 250mg/Kg were administered intraperitoneally (i.p) to 15 Sprague Dawley rats daily by 29 consecutive days. Cotreatment of Oxaliplatin + Metformin (red dots) was administered under the same conditions but metformin was administered 6 hours before Oxaliplatin in the days that required both injections. Rats were euthanized (black X) by CO₂ intoxication 30 days after the first injection and 24 hours post the last injection. (B) Experimental groups (n=15) receiving treatments described in A (Met, Oxal or Oxal + Met) were subdivided to perform sensory testing (n=12) or blood collection and weighting (n=3) until the end of rats survival. After euthanasia, histological analysis was performed in samples from all the rats of each experimental group (n=15).

12.3 Axotomy Protocol.

As a positive control for stress at the DRG induced by damage in the axonal region, we performed axotomy at the Sciatic Nerve of Sprague Dawley rats. Specifically, adults Sprague Dawley were anesthetized with Ketamine/Xilazin (3:1). Sciatic nerve was exposed and completely sectioned at the level of the sciatic notch with surgical scissors. Then, the skin cut was sutured. Three days after the axotomy rats were euthanized by Ketamine/Xilazin (3:1) overdose and dorsal root ganglia (L4, L5, and L6) were extracted and fixed. Finally, those samples were processed by histological preparation for IF and nuclear stress was assayed by ATF3 nuclear translocation.

12.4 Histology Procedures.

After a defined survival time (30 days), animals were terminally anaesthetized with Ketamine/Xilazin (3:1) and transcardially perfused with 4% paraformaldehyde (PFA) in 0.1 M phosphate buffer (PB). Histological analysis included a control group of untreated rats (n=3). We collected glabrous plantar skin, L4, L5 and L6 DRG, and the sciatic nerves. Tissue for immunohistochemistry was post-fixed in 4% PFA for 2 hours, followed by three 10 min washes in Phosphate Buffered Salinum (PBS; 137 mM NaCl, 12 mM Phosphate, 2.7 mM KCl, pH 7.4.), sucrose gradient (5%, 10%, 20% in PBS), and then embedded in OCT.

Samples were cryostat cut at 14 μ m (skin), 8 μ m (nerves and DRGs) and 10 μ m (spinal cords) and were mounted on Superfrost Plus slides. Sections were washed in 1x PBS for 10 min and then blocked/permeabilized in 0.1% Triton X-100, 2% cold water fish skin in 1X PBS for 1h at RT. Sections were incubated in primary antibodies in blocking/permeabilizing solution overnight at 4°C, washed in 1XPBS 3x10 min, and incubated in secondary antibodies for 2h at RT. Sections were washed 3x10 min in 1XPBS and mounted in Vectashield.

12.5 Quantification and Analysis of Immunofluorescences.

Number of axons per area of nerve tissue was assessed in epifluorescence images of neurofilament immunostained explant sections (matched for laser power, photomultiplier tube gain/offset, and post processing) by thresholding and binarization using the particle analysis macro of the open source ImageJ software (Ferreira and Rasband, 2012).

Intraepidermal Nerve fibers were counted live on the microscope at a 60 \times magnification (protocol described by Lauria *et al.*, 2005). Only single fibres crossing the dermal–epidermal junction were counted, excluding secondary branching from quantification. The length of the section was measured using Image J length method (Ferreira and Rasband, 2012) and thus the epidermal innervation density (IENF/mm) was calculated.

For IB4, CGRP, or ATF3 expression in the DRG analysis was performed from 6-8 randomly selected sections from each animal (n=15 for each treatment group); the total number of DRG cell profiles and the number of profiles expressing immunoreactivity for the protein of interest

was counted and reported as percent over the total. Cell profiles were sampled only if the nucleus was visible within the plane of section and if cell profiles exhibited distinctly delineated borders.

GFAP in the spinal cord was measured in 6-8 randomly selected L4, L5 and L6 spinal cord section from each animal. The intensity of immunoreactivity was measured in the dorsal horn and expressed in arbitrary units (A.U.). IB4 and CGRP in the dorsal horn were also analysed measuring the intensity of immunoreactivity in laminae I and II.

12.5.1 TABLE N°1. Primary Antibodies Dilutions.

Species Reactivity in this thesis	Primary Antibody	Host	Immunofluorescence Dilution
Rat	Anti-Neurofilament 200 (Heavy chain); NF-H.	Rabbit	1:1000
Rat	Anti- Acetylated Tubulin	Mouse	1:1000
Rat	Anti -PGP 9.5	Rabbit	1:1000
Rat	Anti-Glial Fibrillary Acidic Protein (GFAP)	Rabbit	1:1000
Rat	Anti-Calcitonin Gene Related Peptide (CGRP)	Rabbit	1:1000
Rat	Anti-Activating Transcription Factor (ATF3)	Mouse	1:1000

12.5.2 TABLE N°2. Secondary Antibodies Dilutions.

Secondary Antibody	Host	Immunofluorescence Dilution
anti-Mouse Alexa 488	Goat	1:1000
Anti-Rabbit Alexa 546	Goat	1:1000

12.5.3 TABLE N°3. Markers Dilutions.

Marker	Immunofluorescence Dilution
IB4	1:200
ExtrAvidin-FITC	1:500

12.6 Assessment of Mechanical Allodynia (Von Frey test).

Mechanical allodynia was assessed as the hind paw threshold withdrawal response to Von Frey filament touch (Bonin *et al.*, 2104; Chaplan *et al.*, 1994). Rats were placed in a transparent box over a mesh floor [Figure N°3C]. There, stimulation was done following the up and down method (Bonin *et al.*, 2104; Chaplan *et al.*, 1994). Von Frey filaments were applied perpendicular to the mid-plantar area of right hind paw starting with the 5.18g filament. A positive response was defined as a paw withdrawal or shaking after 2 seconds touch. After any positive response, the next lower filament was applied, and in case of a negative response the next higher filament was applied. The testing session consist in 5 trials after the first change in response. The sequence of response was converted into 50% withdrawal threshold using the formula:

$$50\% \text{ PWT} = 10^{(X_f + k\delta)} / 10^4$$

where X_f is the value of the final von Frey filament used (in log units), k is a value measured from the pattern of positive/negative responses, and $\delta = 0.21$, which is the average interval (in log units) between the von Frey filaments (Bonin *et al.*, 2104; Chaplan *et al.*, 1994).

Three sessions of habituation (30 min each) to the testing area were conducted in three consecutive days followed by two baseline measurements of hind paw withdrawal threshold in another two consecutive days.

The mechanical allodynia assessment was performed with testing sessions after each rat remained 30 minutes in the testing area to acclimatize. Testing sessions were performed at 0, 14, 17, 21, 24 y 28 days after starting the treatments.

All the studies were analysed by a blinded single observer.

12.7 Assessment of Cold Allodynia (Acetone Test).

To assay cold allodynia, we applied a drop of acetone to the plantar area of right hind paw and the time that the animal spent licking, shaking, or lifting the paw during the following 2 minutes was measured [Figure N°3D], as described before (Vissers and Meert, 2005). Baseline values were taken three times before the first drug administration. Testing sessions were performed after each rat remained 30 minutes in the testing area to acclimatize. Finally, testing sessions were done at 0, 14, 17, 21, 24 y 28 days after starting the treatments.

All the studies were analysed by a blinded single observer.

12.8 Assessment of Thermal Hypoalgesia (Hargreaves Test).

Thermal (heat) hypoalgesia was assayed using a plantar test apparatus (Hargreaves Apparatus), as it has been described before (Banik and Kabadi, 2013). Rats were placed in transparent boxes (95x195x140mm) and acclimatized by 30 min before every testing session. A radiant heat source with constant intensity was focused on the right hind paw [Figure

N°3B]. The thermal latency was defined as the time from initial heat exposure to the withdrawal of the hind paw. The thermal latency was determined in triplicate for each animal in every testing session, with 5 min intervals. A cut-off of 50 seconds was applied to prevent tissue damage. Baseline values were assessed three times before the first drug administration. Testing sessions were done at 0, 15, 18, 22, 25 y 29 days after starting the treatments.

All the studies were analysed by a blinded single observer.

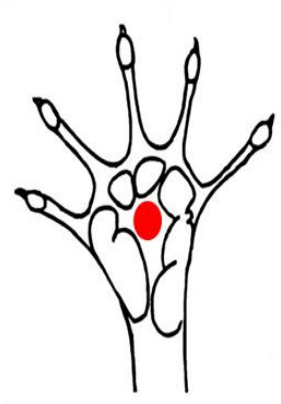
12.9 Blood Collection and Analysis.

Blood samples were collected from tail snip at experimental days 0, 14, 19 and 29. All blood samples were obtained from different rats than the ones undergoing sensory testing. Blood samples designated to cell counting was mixed with EDTA immediately after extraction to avoid coagulation.

Glycaemia was determined using a Code Free blood glucose monitoring system (SD) with blood directly from the tail snip.

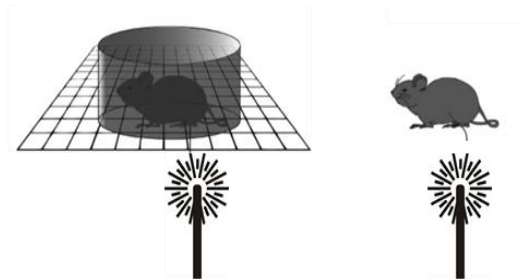
To determinate white blood cells, counting was performed in an automatized Haemocytometer (Hematology Analyzer). An image is taken of stained white cells and the number of cells is then counted by image analysis in the analyzer.

A

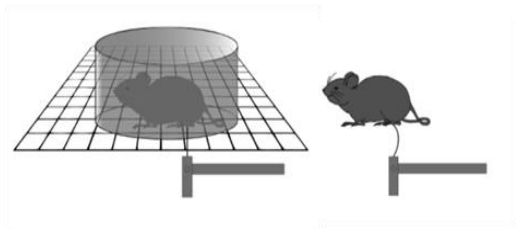


●: Stimulation Area

B Hargreaves test.



C Von Frey test.



D Acetone test.

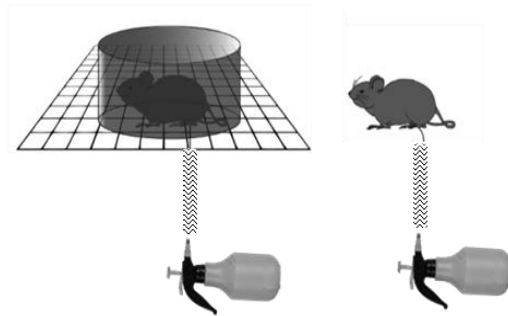


FIGURE N°3. Schemes of the Sensory Testing Procedures.

(A) Stimulation area during the sensory test. Mechanical and thermal stimuli were applied to an area of glabrous skin between the pads of the right hind paw. Each rat received stimulation in the same area and paw on every testing session. Shrinking and /or shaking the hind paw in response to the stimulation were considered a withdrawal response. (B) Hargreaves test device. Sensory response to heat thermal stimulation was performed in individual boxes on top of a thermal panel that allows a localized controlled increase of temperature induced by a high intensity laser immediately below the hind paw. The target area was stimulated by 30 seconds and the latency for a withdrawal response was registered. (C) Von Frey test device. Sensory response to touch mechanical stimulation was performed in individual boxes on top of a grid. Hind paw is stimulated through the grid holes with Semmes-Weinstein filaments that exert a definite force over the stimulation area. The target area was stimulated by 3 seconds and the display of a withdrawal response was registered (D) Acetone test device. Sensory response to cold thermal stimulation was performed through a grid as in C. Hind paw is stimulated by a discrete stream of Acetone discharged to the target area. The duration of the total withdrawal response display was registered by 1 minute after stimulation.

12.10 Cell lines culture, Treatments and Assays.

Human gastric carcinoma cell lines HS746T and Kato III were purchased from ATCC (Manassas, VA, USA). Human gastric adenocarcinoma cell line MKN45 was purchased from Riken (Ibaraki, Japan).

HS746T cells were cultured in Dulbecco's Modified Eagle Medium supplemented with 10% Fetal Bovine Serum. Kato III and MKN45 cells were cultured in Roswell Park Memorial Institute Medium (RPMI) supplemented with 10% and 20% FBS respectively. RPMI and DMEM were supplemented with 2mM L-glutamine, 1x MEM Non-Essential Amino Acids, 100 IU/ml Penicillin and 100 µg/ml Streptomycin, RPMI was also supplemented with 1mM sodium pyruvate. Cell lines were cultured at 37°C and 5% CO₂ humidified atmosphere.

Viability was determined using the MTT (3- [4, 5-dimethylthiazol--2-yl]-2, 5-diphenyl tetrazolium bromide) assay. After incubation in 5% CO₂ humidified air at 37°C, 10 µl of MTT (5mg/ml dissolved in saline solution), was added and cells were incubated for another 4 hours. Subsequently, formazan crystals formed were dissolved by the addition of 100 µl of 0.02N HCl in isopropanol. The absorbance of each well was determined at 595 nm using a BioTek microplate EL800 reader. Cell viability was expressed as the percentage relative to the control. The optical density (OD) is linearly related to the number of viable cells.

Control wells, containing cells with culture medium but no drugs were used to determine the basal cell survival. To determinate the optimal number of cells to perform dose response

assays, we first cultured HS746T, MKN45 and Kato III gastric cancer cell lines until logistic growth (sigmoid). Using this data, we performed linear regression to select the portion of the growth curve with an approximated linear fashion by an exclusion criterion of $R^2=0,98$.

Wells with culture medium only were used as blank. The half maximal inhibitory concentration (IC50) value, the drug concentration needed to inhibit cell growth by 50%, was calculated by extrapolation from the growth inhibition curve. We selected the concentrations of metformin that induced 15% or less inhibition of cell growth *per se* to perform the cotreatment assay of cell growth inhibition.

Adhering cells were treated with two different concentrations of metformin in the range of less than 15% direct cytotoxicity. MKN45 and Kato III were treated with 0.04 and 0.2mM and HS746T with 0.2 and 1mM. After 4 hours cells were exposed to different concentrations of oxaliplatin (0.49, 1.95, 7.81, 31.25, 125, and 500 $\mu\text{g/ml}$) and co-cultured for 68 hours before cell viability analysis.

Cells were cultured in 96 well plates, after 8 hours different concentrations of metformin were added (0.0016, 0.008, 0.04, 0.2, 1, 5mM). After 24 hours cells were exposed to different concentrations of oxaliplatin (0.16, 0.8, 4, 20, 100, and 500 $\mu\text{g/ml}$) and co-cultured for 48 hours before cell viability analysis.

Mean survival values were analyzed as percent of control for every condition.

12.11 *In vitro* Determination of Axonal Degeneration.

To stimulate adherence of dorsal root ganglia, glass coverslips of 13mm diameter were coated 24 hours before DRG explants extraction and seeding. To this goal, coverslips were previously sterilized by 15 min. exposition to UV radiation and treated by 1 hour at RT with a 0, 1 mg/mL poly-L-lysine (poly-L) solution diluted in sterile tridestilated water under a biological safety cabinet. Afterwards, Poly-L excess was removed by washing three times with tridestilated water and coverslips were dried by evaporation at RT. Finally, coverslips were treated with a solution of 10% Collagen of Rat Tail I and 1% Glacial Acetic Acid ON until complete evaporation at the biological safety cabinet.

E16 rat embryos were decapitated, and the vertebral column was removed. Spinal cord with dorsal root ganglia (DRG) were dissected and placed in a Petri dish containing L-15 medium. For DRG explants, complete DRGs were cultured in 24-well dishes containing 400 μ L of Neurobasal medium, 2% B27, 0,3% L-glutamine, 1% streptomycin/penicillin, 4 mM aphidicolin, 7,5 μ g/ml 5-fluoro-2- deoxyuridine, and 50 ng/ml Neural Growth Factor 2,5S (NGF). The mixture of aphidicolin and fluoro-2-deoxyuridine inhibits proliferation of Schwann cells by inhibition of DNA polymerase, and DRGs cultivated in these conditions seldom contain Schwann cells. DRGs were cultured for 7d at 37°C and 5% CO₂. At day 7, ganglia were treated with 10 μ M oxaliplatin and /or 10 mM metformin and remained under these drugs by 48 h until fixation. All the surgical procedures and treatments were done under a biological safety cabinet.

The axonal degeneration percentage was based on the ratio of the areas of fragmented axons versus total axonal area (Villegas *et al.*, 2014). Degenerated axon fragments were detected using the particle analyser algorithm of ImageJ, and the total fragmented axon area versus total axonal area was used to estimate the axonal degeneration Percentage.

12.12 Statistical Analysis.

Data is shown as mean +/- SEM. Two ways ANOVA, One-way ANOVA or student t test were carried out as statistical analysis. Bonferroni's test was used as *post hoc* analysis. $P < 0.05$ was considered as statistically significant. All statistics and graphs were done using *GraphpadPrism6* software.

13. RESULTS.

13.1 Oxaliplatin Antineoplastic Effect after Cotreatment with Metformin in *In Vitro* Cellular Models of Gastric Cancer.

To explore the role of metformin as a potential treatment for CIPN it is relevant to give light on the effect of the cotreatment with metformin and chemotherapy over the antineoplastic effects of anticancer drugs. To this goal we performed dose response effect of metformin and /or oxaliplatin over three gastric cancer cell lines survival.

First, we generated growth curves for HS476T; MKN45 and Kato III gastric cancer cells by optical density determination at 595 nm wavelength (see Methods 12.10). We found that all the three gastric cancer cell lines had logistic growth dynamics. Then we calculated linear regression on the growth curves to select the optimal number of cells to perform the dose response assays [Figure N°4].

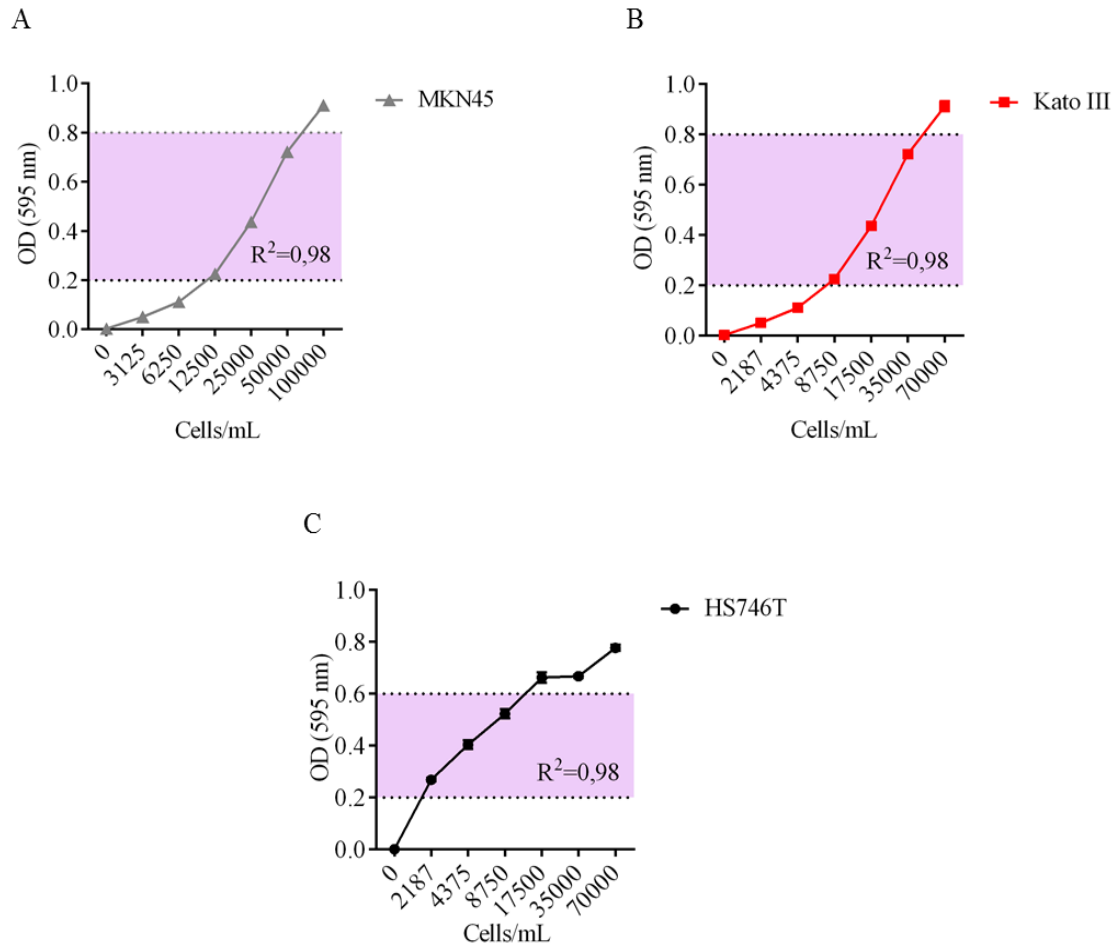


FIGURE N°4. MKN45, KatoIII and HS746T Gastric Cancer Cell Lines Basal Viability. Gastric cancer cell lines were cultured by 72 hours and number of cells per mL was determined by Haemocytometer counting. Optical Density of MTT/formazan crystals was determined at 595nm over dilutions of MKN45 (A), KatoIII (B) or HS746T (C) gastric cancer cells. Range of lineal proportionality between OD and cell concentration was determined by linear regression adjustment. $R^2=0,98$ criteria was used to select the optimal range of number of cells (violet area) to perform the dose response assays of viability in this study. n=3, SEM.

We also cultured HS476T, MKN45 and Kato III gastric cancer cells by 48 h and we then exposed these cells to increasing doses of oxaliplatin or metformin by 68h to determine cell viability by MTT assay (in Methods 12.10). Oxaliplatin and metformin separately induced a dose dependent decrease in HS476T, MKN45 and Kato III gastric cancer cells viability compared to control (vehicle) [Figure N°5]. Next, we cultured cell lines and cotreated them with metformin on the range of the IC50. We selected metformin concentrations that allowed 85% of cell viability or more. Specifically, MKN45 and Kato III were treated with 0.04 and 0.2mM and HS746T with 0.2 and 1mM.

We found that oxaliplatin induced inhibition of cell viability of HS476T, MKN45 and Kato III gastric cancer cell lines were unaffected by any metformin cotreatment concentrations [Figure N°6]. Furthermore, MKN45 and Kato III gastric cancer cell lines viability dose response curves of oxaliplatin treatment and cotreatment between oxaliplatin and metformin were not significantly different. Nevertheless, metformin had a synergistic effect in oxaliplatin-induced cell viability decrease over the HS476T gastric cancer cell line [Figure N°6].

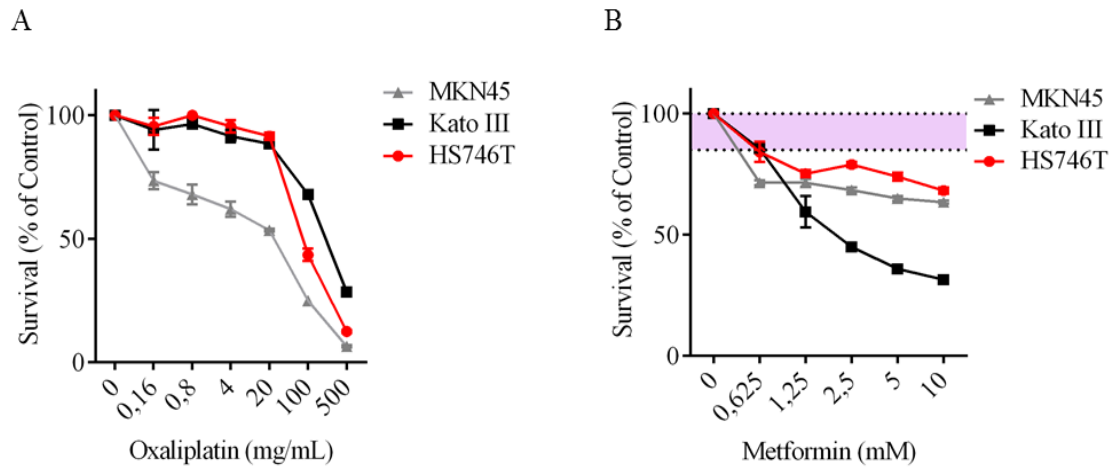


FIGURE N°5. Oxaliplatin and Metformin Effect over Viability of Cancer Cells. HS746T, Kato III and MKN45 cells were cultured until exponential growth and then exposed to (A) Oxaliplatin (0, 16; 0, 8; 4, 20, 100, 500) mg/mL or (B) metformin (0,625; 1, 25; 2, 5; 5, 10) mM by 48h before survival determination. Survival was determined by Optical Density of MTT/Formazan crystals at 595nm. Metformin concentrations that maintained at least 85% of cell survival *per se* (violet area) were considered in the cotreatment viability assays of this study. Mean survival values were analyzed as percent of control for every condition. n=3, SEM.

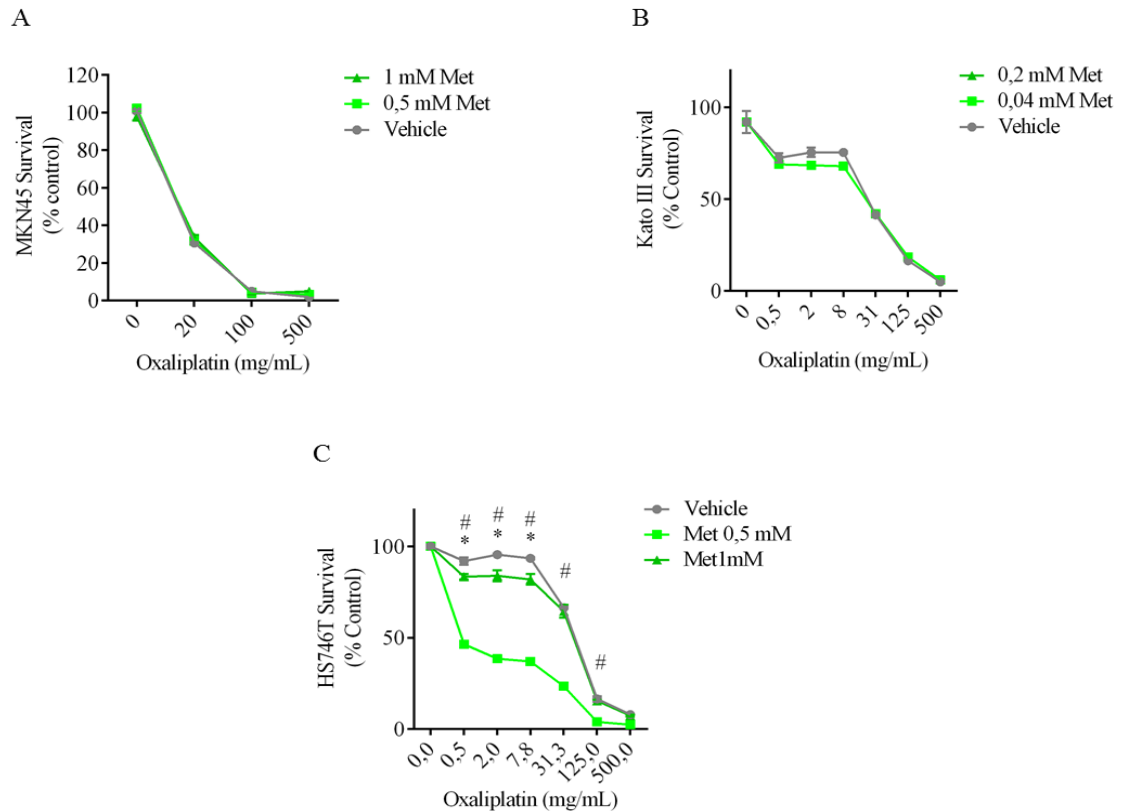


FIGURE N°6. Metformin Effect over Survival of Cancer Cells and Antineoplastic Effect of Oxaliplatin. MKN45 (A), KatoIII (B) or HS746T (C) gastric cancer cells were cultured until exponential growth and then exposed to Oxaliplatin and metformin cotreatment. Effect of metformin in antineoplastic effect of Oxaliplatin in cancer cells was determined by 48 hours cotreatment of Oxaliplatin (0,5; 2; 7,8; 8; 20; 31; 100; 125; 500) mg/mL and metformin (0,04; 0,2; 0,5; 1) mM. Survival was determined by Optical Density of MTT/Formazan crystals at 595nm. (A)Metformin, (B) Oxaliplatin, (C) HS746T Survival under Oxaliplatin and metformin (D) Kato III Survival under Oxaliplatin and metformin (E) MKN45 Survival under Oxaliplatin and metformin. Metformin does not affect toxicity of Oxaliplatin over MKN45 and KatoIII gastric cancer cell lines and increases toxicity of Oxaliplatin over HS746T in a dose response fashion.

Mean survival values were analyzed as percent of control for every condition. $n=3$; * $p<0,05$ indicates significant differences between treatment of lower concentration and Vehicle. # $p<0,05$ indicates differences between treatment of higher concentration and Vehicle treatment. Two Way ANOVA, SEM.

13.2 Metformin Effect over Oxaliplatin Chemotherapy Induced Peripheral Neuropathy.

13.2.1 Inhibitory Effect of Metformin over Oxaliplatin Induced Axonal Degeneration *In Vitro*.

Considering chemotherapy-induced axonal degeneration of peripheral sensory fibers has been suggested as a source of sensory impairment, we wanted to establish if oxaliplatin triggered AD *in vitro* and if metformin was able to inhibit or delay this effect in the same model. To this goal, sensory neurons from rat embryo DRGs were cultured for 7 days and then treated for 3 days with either oxaliplatin (10 μ M) with or without metformin (10 mM). Immunofluorescent staining against the cytoskeleton component Acetylated Tubulin (AcTub) of neurites fields was used to assess axonal fragmentation as readout of AD (see Methods 12.11). In this *in vitro* model oxaliplatin induces a significant degeneration of neurites after 3 days of treatment [Figure N°7]. Notably, a single administration of metformin (10 mM) completely inhibited oxaliplatin induced axonal degeneration at 3 days [Figure N°7], maintaining neurite integrity to control (Vehicle) levels. Metformin treatment separately had no significant effect over neurite integrity after 3 days of treatment [Figure N°7].

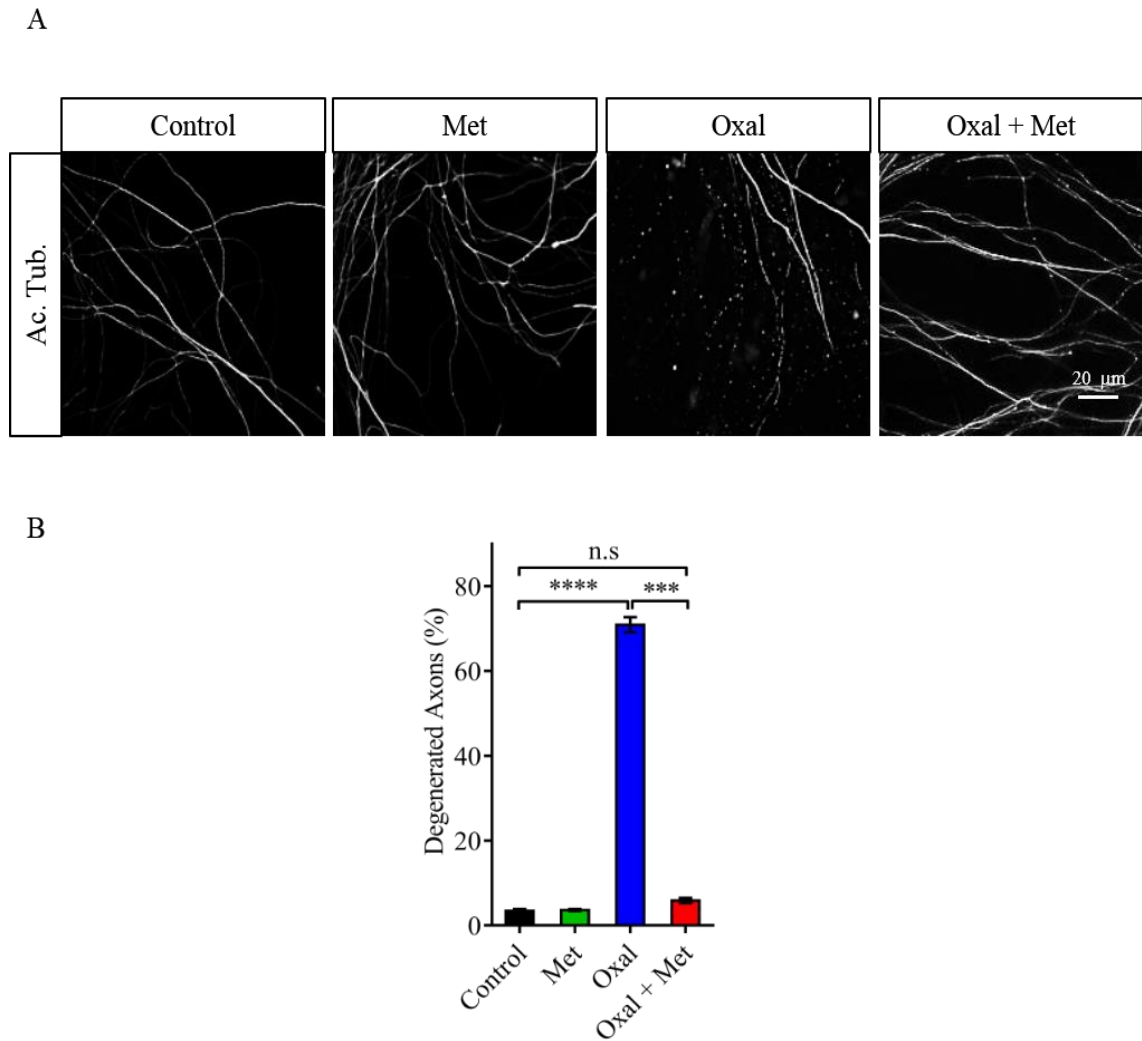


FIGURE N°7. Effect of Metformin over Oxaliplatin Induced Axonal Degeneration *In Vitro*. (A) 40X images of images of neurites from embryo dorsal root ganglia after 3 days treatment with Oxaliplatin (10mM) and /or metformin (10 mM) using Acetylated tubulin (Ac. Tub.) stain for neurite cytoskeleton. Scale Bar: 20 μ m. (B) Degenerated Axons Percentage for all the treatments. Degenerated Axons Percentage was determined by ratio between areas of degenerated neurites by total neurite area. Neurites significantly degenerate after 3 days of Oxaliplatin treatment. Cotreatment with metformin inhibits Oxaliplatin induced degeneration of neurites to control levels.

*** indicates significant differences ($p < 0,001$) ; **** indicates significant differences ($p < 0,0001$) and n.s indicates not significant differences between the groups linked by connectors, using One-Way ANOVA with $n=3$ and Bonferroni's post test for comparison between groups. SEM.

13.2.2 A New Regime of Chemotherapy Administration in the Context of a Murine Model of Oxaliplatin Induced Peripheral Neuropathy.

First, we aimed to develop a model of oxaliplatin chemotherapy induced peripheral neuropathy (OIPN) that would allow a study of sensory function during chronic and acute CIPN and also emulate the administration regime of oxaliplatin in human patients that exhibit OIPN. To this goal, we reviewed references (Ahmet and Ray, 2014; Gamelin *et al.*, 1998; Cho *et al.*, 2006; Beijers *et al.*, 2014) to determine an optimal oxaliplatin concentration and administration method.

During the last years, a discrete number of authors have published murine models of OIPN (Coriat *et al.*, 2014; Park *et al.*, 2015; Renn *et al.*, 2011) reporting weekly administration of one dose of oxaliplatin from 1 mg/Kg to 4 mg/Kg injected intraperitoneally for as long as 4 weeks in studies of chronic sensory impairment induced by oxaliplatin. A higher range of doses between 8 mg/Kg and 16 mg/Kg have been reported as a single administration protocol to study acute effects of oxaliplatin over sensory function (Toyama *et al.*, 2013). Since we aimed to induce clear symptoms of CIPN to study both acute and chronic oxaliplatin induced sensory impairment, we established weekly intraperitoneal 8 mg/Kg cumulative dose of oxaliplatin per four weeks for our study (see Methods 12.2). However, it is worth mentioning that some reports indicate that acute effects of oxaliplatin toxicity include an increase in the incidence of serious side effects such as severe chemotherapy induced diarrhea (CID or necrotic diarrhea), dehydration and death (Boussios *et al.*, 2012; Maroun *et al.*, 2007). In order to reduce those potentially lethal side effects, we decided to administer oxaliplatin separated in

intraperitoneal doses of 4 mg/Kg two consecutive days each week per four weeks [Figure N°2]. Additionally, we daily administered intraperitoneally ringer-lactate serum to all the rats in the study to hydrate them. This led to a final cumulative dose of 32 mg/Kg oxaliplatin per rat after four weeks into the Oxal and Oxal + Met (cotreatment) groups (see Methods 12.2). Here we report for the first time oxaliplatin used in the dose and regimen mentioned before to study OIPN.

Finally, to determine the metformin dose and administration protocol, we reviewed the literature for the role of metformin as a treatment in murine models of diabetes. We found that a significant amount of studies report between 200 mg/Kg and 300 mg/Kg as a widely accepted range of dose of metformin in the context of diabetes treatment in rats (Wilcock and Bailey, 1994; Beatriz *et al.*, 2013; Hostalek *et al.*, 2015). Human treatment dose of metformin ranges between 1000 to 2500 mg per day, normally administrated separately in two equivalent doses each day (Scheen, 1996; Grant, 1996).

Considering this, we decided to daily administer 250 mg/Kg intraperitoneally to the Met and Oxal + met (cotreatment) groups by 30 days (see Methods 12.2). This can be extrapolated to the human equivalent dose by using the Reagan-Shaw method (Reagan-Shaw *et al.*, 2008). Thus, the human equivalent of murine dose of 250 mg/Kg is 1250 mg for an average size of 60 Kg adult human as we extensively described in Methods 12.2. Therefore, the selected dose in the present study is in the lower portion of the safe therapeutic range recorded in humans.

Here we assayed for the first time metformin as a cotreatment of oxaliplatin not as a coadjuvant in the chemotherapy of cancer but as a potential treatment for secondary effects of

chemotherapy over the nervous system [Figure N°2].

13.2.3 Metformin Inhibits Oxaliplatin Induced Intraepidermal Nerve Fibers Degeneration.

Sensory function relies in the reception of stimuli, transduction and retrograde transmission of signals on the terminals of sensory neurons of the nervous system. Sensory neurons of the peripheral nervous system extend unmyelinated terminals (or IENF) through skin layers where specific receptors receive mechanical, thermal and chemical stimuli (Kuner, 2010). It has been extensively reported that vinca alkaloids, taxanes and platinum derivatives chemotherapies induce loss of intraepidermal nerve fibers (IENF) in human and murine models (Boyette-Davis *et al.*, 2011b; Han and Smith, 2013; Ko *et al.*, 2014). To evaluate IENF loss, we examined the skin of oxaliplatin and /or metformin treated rats after 30 days of administration (see Methods 12.5).

IENF were stained against Permeability Glycoprotein 9.5 (PGP 9.5) and positive fibers crossing from the dermis to the epidermis were counted. IENF density (IENFD) was determined by the ratio between total number of IENF and the length of the epidermis portion analyzed (see Methods 12.5). We found that rats treated with metformin alone had an IENFD that was not significantly different from IENFD of control rats after 30 days of treatment [Figure N°8]. However, during the same time of treatment oxaliplatin induced a significant reduction in IENFD. Interestingly, cotreatment of oxaliplatin and metformin treated rats had an IENF that was not significantly different from control [Figure N°8].

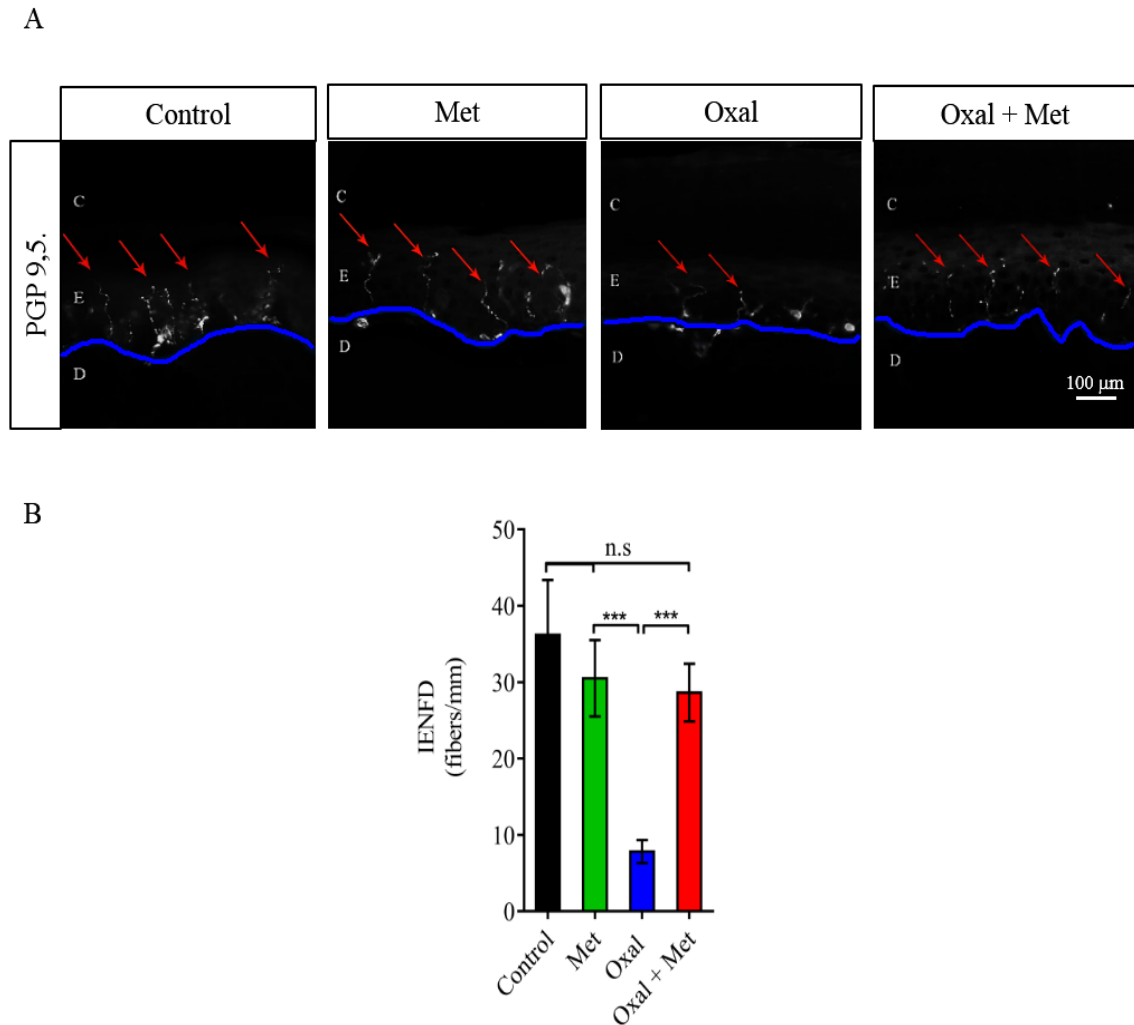


FIGURE N°8. Effect of Metformin over Oxaliplatin Induced Intraepidermal Nerve Fiber (IENF) Degeneration.

Rats were treated as indicated in Figure N°2. (A) 60X images of Intraepidermal Nerve Fibers (red arrows) from rat paw skin biopsies after 30 days of treatment with Oxaliplatin (4mg/Kg) and /or metformin (250mg/Kg) as indicated in experimental model, using anti PGP 9,5 stain for sensory neurons terminals. Skin sublayers listed as follows: C: *Stratum Corneum*; E: Epidermis; D: Dermis. Borderline between dermis and epidermis is indicated by blue line. Bar length: 100 μm . (B) Intraepidermal Nerve Fiber density quantification for all the treatments. Density of Intraepidermal was determined by normalizing total IENF crossing from dermis to epidermis for length of the biopsy.

*** indicates significant differences ($p < 0,001$); n.s. indicates not significant differences between the groups linked by connectors, using One-Way ANOVA with $n=15$ in all groups except control ($n=3$) and Bonferroni's post test for comparison between groups. SEM.

13.2.4 Effect of Oxaliplatin and Metformin Treatment over Axonal Integrity *In Vivo*.

Murine models of CIPN report that IENFD is not always an indicator of degeneration of the axonal shaft of peripheral sensory neurons. In the case of platinum derivatives (oxaliplatin, cisplatin and carboplatin) a dose and length of the treatment dependent focal demyelination and occasional axonal degeneration has been reported (Han and Smith, 2013). However, other authors report a significant IENFD with absence of axonal degeneration (Aley *et al.*, 1996; Tanner *et al.*, 1998; Topp *et al.*, 2000; Siau and Bennett, 2006; Bennett *et al.*, 2011).

To establish if our oxaliplatin treatment affects not only the IENF integrity but also the axonal shaft, sciatic nerves from the same experimental groups were analyzed by staining cross section using an anti heavy neurofilament chain antibody. Axonal density was determined quantitatively by automatized counting of axons per area (see Methods 12.5). We found that axonal density of oxaliplatin treated rats did not induced a significant change in axonal density in comparison to control [Figure N°9]. Furthermore, no significant differences in axonal density were found between metformin treatment or the oxaliplatin and metformin cotreatment in comparison to control [Figure N°9].

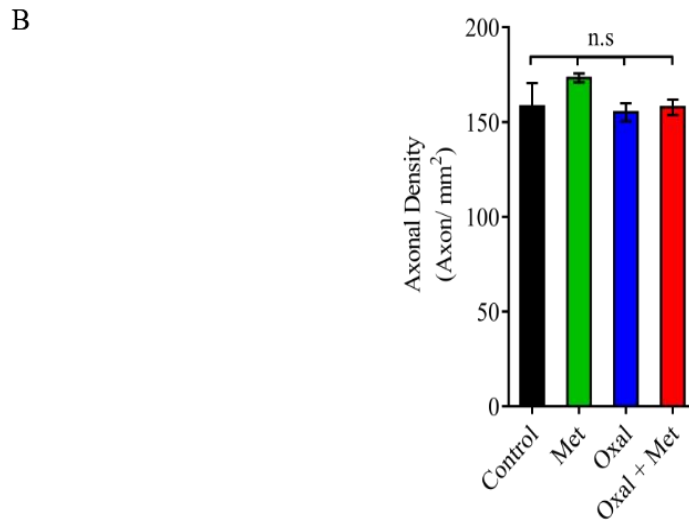
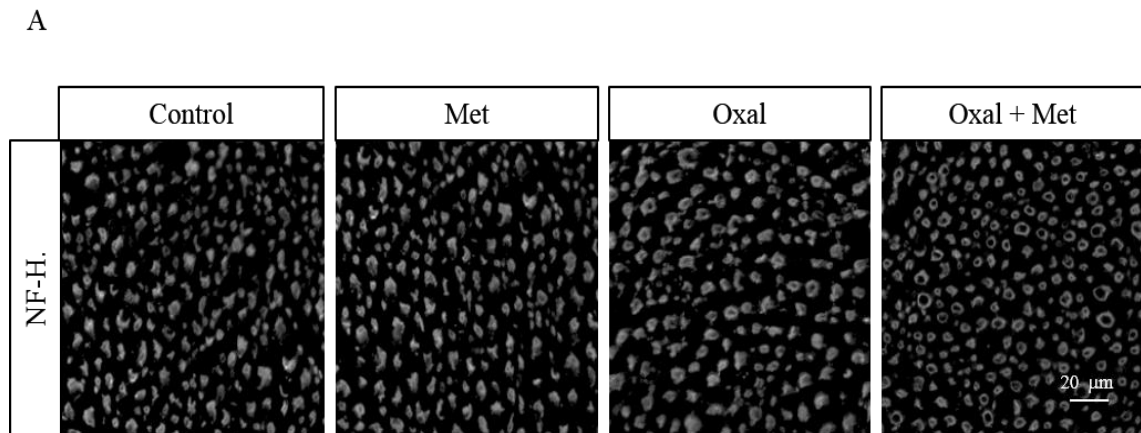


FIGURE N°9. Effect of Metformin and Oxaliplatin Cotreatment over Axonal Density. (A) 40X transversal images of axons from rat sciatic nerve after 30 days of treatment with Oxaliplatin (4mg/Kg) and /or metformin (250mg/Kg) as indicated in experimental model Figure N°2, using anti NF-H stain for axonal cytoskeleton. Axonal density was determined by binarization of immunofluorescence images of all conditions and counting particles. (B) Axonal Density quantification of all the conditions. There were no significant differences between groups.

One-Way ANOVA ($p > 0,05$) with $n=15$ in all groups except for control ($n=3$) and Bonferroni's post test for comparison between groups. n.s. indicates not significant differences between the groups linked by connectors. SEM. Bar length: 20 μm .

13.2.5 Effect of Metformin and Oxaliplatin Treatment over Sensory Neurons Cell Bodies Numbers and Expression of Cellular Stress Markers.

Sensory DRG are composed by satellite cells and mainly by diverse populations of neurons with distinctive anatomical, electrophysiological, and neurochemical characteristics (Kuner, 2010). At this respect, it has been extensively described that non-peptidergic DRG neurons are stained by IB4 biotin and peptidergic DRG neurons are positive for CGRP protein (Barabas *et al.*, 2012; Kuner, 2010). However, IB4 and CGRP staining is not completely exclusive of separate populations at DRG neurons. In this context, approximately 40% of CGRP neurons also express IB4 (Price and Flores, 2007). Having this in count and considering that it is known that sensory cell bodies could be affected by some chemotherapeutic drugs (Park *et al.*, 2015), we analyzed DRGs (L4, L5 and L6) from metformin, oxaliplatin and oxaliplatin and metformin treatments after 30 days and also from control (untreated) rats. Cross sections were stained against IB4 and CGRP to visualize non-peptidergic and peptidergic small neurons. The number of IB4 and CGRP positive neurons per ganglia were counted separately and the percentage of each of them was calculated (see Methods 12.5). We found that there were no significant differences in number of neither IB4 nor CGRP positive neurons between all groups analyzed [Figure N°10]. Additionally, the percentage of IB4 and CGRP positive neurons was in the range of the values previously reported (Swett *et al.*, 1991; Tandrup, 2004) [Figure N°10].

To evaluate if the intact number of IB4 or CGRP positive neurons were not under cellular stress, we assayed the potential presence of an injury inducible protein in our groups of treatments. To this goal, the nuclear localization of the transcription factor ATF3 was used as a reporter of neuronal stress in response to chemotherapy toxicity, as it has been described before (Sisignano *et al.*, 2014). We performed immunofluorescence against ATF3 in DRGs of all the treatments to assess stress responses not evidenced by changes in cell numbers (see Methods 12.5). It is worth mentioning previous reports indicate that taxanes based chemotherapy induces ATF3 nuclear localization in sensory DRG neurons (Sisignano *et al.*, 2014). However, ATF3 presence in response to oxaliplatin toxicity remains mostly unexplored. Considering this, we generated a positive control by performing a complete transection of the sciatic nerve (axotomy; Axot), a known inductor of ATF3 nuclear localization (Tsujino *et al.*, 2000), in a group of untreated rats (see Methods 12.3). Axotomized rats DRGs were extracted three days after transection. Number of ATF3 positive neurons was counted in all groups and normalized by the total number of neurons.

We found that a percentage of DRG neurons from axotomized rats exhibited a strong nuclear localization of ATF3 three days after nerve damage. In contrast, no significant differences were found between metformin, oxaliplatin or oxaliplatin and metformin cotreatment groups [Figure N°11].

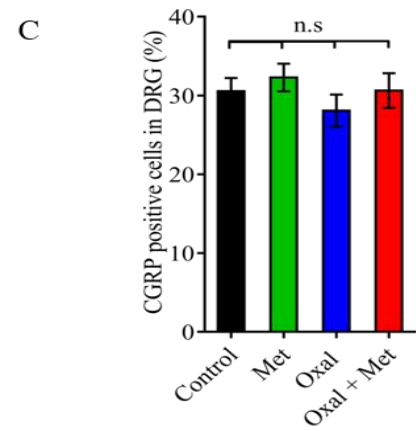
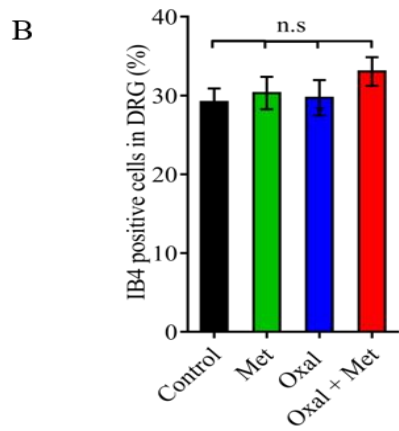
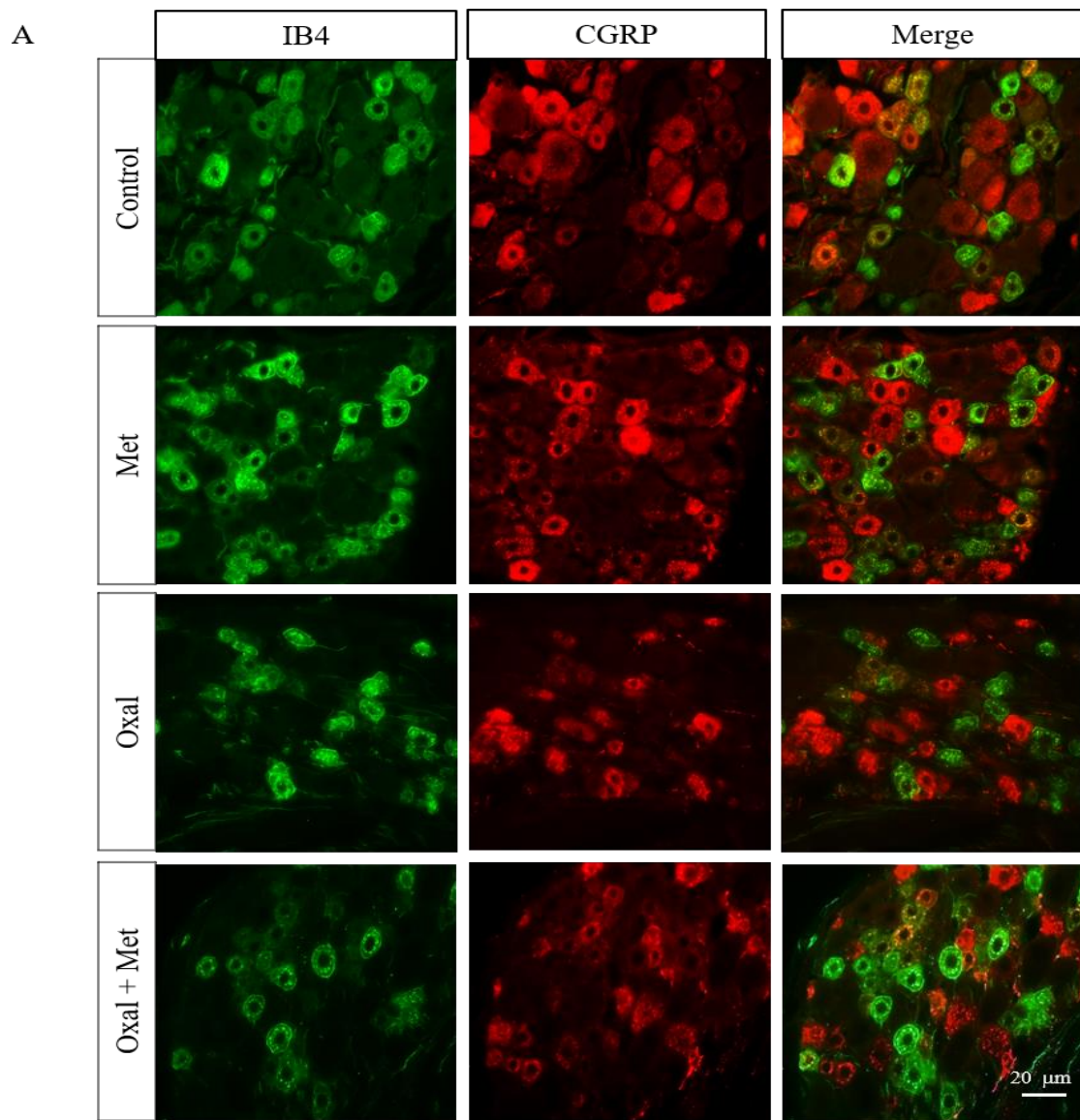
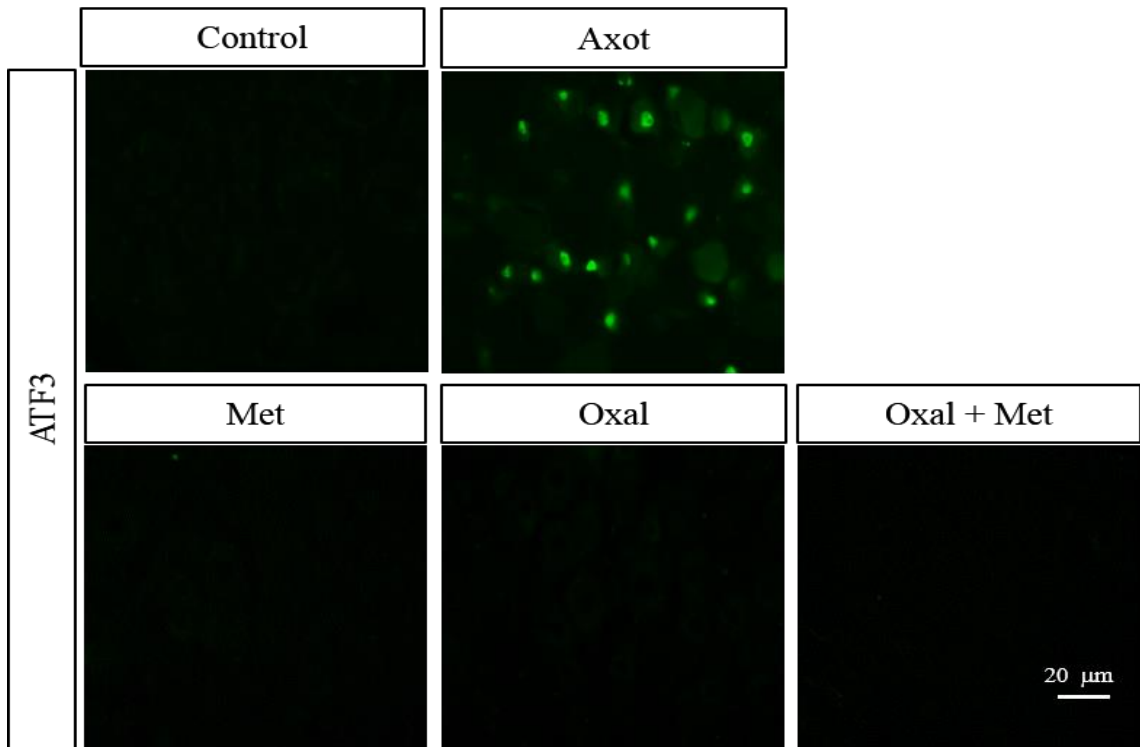


FIGURE N°10. Effect of Oxaliplatin and Metformin Cotreatment over Sensory Peptidergic and Non-peptidergic Neurons Populations at Sensory DRG. (A) 40X transversal images of sensory L4, L5 or L6 dorsal root ganglia (DRG) from rats after 30 days of treatment with Oxaliplatin (4mg/Kg) and /or metformin (250mg/Kg) as indicated in experimental model (Figure N°2). (A) L4, L5 and L6 DRG were stained for IB4 and CGRP for non-peptidergic and peptidergic neurons respectively. Cells positive for IB4 or CGRP were counted and normalized by total number of cells of each DRG. (B) IB4 positive cells percentage quantification for all the conditions. There were no significantly different numbers of IB4 positive cells between treatments. (C) CGRP positive cells percentage quantification for all the conditions. There were no significantly different numbers of CGRP positive cells between treatments.

One-Way ANOVA ($p > 0,05$) with $n=15$ in all groups except control ($n=3$) and Bonferroni's post test for comparison between groups. SEM. Bar length: 20 μm .

A



B

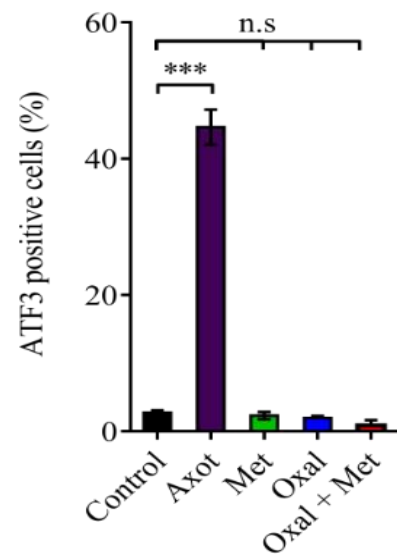


FIGURE N°11. Effect of Oxaliplatin and Metformin over ATF3 Nuclear Localization. 40X transversal images of sensory L4, L5 or L6 dorsal root ganglia (DRG) from rats after 30 days of treatment with Oxaliplatin (4mg/Kg) and /or metformin (250mg/Kg) as indicated in experimental model (Figure N°2). (A) L4, L5 and L6 DRG were stained for ATF3 and positive cells were counted and normalized by total number of cells of each DRG. (B) ATF3 positive cells percentage quantification for all the conditions. There were no ATF3 positive cells in any of the treatments or control. As expected, Axotomy (Axot; positive control) presented a notorious number of ATF3 positive cells.

*** indicates significant differences ($p < 0,001$) and n.s. indicates not significant differences between the groups linked by connectors, One-Way ANOVA with $n=15$ in all groups except Axot ($n=3$) and Bonferroni's post test for comparison between groups. SEM. Bar length: 20 μm .

13.2.6 Oxaliplatin Induced Astrocyte Activation in the Spinal Cord is Inhibited by Metformin Cotreatment.

It has been previously shown that neurotoxins produce degeneration of central terminals in the spinal cord as well as degeneration of peripheral terminals in the skin (Bennett *et al.*, 2011; Huang *et al.*, 2013). However, the current paradigm of CIPN has led to focus most of the studies in the toxicity of chemotherapy over peripheral nervous system.

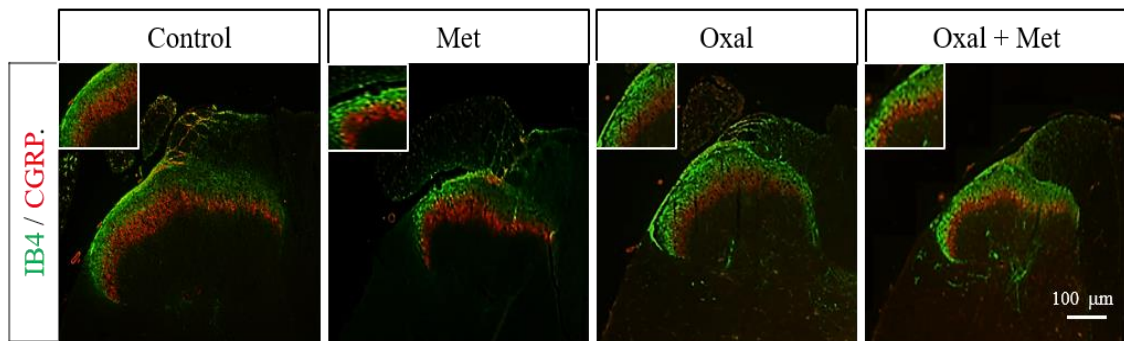
Considering this, we ought to determine if oxaliplatin treatment produced degeneration of central terminals and if this could be prevented by a cotreatment with metformin. To this goal, we stained transversal section of L4, L5 or L6 spinal dorsal horn against IB4 and CGRP, in order to visualize central terminals of sensory neurons in laminae I and II of L4, L5 or L6 spinal dorsal horn respectively. Then we measured the fluorescence intensity of IB4 and CGRP in all treatments (see Methods 12.5).

As expected, we found a characteristic clear delimitation between laminae I and II in control conditions, evident by the presence of two clearly separated areas positive for either IB4 or CGRP. Furthermore, all treatments showed this delimitation between Laminae I and Laminae II [Figure N°12]. Additionally, we found no significant differences between fluorescence intensity of IB4 or CGRP between any of the treatments [Figure N°12].

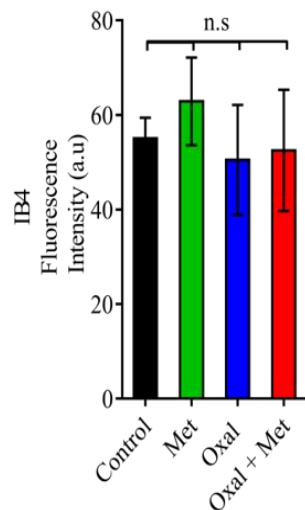
Another known characteristic of chemotherapy toxicity is induction of glial reaction at the spinal cord (Sisignano *et al.*, 2014). It has been proposed that spinal cord glial activation is an essential component on the pathogenesis of sensory impairment during CIPN (Kuner, 2010).

Specifically, glial reaction to chemotherapy involves hypertrophy and increased microglial expression of ionizing calcium binding adapter molecule 1 (Iba1) and Cd11b (complement receptor 3 antigen) (Zheng, *et al.*, 2011). Also, it has been reported an increase of astrocyte area covered by immunoproducts positive to GFAP in response to chemotherapy (Robinson *et al.*, 2014). To explore this, we studied astrocytic activation in transverse cuts in L4, L5 or L6 region of spinal cord from all the experimental conditions by immunostaining against GFAP. For quantification in each experimental condition, the area covered by GFAP positive astrocytes was measured and normalized by the total area. We found that oxaliplatin treatment induced a significant increase in the GFAP positive area in comparison to control (untreated) condition. We also found that astrocyte reactivity was unaffected by metformin treatment alone [Figure N°13]. Interestingly, oxaliplatin and metformin cotreatment significantly inhibited the oxaliplatin induced increase in astrocyte reactivity to control levels [Figure N°13]. Furthermore, morphology of GFAP astrocyte processes under oxaliplatin treatment was qualitatively more branched, which was qualitatively infrequent on the control, metformin and oxaliplatin treatments and in the oxaliplatin and metformin cotreatment. However, further analysis is needed to elucidate this observation.

A



B



C

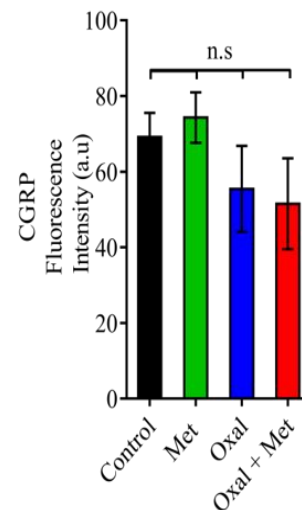
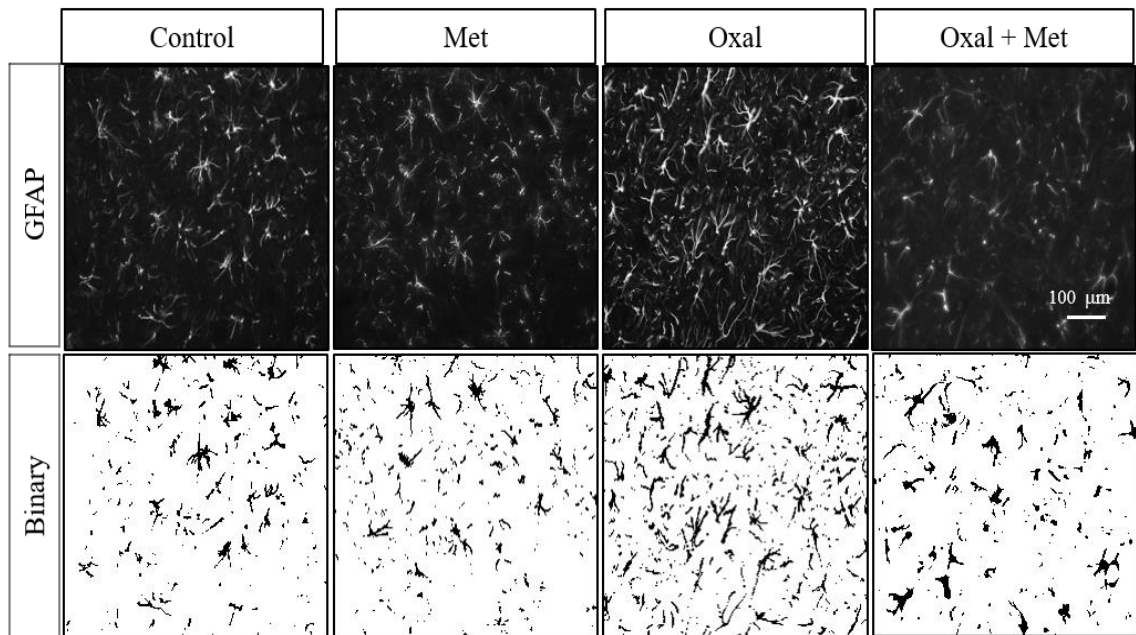


FIGURE N°12. Effect of Oxaliplatin and Metformin Cotreatment over Sensory Peptidergic and Non-peptidergic Neurons Terminals at L4, L5 and L6 Spinal Cord Region Dorsal Horn. (A) 20X transversal images of L4, L5 and L6 spinal cord region at Laminae I/II of dorsal horn from rats after 30 days of treatment with Oxaliplatin (4mg/Kg) and/or metformin (250mg/Kg) as indicated in experimental model (Figure N°2). (A) L4, L5 and L6 spinal cord regions were stained for IB4 (Laminae I) and CGRP (Laminae II) for non-peptidergic and peptidergic neurons respectively. Fluorescence intensity for IB4 or CGRP was measured in images with the same acquisition settings from all the conditions. (B) IB4 positive fluorescence intensity quantification for all the conditions. There were no significant differences. (C) CGRP positive fluorescence intensity quantification for all the conditions. There were no significant differences between groups.

One-Way ANOVA with $n=15$ in all groups except control ($n=3$) and Bonferroni's post test for comparison between groups. SEM. Bar length: 100 μm .

A



B

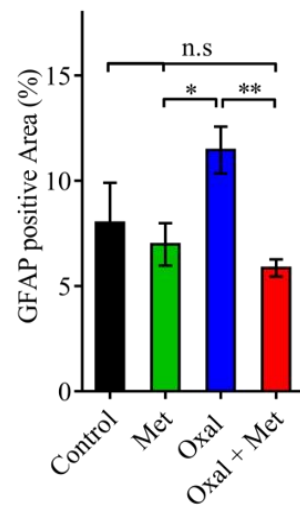


FIGURE N°13. Effect of Oxaliplatin and Metformin Cotreatment over Astrocyte Reactivity at Spinal Cord. (A) 40X transversal images of L4, L5 and L6 sensory spinal cord region at Laminae I/II of dorsal horn from rats after 30 days of treatment with Oxaliplatin (4mg/Kg) and /or metformin (250mg/Kg) as indicated in experimental model (Figure N°2). L4, L5 and L6 spinal cord region were stained with GFAP for astrocyte reactivity. Total area positive for GFAP was determined using binarization mask as it is shown. (B) GFAP positive area quantification for all the conditions. Oxaliplatin treatment induced a significant increase in the area covered by GFAP positive astrocytes. Metformin cotreatment inhibits the Oxaliplatin induced astrocyte reactivity.

* indicates significant differences ($p < 0, 05$); ** indicates significant differences ($p < 0, 01$) and n.s. indicates not significant differences between the groups linked by connectors, using One-Way ANOVA with $n=15$ in all groups except control ($n=3$) and Bonferroni's post test for comparison between groups. SEM. Bar length: 100 μm .

13.3 Metformin Effect over Oxaliplatin Induced Sensory Impairment.

Sensory impairment due to neurotoxicity of oxaliplatin has been described in nearly all patients (Boyette-Davis, *et al.*, 2015; Ocean and Vahdat, 2004) as both an acute and chronic manifestation of paresthesias and dyesthesias on the distal extremities that starts hours after oxaliplatin administration and persist as long as 12 months after (Hershman *et al.*, 2014; Saif and Reardon, 2005). In this respect, on the wide range of oxaliplatin administration regimes and doses described in references for OIPN animal models, lower cumulative doses have been related with acute sensory symptoms in absence of histological markers of degeneration at DRGs, while higher cumulative doses of oxaliplatin have been related with dose dependent chronic sensory manifestations and histological markers of DRGs degeneration (Saif and Reardon, 2005).

Having demonstrated a strong effect of metformin over morphological and cytological changes at pain circuitry induced by oxaliplatin, including loss of IENFs and astrocyte activation, we performed behavioral tests to evaluate sensory impairment induced by oxaliplatin and the potential prevention by metformin. As in our morphological and cytological studies we never found any difference between untreated rats and rats treated with metformin alone, we performed sensory test in metformin treatment, oxaliplatin treatment and oxaliplatin and metformin cotreatment groups. Based on this, we used metformin treatment as the control group to compare with oxaliplatin and cotreatment in the behavioral test studies.

Based on the analogous phenotypic traits of our OIPN model and the human patients suffering from CIPN (Saif and Reardon, 2005; Brzeziński, 2012a; Brzeziński, 2012b), we aimed to perform behavioral tests to specifically evaluate mechanical and thermal sensitivity.

As we mentioned in Methods 12.2, rats were treated with oxaliplatin (4mg/Kg, i.p.) twice per week for four weeks and /or metformin (250 mg/Kg, i.p.) by 30 days. Metformin injections started one day before oxaliplatin in the co-treated experimental groups [Figure N°2]. Baseline trials were done three times after the first injection of oxaliplatin. Based on preliminary results (not shown), trials were done before and after the third and last row of injections to explore both acute and chronic effects of oxaliplatin.

13.3.1 Metformin Inhibits Oxaliplatin Induced Acute Mechanical Allodynia.

We assayed the response of rats to mechanical stimulus using the Von Frey filaments. Rats were touched in the right hind paw with Von Frey filaments of increasing force and the mean threshold force that produced a withdrawal response was registered every time rats retracted the hind paw or manifested aversive behavior. Basal mean threshold withdrawal response was registered three times before starting the treatments. Testing sessions were performed at days 14, 17, 21, 24 and 28 after the first treatment (see Methods 12.6). We found that the mean threshold withdrawal response of the group treated with metformin alone remained the same as the basal conditions at all times tested [Figure N°14]. Importantly, we did not find significant differences between the mean threshold withdrawal responses of all experimental conditions [Figure N°14].

On the other hand, oxaliplatin treatment induced a significant decrease in the mean threshold withdrawal response at days 17 and 24 but reversed to basal levels at day 28 [Figure N°14]. Notably, at the same days, mean threshold withdrawal response of metformin treatment and oxaliplatin and metformin cotreatment remained indistinguishable from basal [Figure N°14].

A

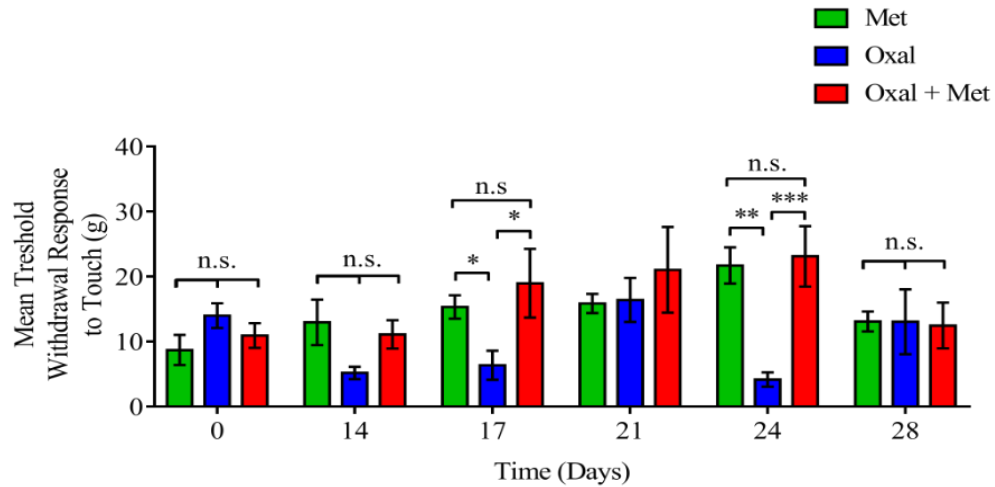


FIGURE N°14. Effect of Oxaliplatin and Metformin Cotreatment over Mean Threshold Withdrawal Response to Touch. Rats were treated as indicated in Figure N°2. Withdrawal response was registered as hind paw retraction or aversive reaction in response to touch with Semmes-Weinstein filaments following the up and down method of Von Frey test. Testing sessions of Von Frey test were performed at days 14, 17, 21, 24 and 28 of this study. (A) Mean threshold withdrawal response quantification for all the conditions. We found a significant decrease in mean threshold withdrawal response to Touch after the injections in the third and fourth week of this study in the group of Oxaliplatin treatment in comparison with metformin treatment. Cotreatment of Oxaliplatin and metformin significantly prevented this decrease in the mean threshold withdrawal response to Touch. These results suggest that Oxaliplatin induces an acute allodynia in response to touch. Furthermore, cotreatment of Oxaliplatin and metformin inhibits the Oxaliplatin induced acute allodynia in response to touch.

* indicates significant differences with ($p < 0, 05$); ** indicates differences with ($p < 0, 01$); *** indicates differences with ($p < 0,001$) and n.s. indicates not significant differences between the groups linked by connectors, using Two-Way ANOVA with $n=12$ in all groups and Bonferroni's post test for comparison between groups. SEM.

13.3.2 Metformin Reverses Oxaliplatin Induced Chronic Thermal Hypoalgesia in Response to Heat.

To assess sensitivity to heat we used the Hargreaves test. We measured the duration of the latency before the withdrawal response to a focal heat stimulus from a laser source. Withdrawal response was considered every time rats retracted the hind paw or manifested aversive behavior. Basal latency of withdrawal response to heat was registered three times before starting the treatments. Testing sessions were performed at days 15, 18, 22, 25 and 29 after the first treatment (see Methods 12.8). We found that rats under metformin treatment had a withdrawal latency in response to heat that was at basal levels at all the testing sessions [Figure N°15]. Furthermore, considering that our first testing session was at day 14 after treatment initiation, earlier withdrawal latency response in the metformin treated rats remains unexplored.

On the other hand, oxaliplatin treatment induced a chronic increase in the withdrawal latency in response to heat from 15 days post oxaliplatin injection and remained significantly higher than metformin treatment until the last testing session (day 29) [Figure N°15]. Interestingly, oxaliplatin and metformin cotreatment rats also had significantly higher withdrawal latency in response to heat at days 15 and 18 after the first injection in comparison to metformin treatment. These days, withdrawal latency in response to heat of oxaliplatin and metformin cotreatment was not significantly different from the oxaliplatin treatment [Figure N°15]. Surprisingly, oxaliplatin and metformin cotreatment had a significantly lower latency withdrawal in response to heat than oxaliplatin treatment in the next experimental days (22, 25

and 29). However, withdrawal latency of the oxaliplatin and metformin at days 22, 25 and 29 cotreatment still remained significantly higher than the metformin treatment [Figure N°15].

A

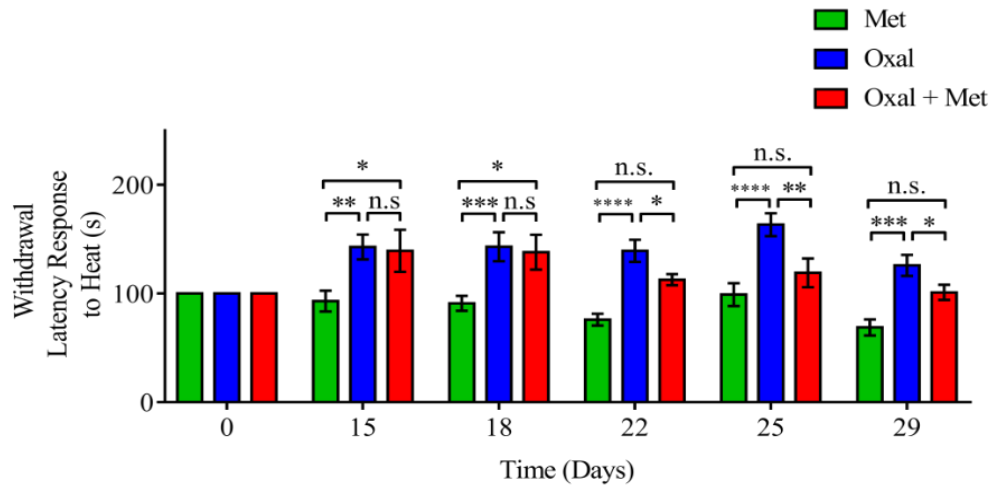


FIGURE N°15. Effect of Oxaliplatin and Metformin Cotreatment over Withdrawal Latency Response to Heat. Rats were treated as indicated in Figure N°2. Withdrawal response latency was registered as the time required to induce hind paw retraction or aversive reaction in response to heat from a regulated laser source with Hargreaves test. Testing sessions of Hargreaves test were performed at days 15, 18, 22, 25 and 29 of this study. (A) Normalized Withdrawal response latency to Heat quantification for all the conditions. We found significantly higher normalized withdrawal response latency to Heat with the Oxaliplatin treatment and with the Oxaliplatin and metformin cotreatment in all the testing sessions compared to metformin treatment. Interestingly, normalized withdrawal response latency to Heat significantly decreased in comparison to Oxaliplatin treatment at days 22, 25 and 29. These results suggest that Oxaliplatin treatment induces chronic hyperalgesia in response to Heat. Furthermore, cotreatment of Oxaliplatin and metformin would reverse the sensitization to Heat in a delayed fashion.

* indicates significant differences with ($p < 0, 05$), ** indicates differences ($p < 0, 01$), *** indicates differences ($p < 0,001$) and **** ($p < 0, 0001$) between the groups linked by connectors, using Two-Way ANOVA with $n=12$ in all groups except and Bonferroni's post test for comparison between groups. SEM.

13.3.3 Metformin Inhibits Oxaliplatin Induced Chronic Thermal Allodynia in Response to Cold.

Finally, we tested the sensitivity to cold stimuli by the acetone test. A mild stream of acetone was applied to the hind paw to induce cold sensation and duration of the withdrawal response was registered. Withdrawal response duration was considered as the time spent retraction the hind paw or doing pain like behavior. Basal latency of withdrawal response to heat was registered three times before starting the treatments. Testing sessions were performed at days 14, 17, 21, 24 and 28 after the first treatment (see Methods 12.7).

We found that basal withdrawal response to cold duration was not significantly different between all the treatments [Figure N°16]. Also, withdrawal response to cold duration of the metformin treatment remained as basal during all the experimental time [Figure N°16].

In contrast, oxaliplatin treatment induced a significant increase of the withdrawal response to cold duration from form day 21 to day 28 in comparison to metformin treatment. Interestingly, metformin cotreatment completely inhibited the oxaliplatin induced increase in the duration of the withdrawal response to cold and remained not significantly different than metformin treatment during the whole experimental time [Figure N°16].

A

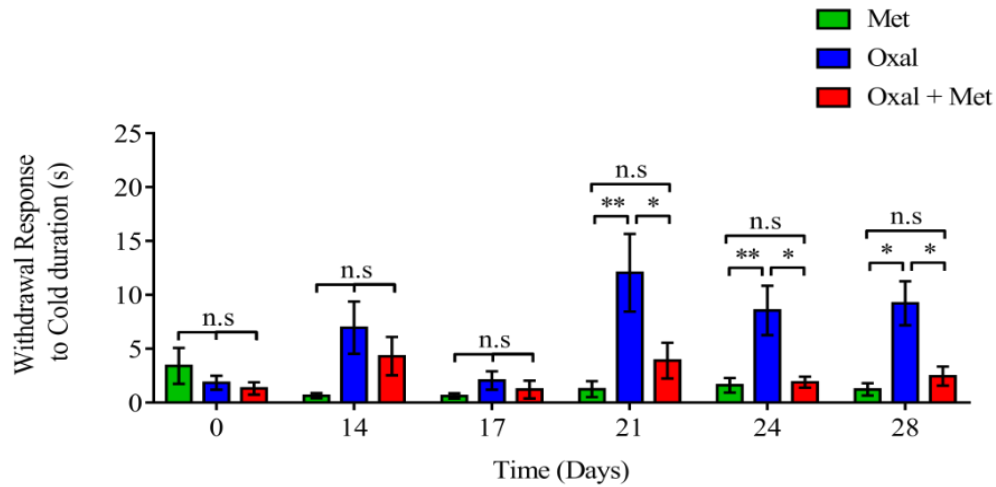


FIGURE N°16. Effect of Oxaliplatin and Metformin Cotreatment over Withdrawal Response to Cold Duration. Rats were treated as indicated in Figure N°2. Withdrawal response to Cold duration was registered as the time while hind paw retraction or aversive reaction was performed in response to Cold from Acetone evaporation during Acetone test. Testing sessions of Acetone test were performed at days 14, 17, 21, 24 and 28 of this study. (A) Normalized Withdrawal response latency to Heat quantification for all the conditions. We found a significantly higher withdrawal response to Cold duration with the Oxaliplatin treatment at days from days 21 to 29 of this study. Interestingly, Oxaliplatin and metformin cotreatment significantly prevented the Oxaliplatin induced increase in the withdrawal response to Cold latency during all days to the levels found with the metformin treatment. These results suggest that Oxaliplatin treatment induces chronic hyperalgesia in response to cold stimulus. Notably, Oxaliplatin and metformin cotreatment inhibits the Oxaliplatin induced cold hyperalgesia.

* indicates significant differences with ($p < 0, 05$), ** indicates differences ($p < 0, 01$) and n.s. indicates not significant differences between the groups linked by connectors, using Two-Way ANOVA with $n=12$ in all groups except and Bonferroni's post test for comparison between groups. SEM.

13.4 Effect of Oxaliplatin and Metformin over Glycaemia, Weight and White Blood Cells Counting.

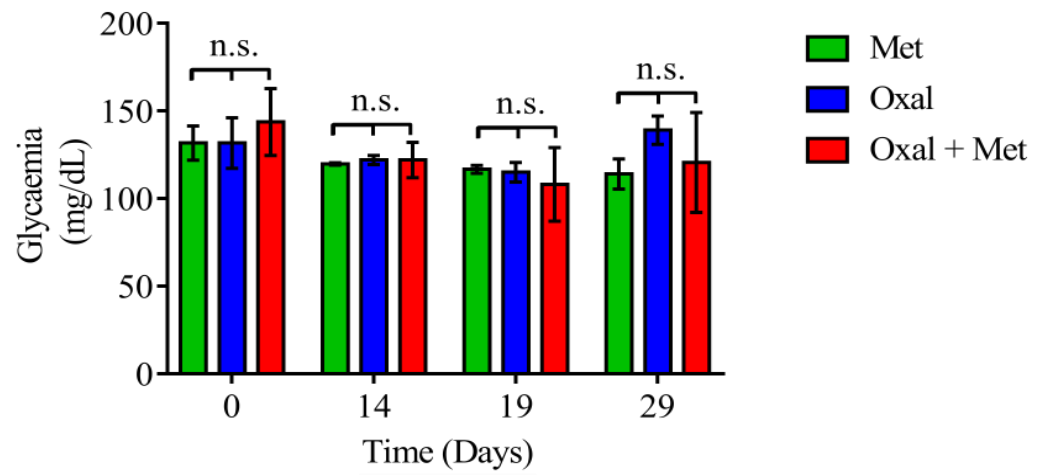
To control the effect of our experimental treatments over relevant physiological parameters we registered weight and white blood cells counting of all the experimental treatments. Since metformin is a strong regulator of glycaemia (Gonga, *et al.*, 2012), we registered the effect of oxaliplatin and/or metformin treatment over blood sugar concentration by automatized analysis of blood samples from tail snips at days 0, 14, 19 and 29 (see Methods 12.9). In parallel, we registered weight at the same days (see Methods 12.9).

We found that glycaemia was not significantly different from basal levels in all experimental groups during the whole experimental time [Figure N°17]. Also, there were no significant differences of glycaemia between experimental groups and all of them remained in physiological range reported in literature (Luippold *et al.*, 2016) [Figure N°17].

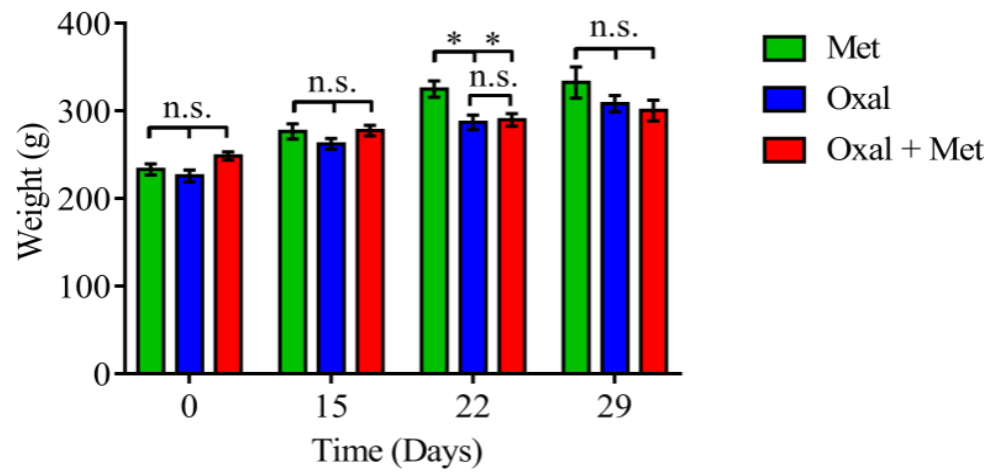
All the experimental treatments registered a sustained increase in weight, consistent with the expected growth for rats of the Sprague Dawley strain from Harlan Biosciences at the ages groups shown along our study (Brower *et al.*, 2015). Interestingly, oxaliplatin treatment and oxaliplatin and metformin cotreatment had a significantly lower weight specifically at day 22 [Figure N°17] in comparison to metformin treated rats. However, the range of weight was normal in every group during the whole experimental time (Brower *et al.*, 2015).

On the other hand, it has been reported that secondary effects of oxaliplatin toxicity include leukopenia (low white blood cells levels) (Petterino and Argentino-Storino, 2006; Hussien and Rasha, 2013). Considering this, we registered white blood cells counting by automatized analysis of blood samples from tail snips at days 0, 14, 19 and 29 (see Methods 12.9). We found that basal levels of white blood cells counting were in previously reported physiological ranges (Petterino and Argentino-Storino, A., 2006; Hussien and Rasha, 2013). Also, all the experimental treatments had no significant differences of white blood cell counting in comparison to basal [Figure N°17].

A



B



C

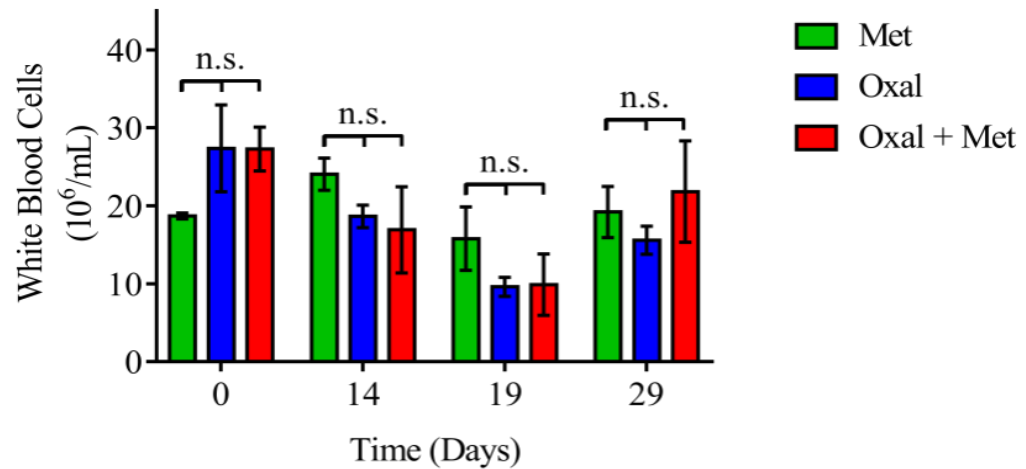


FIGURE N°17. Effect of Oxaliplatin and Metformin Cotreatment over Relevant Physiological Parameters in the Context of Chemotherapy. Rats were treated as indicated in Figure N°2. In order to evaluate relevant physiological parameters in the context of metformin administration and chemotherapy, we measured weight, glycaemia and white blood cells concentration in all groups. (A) Blood sugar quantification for all treatments. Glycaemia was determined by analysis of blood samples extracted from the tails into a blood glucose monitor at days 0, 14, 19 and 29 of this study. We found that all groups had physiological basal levels of glycaemia. Moreover, neither metformin nor Oxaliplatin treatments induced significant changes in the levels of glycaemia. (B) Mean weight quantification for all the treatments. Weight of all rats ranged between 200g and 250g at the beginning of this study. Mean weight was determined by normalizing data with the previous time point at days 0, 15, 22 and 29 of this study. All the groups showed a sustained significant increase in weight along this study. However, Oxaliplatin and cotreatment induced a significant delay in mean weight at day 22 of this study. (C) White blood cell concentration for all treatments. White blood cells levels were determined by analysis in Haemocytometer of blood samples extracted from the tails at days 0, 14, 19 and 29 of this study. We found that all groups had physiological basal levels of white blood cells. There were no significant differences in white blood cells levels dynamics between the treatments.

* indicates significant differences with ($p < 0, 05$) and n.s. indicates not significant differences between the groups linked by connectors, using Two-Way ANOVA with $n=15$ in all groups of weight determination and $n=3$ in all groups of blood analysis. Bonferroni's post test was used for comparison between groups. SEM.

14. DISCUSSION.

In this thesis we explored the effect of anti-diabetic drug metformin over the progression of oxaliplatin induced peripheral neuropathy and its associated sensory symptoms. Our focus was to use a murine model of oxaliplatin toxicity to generate a solid set of experimental data to support further research of metformin as a potential treatment against oxaliplatin toxicity over the pain circuitry in the context of cancer treatment.

The results of this thesis show that metformin significantly inhibits the oxaliplatin induced peripheral neuropathy *in vivo*.

14.1 Relevance of the Exploration of the Effect of Metformin over Oxaliplatin Induced Peripheral Neuropathy in the Context of other Platinum Derivative Toxicities.

As we described in the introduction of this thesis, neuropathic pain arises when pathological conditions induce morphofunctional changes in sensory circuits leading to pain in response to stimuli that normally does not produce it in physiological conditions or exacerbated pain in response to noxious stimuli (Kuner, 2010). In this context, chemotherapeutic treatment has been extensively related with morphological and cytological changes in sensory circuits which lead to neuropathic pain (Stubblefield *et al.*, 2009; Argyriou *et. al* 2014). The current

evidences indicate that anticancer drugs that are neurotoxic affect mainly the peripheral sensory nerves by targeting mitochondrial function and producing oxidative stress, and by functionally impairing the ion channels and /or by triggering immunological mechanisms through the activation of satellite glial cells (Robinson *et al.*, 2014). In this respect, platinum derivative agents based chemotherapies include around a half of the total chemotherapeutics treatments and thus originate a significant proportion of CIPN clinical incidences (Johnstone *et al.*, 2014).

During the execution of this thesis, Mao-Ying *et al.* (2014), reported that metformin inhibits degeneration of IENF in the context of carboplatin induced peripheral neuropathy in mice. Furthermore, these results indicate that metformin also inhibits sensory dysfunction in response to touch. Metformin protective effect over sensory function was proposed as a consequence of IENF morphological preservation reported in the mice treated with metformin as a cotreatment of carboplatin. This result is relevant because carboplatin is the main indication against ovarian cancer (Bookman *et al.*, 2003). On the other hand, colorectal cancer affects around 50% of the total patients undergoing chemotherapies (Yothers *et al.*, 2011; Park and Chun, 2013). As we mentioned in the introduction of this thesis, chemotherapy against colorectal cancer drug is preferentially oxaliplatin (Xiao *et al.*, 2012). Beyond the different clinical targets for cisplatin and oxaliplatin, CIPN in response to platinum derivatives shares some commonalities and distinctive patterns (Xiao, *et al.*, 2012). The neurologic complications of these three drugs occur in most cases, in a cumulative manner (Ling *et al.*, 2007). Cisplatin and carboplatin related neuropathies are often not completely reversible and are seen as paresthesias at the limbs, areflexia, and loss of proprioception and vibratory

sensation (Cavaletti and Marmiroli, 2010). Notably, the neurotoxicity resulting from carboplatin administration is less frequent ranging between 4-6% than that observed with cisplatin or oxaliplatin which ranges between 15–60% (McWhinney *et al.*, 2009), and is frequently less severe. Also, oxaliplatin induces both an acute cold aggravated but transient condition and a more chronic form which has onset after multiple exposures to the drug and which often improves but does not disappear with drug cessation (McWhinney *et al.*, 2009). Despite this, oxaliplatin is a preference treatment for the higher incidence types of cancer because it has twice the antineoplastic effect that other platinum derivative based anticancer drugs (McWhinney *et al.*, 2009).

Altogether, these very relevant clinical differences between carboplatin and oxaliplatin toxicities justify the necessity of specifically explore metformin effect over oxaliplatin induced peripheral neuropathy.

14.2 Metformin and Oxaliplatin Antineoplastic Effect over Gastric Cancer.

In the last years, metformin has been tested as an antineoplastic drug *per se* due to its capacity to activate AMPK and mildly reduce mitochondrial complex I activity, which interferes with energetic dependence of cancer cells in glycolysis (Viollet *et al.*, 2012).

Our first specific goal was to determinate whether metformin modified the oxaliplatin antineoplastic effect over the viability of gastric cancer cell lines. To this goal, we performed cell viability assays in Kato III, MKN45, and HS746T gastric cancer cell lines treated with oxaliplatin and /or metformin *in vitro*. We found that oxaliplatin induced a significant dose dependent reduction in cell viability over Kato III, MKN45, and HS746T gastric cancer cell

lines [Figure N°5A]. Specifically, MKN45 gastric cancer cells viability was significantly reduced by all oxaliplatin concentrations tested (0, 16; 0, 8; 4; 20 and 100 mg/mL) [Figure N°5A].

On the other hand, Kato III and HS746T gastric cancer cells viability was significantly reduced by 20 mg/mL and 100 mg/mL oxaliplatin [Figure N°5A]. This result indicates that oxaliplatin is antineoplastic for Kato III, MKN45, and HS746T gastric cancer cell lines *in vitro* as expected for poorly differentiated carcinomas cell lines based on previous reports (Zhou *et al.*, 2014; Eriguchi *et al.*, 2003). Surprisingly, we found that metformin treatment alone also exerted a significant reduction of Kato III, MKN45, and HS746T cells viability in a dose dependent fashion [Figure N°5B]. To our knowledge, this is the first time the effect of metformin over HS746T and Kato III gastric cancer cell lines is reported. This indicates that metformin is antineoplastic for HS746T and Kato III gastric cancer cell lines *in vitro*.

Regarding MKN45 gastric cancer cell lines, a previous report by Kato *et al.* (2012) has suggested that reduction in MKN45 gastric cancer cells *in vitro* viability by metformin proceeds by cell cycle arrest. Altogether, these results show that metformin treatment *per se* is antineoplastic against a several gastric cancer cell types *in vitro*.

On the other hand, multiple *in vivo* models have provided evidence for the antineoplastic effect of metformin (Lee, *et al.*, 2011; Franciosi *et al.*, 2013). For example, it has been found that metformin inhibits the growth of p53 null cancer cells *in vivo* and slows the proliferation of triple negative breast cancer cells also *in vivo* (Liu *et al.*, 2009; Buzzai *et al.*, 2007). However, antineoplastic effect of metformin in conditions with different levels of glycaemia remains

unexplored. Considering this, several authors suggest antineoplastic effect of metformin *in vivo* is attributable to its extended systemic effects over gluconeogenesis and glycaemia of type II diabetes models (Algire *et al.*, 2010). Actually, results of Algire *et al.* (2010), have shown that metformin significantly reduces tumor growth in a murine model of type II diabetes and has no significant effect over tumor growth in mice under a control diet with physiological levels of glycaemia. Considering this, it has been suggested that metformin exerts its antineoplastic effect due to insulin lowering rather than through a direct effect over AMPK and mitochondrial complex I activity in tumor cells (Algire *et al.*, 2008). Concomitantly, *in vivo* assays of the effect of metformin gastric cancer risk have been performed mostly in diabetes type II patients (Lee, *et al.*, 2011; Franciosi *et al.* 2013). These studies indicate that long term metformin treatment significantly lowers gastric cancer incidence in type II diabetes patients. However, our above-mentioned results indicate that metformin reduces cell viability of gastric cancer cells lines in our *in vitro* model in absence of the systemic effect of this drug and thus supports a potential direct antineoplastic effect over cancer cells. Actually, other *in vivo* studies have suggested that metformin reduces viability and proliferation of osteosarcoma, carcinoma, breast and pancreatic cancer cells (Hernández-Díaz and Adami, 2010; Franciosi *et al.*, 2013). Those studies indicate that metformin modulate energetic state of cells through AMPK pathway and mitochondrial complex I activity and induce apoptosis of cancer cells. Thus, a potential direct antineoplastic effect of metformin over gastric cancer cells is plausible and further research is needed to elucidate this topic and differentiate it from the pathological conditions of type II Diabetes.

Synergy between metformin and chemotherapeutics has been also extensively explored both in *in vitro* and *in vivo* assays. As we mentioned in the introduction of this thesis, metformin

sensitizes pancreatic, bile duct cancer, colon and glioma cancer cells to the toxicity of chemotherapeutics (Lin *et al.*, 2014; Honjo *et al.*, 2014; Qu *et al.* 2014; Lau *et al.* 2014). Furthermore, there are many reports of synergetic effect of metformin with chemotherapeutics such as Gemcitabine (Chai *et al.*, 2015), Paclitaxel (Hanna *et al.*, 2012), 5-Fluoracil (Cho *et al.*, 2006), Dasatinib (Lin, 2014), cisplatin (Yu *et al.*, 2014), Erlotinib (Lau *et al.*, 2014), and radiation (Koritzinsky *et al.*, 2015) in a wide spectrum of cancer such as, carcinoma, breast cancer, pancreatic cancer, and colon cancer. Regarding the specific case of oxaliplatin and metformin cotreatment, it has been shown that metformin significantly reduces colon cancer tumor proliferation and angiogenesis in mice (Zaafar *et al.*, 2014). In this respect, our results indicate that viability of MKN45 and Kato III gastric cancer cells under cotreatment of oxaliplatin and metformin is not significantly different than viability under oxaliplatin treatment [Figure N°6A-B]. On the other hand, we observed a significant sensitization to oxaliplatin in HS746T gastric cancer cells under metformin cotreatment *in vitro* [Figure N°6C]. These results suggest that sensitization to oxaliplatin by metformin cotreatment *in vitro* depends on the specific cell line assayed. Furthermore, our results suggest that *in vitro* sensibility to oxaliplatin alone is uncorrelated to sensitization to oxaliplatin under cotreatment with metformin, considering that MKN45 cells showed a higher reduction in cell viability in response to oxaliplatin treatment in comparison to Kato III and HS746T cells [Figure N°5], but were not sensitized by metformin [Figure N°6]. Accordingly, Richard and Martinez Marignac (2016) have shown that metformin in cotreatment with oxaliplatin significantly reduces colorectal cancer HT29 cells viability while the presence of metformin does not affect the viability of HCT1116 cells in the same conditions. In this respect, several authors have suggested that differential susceptibility to sensitization to oxaliplatin by cotreatment could be

explained by differences in the use of nutrients and the metabolic status of particular cells which sustain their survival and response to stressors (Cheng *et al.*, 2001; Vizan *et al.*, 2009). These suggested differences in metabolic status could be particularly relevant to explain differential sensitization to oxaliplatin in the presence of metformin in our gastric cancer cell lines, considering that the main cellular effect of metformin is precisely modify the energetic metabolism. Further research is needed to elucidate the origin of differential sensitization to oxaliplatin by metformin cotreatment between HS746T, MKN45 and Kato III gastric cancer cells.

Altogether, in terms of our specific goal, our results suggest that metformin either does not affect antineoplastic effect of oxaliplatin over gastric cancer cells or sensitizes gastric cancer cells to this effect.

14.3 Use of Metformin as a Treatment Against Oxaliplatin Induced Peripheral Neuropathy: Morphological and Cytological Changes in Sensory Circuits.

As we mentioned in the last section, one of the main metformin cellular targets is mitochondrial complex I at the electron transport chain (Viollet *et al.*, 2012). Considering this, it has been proposed that metformin regulates mitochondrial activity, inhibiting ROS production (Batandier *et al.*, 2006). This fact is highly relevant considering that ROS are major regulators of mitochondrial permeability transition pore (mPTP) opening, a central step of axonal degeneration (AD) pathway (Barrientos *et al.*, 2011). Coincidentally, modulators of mitochondrial activity have been successfully probed as regulators of AD (Barrientos *et al.*,

2011). On the other hand, it has been proposed that oxaliplatin induces a nuclear-DNA independent apoptotic response in cells, which also involves mitochondrial components (Ta *et al.*, 2006). Altogether, this suggests that oxaliplatin neurotoxicity could target mitochondria in peripheral sensory neurons and induce AD. In this context, chemotherapies are known inductors of degeneration in terminals and focal degeneration in axonal shafts of sensory neurons (Pachman *et. al* 2014; Argyriou *et. al* 2014). We found that metformin was able to inhibit oxaliplatin induced AD *in vitro*. Specifically, oxaliplatin induces a significant degeneration of neurites in DRGs which is completely inhibited in the presence of metformin [Figure N°7]. Furthermore, in our model of oxaliplatin induced peripheral neuropathy *in vivo*, presence of metformin was able to inhibit degeneration of IENF. Specifically, after 30 days of oxaliplatin and metformin cotreatment, as described in Figure N°8, the number of IENF was significantly higher than oxaliplatin treatment alone and indistinguishable from control. To our knowledge, this is the first time metformin is reported as an inhibitor of axonal degeneration *per se*. In this context, it is important to mention that murine sciatic nerves *in vivo* are composed by approximately 6% myelinated motor axons, 23% myelinated and 48% unmyelinated sensory axons, with 23% unmyelinated sympathetic axons (Schmalbruch H., 1986). However, the specific dorsal root ganglia extracted and the protocol we used in this thesis establishes a culture highly enriched in DRG sensory neurons (Melli G. and Höke A., 2009). This suggest that metformin protects sensory neurons from degeneration induced by oxaliplatin toxicity. Thus, further evidence is needed to explore the potential neuroprotective effect of metformin over motor or sympathetic axons. Furthermore, considering the absence of axonal degeneration at sciatic nerves in our *in vivo* model [Figure N°9], further evidence is also needed to elucidate whether metformin protects from axonal degeneration *in vivo*.

Even more, oxaliplatin induced degeneration of IENF was presented in the absence of significant degeneration of axons in the peripheral branch of sensory neurons [Figure N°9] in the same conditions. We propose that these results suggest that metformin exerts a direct neuroprotective effect over sensory terminals, considering that the same neuroprotection is observed *in vivo* and *in vitro*, dismissing an indirect effect through systemic regulation of glycaemia by metformin. To elucidate the potential direct neuroprotective effect of metformin over sensory terminals, further evidence could be extracted from compartmentalized cultures of dorsal root ganglia neurons, assaying terminals integrity after local addition of oxaliplatin and/or metformin in the axonal terminals compartment. However, as we mentioned before, *in vitro* addition of oxaliplatin to unmyelinated sensory neurons (DRGs) culture induces axonal degeneration and metformin is able to inhibit the degeneration of the complete extension of the axon [Figure N°7]. This suggests that *in vivo* oxaliplatin would affect differentially to IENF and metformin is actually able to protect unmyelinated axons from toxicity of chemotherapy. Our *in vivo* results reproduce these findings and show for the first time that metformin inhibits oxaliplatin induced IENF degeneration in the context of OIPN. In this respect, it is possible that degeneration of IENF in absence of degeneration of axons in the shaft *in vivo* can be explained by differences in the local levels of oxaliplatin toxicity due to interference of the presence of Blood Nerve Barrier (BNB).

We suggest that metformin inhibits the canonical pathway of peripheral axonal degeneration in this model. i.e. that metformin could inhibit mitochondrial oxidation state (Press C., and Milbrandt J., 2008; O'Donnell. *et al.*, 2013) by modulation electron transport chain

activity. Beyond, this result shows that metformin inhibits oxaliplatin induced AD in unmyelinated axons. However, it remains unclear whether oxaliplatin activates canonical AD mechanism. This possibility is highly interesting, because in that hypothetical case, metformin could be a general inhibitor of AD and points the interest to evaluate metformin effect over others degenerative conditions. Further evidence is needed to support this claim and open an interesting topic of research with metformin as potential inhibitor of AD in response to other neurodegenerative stimuli.

Altogether, these results along with the fact that metformin inhibits IENF in the context of carboplatin CIPN *in vivo*, suggest that metformin could be also protective in the context of clinical oxaliplatin treatment.

Degeneration of axons has been reported under certain chemotherapies and particularly IENF during platinum compound treatments (Mao-Ying *et al.* 2014). Sensibility and transmission to thermal and mechanical stimuli is executed by IENF and axons of sensory DRGs (Kuner, 2010). Thus, morphological stability maintenance is a key condition to normal sensory function. IENF degeneration has been proposed as a major cause of neuropathic pain during CIPN (Han and Smith, 2013). As we said earlier, preservation of IENF morphology by metformin during carboplatin chemotherapy has been correlated with sensory function maintenance (Mao-Ying *et al.* 2014). However, if metformin was able to protect the axonal bundle remained unexplored on that study. Furthermore, several studies report that patients treated particularly with oxaliplatin exhibit little or absent axonal degeneration (Grisold, *et al.*, 2012). This fact is coherent with our findings where no axonal degeneration was shown in our

model [Figure N°9].

Besides, morphological stability of the central terminals of DRG at spinal cord during oxaliplatin treatment has never been explored before. In this context, we found that sensory DRGs central terminals at the spinal cord were unaffected by our oxaliplatin treatment. Specifically, areas covered by peptidergic (IB4) and non-peptidergic (CGRP) neurons terminals at the dorsal horn of spinal cord in rats treated with oxaliplatin were indistinguishable from control areas [Figure N°12]. Considering this, whether *in vivo* IENF are either intrinsically more susceptible to oxaliplatin toxicity or alternatively they are exposed to a higher local dose of oxaliplatin than axonal bundle and sensory DRG central terminals remains unclear and it is beyond the objectives of this thesis. At this respect, it has been proposed that degeneration of axonal terminals have different rates than axonal shafts, due to differential susceptibility to mitochondrial dysfunction as a consequence of local differences in mitochondrial populations (Gillingwater *et al.*, 2001; Oyebode *et al.*, 2012). This fact is coherent with the fashion of AD in response to chemotherapies toxicity observed in human patients, where longer axons degenerate preferentially by dying back (Cavaletti and Marmiroli, 2010). We suggest that axonal terminals and axonal shaft reproduce this model of differential susceptibility in response to oxaliplatin toxicity. In summary, preservation of IENF by metformin during OIPN could explain the sensory effects we will discuss later.

On the other hand, there have been reports indicating that overdose of metformin induces axonal degeneration due to B12 Vitamin deficiency (Kibirige and Mwebaze, 2013). The absence of degeneration of nerves in the metformin group suggests that the dose of metformin

used in this study (250 mg/Kg) is physiological and does not induce neurodegeneration *per se*. Furthermore, rats treated with metformin have a normal glycaemia, white blood cells counting and weight in comparison to previous reports [Figure N°17]. It is worth to mention that in the concentration range used in this thesis (150-300 mg/kg), oral administration of metformin leads to absorption by the small intestine and later renal excretion of approximately 90% of absorbed metformin up to 17.6 hours after administration (Wang *et al.*, 2018; Łabuzek *et al.*, 2010). However, metformin concentration peaks at the CSF only after 6 hours of administration and is already undetectable 12 hours after oral administration. Importantly, it has been reported that chronic metformin treatment in the same concentration range does not significantly changes metformin clearance or absorption dynamics (Wang *et al.*, 2018; Łabuzek *et al.*, 2010). Altogether, these facts indicate that metformin dose and administration regime used in our model is an adequate referential method to explore metformin effect over CIPN in murine models without significant secondary effects over relevant physiological variables or nerve tissue integrity. Importantly, as we explained in 13.2.2 of Methods section of this thesis, the dose of metformin we used in our studies was extrapolated from the human clinical dose indicated to treat Type II diabetes. Consequently, these results are highly relevant because they suggest that the findings we have obtained in our murine could be similar to potential findings in future clinical studies.

Chemotherapy toxicity also affects dorsal root ganglia morphology and cytology. At this respect, there have been reports of oxaliplatin induced atrophy in a subpopulation of larger dorsal root ganglia neurons positive to parvalbumin without neuronal loss (Jamieson and Mckeage, 2005). Considering that rat DRGs neuron somatic size correlates with conduction

velocity (Harper and Lawson, 1985), it is possible that oxaliplatin alters sensory function without neuronal loss. This may be the case in our model given that oxaliplatin treatment does not induce a significant reduction in the density neither of peptidergic nor non-peptidergic neurons at the DRG [Figure N°10]. However, our experimental procedures do not allow a proper study of neuronal size at the sensory DRGs.

On the other hand, it is widely known that axonal injury triggers an ATF3 mediated cellular stress response in neuronal soma (Bráz and Basbaum., 2010). This could be the case of our model, considering that we found significant IENF degeneration in response to oxaliplatin treatment [Figure N°8]. However, surprisingly, ATF3 was not activated in response to oxaliplatin treatment in our model [Figure N°11]. In this context, it is important to notice that we did not evaluate other markers of AD or activation of the molecular mechanism of AD at the axonal shaft in response to oxaliplatin. The fact that a potential damage in axonal shaft is theoretically able to produce stress in soma in our model is relevant to this discussion. To give light about this, we found that activation in axotomized sciatic nerves (positive control) was significantly higher than ATF3 levels in our drugs treatments [Figure N°11]. Actually, not a single nucleus with ATF3 activation was found in DRGs with our drugs treatments or in control condition. We suggest that the absence of ATF3 activation in neurons with evident oxaliplatin induced IENF degeneration reveals that this degenerative process does not involve ATF3 pathway stress signaling in the soma during our treatment. However, it has been demonstrated that neuronal stress signaling is regulated by a complex network that involves phosphorylation and nuclear localization of 39 transcription factors, implicated in the sensory neurons response to injury (Michaevski *et al.*, 2010). These transcription factors include c-

Jun, Jun D, activating transcription factor 3 (ATF3), cAMP response element binding protein (CREB), signal transducer and activator of transcription (STAT3), CCAAT/enhancer binding proteins (C/EBPs), p53, Oct-6, nuclear factor kappa-light-chain-enhancer of activated B cells (NF- κ B), nuclear factor of activated T-cells (NFATs), Kruppel-like factors (KLFs), Sox11, SnoN, ELK3, P311, and E47 (Schwaiger *et al.*, 2000; Mason *et al.*, 2003; Raivich *et al.*, 2004; Nadeau *et al.*, 2005; Di Giovanni *et al.*, 2006; Jankowski *et al.*, 2009; Ruff *et al.*, 2009; Magoulas and Lopez-de Heredia, 2010; Moore and Goldberg, 2011; Raivich, 2011). Once in the nucleus, they bind to selective DNA promoter regions to increase or repress transcription of specific target genes. Nerve injury can also result in reduced activation of transcription factors such as islet-1, Fra-2, ATF2, and TDP43 (Doyle and Hunt, 1997; Herdegen *et al.*, 1997; Hol *et al.*, 1999; Moisse *et al.*, 2009; Sato *et al.*, 2009). The activation of transcriptional programs is critical for expression of many target genes implicated in successful regeneration and blocking of transcription at an early time point after injury changes the regenerative response of injured neurons (Smith and Skene, 1997). Importantly, most of the sensory neurons response to stress has been studied using models of mechanical damage. In this context, mitochondrial accumulation of p53 in DRG neurons has been recently related to sensory symptoms of cisplatin induced peripheral neuropathy (Maj *et al.*, 2017). Altogether, substantial further evidence is needed to elucidate the role of transcription factors in response to potential stress induced by oxaliplatin treatment in sensory neurons.

Considering the absence of degeneration in peptidergic and non-peptidergic terminals at spinal cord [Figure N°12], we suggest that peripheral and central terminals of the same sensory

neurons have a different fate after oxaliplatin treatment. This implies that either the response to oxaliplatin toxicity between central and peripheral branches of DRG neurons is different or peripheral and central branches are under a different degenerative environment or even a complex combination of these two scenarios.

In one hand, there could be an intrinsic differential susceptibility to oxaliplatin between peripheral and central axonal terminals studied here. It is important to remember that preferential degeneration of longer peripheral axons is a characteristic of CIPN (Cavaletti and Marmiroli, 2010; Brown *et al.*, 2014) as we discussed earlier. This suggest that peripheral terminals of DRG neurons could have a higher susceptibility to degeneration in response to oxaliplatin toxicity. Considering this, degeneration of IENF in our model [Figure N°8], reproduces this previously reported characteristic of CIPN (Pachman, *et. al* 2014; Argyriou *et. al* 2014; Wolf *et. al* 2008; Bennett, *et al.*, 2011). Furthermore, peripheral and central branches could have differential stress signaling in response to oxaliplatin toxicity. However, this scenario remains unexplored. Even though, as we mentioned earlier, the activation of the downstream transcriptional program of regeneration in DRG neurons after injury relays in the stress signaling mediated by a myriad of transcription factors (Michaevlevski *et al.*, 2010). Interestingly, it has been widely demonstrated peripheral branches of DRG regenerate while the central branches of the same neurons are poorly regenerative (Saijilafu and Zhou, 2012; Huebner and Strittmatter, 2009; Gordon 2016; He and Jin, 2016). These phenotypes could underlie a differential stress signaling between peripheral and central branches of DRG in response to stress. Actually, it has been reported that c-Jun signaling and PTEN/mTOR pathways have differential activation pattern whether the injury affects central or peripheral branches of DRG neurons (Niekerk *et al.*, 2016; Park *et al.*, 2010). Unfortunately, the stress

signaling of DRG sensory neurons in response to oxaliplatin has not been explored. Considering this, further research is needed to elucidate the potential intrinsic differences in stress signaling between peripheral and central branches of DRG neurons in response to oxaliplatin. In this respect, comparison of ATF3 or other stress markers patterns between central and peripheral neuronal models *in vitro* would be interesting to perform, in order to elucidate potential intrinsic differences in central/peripheral response to oxaliplatin toxicity. Furthermore, neuronal stress markers induction after *in vivo* local administration of oxaliplatin to either peripheral or central branches of DRG neurons would be also highly informative.

On the other hand, central and peripheral DRG branches could also have differential exposition to oxaliplatin. As we mentioned in the introduction of this thesis, oxaliplatin concentrations in CSF are significantly lower than in plasma ultrafiltrates after intravenous administration (Jacobs *et al.*, 2005). Also mentioned before, efflux of oxaliplatin through OCTNs at the BBB has been proposed to explain these differences in oxaliplatin concentration between CSF and plasma ultrafiltrates (Sawchuk and Elmquist, 2000; Kusuhara and Sugiyama, 2005). Based on this, it is possible that in our model central branches of DRG neurons receive a much lower concentration of oxaliplatin after each administration, resulting in a lower cumulative local concentration by the time we extracted the samples at the end of our study. In this respect, it is important to remember that studies from Huang *et al.* (2016) indicate that when oxaliplatin is directly administered into the spinal cord there are local increases in abnormal field potential firing activity at the dorsal horn of rats (Huang *et al.*, 2016). Moreover, concentration used by Huang Z.Z., *et al.* (2016) is in the range of concentrations that oxaliplatin reaches at CSF after *i.v.* administration (Jacobs *et al.*, 2005).

However, considering the results regarding terminals of central branches after oxaliplatin administration under our experimental design [Figure N°12] whether this local concentration of oxaliplatin induces degeneration of central branches of DRG remains unknown. In contrast, the degeneration of terminals at peripheral branches (IENF) of DRG neurons after oxaliplatin administration is significant in our model [Figure N°8] and has been widely reported before as a main characteristic of CIPN (Pachman *et al.* 2014; Argryriou *et al.* 2014; Wolf *et al.* 2008; Bennett, *et al.*, 2011).

Altogether, in our study oxaliplatin toxicity induced morphological changes are focalized on IENF in the peripheral nervous system. However, modulation of pain transmission is also affected by astrocyte reactivity (Bradesi, 2010). More specifically, as we mentioned in the introduction of this thesis, it has been found that astrocyte activation sensitizes pain transmission (Bradesi, 2010). Accordingly, we found that Laminae I and II spinal cord of oxaliplatin treated rats had a significantly higher reactivity of astrocytes (GFAP) [Figure N°13]. This suggests that sensory transmission occurs in an inflammatory environment at spinal cord. In this context, it has been reported that activated astrocytes and presence of proinflammatory cytokines (e.g., interleukin [IL]-1 β) and chemokines (e.g., monocyte chemoattractant protein-1 [MCP-1]/also called CCL2) at the spinal cord is a common characteristic of neuropathic pain models (Hald *et al.*, 2009; Gao and Ru-Rong, 2010). Furthermore, proinflammatory cytokines have been related with changes in the excitability of sensory neurons in the context of neuropathic pain (Miller *et al.*, 2009). Considering this, we suggest that astrocyte reactivity after oxaliplatin administration [Figure N°13] could be correlated with sensory manifestations we report here through the release of proinflammatory

cytokines at spinal cord during our treatment. However, the potential release of proinflammatory cytokines during the oxaliplatin regime and dosage we present in this thesis, remains unexplored.

Interestingly, other authors have also studied the glial role during OIPN. However, important variables as administration regime and cumulative dose of oxaliplatin are considerably different between the studies. Beyond this, post the experimental execution of this thesis, astrocyte reactivity (GFAP) and absence of microglial activation after oxaliplatin treatment was reported by Robinson, C. R. *et al.* (2014) at day 7 under a cumulative dose of 24 mg/Kg oxaliplatin. Furthermore, we collected the spinal cord samples under our final cumulative dose of 32 mg/Kg [Figure N°2]. At this respect, cumulative dose of oxaliplatin at day 7 in our administration regime was only 8 mg/Kg. This would suggest that microglial activation was unlikely at day 7 under our experimental conditions, because at that day our cumulative dose of oxaliplatin was comparatively lower than in the study performed by Robinson, C. R. *et al.* (Robinson, C. R., *et al.*, 2014).

In parallel, Di Cesare Mannelli L. *et al.* (2013; 2014) reported microglial activation under a cumulative dose of 12 mg/Kg at the first week of their study, but surprisingly, the microglial activation was absent later under higher cumulative doses of oxaliplatin on the second and third week of the same study (24 mg/Kg and 36 mg/Kg cumulative doses, respectively). In the same study, astrocyte reactivity was present during all the cumulative doses of oxaliplatin they explored. Altogether, Di Cesare Mannelli *et al.* results (2013; 2014) suggest that microglial activation could have occurred during the second week of our study when we reached a

cumulative dose of 14 mg/Kg, but it would have been unnoticed because we collected our samples later [Figure N°13]. Even more, reversal of microglial activation reported by Di Cesare Mannelli *et al.* (2014) at higher cumulative concentrations of oxaliplatin, could have also occurred in our model and would have been potentially overlooked by the same reasons [Figure N°13]. Beyond this, is important to mention that these comparisons between our results and the results reported by Robinson, C. R. *et al.* (Robinson, C. R., *et al.*, 2014) or Di Cesare Mannelli *et al.* (Di Cesare Mannelli, L., *et al.*, 2013; Di Cesare Mannelli, L., *et al.*, 2014) are informative but remain speculative, because the administration regimes of oxaliplatin are different between these studies. More importantly, cumulative doses of oxaliplatin in relationship with the days of samples collection are also not coincident, and as we mention along the introduction and discussion of this Thesis, OIPN characteristics strongly rely on the chemotherapeutics administered and may be different during acute or chronic regimes. Altogether, the potential microglial activation at the initial experimental times and lower cumulative doses under our oxaliplatin dosage and regime remains unexplored and further research on this topic is needed.

Notably, here for the first time, anti-astrocyte (GFAP) reactivity effect of daily i.p administration of 250 mg/Kg metformin is reported after 30 days in cotreatment with a final cumulative dose of 32 mg/Kg oxaliplatin [Figure N°13]. It is important to mention that metformin is an antiinflammatory of CNS, as it has been demonstrated in a model of multiple sclerosis (Nath *et al.*, 2009). In that model of multiple sclerosis, metformin reduces the induction of proinflammatory cytokines (IFN- γ , TNF- α , IL-6, IL-17, and inducible NO synthase (iNOS) at the spinal cord (Nath *et al.*, 2009). This suggests that metformin could

significantly reduce inflammatory environment in spinal cord induced by oxaliplatin, under our experimental conditions. Additionally, this previously reported antiinflammatory effect of metformin over CNS could explain the significantly lower levels of astrocyte activation in spinal cord of rats treated with metformin and oxaliplatin compared with oxaliplatin treated alone [Figure N°13]. However, further research is needed to establish the potential role of metformin as an antiinflammatory in the context of oxaliplatin toxicity over nervous system.

Finally, we discuss that studies presented in this thesis have generated a significant amount of results that support metformin as an inhibitor of morphological and cytological changes in sensory circuits induced by oxaliplatin toxicity.

14.4 Use of Metformin as a Treatment Against Oxaliplatin Induced Peripheral Neuropathy: Sensory Symptoms.

Morphological and cytological changes in neuronal and non-neuronal cells under chemotherapy and sensory functional impairment characterize CIPN (Ahles and Saykin., 2007). In this context, specific chemotherapeutics and their cumulative dosage determinate the variable onset and reversibility observed on CIPN (Fehrenbacher, 2015). In the particular case of OIPN, there have been reported acute and chronical phases with increase of mechanical and cold sensitivity in preclinical models (Toyama, *et al.*, 2013). Notably, only the study by Xiao *et al.* (2012) has performed assays over heat sensitivity in response to oxaliplatin and it has found no significant differences between groups in rats.

Our results indicate that oxaliplatin induces mechanical allodynia inhibitable by metformin

cotreatment. Specifically, we found that oxaliplatin induced a significant decrease in the mean threshold withdrawal response at the Von Frey test [Figure N°14]. Interestingly, this sensitization to mechanical stimuli in oxaliplatin treated rats was markedly acute, considering that it occurred only immediately one day after oxaliplatin administration [Figure N°14]. Presence of metformin as cotreatment completely inhibited this sensitization to mechanical stimulus [Figure N°14]. Since we studied biopsies from pain circuitry extracted from rats at the end of this study [Figure N°2], we can only suggest that this sustained exacerbated response to touch in oxaliplatin treated rats along our study correlates with the IENF degeneration [Figure N°8] and spinal cord inflammation [Figure N°13] reported in this thesis. Importantly, here discussed exacerbated sustained response to touch, morphological and cytological changes during OPIN, are all inhibitable by metformin. However, further research is needed to study IENF morphological stability and spinal cord inflammation specifically at days of acute significant sensitization to mechanical stimuli during OIPN. Consequently, further research is also needed to test the protective role of metformin over oxaliplatin induced sensitization to mechanical stimulus in a proper model of acute administration alone.

Besides, it has been repeatedly proposed that pain response comprehend dysfunction along the whole pain circuitry (West *et al.*, 2015). Considering this, it is also possible that another pathological dysfunction that do not include a degenerative process could be present in here, such as action potential conduction alterations, and sensitization of pain receptors or pain transmission in central nervous system pain regulatory centers. Furthermore, it remains unknown whether here discussed significant acute sensitization in response to touch in oxaliplatin treated rats [Figure N°14] occurs in a framework of sustained chronic progression

of IENF degeneration and inflammation at spinal cord, associated with the cumulative effect of oxaliplatin, or in a more complex framework with potential stages of acute increase in IENF degeneration or inflammation at the spinal cord specifically after oxaliplatin administration, in addition to the chronic process (i.e. summation of acute events). Altogether, the specific origin of the acute mechanical allodynia in response to oxaliplatin remains unexplained. However, our model of OIPN reproduces the emergence of mechanical allodynia reported before in response to different regimes and dosages of oxaliplatin treatments (Xiao *et al.*, 2012; Yamamoto *et al.*, 2016).

It is important to mention that the design of our study excluded a comparison of the behavior in response to sensory stimulation between metformin treated and a control group of vehicle treated rats. In the case of having included these comparisons, it would have provided a stronger set of data to suggest metformin as an inhibitor of OIPN with potential clinical applications.

However, the effect of similar doses of metformin treatment over sensory response has been previously studied using the same touch and heat assays reported in this thesis. Specifically, metformin treatment (250 mg/kg i.p.) effect over response to touch using the Von Frey assay has been previously reported in the context of peripheral neuropathy induced by cisplatin (Zhou *et al.*, 2016). These authors report no significant differences in the percentage of withdrawal threshold in response to touch between metformin and saline treated mice. Additionally, the innocuity of metformin (200 mg/kg) over sensory response to touch using the Von Frey test has been extensively reported in the context of murine models of diabetic

neuropathy (Gao and Zheng, 2014; Barragán-Iglesias *et al.*, 2018). Based on these reports, if further experiments are going to be performed, we expect no significant differences in withdrawal response to touch between metformin and vehicle treated rats. Furthermore, metformin effect over sensory response to cold stimulation has also been previously explored using the same acetone test we present in this thesis. In the context of diabetic neuropathy, Ma *et al.* 2015 found no significant differences in paw withdrawal latency duration between metformin (200 mg/kg and 500 mg/kg) and vehicle treated rats (Ma et al., 2015). Considering this, if further experiments are going to be performed, we expect no significant differences in paw withdrawal latency duration in response to cold stimulation between metformin and saline treated rats.

Unfortunately, metformin effect over sensory response to heat stimulation using Hargreaves test has not been explored before. Consequently, metformin treated rats withdrawal latency in response to heat has not been compared with vehicle treated rats. In this context, absence of significant differences in response to touch and cold stimulation between metformin and vehicle treated rats suggest also an absence of comparative significance in response to heat.

As we mentioned before, inhibition of oxaliplatin induced chronic mechanical allodynia by metformin treatment has been previously reported in mice (Xiao *et al.*, 2012). This suggests that our oxaliplatin CIPN model not only reproduces oxaliplatin induced mechanical allodynia, but also reproduces metformin complete inhibition of oxaliplatin induced mechanical allodynia. At this respect, the results of this thesis detail for the first time that

metformin can inhibit an acute mechanical allodynia in response to oxaliplatin treatment, beyond the previously reported effect over chronic mechanical allodynia. This extends the potential clinical applications of metformin in the context of CIPN to avoid sensory symptoms in patients who do not develop chronic CIPN. However, OIPN also induces cold and heat sensing impairment (Xiao *et al.*, 2012), and potential of metformin to inhibit either cold allodynia or heat allodynia has remained unexplored. We found that metformin cotreatment was able to inhibit oxaliplatin induced hypoalgesia and cold allodynia in response to heat and cold stimuli, respectively [Figure N° 15 and Figure N°16, respectively]. Notably, we found that metformin cotreatment was able to abolish cold allodynia observed in response to oxaliplatin cotreatment alone [Figure N°16]. Specifically, withdrawal response to cold stimulus duration was significantly and chronically higher in oxaliplatin treated rats from day 21 to the end of this study, while withdrawal response to cold stimulus duration under cotreatment of oxaliplatin and metformin was indistinguishable from metformin alone [Figure N°16]. Furthermore, the results of this thesis indicate for the first time that cotreatment of metformin and oxaliplatin reverses heat hypoalgesia induced by oxaliplatin administration alone [Figure N°15]. However, metformin does not inhibit oxaliplatin induced heat hypoalgesia during the second week, but only from the third week to the end of this study [Figure N°15]. We suggest that there is a critical event between second and third week of oxaliplatin induced heat hypoalgesia. In this respect, considering that oxaliplatin is a cumulative drug, it is utterly improbable that oxaliplatin induced CIPN reverts after third week in cotreatment with metformin. Actually, oxaliplatin treated rats maintain oxaliplatin induced thermal allodynia in response to cold and show morphological and cytological changes in pain circuits until fourth week of this study, suggesting that the effect of oxaliplatin toxicity is present. Another

possibility is that metformin could reach a critical cumulative dose by the fourth week of this study. This possibility is also highly improbable given that metformin is not a cumulative drug and has a very high clearance in the range of hours (Kajbaf *et al.*, 2015). Thus, we discuss that the only possible alternative scenario is that metformin potentiates an intrinsically generated response to oxaliplatin toxicity over pain circuitry and thus regulates thermal hypoalgesia in response to heat since the third week of this study. This possibility has a major importance, because it implies that there is a compensatory event in thermal sensory function during oxaliplatin CIPN. Further research is needed to explore the intrinsic compensatory abilities of the sensory system as a target of metformin treatment. Furthermore, reversion of oxaliplatin induced thermal hypoalgesia in response to heat remains unexplained and shows an unexpected dynamic which underlying mechanism appears of major interest.

In conclusion, we have demonstrated that metformin significantly inhibits OIPN. Thence, we propose that those results contribute to extend the safe and neuroprotective effect of metformin in the context of chemotherapy side effects over sensory circuitry stability and functionality. Additionally, we considerate that metformin beneficial effects over CIPN have been amply demonstrated in the subclinical level in this thesis. Moreover, considering the existence of the toxicity studies underlying its current status of approved drug, we suggest that this potential second medical application of metformin could have a considerably shorter process of approval in comparison to a potential newly developed drug. This emphasizes the current need of additional exploration of metformin as a coadjuvant of chemotherapy in future clinical trials.

15. CONCLUSIONS.

This thesis demonstrates inhibition of oxaliplatin induced peripheral neuropathy in a murine model using the anti-diabetic clinical drug metformin in dosage and administration regimes which can be extrapolated to human clinical models of OIPN.

In brief, we were able to establish that metformin as a cotreatment inhibits morphological and cytological changes in the sensory circuits and associated functional symptoms induced by oxaliplatin toxicity. Specifically, we confirm the previously reported neuroprotective effect of metformin against oxaliplatin induced degeneration of Intraepidermal Nerve Fibers. More importantly, here we provide for the first time, experimental evidence to support the role of metformin as an antiinflammatory against astrocyte reactivity in the context of OIPN. Finally, here we demonstrate for the first time that metformin inhibits oxaliplatin induced mechanical allodynia, cold allodynia and heat hypoalgesia.

Altogether, our results reproduce the morphological, cytological and functional symptoms observed in human patients under oxaliplatin chemotherapy and suggest they are inhibitable by metformin. Therefore, we report metformin as the most significant treatment against OIPN explored up to date and strongly encourage further research to translate these preclinical results to the clinical context where millions of patients are being affected by this pathology.

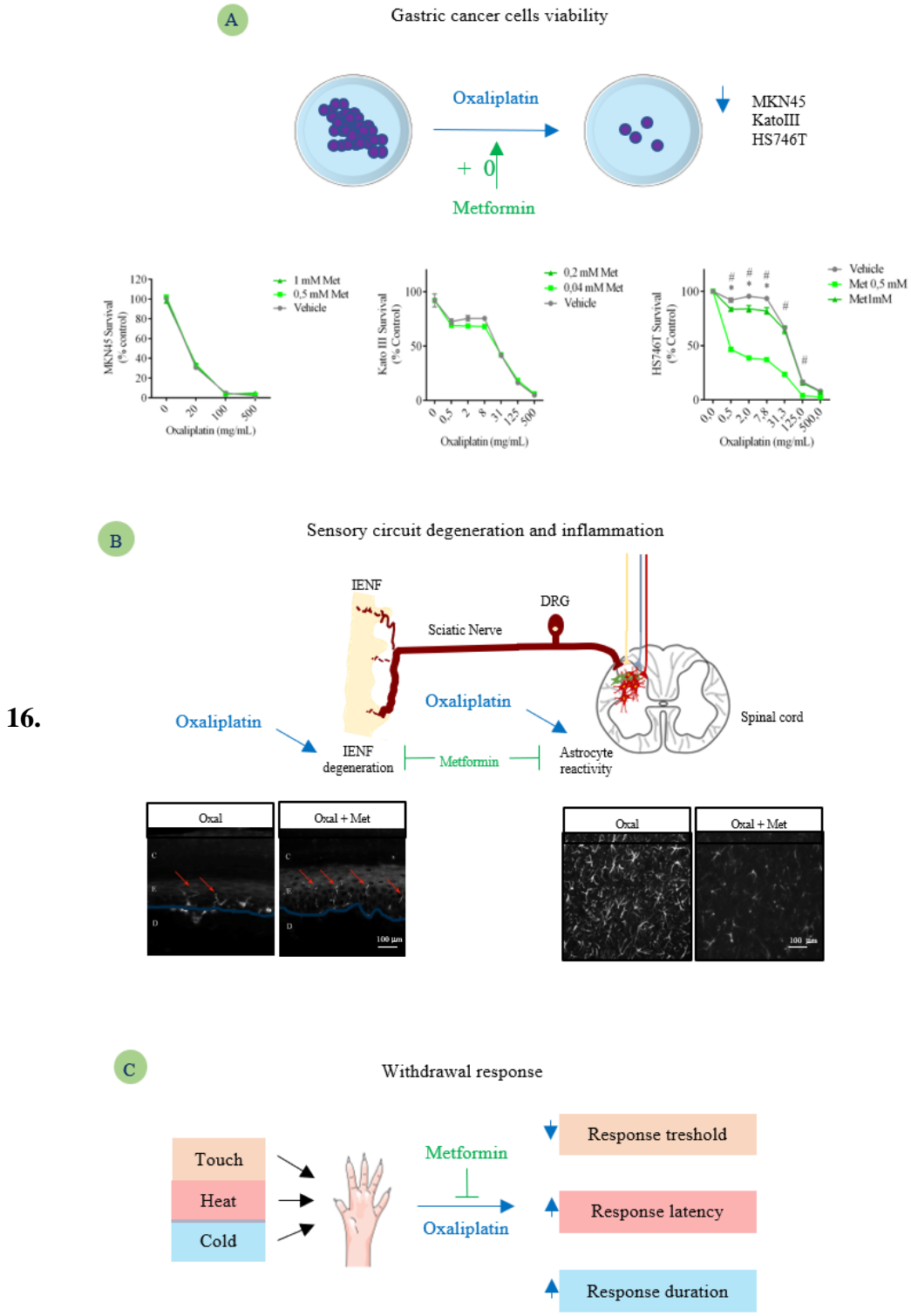


FIGURE N°18. GRAPHICAL ABSTRACT. Metformin does not interfere or synergizes with *in vitro* antineoplastic effect of oxaliplatin over cancer cell lines (A) and inhibits sensory circuits degeneration, inflammation (B) plus painful neuropathy induced by oxaliplatin *in vivo*(C).

BIBLIOGRAPHY.

1. Ahmet H. and Ray, M. (2014). Rodent Models of Chemotherapy-Induced Peripheral Neuropathy. *ILAR Journal*, Volume 54, Number 3.
2. Aiyer R., Mehta N., Gungor S., Gulati A. A. (2018). Systematic Review of NMDA Receptor Antagonists for Treatment of Neuropathic Pain in Clinical Practice. *Clin J Pain*. 2018 May;34(5):450-467.
3. Aley K. O., Reichling D. B., Levine J. D. (1996). Vincristine hyperalgesia in the rat: a model of painful vincristine neuropathy in humans. *Neuroscience* 73, 259–265.
4. Algire C, Zakikhani M, Blouin M-J, Shuai JH, Pollak M. (2008). Metformin attenuates the stimulatory effect of a high energy diet on *in vivo* H59 carcinoma growth. *Endocr Relat Cancer* 15: 833–839.
5. Algire, C., Amrein, L., Bazile, M., David, S., Zakikhani, M., and Pollak, M. (2010). Diet and tumor LKB1 expression interact to determine sensitivity to anti-neoplastic effects of metformin *in vivo*. *Oncogene*, 30(10), 1174–1182.
6. Argyriou, A. A., Chroni, E., Koutras, a., Ellul, J., Papapetropoulos, S., Katsoulas, G., Kalofonos, H. P. (2005). Vitamin E for prophylaxis against chemotherapy-induced neuropathy: A randomized controlled trial. *Neurology*, 64(1), 26–31.

7. Argyriou, A. A., Kyritsis, A. P., Makatsoris, T., and Kalofonos, H. P. (2014). Chemotherapy-induced peripheral neuropathy in adults: A comprehensive update of the literature. *Cancer Management and Research*, 6(1), 135–147.
8. Ashabi, G., Khalaj, L., and Khodagholi, F. (2014). Pre-treatment with metformin activates Nrf2 antioxidant pathways and inhibits inflammatory responses through induction of AMPK after transient global cerebral ischemia. *Metab Brain Dis.* 2015 Jun; 30(3):747-54.
9. Ateron, K. (2010). Metformin Associated with Lower Cancer Mortality in Type 2 Diabetes. *Diabetes Care*, Volume 33, Number 2, February 2010.
10. Baba H., Doubell T.P., Moore K.A., Woolf C.J. (2000) Silent NMDA receptor-mediated synapses are developmentally regulated in the dorsal horn of the rat spinal cord. *J Neurophysiol.* 2000 Feb;83(2):955-62.
11. Barabas, M. E., Kossyрева, E. A., and Stucky, C. L. (2012). TRPA1 Is Functionally Expressed Primarily by IB4- Binding, Non-Peptidergic Mouse and Rat Sensory Neurons. *PLoS One.* 2012; 7(10): e47988.
12. Barragán-Iglesias P., Oidor-Chan V.H., Loeza-Alcocer E., Pineda-Farias J.B., Velazquez-Lagunas I., Salinas-Abarca A.B., Hong E., Sánchez-Mendoza A., Delgado-Lezama R., Price T.J., Granados-Soto V. Evaluation of the neonatal streptozotocin model of diabetes in rats: Evidence for a model of neuropathic pain. *Pharmacol Rep.* 2018 Apr;70(2):294-303.
13. Barrientos, S., Martinez, N. W., Yoo, S., Jara, J. S., Zamorano, S., Hetz, C., Court, F. A. (2011). Axonal degeneration is mediated by the mitochondrial

- permeability transition pore. *The Journal of Neuroscience: The Official Journal of the Society for Neuroscience*, 31(3), 966–78.
14. Basbaum A.I. and Jessell T. (2000). The perception of pain. In: Kandel ER, Schwartz JH, Jessell TM, editors. *Principles of Neural Science*. 4th ed. New York: McGraw-Hill, Health Professions Division; 2000.
 15. Basbaum A.I. and Woolf C.J. (2009). Recognition and Alleviation of Pain in Laboratory Animals Committee on Recognition and Alleviation of Pain in Laboratory Animals, National Research Council (2009) ISBN: 0-309-12835-8.
 16. Basbaum, A. I., Bautista, D. M., Scherrer, G., and Julius, D. (2010). Cellular and Molecular Mechanisms of Pain. *Cell*. 2009 October 16; 139(2): 267–284.
 17. Batandier, C., Guigas, B., Detaille, D., El-Mir, M.-Y., Fontaine, E., Rigoulet, M., and Leverve, X. M. (2006). The ROS production induced by a reverse-electron flux at respiratory-chain complex 1 is hampered by metformin. *Journal of Bioenergetics and Biomembranes*, 38(1), 33–42.
 18. Bayliss, J. A., Lemus, M. B., Santos, V. V, Deo, M., Davies, S., Kemp, B. E., Andrews, Z. B. (2016). Metformin Prevents Nigrostriatal Dopamine Degeneration Independent of AMPK Activation in Dopamine Neurons. *PLoS One*. 2016 jul 28;11(7): e0159381.
 19. Beatriz, L., Rojas, A., and Gomes, M. B. (2013). Metformin: an old but still the best treatment for type 2 diabetes. *Diabetology and Metabolic Syndrome* 2013, 5:6.

20. Beijers, A. J. M., Mols, F., and Vreugdenhil, G. (2014). A systematic review on chronic oxaliplatin-induced peripheral neuropathy and the relation with oxaliplatin administration. *Support Care Cancer*. 2014 jul; 22(7):1999-2007.
21. Bennett G. J., Liu G. K., Xiao W. H., Jin H. W., Siau C. (2011). Terminal arbor degeneration – a novel lesion produced by the antineoplastic agent paclitaxel. *Eur. J. Neurosci*. 33, 1667–1676.
22. Berger, J. V, Knaepen, L., Janssen, S. P. M., Jaken, R. J. P., Marcus, M. A. E., Joosten, E. A. J., and Deumens, R. (2011). Cellular and molecular insights into neuropathy-induced pain hypersensitivity for mechanism-based treatment approaches. *Brain Research Reviews*, 67(1–2), 282–310.
23. Bhatnagar, B., Gilmore, S., Goloubeva, O., Pelsler, C., Medeiros, M., Chumsri, S., Bao, T. (2014). Chemotherapy dose reduction due to chemotherapy induced peripheral neuropathy in breast cancer patients receiving chemotherapy in the neoadjuvant or adjuvant settings: a single-center experience. *SpringerPlus*, 3, 366.
24. Boland, E. G., Selvarajah, D., Hunter, M., Ezaydi, Y., Tesfaye, S., Ahmedzai, S. H., Wilkinson, I. D. (2014). Central Pain Processing in Chronic Chemotherapy-Induced Peripheral Neuropathy: A Functional Magnetic Resonance Imaging Study. *PLoS ONE*, 9(5), e96474.
25. Bonin, R. P., Bories, C., and Koninck, Y. De. (2014). MOLECULAR PAIN A simplified up-down method (SUDO) for measuring mechanical nociception in rodents using von Frey filaments A simplified up-down

- method (SUDO) for measuring mechanical nociception in rodents using von Frey filaments. *Mol Pain*. 2014; 10: 26.
26. Bookman MA, Greer BE, Ozols RF. (2003). Optimal therapy of advanced ovarian cancer: carboplatin and paclitaxel versus cisplatin and paclitaxel (GOG158) and an update on GOG0182-ICON5. *Int J Gynecol Cancer*. 2003 nov-dec; 13 Suppl 2:149-55.
27. Boussios, S., Pentheroudakis, G., Katsanos, K., and Pavlidis, N. (2012). Systemic treatment-induced gastrointestinal toxicity: incidence, clinical presentation and management. *Annals of Gastroenterology* (2012) 25, 106-118.
28. Boyette-Davis J. and P.M. Dougherty. (2011). Protection against oxaliplatin-induced mechanical hyperalgesia and intraepidermal nerve fiber loss by minocycline. *Exp Neurol*. 2011 June; 229(2): 353–357.
29. Boyette-Davis J., Edgar T Walters, and Patrick M Dougherty. (2015). Mechanisms involved in the development of chemotherapy-induced neuropathy. *Pain Mag*. 2015; 5(4): 285–296.
30. Boyette-Davis J.A., Cata J.P., Driver L.C., Novy D.M., Bruel B.M., Mooring D.L., Wendelschaefer-Crabb G., Kennedy W.R., Dougherty P.M. (2013). Persistent chemoneuropathy in patients receiving the plant alkaloids paclitaxel and vincristine. *Cancer Chemother Pharmacol*. 2013; 71(3):619–626.
31. Bradesi S. (2010). Role of spinal cord glia in the central processing of peripheral pain perception. *Neurogastroenterol Motil*. 2010 May; 22(5):

- 499–511.
32. Brower, M., Grace, M., Kotz, C. M., and Koya, V. (2015). Comparative analysis of growth characteristics of Sprague Dawley rats obtained from different sources. *Lab Anim Res.* 2015 Dec; 31(4): 166–173.
 33. Brown, M. R. D., Ramirez, J. D., and Farquhar-smith, P. (2014). Pain in cancer survivors. *British Journal of Pain* 2014, Vol. 8(4) 139–153.
 34. Brzeziński K. (2012). Chemotherapy-induced peripheral neuropathy. Part II. Prevention. *Contemp Oncol (Pozn)*. 2012; 16(3): 258–261.
 35. Brzeziński, K. (2012). Chemotherapy-induced peripheral neuropathy. Part I. Pathophysiology, *Wspolczesna Onkol* 2012; 16 (1): 72–78
 36. Burstein H. J., Burton A. W., Custodio C. M., Deng G. E., Ho M., Von Roenn J. H. (2009). NCCN task force report: Management of neuropathy in cancer. *Journal of the National Comprehensive Cancer Network*.2009; 7: S1–S26
 37. Buzzai M., Jones R.G., Amaravadi R.K., Lum J.J., DeBerardinis R.J., Zhao F., Viollet B., Thompson C.B. (2007). Systemic treatment with the antidiabetic drug metformin selectively impairs p53-deficient tumor cell growth. *Cancer Res* 67: 6745–6752.
 38. Campbell J.N. and Meyer R.A. (2006). Mechanisms of neuropathic pain. *Neuron*. 2006;52(1):77–92.
 39. Cascinu, S. (2002). Neuroprotective Effect of Reduced Glutathione on Oxaliplatin-Based Chemotherapy in Advanced Colorectal Cancer: A Randomized, Double-Blind, Placebo-Controlled Trial. *Journal of Clinical*

- Oncology, 20(16), 3478–3483.
40. Cavaletti, G., and Marmiroli, P. (2010). Chemotherapy-induced peripheral neurotoxicity. Nature Publishing Group. *Nat. Rev. Neurol.* 2010 Dec;6(12):657-66.
41. Cavaletti, G., Tredici, G., Petruccioli, M. G., Dondè, E., Tredici, P., Marmiroli, P., Etienne, G. G. (2001). Effects of different schedules of oxaliplatin treatment on the peripheral nervous system of the rat. *European Journal of Cancer (Oxford, England: 1990)*, 37(18), 2457–63.
42. Chai, X., Chu, H., Yang, X., Meng, Y., Shi, P., and Gou, S. (2015). Metformin Increases Sensitivity of Pancreatic Cancer Cells to Gemcitabine by Reducing CD133+ Cell Populations and Suppressing ERK/P70S6K Signaling. *Scientific Reports*, 5(August), 14404.
43. Chaplan, S. R., Bach, F. W., Pogrel, J. W., Chung, J. M., and Yaksh, T. L. (1994). Quantitative assessment of tactile allodynia in the rat paw. *J Neurosci Methods*. 1994 Jul; 53(1):55-63.
44. Chatterjee, S., Thaker, N., and De, A. (2015). Combined 2-deoxy glucose and metformin improves therapeutic efficacy of sodium-iodide symporter-mediated targeted radioiodine therapy in breast cancer cells. *Breast Cancer (Dove Med Press)*. 2015 Aug 31; 7:251-65.
45. Chen J, Huang XF, Qiao L, Katsifis A. (2011). Insulin caused drug resistance to oxaliplatin in colon cancer cell line HT29. *J Gastrointest Oncol* 2011; 2:27-33.
46. Chiang, M., Cheng, Y., Chen, S., Yen, C., and Huang, R. (2016).

- Experimental Cell Research. Volume 347, Issue 2, 1 October 2016, Pages 322–331.
47. Cho H.K., Lee E.S., Lee J.W., Park J.K., Kang J.H., Lee K.S., Shim C.K., Chung S.J., Kim D.D., Kuh H.J. (2006). Clinical pharmacokinetics of oxaliplatin and 5-fluorouracil administered in combination with Leucovorin in Korean patients with advanced colorectal cancer. *J Cancer Res Clin Oncol.* 2006 May; 132(5):320-6.
48. Colleoni, M., and Sacerdote, P. (2010). *Biochimica et Biophysica Acta* Murine models of human neuropathic pain. *BBA - Molecular Basis of Disease*, 1802(10), 924–933.
49. Common Terminology Criteria for Adverse Events. 2009. V5.0. National Cancer Institute. Cancer Therapy Evaluation Program. (2009). U.S. Department of health and human services. National Institutes of Health
National Cancer Institute.
https://ctep.cancer.gov/protocolDevelopment/electronic_applications/ctc.htm
50. Coriat, R., Alexandre, J., Nicco, C., Quinquis, L., Benoit, E., Chéreau, C., Batteux, F. (2014). Treatment of oxaliplatin-induced peripheral neuropathy by intravenous Mangafodipir. *J Clin Invest.* 2014 Jan; 124(1):262-72.
51. Costigan M., Befort K., Karchewski L., Griffin R.S., D’Urso D. Replicate high-density rat genome oligonucleotide microarrays reveal hundreds of regulated genes in the dorsal root ganglion after peripheral nerve injury. *BMC Neurosci.* 2002; 3:16.

52. Costigan M., Scholz J., Woolf C.J. (2009). Neuropathic pain: a maladaptive response of the nervous system to damage. *Annu Rev Neurosci.* 2009; 32:1-32.
53. Cox, J. J., Reimann, F., Nicholas, A. K., Thornton, G., Roberts, E., Springell, K., Woods, C. G. (2006). An SCN9A channelopathy causes congenital inability to experience pain, 444(December), 3–7.
54. David M. Owens and Ellen A. Lumpkin. (2014). Diversification and Specialization of Touch Receptors in Skin. *Cold Spring Harb Perspect Med.* 2014 Jun; 4(6): a013656.
55. de Gramont, A., Figuer, A., Seymour, M., Homerin, M., Hmissi, A., Cassidy, J., Boni, C., Cortes- Funes, H., Cervantes, A., Freyer, G., Papamichael, D., Le Bail, N., Louvet, C., Hendler, D., de Braud, F., Wilson, C., Morvan, F., Bonetti, A. (2000). Leucovorin and fluorouracil with or without oxaliplatin as first line treatment in advanced colorectal cancer. *J. Clin. Oncol.* 18, 2938–2947.
56. Denk, F., McMahon, S. B., and Tracey, I. (2014). Pain vulnerability: a neurobiological perspective. *Nature Publishing Group*, 17(2), 192–200.
57. Di Cesare Mannelli, L., Pacini, A., Bonaccini, L., Zanardelli, M., Mello, T., Ghelardini, C. (2013). Morphologic features and glial activation in rat oxaliplatin-dependent neuropathic pain. *J Pain.* 2013; 14(12): 1585- 600.
58. Di Cesare Mannelli, L., Pacini, A., Corti, F., Boccella, S., Luongo, L., Esposito, E., Cuzzocrea, S., Maione, S., Calignano, A., Ghelardini, C. (2015). Antineuropathic profile of N-palmitoylethanolamine in a rat model

- of oxaliplatin-induced neurotoxicity. *PLoS One*. 2015a; 10(6): e0128080.
59. Di Cesare Mannelli, L., Pacini, A., Micheli, L., Tani, A., Zanardelli, M., Ghelardini C. (2014). Glial role in oxaliplatin-induced neuropathic pain. *Exp Neurol*. 2014; 261: 22–33.
60. Di Francesco A.M., Ruggiero A., Riccardi R. (2002). Cellular and molecular aspects of drugs of the future: oxaliplatin. *Cell Mol Life Sci*. 2002 Nov;59(11):1914-27.
61. Di Giovanni, S., Knights, C. D., Rao, M., Yakovlev, A., Beers, J., Catania, J., Avantaggiati, M. L., and Faden, A. I. (2006). The tumor suppressor protein p53 is required for neurite outgrowth and axon regeneration. *EMBO J*. 25, 4084–4096.
62. Dong X.W., Goregoaker S., Engler H., Zhou X., Mark L. Small interfering RNA-mediated selective knockdown of Na(V)1.8 tetrodotoxin-resistant sodium channel reverses mechanical allodynia in neuropathic rats. *Neuroscience*. 2007; 146:812–21.
63. Doyle, C. A., and Hunt, S. P. (1997). Reduced nuclear factor kappa B (p65) expression in rat primary sensory neurons after peripheral nerve injury. *Neuroreport* 8, 2937–2942.
64. Ekberg J., Jayamanne A., Vaughan C.W., Aslan S., Thomas L. muO-conotoxin MrVIB selectively blocks Nav1.8 sensory neuron specific sodium channels and chronic pain behavior without motor deficits. *Proc. Natl. Acad. Sci. USA*. 2006; 103:17030–35.
65. Ellis, A., and Bennett, D. L. H. (2013). Neuroinflammation and the

- generation of neuropathic pain. *British Journal of Anaesthesia*, 111(1), 26–37.
66. Eriguchi, M., Nonaka, Y., Yanagie, H., Yoshizaki, I., Takeda, Y., and Sekiguchi, M. (2003). A molecular biological study of anti-tumor mechanisms of an anti-cancer agent oxaliplatin against established human gastric cancer cell lines. *Biomed Pharmacother.* 2003 nov; 57(9):412-5.
67. Ewertz, M., Qvortrup, C., and Eckhoff, L. (2015). Chemotherapy-induced peripheral neuropathy in patients treated with taxanes and platinum derivatives. *Acta Oncologica*, (September 2014), 1–5.
68. F. Y. Zheng, W.-H. Xiao and G. J. Bennett. (2011). The response of spinal microglia to chemotherapy-evoked painful peripheral neuropathies is distinct from that evoked by traumatic nerve injuries. *Neuroscience*. 2011 Mar 10; 176: 447–454.
69. Fehrenbacher, J. C. (2015). *Chemotherapy-Induced Peripheral Neuropathy. Molecular and Cell Biology of Pain* (1st ed., Vol. 131). Elsevier Inc.
70. Ferreira T. and Rasband W. (2012). ImageJ 1.46r ImageJ User Guide User Guide ImageJ. Tuesday 2nd October 2012. <https://imagej.nih.gov/ij/docs/guide/user-guide.pdf>.
71. Ferrier, J., Pereira, V., Busserolles, J., Authier, N., and Balayssac, D. (2013). Emerging trends in understanding chemotherapy-induced peripheral neuropathy. *Current Pain and Headache Reports*, 17(10), 1–9.
72. Fields H.L., Rowbotham M., Baron R. (1998). Postherpetic neuralgia: irritable nociceptors and deafferentation. *Neurobiol. Dis.* 1998; 5:209–27.

73. Francesca, P., Ismail, P., Ishola, O., and Contu, L. (2016). Metformin Prevented Dopaminergic Neurotoxicity Induced by 3, 4-Methylenedioxymethamphetamine Administration. *Neurotoxicity Research*. *Neurotox Res*. 2016 Jul; 30(1):101-9.
74. Franciosi, M., Lucisano, G., Lapice, E., Strippoli, G. F. M., and Nicolucci, A. (2013). Metformin Therapy and Risk of Cancer in Patients with Type 2 Diabetes: Systematic Review. *PLoS One*. 2013 Aug 2; 8(8): e71583.
75. Fullerton S.M., Shirman G.A., Strittmatter W.J., Matthew W.D. (2001). Impairment of the blood-nerve and blood-brain barriers in apolipoprotein e knockout mice. *Exp Neurol*. 2001 May;169(1):13-22.
76. Gamelin E., Boisdron-Celle M, Lebouil A, Turcant A, Cailleux A, Krikorian A, Brienza S, Cvitkovic E, Larra F, Robert J, Allain P (1998). Determination of unbound platinum after oxaliplatin administration: comparison of currently available methods and influence of various parameters. *Anticancer Drugs*. 1998 Mar; 9(3):223-8.
77. Gamelin, E., Gamelin, L., Bossi, L., Quasthoff, S. (2002). Clinical aspects and molecular basis of oxaliplatin neurotoxicity: Current management and development of preventive measures. *Semin Oncol* 2002; 29: 21-33.
78. Gamelin, L., Boisdron-Celle M, Delva R., Guérin-Meyer V., Ifrah N., Morel A., Gamelin E. (2004). Prevention of oxaliplatin-related neurotoxicity by calcium and magnesium infusions: a retrospective study of 161 patients receiving oxaliplatin combined with 5-Fluorouracil and leucovorin for advanced colorectal cancer. *Clin Cancer Res*, 2004. 10(12 Pt

- 1): p. 4055-61.
79. Gao F. and Zheng Z.M. Animal models of diabetic neuropathic pain. *Exp Clin Endocrinol Diabetes*. 2014 Feb;122(2):100-6.
80. Gardner E.P. and Johnson K.O. (2013). Touch. In *Principles of neural science* (ed. Kandel ER, Schwartz JH, Jessell TM, Siegelbaum SA, Hudspeth AJ), pp. 498–529 McGraw-Hill, New York.
81. Gary J. Bennett, Guo Kai Liu, Wen Hua Xiao, Hai Wei Jin, and Chiang Siau. (2011). Terminal arbor degeneration (TAD): a novel lesion produced by the antineoplastic agent, paclitaxel. *Eur J Neurosci*. (2011) May; 33(9): 1667–1676.
82. Geier E.G., Chen E.C., Webb A., Papp A.C., Yee S.W., Sadee W., Giacomini K.M. (2013). Profiling solute carrier transporters in the human blood-brain barrier. *Clin Pharmacol Ther* 2013; 94:636–639.
83. Gillingwater, T. H., and Ribchester, R. R. (2001). Compartmental neurodegeneration and synaptic plasticity in the *Wld(s)* mutant mouse. *The Journal of Physiology*, 534(Pt 3), 627–39.
84. Gold M.S., Weinreich D., Kim C.S., Wang R., Treanor J. Redistribution of Na(V)1.8 in uninjured axons enables neuropathic pain. *J. Neurosci*. 2003; 23:158–66.
85. Gold, M. S., and Gebhart, G. F. (2016). Nociceptor sensitization in pain pathogenesis. *Nat Med Nat Med*. 2010 November; 16(11): 1248–1257
86. Gordon T. (2016). Nerve regeneration in the peripheral and central nervous systems. *J Physiol*. 2016 Jul 1; 594(13): 3517–3520.

87. Grant P.J. (1996). The effects of high- and medium-dose metformin therapy on cardiovascular risk factors in patients with type II diabetes. *Diabetes Care*.1996 Jan; 19(1):64-6.
88. Gregg R.W., Molepa J.M., Monpetit V.J.A., Mikael N.Z., Redmond D, Gadia M. and Stewart D.J. (1992) Cisplatin neurotoxicity: The relationship between dosage, time and platinum concentration in neurological tissues, and morphologic evidence of toxicity. *J Clin Oncol* 10: 795–803.
89. Grisold, W., Cavaletti, G., and Windebank, A. J. (2012). Peripheral neuropathies from chemotherapeutics and targeted agents. *Neuro-Oncology* 14: iv45–iv54, 2012.
90. Grolleau, F., Gamelin, L., Boisdron-Celle M. (2001). A possible explanation for a neurotoxic effect of the anticancer agent oxaliplatin on neuronal voltage-gated sodium channels. *J Neurophysiol*. 2001; 85: 2293-7.
91. Gwak Y.S., Hulsebosch C.E., Leem J.W. (2017). Neuronal-Glial Interactions Maintain Chronic Neuropathic Pain after Spinal Cord Injury. *Neural Plast*. 2017; 2017:2480689.
92. Hains B.C, Klein J.P., Saab C.Y., Craner M.J., Black J.A., Waxman S.G. Upregulation of sodium channel Nav1.3 and functional involvement in neuronal hyperexcitability associated with central neuropathic pain after spinal cord injury. *J. Neurosci*. 2003; 23:8881–92.
93. Hald, A., Nedergaard, S., Hansen, R. R., Ding, M., and Heegaard, A. (2009). Differential activation of spinal cord glial cells in murine models of neuropathic and cancer pain. *European Journal of Pain* 13 (2009) 138–145.

94. Hall, M. D., Okabe, M., Shen, D.-W., Liang, X.-J., and Gottesman, M. M. (2008). The Role of Cellular Accumulation in Determining Sensitivity to Platinum-Based Chemotherapy. *Annual Review of Pharmacology and Toxicology*, 48(1), 495–535.
95. Han, L., Ma, C., Liu, Q., Weng, H.-J., Cui, Y., Tang, Z., Kim, Y., Nie, H., Qu, L., Patel, K.N., *et al.* (2013). A subpopulation of nociceptors specifically linked to itch. *Nat. Neurosci.* 16, 174–182.
96. Han, Y., and Smith, M. T. (2013). Pathobiology of cancer chemotherapy-induced peripheral neuropathy (CIPN). *Frontiers in Pharmacology*, 4 DEC (December), 1–16.
97. Hanna, R. K., Zhou, C., Malloy, K. M., Sun, L., Zhong, Y., Gehrig, P. A., and Bae-Jump, V. L. (2012). Metformin potentiates the effects of paclitaxel in endometrial cancer cells through inhibition of cell proliferation and modulation of the mTOR pathway. *Gynecologic Oncology*, 125(2), 458–69.
98. Harper, B. Y. A. A., and Lawson, S. N. (1985). Conduction velocity is related to morphological cell type in rat dorsal root ganglion neurones. *J Physiol.* 1985 feb; 359: 31–46.
99. He Z. and Jin Y. (2016) Intrinsic Control of Axon Regeneration. *Neuron.* 2016 May 4;90(3):437-51.
100. Herdegen, T., Blume, A., Buschmann, T., Georgakopoulos, E., Winter, C., Schmid, W., Hsieh, T. F., Zimmermann, M., and Gass, P. (1997a). Expression of activating transcription factor-2, serum response factor and cAMP/Ca response element binding protein in the adult rat brain following

- generalized seizures, nerve fibre lesion and ultraviolet irradiation. *Neuroscience* 81, 199–212.
101. Hernández-Díaz S, Adami HO. (2010). Diabetes therapy and cancer risk: causal effects and other plausible explanations. *Diabetologia*. 2010; 53:802–808.
 102. Hershman, D. L., Lacchetti, C., Dworkin, R. H., Lavoie Smith, E. M., Bleeker, J., Cavaletti, G., Loprinzi, C. L. (2014). Prevention and Management of Chemotherapy-Induced Peripheral Neuropathy in Survivors of Adult Cancers: American Society of Clinical Oncology Clinical Practice Guideline. *Journal of Clinical Oncology*, 32(18), 1–30.
 103. Hol, E. M., Schwaiger, F. W., Werner, A., Schmitt, A., Raivich, G., and Kreutzberg, G. W. (1999). Regulation of the LIM-type homeobox gene *islet-1* during neuronal regeneration. *Neuroscience* 88, 917–925.
 104. Holmes, J., Stanko, J., Varchenko, M., Ding, H., Madden, V.J., Bagnell, C.R., Wyrick, S.D., Chaney S.G. (1998). Comparative neurotoxicity of oxaliplatin, cisplatin, and ormaplatin in a Wistar rat model. *Toxicol Sci*. 1998 Dec;46(2):342-51.
 105. Honjo, S., Ajani, J. A., Scott, A. W., Chen, Q., Skinner, H. D., Stroehlein, J., Song, S. (2014). Metformin sensitizes chemotherapy by targeting cancer stem cells and the mTOR pathway in esophageal cancer. *Int J Oncol*. 2014 Aug;45(2):567-74.
 106. Hostalek, U., Gwilt, M., and Hildemann, S. (2015). Therapeutic Use of Metformin in Prediabetes and Diabetes Prevention. *Drugs* (2015) 75:1071–

- 1094.
107. Howe J.F., Loeser J.D., Calvin W.H. (1977). Mechanosensitivity of dorsal root ganglia and chronically injured axons: a physiological basis for the radicular pain of nerve root compression. *Pain*. 1977; 3:25–41.
108. Hoyt S.B., London C., Ok H., Gonzalez E., Duffy J.L. Benzazepinone Nav1.7 blockers: potential treatments for neuropathic pain. *Bioorg. Med. Chem. Lett*. 2007; 17:6172–77.
109. Huang W, Calvo M, Karu K, Olausen HR, Bathgate G, Okuse K, Bennett DL, Rice AS. (2013). A clinically relevant rodent model of the HIV antiretroviral drug stavudine induced painful peripheral neuropathy. *Pain*. 2013 Apr; 154(4):560-75.
110. Huang, Z.Z., Li, D., Ou-Yang, H.D., Liu, C.C., Liu, X.G., Ma, C., Wei, J.Y., Liu, Y., Xin, W.J. (2016). Cerebrospinal fluid oxaliplatin contributes to the acute pain induced by systemic administration of oxaliplatin. *Anesthesiology*. 2016; 124(5): 1109-21.
111. Huebner E.A. and Strittmatter Strittmatter, S.M (2009). Axon Regeneration in the Peripheral and Central Nervous Systems. *Results Probl Cell Differ*. 2009; 48: 339–351.
112. Hussien, A., and Rasha, A. (2013). The safety and efficacy of fluorouracil, Leucovorin, oxaliplatin, and docetaxel (FLOT) combination in the front-line treatment for patients with advanced gastric or gastroesophageal adenocarcinoma: phase II trial, 1–6. *Med Oncol*. 2013 Mar; 30(1):451.

113. Ibrahim A., Hirschfeld S, Cohen MH, Griebel DJ, Williams GA, Pazdur R. (2004). FDA drug approval summaries: oxaliplatin. *Oncologist*. 2004; 9:8–12.
114. Imamachi, N., Park, G.H., Lee, H., Anderson, D.J., Simon, M.I., Basbaum, A.I., and Han, S.-K. (2009). TRPV1-expressing primary afferents generate behavioral responses to pruritogens via multiple mechanisms. *Proc. Natl. Acad. Sci. USA* 106, 11330–11335.
115. Indo Y. (2001). Molecular basis of congenital insensitivity to pain with anhidrosis (CIPA): mutations and polymorphisms in TRKA (NTRK1) gene encoding the receptor tyrosine kinase for nerve growth factor. *Hum Mutat*. 2001 Dec;18(6):462-71.
116. Inquimbert P., Moll M., Latremoliere A., Tong C.K., Whang J., Sheehan G.F., Smith B.M., Korb E., Athié M.C.P., Babaniyi O., Ghasemlou N., Yanagawa Y., Allis C.D., Hof P.R., Scholz J. (2018). NMDA Receptor Activation Underlies the Loss of Spinal Dorsal Horn Neurons and the Transition to Persistent Pain after Peripheral Nerve Injury. *Cell Rep*. 2018 May 29;23(9):2678-2689.
117. Ivannikov M.V. and Sugimori M., Llinás R.R. (2010). Calcium clearance and its energy requirements in cerebellar neurons. *Cell Calcium*. 2010 Jun;47(6):507-13.
118. J. Boyette-Davis, W. Xin, H. Zhang and P.M. Dougherty. (2011). Intraepidermal nerve fiber loss corresponds to the development of Taxol-induced hyperalgesia and can be prevented by treatment with minocycline.

- Pain. 2011 Feb; 152(2): 308–313.
119. Jacobs J.M. (1978). Vascular permeability and neurotoxicity. *Environ Health Perspect.* 1978 Oct; 26:107-16.
120. Jacobs, S.S., Fox, E., Dennie, C., Morgan, L.B., McCully, C.L., Balis, F.M. (2005). Plasma and cerebrospinal fluid pharmacokinetics of intravenous oxaliplatin, cisplatin, and carboplatin in nonhuman primates. *Clin Cancer Res.* 2005; 11: 1669-1674.
121. Jamieson, S. M. F., and Mckeage, M. J. (2005). Oxaliplatin causes selective atrophy of a subpopulation of dorsal root ganglion neurons without inducing cell loss. *Cancer Chemother Pharmacol.* 2005 oct;56(4):391-9.
122. Jankowski, M. P., McIlwrath, S. L., Jing, X. T., Cornuet, P. K., Salerno, K. M., Koerber, H. R., and Albers, K. M. (2009). Sox11 transcription factor modulates peripheral nerve regeneration in adult mice. *Brain Res.* 1256, 43–54.
123. Jarvis M.F., Honore P., Shieh C.C., Chapman M., Joshi S. A-803467, a potent and selective Nav1.8 sodium channel blocker, attenuates neuropathic and inflammatory pain in the rat. *Proc. Natl. Acad. Sci. USA.* 2007; 104:8520–25.
124. Jensen T. S. And Finnerup N.B (2014). Allodynia and hyperalgesia in neuropathic pain: clinical manifestations and mechanisms. *Lancet Neurol.* 2014 Sep; 13(9):924-35.
125. Ji R.R., Berta T., Nedergaard M. (2013). Glia and pain: is chronic pain a

- gliopathy? *Pain*. 2013 Dec;154 Suppl 1: S10-28.
126. Jiménez-Andrade, J. M., Herrera, M. B., Ghilardi, J. R., Vardanyan, M., Melemedjian, O. K., and Mantyh, P. W. (2008). Vascularization of the dorsal root ganglia and peripheral nerve of the mouse: Implications for chemical-induced peripheral sensory neuropathies. *Mol Pain*. 2008 Mar 19; 4:10.
127. Jimenez-Diaz L., Geranton S.M., Passmore G.M., Leith J.L., Fisher A.S. Local translation in primary afferent fibers regulates nociception. *PLoS ONE*. 2008;3: e1961.
128. Jin X., Gereau R.Wt. Acute p38-mediated modulation of tetrodotoxin-resistant sodium channels in mouse sensory neurons by tumor necrosis factor-alpha. *J. Neurosci*. 2006; 26:246–55.
129. João M. Bráz and Allan I. Basbaum. (2010). Differential ATF3 expression in dorsal root ganglion neurons reveals the profile of primary afferents engaged by diverse noxious chemical stimuli. *Pain*. 2010 Aug; 150(2): 290–301.
130. Jong, N. N., Nakanishi, T., Liu, J. J., Tamai, I., and Mckeage, M. J. (2011). Oxaliplatin Transport Mediated by Organic Cation / Carnitine Transporters OCTN1 and OCTN2 in Overexpressing Human Embryonic Kidney 293 Cells and Rat Dorsal Root Ganglion Neurons, 338(2), 537–547.
131. Joshi S.K., Mikusa J.P., Hernandez G., Baker S., Shieh C.C. Involvement of the TTX-resistant sodium channel Nav 1.8 in inflammatory and neuropathic, but not post-operative, pain states. *Pain*. 2006; 123:75–82.

132. Kajbaf F, Bennis Y, Hurtel-Lemaire AS, And réjak M, Lalau JD. (2015). Unexpectedly long half-life of metformin elimination in cases of metformin accumulation. *Diabet Med*. 2015 Sep 4.
133. Kannarkat, G., Lasher, EE, Schiff, D. (2007). Neurologic complications of chemotherapy agents. *Curr Op Neurol*. 2007; 20: 719–725.
134. Kasia J. Lipska, Clifford J. Bailay, Silvio E. Inzucchi (2011). Use of Metformin in the Setting of Mild-to-Moderate Renal Insufficiency. *Diabetes Care*, Volume 34, June (2011) 1431-1437.
135. Kawashiri, T., Egashira, N., Watanabe, H., Ikegami, Y., Hirakawa, S., Mihara, Y., Oishi, R. (2011). Prevention of oxaliplatin-induced mechanical allodynia and neurodegeneration by neurotrophin in the rat model. *European Journal of Pain (London, England)*, 15(4), 344–50.
136. Keller A.F., Beggs S., Salter M.W., De Koninck Y. (2007). Transformation of the output of spinal lamina I neurons after nerve injury and microglia stimulation underlying neuropathic pain. *Mol Pain*. 2007 Sep 27; 3:27.
137. Kibirige, D., and Mwebaze, R. (2013). Vitamin B12 deficiency among patients with diabetes mellitus: is routine screening and supplementation justified? *J Diabetes Metab Disord*. 2013; 12: 17.
138. Kidd, B. L., and Urban, L. A. (2001). Mechanisms of inflammatory pain. *British Journal of Anaesthesia*, 87(1), 3–11.
139. Kiernan J.A. (1996). Vascular permeability in the peripheral autonomic and somatic nervous systems: controversial aspects and comparisons with

- the blood-brain barrier. *Microsc Res Tech.* 1996 Oct 1;35(2):122-36.
140. Kilkenney C, Browne WJ, Cuthill IC, Emerson M., Altman D.G. (2010). Improving bioscience research reporting: The ARRIVE guidelines for reporting animal research. *J Pharmacol Pharmacother* 2010; 1(2):94-9.
141. Kim L.S., Axelrod L.J., Howard P., Buratovich N., Waters R.F. (2005). Efficacy of methylsulfonylmethane (MSM) in osteoarthritis pain of the knee: a pilot clinical trial. *Osteoarthritis Cartilage.* 2006 Mar;14(3):286-94. Epub 2005 Nov 23.
142. Ko M.H., Hu ME, Hsieh YL, Lan CT, Tseng TJ. (2014). Peptidergic intraepidermal nerve fibers in the skin contribute to the neuropathic pain in paclitaxel-induced peripheral neuropathy. *Neuropeptides.* 2014 Jun; 48(3):109-17.
143. Kodji, X., Aubdool, A. A., and Brain, S. D. (2016). Evidence for physiological and pathological roles for sensory nerves in the microvasculature and skin. *Current Research in Translational Medicine,* 64(4), 195–201.
144. Koltzenburg M., Torebjork H.E., Wahren L.K. (1994). Nociceptor modulated central sensitization causes mechanical hyperalgesia in acute chemogenic and chronic neuropathic pain. *Brain.* 1994;117(Pt 3):579–91.
145. Koritzinsky M. (2015). Metformin: A Novel Biological Modifier of Tumour Response to Radiation Therapy. *Int J Radiat Oncol Biol Phys.* 2015 Oct 1; 93(2):454-64.
146. Kuner, R. (2010). Central mechanisms of pathological pain. *Nature*

- Medicine, 16 (11), 1258–1266.
147. Kusuhara, H., and Sugiyama, Y. (2005). Active efflux across the blood-brain barrier: Role of the solute carrier family. *NeuroRx*, 2(1), 73–85.
 148. Łabuzek K., Suchy D., Gabryel B., Bielecka A., Liber S., Okopień B. Quantification of metformin by the HPLC method in brain regions, cerebrospinal fluid and plasma of rats treated with lipopolysaccharide. *Pharmacol Rep.* 2010 Sep-Oct;62(5):956-65.
 149. Lallemand, F., and Ernfors, P. (2012). Molecular interactions underlying the specification of sensory neurons. *Trends in Neurosciences*, 35(6), 373–81.
 150. Lau, Y.-K. I., Du, X., Rayannavar, V., Hopkins, B., Shaw, J., Bessler, E., Maurer, M. a. (2014). Metformin and erlotinib synergize to inhibit basal breast cancer. *Oncotarget*, 5(21), 10503–17.
 151. Leandri, M., Ghignotti, M., Emionite, L., Leandri, S., and Cilli, M. (2012). Electrophysiological features of the mouse tail nerves and their changes in chemotherapy induced peripheral neuropathy (CIPN). *Journal of Neuroscience Methods*, 209(2), 403–409.
 152. Lersch C., Schmelz R., Eckel F., Erdmann J., Mayr M., Schulte-Frohlinde E., Quasthoff S., Grosskreutz J., Adelsberger H. (2002). Prevention of oxaliplatin-induced peripheral sensory neuropathy by carbamazepine in patients with advanced colorectal cancer. *Clin Colorectal Cancer*, 2002. 2(1): p. 54-8.
 153. Li Gongga, Srijib Goswamic, Kathleen M. Giacomini, Russ B. Altmana,

- and Teri E. Kleina (2012). Metformin pathways: pharmacokinetics and pharmacodynamics. *Pharmacogenet Genomics*. 2012 November; 22(11): 820–827.
154. Lin C.J., Tai Y., Huang M.T., Tsai Y.F., Hsu H.J., Tzen K.Y., Liou, H.H. (2010). Cellular localization of the organic cation transporters, OCT1 and OCT2, in brain microvessel endothelial cells and its implication for MPTP transport across the blood-brain barrier and MPTP induced dopaminergic toxicity in rodents. *J Neurochem* 2010; 114:717–727.
155. Lin, P.-C., Lee, M.-Y., Wang, W.-S., Yen, C.-C., Chao, T.-C., Hsiao, L.-T., Chiou, T.-J. (2006). N-acetylcysteine has neuroprotective effects against oxaliplatin-based adjuvant chemotherapy in colon cancer patients: preliminary data. *Supportive Care in Cancer*, 14(5), 484–487.
156. Lin, Y.-C., Wu, M.-H., Wei, T.-T., Lin, Y.-C., Huang, W.-C., Huang, L.-Y., Chen, C.-C. (2014). Metformin sensitizes anticancer effect of dasatinib in head and neck squamous cell carcinoma cells through AMPK-dependent ER stress. *Oncotarget*, 5(1), 298–308.
157. Ling, B., Coudoré-Civiale, M.-A., Balayssac, D., Eschalier, A., Coudoré, F., and Authier, N. (2007). Behavioral and immunohistological assessment of painful neuropathy induced by a single oxaliplatin injection in the rat. *Toxicology*, 234(3), 176–184.
158. Liu B, Fan Z, Edgerton SM, Deng XS, Alimova IN, Lind SE *et al.* (2009). Metformin induces unique biological and molecular responses in triple negative breast cancer cells. *Cell Cycle* 8: 2031–2040.

159. Liu, Q., Tang, Z., Surdenikova, L., Kim, S., Patel, K.N., Kim, A., Ru, F., Guan, Y., Weng, H.J., Geng, Y., *et al.* (2009). Sensory neuron-specific GPCR Mrgprs are itch receptors mediating chloroquine-induced pruritus. *Cell* 139, 1353–1365.
160. Llorente-Folch I., Rueda C.B., Pardo B., Szabadkai G., Duchen M.R., Satrustegui J. (2015). The regulation of neuronal mitochondrial metabolism by calcium. *J Physiol.* 2015 Aug 15;593(16):3447-62.
161. Loprinzi, C.L., *et al.* (2014). Phase III randomized, placebo-controlled, double-blind study of intravenous calcium and magnesium to prevent oxaliplatin-induced sensory neurotoxicity (N08CB/Alliance). *J Clin Oncol*, 2014. 32(10): p. 997-1005.
162. Lu, M., Su, C., Qiao, C., and Bian, Y. (2016). Metformin Prevents Dopaminergic Neuron Death in MPTP / P-Induced Mouse Model of Parkinson's Disease via Autophagy and Mitochondrial ROS Clearance. *Int J Neuropsychopharmacol.* 2016 Sep 21;19(9).
163. Luippold, G., Bedenik, J., Voigt, A., and Grempler, R. (2016). Short- and Longterm Glycemic Control of Streptozotocin-Induced Diabetic Rats Using Different Insulin Preparations. *PLoS One.* 2016 Jun 2; 11(6): e0156346.
164. Luo F.R., Wyrick S.D., Chaney S.G. (1999). Comparative neurotoxicity of oxaliplatin, ormaplatin, and their biotransformation products utilizing a rat dorsal root ganglia *in vitro* explant culture model. *Cancer Chemother Pharmacol.* 1999;44(1):29-38.

165. Luo L., Chang L., Brown S.M., Ao H., Lee D.H. Role of peripheral hyperpolarization-activated cyclic nucleotide-modulated channel pacemaker channels in acute and chronic pain models in the rat. *Neuroscience*. 2007; 144:1477–85.
166. M Wasif Saif and John Reardon (2005). Management of oxaliplatin-induced peripheral neuropathy. *Ther Clin Risk Manag*. 2005 Dec; 1(4): 249–258.
167. Ma J., Yu H., Liu J., Chen Y., Wang Q., Xiang L (2015). Metformin attenuates hyperalgesia and allodynia in rats with painful diabetic neuropathy induced by streptozotocin. *Eur J Pharmacol*. 2015 Oct 5; 764:599-606.
168. Magoulas, B., and Lopez-de Heredia, L. (2010). Functional analysis of the transcription factor C/EBPdelta in neuronal repair. *FENS Abstr*. 5, 040.12.
169. Mahmood, K., Naeem, M., and Rahimnajjad, N. A. (2013). Metformin: the hidden chronicles of a magic drug. *European Journal of Internal Medicine*, 24(1), 20–6.
170. Maj M.A., Ma J., Krukowski K.N., Kavelaars A., Heijnen C.J. Inhibition of Mitochondrial p53 Accumulation by PFT- μ Prevents Cisplatin-Induced Peripheral Neuropathy. *Front Mol Neurosci*. 2017 Apr 18; 10:108.
171. Mao-Ying, Q. L., Kavelaars, A., Krukowski, K., Huo, X. J., Zhou, W., Price, T. J., Heijnen, C. J. (2014). The anti-diabetic drug metformin protects

- against chemotherapy-induced peripheral neuropathy in a mouse model. *PLoS ONE*, 9(6), 3–10.
172. Maroun, J. A., Anthony, L. B., Blais, N., Burkes, R., Dowden, S. D., Mpharm, G. D., Thirlwell, M. P. (2007). Prevention and management of chemotherapy-induced diarrhea in patients with colorectal cancer: a consensus statement by the Canadian Working Group on Chemotherapy-Induced Diarrhea. *Curr Oncol*. 2007 Feb; 14(1): 13–20.
173. Mason, M. R., Lieberman, A. R., and Anderson, P. N. (2003). Corticospinal neurons up-regulate a range of growth-associated genes following intracortical, but not spinal, axotomy. *Eur. J. Neurosci*. 18, 789–802.
174. Matthew B. Potts and Daniel A. Lim. (2012). an Old Drug for New Ideas: Metformin Promotes Adult Neurogenesis and Spatial Memory Formation. *Cell Stem Cell*. 2012 July 6; 11(1): 5–6.
175. McMahon S.B., Bennett D.L., Bevan S. (2005). Inflammatory mediators and modulators of pain. In: Koltzenburg M, McMahon S, editors. *Wall and Melzack's Textbook of Pain*. 5th ed. Churchill-Livingstone; 2005. pp. 49–72.
176. McWhinney S.R., Goldberg RM, McLeod HL. (2009). Platinum neurotoxicity pharmacogenetics. *Mol Cancer Ther*. 2009 Jan; 8(1):10-6.
177. Meei-Shyuan Lee, Chih-Cheng Hsu, Mark L Wahlqvist, Hsin-Ni Tsai, Yu-Hung Chang and Yi-Chen Huang (2011). Type 2 diabetes increases, and metformin reduces total, colorectal, liver and pancreatic cancer

- incidences in Taiwanese: a representative population prospective cohort study of 800,000 individuals. *BMC Cancer*. 2011 Jan 18; 11:20.
178. Melli G. and Höke A. Dorsal Root Ganglia Sensory Neuronal Cultures: a tool for drug discovery for peripheral neuropathies. *Expert Opin Drug Discov*. 2009 Oct 1;4(10):1035-1045.
179. Michaelevski, I., Segal-Ruder, Y., Rozenbaum, M., Medzihradzky, K. F., Shalem, O., Coppola, G., Horn-Saban, S., Ben-Yaakov, K., Dagan, S. Y., Rishal, I., Geschwind, D. H., Pilpel, Y., Burlingame, A. L., and Fainzilber, M. (2010). Signalling to transcription networks in the neuronal retrograde injury response. *Sci. Signal*. 3, 1–11.
180. Michaelis M., Blenk K.H., Vogel C., Janig W. (1999). Distribution of sensory properties among axotomized cutaneous C-fibers in adult rats. *Neuroscience*. 1999; 94:7–10.
181. Miller J.R., Jung H., Bhangoo S.K., and White F.A. (2009). Cytokine and Chemokine Regulation of Sensory Neuron Function. *Handb Exp Pharmacol*. 2009; (194): 417–449.
182. Miltenburg, N. C., and Boogerd, W. (2014). Chemotherapy-induced neuropathy: A comprehensive survey. *Cancer Treatment Reviews*, 40(7), 872–882.
183. Mogil J.S., Wilson S.G., Bon K., Lee S.E., Chung K. Heritability of nociception II. (1999). ‘Types’ of nociception revealed by genetic correlation analysis. *Pain*. 1999; 80:83–93.
184. Mohty, B., El-cheikh, J., Yakoub-aga, I., Moreau, P., Harousseau, J.,

- and Mohty, M. (2010). Decision Making And Problem Solving Peripheral neuropathy and new treatments for multiple myeloma: background and practical recommendations. *Haematologica*. 2010 feb; 95(2): 311–319.
185. Moisse, K., Volkening, K., Leystra-Lantz, C., Welch, I., Hill, T., and Strong, M. J. (2009). Divergent patterns of cytosolic TDP-43 and neuronal progranulin expression following axotomy: implications for TDP-43 in the physiological response to neuronal injury. *Brain Res*. 1249, 202–211.
186. Moore K.A., Kohno T., Karchewski L.A., Scholz J., Baba H., Woolf C.J. (2002). Partial peripheral nerve injury promotes a selective loss of GABAergic inhibition in the superficial dorsal horn of the spinal cord. *J Neurosci*. 2002 Aug 1;22(15):6724-31.
187. Moore, D. L., and Goldberg, J. L. (2011). Multiple transcription factor families regulate axon growth and regeneration. *Dev. Neurobiol*. 71, 1186–1211.
188. Nadeau, S., Hein, P., Fernandes, K. J., Peterson, A. C., and Miller, F. D. (2005). A transcriptional role for C/EBP beta in the neuronal response to axonal injury. *Mol. Cell. Neurosci*. 29, 525–535.
189. Nair A.B. and Jacob S. A (2016). simple practice guide for dose conversion between animals and human. *J Basic Clin Pharm*. 2016 Mar;7(2):27-31.
190. Nath N, Khan M, Paintlia MK, Singh I, Hoda MN, Giri S. (2009). Metformin attenuated the autoimmune disease of the central nervous system in animal models of multiple sclerosis. *J Immunol*. 2009 jun 15;

- 182(12):8005-14.
191. Niekerk E.A., Tuszynski M.H., Lu P., Dulin J.N. (2016). Molecular and Cellular Mechanisms of Axonal Regeneration After Spinal Cord Injury. *Mol Cell Proteomics*. 2016 Feb; 15(2): 394–408.
192. Ocean, A. J., and Vahdat, L. T. (2004). Chemotherapy-induced peripheral neuropathy: pathogenesis and emerging therapies. *Support Care Cancer*. 2004 Sep.; 12(9):619-25.
193. O'Donnell K.C., Vargas M.E., Sagasti A. (2013). WldS and PGC-1 α regulate mitochondrial transport and oxidation state after axonal injury. *J Neurosci*. 2013 Sep 11;33(37):14778-90.
194. Oyebode, O. R. O., Hartley, R., Singhota, J., Thomson, D., and Ribchester, R. R. (2012). Differential protection of neuromuscular sensory and motor axons and their endings in Wld(S) mutant mice. *Neuroscience*, 200, 142–58.
195. Pace, A. (2003). Neuroprotective Effect of Vitamin E Supplementation in Patients Treated with cisplatin Chemotherapy. *Journal of Clinical Oncology*, 21(5), 927–931.
196. Pachman, D. R., Watson, J. C., Lustberg, M. B., Wagner-Johnston, N. D., Chan, A., Broadfield, L., Loprinzi, C. L. (2014). Management options for established chemotherapy-induced peripheral neuropathy. *Supportive Care in Cancer*, 22(8), 2281–2295.
197. Pak, D. J., Yong, R. J., Kaye, A. D., and Urman, R. D. (2018). Chronification of Pain: Mechanisms, Current Understanding, and Clinical

- Implications. *Current Pain and Headache Reports* (2018) 22:9.
198. Park K.K., Liu K., Hu Y., Kanter J.L., He Z (2010). PTEN/mTOR and axon regeneration. *Exp Neurol*. 2010 May;223(1):45-50.
199. Park, J. O., Chen, L., Orlando, M., and Kim, J. S. (2015). Gemcitabine Plus cisplatin for Advanced Biliary Tract Cancer: A Systematic Review. *Cancer Res Treat*. 2015 Jul; 47(3): 343–361.
200. Park, J., Chae, J., Roh, K., Kil, E., and Lee, M. (2015). Oxaliplatin-Induced Peripheral Neuropathy via TRPA1 Stimulation in Mice Dorsal Root Ganglion Is Correlated with Aluminum Accumulation. *PLoS One*. 2015 Apr 30; 10(4): e0124875.
201. Park, S. C., and Chun, H. J. (2013). Chemotherapy for Advanced Gastric Cancer: Review and Update of Current Practices. *Gut Liver*. 2013 Jul; 7(4): 385–393.
202. Park, S.A., Choi, K.S., Bang, J.H., Huh, K., Kim, S.U. (2000). Cisplatin-induced apoptotic cell death in mouse hybrid neurons is blocked by antioxidants through suppression of cisplatin mediated accumulation of p53 but not of Fas/Fas ligand. *J Neurochem*. 2000; 75: 946-953.
203. Peng J., Gu N., Zhou L., B Eyo U., Murugan M., Gan W.B., Wu L.J (2016). Microglia and monocytes synergistically promote the transition from acute to chronic pain after nerve injury. *Nat Commun*. 2016 Jun 28; 7:12029.
204. Penz M., Kornek G.V., Raderer M., Ulrich-Pur H., Fiebiger W., Scheithauer W. (2001) Subcutaneous administration of amifostine: a

- promising therapeutic option in patients with oxaliplatin-related peripheral sensitive neuropathy. *Ann Oncol*, 2001. 12(3): p. 421-2.
205. Pertin M., Ji R.R, Berta T., Powell A.J., Karchewski L., Upregulation of the voltage-gated sodium channel beta2 subunit in neuropathic pain models: characterization of expression in injured and non-injured primary sensory neurons. *J. Neurosci*. 2005; 25:10970–80.
206. Peters E.M., Ericson M.E., Hosoi J., Seiffert K., Hordinsky M.K., Ansel J.C., Paus R., Scholzen T.E. Neuropeptide control mechanisms in cutaneous biology: physiological and clinical significance. *J Invest Dermatol*. 2006 Sep;126(9):1937-47.
207. Petterino, C., and Argentino-storino, A. (2006). Clinical chemistry and haematology historical data in control Sprague-Dawley rats from pre-clinical toxicity studies. *Exp Toxicol Pathol*. 2006 Jan; 57(3):213-9.
208. Pitts, M. (2002) NIH Care and Use Institutional Animal Care and Use. 2^oEdition.
209. Polgár E. and Todd A.J, (2008). Tactile allodynia can occur in the spared nerve injury model in the rat without selective loss of GABA or GABA_A receptors from synapses in laminae I–II of the ipsilateral spinal dorsal horn. *Neuroscience*. 2008;156(1):193-202.
210. Polgár E., Hughes D.I., Arham A.Z., Todd A.J, (2005). Loss of neurons from laminae I-III of the spinal dorsal horn is not required for development of tactile allodynia in the spared nerve injury model of neuropathic pain. *J Neurosci*. 2005 Jul 13;25(28):6658-66.

211. Press C., and Milbrandt J. (2008). Nmnat delays axonal degeneration caused by mitochondrial and oxidative stress. *J Neurosci*. 2008 May 7;28(19):4861-71.
212. Purves D., Augustine G.J, Fitzpatrick D, (2001). Editors. Sunderland (MA). Neuroscience. 2nd edition. Sinauer Associates; 2001.
213. Qu, C., Zhang, W., Zheng, G., Zhang, Z., Yin, J., and He, Z (2014). Metformin reverses multidrug resistance and epithelial-mesenchymal transition (EMT) via activating AMP-activated protein kinase (AMPK) in human breast cancer cells. *Molecular and Cellular Biochemistry*, 386(1–2), 63–71.
214. Raivich, G. (2011). Transcribing the path to neurological recovery-from early signals through transcription factors to downstream effectors of successful regeneration. *Ann. Anat.* 193, 248–258.
215. Raivich, G., Bohatschek, M., Da Costa, C., Iwata, O., Galiano, M., Hristova, M., Nateri, A. S., Makwana, M., Riera-Sans, L., Wolfer, D. P., Lipp, H. P., Aguzzi, A., Wagner, E. F., and Behrens, A. (2004). The AP-1 transcription factor c-Jun is required for efficient axonal regeneration. *Neuron*43, 57–67.
216. Ratan K. Banik and Rajiv A. Kabadi (2013). A modified Hargreaves method for assessing threshold temperatures for heat nociception. *J Neurosci Methods*. 2013 September 30; 219(1): 41–51.
217. Reagan-Shaw, S., Nihal, M., and Ahmad, N. (2008). Dose translation from animal to human studies revisited. *FASEB J*. 2008 Mar; 22(3):659-61.

218. Renn, C. L., Carozzi, V. a, Rhee, P., Gallop, D., Dorsey, S. G., and Cavaletti, G. (2011). Multimodal assessment of painful peripheral neuropathy induced by chronic oxaliplatin-based chemotherapy in mice. *Molecular Pain*, 7(1), 29.
219. Rice F.L. and Albrecht P.J. (2008). Cutaneous mechanisms of tactile perception: morphological and chemical organization of the innervation to the skin. In: Basbaum AI, Kaneko A, Shepherd GM, Westheimer G, editors. *The Senses: A Comprehensive Reference*. Academic Press; San Diego: 2008. pp. 1–32.
220. Richard S.M. and Martinez Marignac V.L (2016). Sensitization to oxaliplatin in HCT116 and HT29 cell lines by metformin and ribavirin and differences in response to mitochondrial glutaminase inhibition, 11(2), 9–13.
221. Roberts, J. a, Jenison, E. L., Kim, K., Clarke-Pearson, D., and Langleben, a. (1998). A randomized, multicenter, double-blind, placebo-controlled, dose-finding study of org 2766 in the prevention or delay of cisplatin-induced neuropathies in women with ovarian cancer. *International Journal of Gynecology and Obstetrics*, 61(1), 95.
222. Robinson, C. R., Zhang, H., and Dougherty, P. M. (2014). Astrocytes, but not microglia, are activated in oxaliplatin and bortezomib-induced peripheral neuropathy in the rat. *Neuroscience*, 274, 308–317.
223. Rowbotham M.C. and Fields H.L. (1996). The relationship of pain, allodynia and thermal sensation in post-herpetic neuralgia. *Brain*.

- 1996;119(Pt 2):347–54.
224. Roza C., Laird J.M., Souslova V., Wood J.N., Cervero F. The tetrodotoxin-resistant Na⁺ channel Nav1.8 is essential for the expression of spontaneous activity in damaged sensory axons of mice. *J. Physiol.* 2003; 550:921–26.
225. Ruff, C., Da Costa, C., Staak, N., Rumajogee, P., Makwana, M., Acosta-Saltos, A., Kaswich, M., Brecht, S., Hristova, M., Riera-Sans, L., Mirsky, R., Herdegen, T., Jessen, K., Behrens, A., and Raivich, G. (2009). The role of c-Jun and its N-terminal phosphorylation in facial nerve regeneration. *Abstr. Soc. Neurosci.* 510.9/B42.
226. Saijilafu and Zhou F.Q (2012). Genetic study of axon regeneration with cultured adult dorsal root ganglion neurons. *J Vis Exp.* 2012 Aug 17;(66). pii: 4141.
227. Samera Azeem Qureshi, Bernadette N. Kumar and Giske Ursin (2014). Incidence and associated risk factors for cancer among immigrants. Major Challenges for Norway a Review Report. NAKMI, Nasjonal Kompetanseenhet for Minoritetshelse 2014. Trykk: 07 Gruppen AS
228. Sato, T., Takeuchi, S., Saito, A., Ding, W., Bamba, H., Matsuura, H., Hisa, Y., Tooyama, I., and Urushitani, M. (2009). Axonal ligation induces transient redistribution of TDP-43 in brainstem motor neurons. *Neuroscience* 164, 1565–1578.
229. Sawchuk R.J., and Elmquist, W.F. Microdialysis in the study of drug transporters in the CNS. (2000). *Adv Drug Deliv Rev.* 2000 Dec 15;45(2-

- 3):295-307.
230. Scheen AJ. Clinical pharmacokinetics of metformin. (1996). *Clin Pharmacokinet.* 1996 May; 30(5):359-71.
231. Schmalbruch H. Fiber composition of the rat sciatic nerve. *Anat Rec.* 1986 May;215(1):71-81.
232. Schmalhofer W., Calhoun J., Burrows R., Bailey T., Kohler M.G. ProTx-II, a selective inhibitor of NaV1.7 sodium channels, blocks action potential propagation in nociceptors. *Mol. Pharmacol.* 2008;74(5):1476–84.
233. Schwaiger, F. W., Hager, G., Schmitt, A. B., Horvat, A., Hager, G., Streif, R., Spitzer, C., Gamal, S., Breuer, S., Brook, G. A., Nacimiento, W., and Kreutzberg, G. W. (2000). Peripheral but not central axotomy induces changes in Janus kinases (JAK) and signal transducers and activators of transcription (STAT). *Eur. J. Neurosci.* 12, 1165–1176.
234. Screnci D., Er H.M., Hambley T.H., Galettis P., Brouwer W. and McKeage M.J. (1997) Stereo-selective peripheral sensory neurotoxicity of diaminocyclohexane platinum enantiomers related to ormaplatin and oxaliplatin. *Br J Cancer* 76: 502–510.
235. Screnci, D., McKeage, M. J., Galettis, P., Hambley, T. W., Palmer, B. D., and Baguley, B. C. (2000). Relationships between hydrophobicity, reactivity, accumulation and peripheral nerve toxicity of a series of platinum drugs. *British Journal of Cancer*, 82(4), 966–972.
236. Seiffers R., Mills C.D., Woolf C.J. ATF3 increases the intrinsic growth state of DRG neurons to enhance peripheral nerve regeneration. *J.*

- Neurosci. 2007; 27:7911–20
237. Seretny, M., Currie, G. L., Sena, E. S., Ramnarine, S., Grant, R., MacLeod, M. R., Fallon, M. (2014). Incidence, prevalence, and predictors of chemotherapy-induced peripheral neuropathy: A systematic review and meta-analysis. *Pain*, 155(12), 2461–2470.
238. Sharma, A. K., Sharma, A., Kumari, R., Kishore, K., Sharma, D., Srinivasan, B. P., Munajjam, A. (2012). Sitagliptin, Sitagliptin and metformin, or Sitagliptin and amitriptyline attenuate streptozotocin - nicotinamide induced diabetic neuropathy in rats. *J Biomed Res*. 2012 May;26(3):200-10.
239. Shi, Y., He, Z., Jia, Z., and Xu, C. (2016). Inhibitory effect of metformin combined with gemcitabine on pancreatic cancer cells *in vitro* and *in vivo*. *Mol Med Rep*. 2016 Oct;14(4):2921-8.
240. Siau C., Bennett G. J. (2006). Dysregulation of cellular calcium homeostasis in chemotherapy-evoked painful peripheral neuropathy. *Anesth. Analg*. 102, 1485–1490.
241. Sisignano, M., Baron, R., Scholich, K., and Geisslinger, G. (2014). Mechanism-based treatment for chemotherapy-. *Nat Rev Neurol*. 2014 Dec; 10(12):694-707.
242. Smith, D. S., and Skene, J. H. P. (1997). A transcription-dependent switch controls competence of adult neurons for distinct modes of axon growth. *J. Neurosci*. 17, 646–658.
243. Soo, J. S.-S., Ng, C.-H., Tan, S. H., Malik, R. A., Teh, Y.-C., Tan, B.-S.,

- Leong, C.-O. (2015). Metformin synergizes 5-fluorouracil, epirubicin, and cyclophosphamide (FEC) combination therapy through impairing intracellular ATP production and DNA repair in breast cancer stem cells. *Apoptosis*, 20(10), 1373–1387.
244. Souglakos, J., Mavroudis, D., Kakolyris, S., Kourousis, Ch., Vardakis, N., Androulakis, N., Agelaki, S., Kalbakis, K., Tsetis, D., Athanasiadis, N., Samonis, G., Georgoulas, V. (2002). Triplet combination with irinotecan plus oxaliplatin plus continuous-infusion fluorouracil and leucovorin as first-line treatment in metastatic colorectal cancer: amulticenter phase II trial. *J. Clin. Oncol.* 20, 2651–2657.
245. Swett, E., Torigoe, Y., Elie, V. R., Bourassa, C. M., and Miller, P. G. (1991). Sensory Neurons of the Rat Sciatic Nerve. *Exp Neurol.* 1991 Oct; 114(1):82-103.
246. Ta, L.E., Espeset, L., Podratz, J., Windebank, A.J. (2006). Neurotoxicity of oxaliplatin and cisplatin for dorsal root ganglion neurons correlates with platinum-DNA binding. *Neurotoxicology.* 2006 Dec;27(6):992-1002.
247. Tandrup T. (2004). Unbiased estimates of number and size of rat dorsal root ganglion cells in studies of structure and cell survival. *Journal of Neurocytology* 33, 173–192 (2004).
248. Tanner K. D., Levine J. D., Topp K. S. (1998). Microtubule disorientation and axonal swelling in unmyelinated sensory axons during vincristine-induced painful neuropathy in rat. *J. Comp. Neurol.* 395, 481–492.

249. Thacker M.A., Clark A.K., Marchand F., McMahon S.B. (2007). Pathophysiology of peripheral neuropathic pain: Immune cells and molecules. *Anesth Analg.* 2007;105(3):838–847.
250. Theodore J. Price and Christopher M. Flores (2007). Critical evaluation of the colocalization between calcitonin gene-related peptide, substance P, transient receptor potential vanilloid subfamily type 1 immunoreactivities and isolectin B₄ binding in primary afferent neurons of the rat and mouse. *J Pain.* 2007 Mar; 8(3): 263–272.
251. Tim A. Ahles and Andrew J. Saykin. Candidate mechanisms for chemotherapy-induced cognitive changes. (2007). *Nat Rev Cancer.* 2007 Mar; 7(3): 192–201.
252. Timothy C. Johnstone, Ga Young Park, and Stephen J. Lippard. (2014). Understanding and Improving Platinum Anticancer Drugs—Phenanthriplatin. *Anticancer Res.* 2014 Jan; 34(1): 471–476.
253. Todd, A. J. (2010). Neuronal circuitry for pain processing in the dorsal horn. *Nature Reviews Neuroscience* volume11, pages823–836.
254. Topp K. S., Tanner K. D., Levine J. D. (2000). Damage to the cytoskeleton of large diameter sensory neurons and myelinated axons in vincristine-induced painful peripheral neuropathy in the rat. *J. Comp. Neurol.* 424, 563–576.
255. Torres L., Dunlop D.D., Peterfy C., Guermazi A., Prasad P. (2006). The relationship between specific tissue lesions and pain severity in persons with knee osteoarthritis. *Osteoarthritis Cartilage.* 2006; 14:1033–40.

256. Torsney C. and MacDermott A.B. (2006). Disinhibition opens the gate to pathological pain signaling in superficial neurokinin 1 receptor-expressing neurons in rat spinal cord. *J Neurosci.* 2006 Feb 8;26(6):1833-43.
257. Toyama, S., Shimoyama, N., Ishida, Y., Koyasu, T., Szeto, H. H., and Shimoyama, M. (2013). Characterization of Acute and Chronic Neuropathies Induced by oxaliplatin in Mice and Differential Effects of a Novel Mitochondria-targeted Antioxidant on the Neuropathies. *Anesthesiology*, (Xx), 1–15.
258. Treede R.D., Meyer R.A., Raja S.N., Campbell J.N. (1992). Peripheral and central mechanisms of cutaneous hyperalgesia. *Prog Neurobiol.* 1992;38(4):397–421.
259. Tsujino H., Kondo E., Fukuoka T., Dai Y., Tokunaga A., Miki K., Yonenobu K., Ochi T, Noguchi K. (2000). Activating transcription factor 3 (ATF3) induction by axotomy in sensory and motoneurons: A novel neuronal marker of nerve injury. *Mol Cell Neurosci.*2000;15:170–182.
260. Urban M.O. and Gebhart G.F. (1999). Supraspinal contributions to hyperalgesia. *Proc Natl Acad Sci U S A.* 1999; 96:7687–7692.
261. Van der Hoop R. G. *et al.* (1990), Prevention of cisplatin neurotoxicity with an ACTH (4-9) analogue in patients with ovarian cancer. *N Engl J Med.* 1990 Jan 11; 322(2):89-94.
262. Victoria E. Abraira and David D. Ginty. (2013). The Sensory Neurons of Touch. *Neuron.* 2013 August 21; 79(4).

263. Villegas, R., Martinez, N. W., Lillo, J., Pihan, P., Hernandez, D., Twiss, J. L., and Court, F. a. (2014). Calcium Release from Intra-Axonal Endoplasmic Reticulum Leads to Axon Degeneration through Mitochondrial Dysfunction. *The Journal of Neuroscience: The Official Journal of the Society for Neuroscience*, 34(21), 7179–89.
264. Viollet, B., Guigas, B., Sanz Garcia, N., Leclerc, J., Foretz, M., and Andreelli, F. (2012). Cellular and molecular mechanisms of metformin: an overview. *Clinical Science (London, England: 1979)*, 122(6), 253–70.
265. Vissers, K., and Meert, T. (2005). A Behavioral and Pharmacological Validation of the Acetone Spray Test in Gerbils with a Chronic Constriction Injury. *Anesthesia and Analgesia: August 2005 - Volume 101 - Issue 2 - pp 457-464*.
266. Vizan P, Alcarraz-Vizan G, Diaz-Moralli S, Solovjeva ON, Frederiks WM, Cascante M. (2009). Modulation of Pentose Phosphate Pathway during cell cycle progression in human colon adenocarcinoma cell line HT29. *Int J Cancer* 2009; 124:2789-96.
267. W. H. Xiao, H. Zheng and G. J. Bennett. (2012). Characterization of oxaliplatin-induced chronic painful peripheral neuropathy in the rat and comparison to the neuropathy induced by paclitaxel. *Neuroscience*. 2012 feb 17; 203: 194–206.
268. Wang G.S., Hoyte C. Review of Biguanide (Metformin) Toxicity. *J Intensive Care Med*. 2018 Aug 21:885066618793385.
269. Wang, W.S., *et al.* (2007). Oral glutamine is effective for preventing

- oxaliplatin-induced neuropathy in colorectal cancer patients. *Oncologist*, 2007. 12(3): p. 312-9.
270. Webster, R.G., Brain, K.L., Wilson, R.H., Grem, J.L., Vincent, A. (2005). Oxaliplatin induces hyperexcitability at motor and autonomic neuromuscular junctions through effects on voltage-gated sodium channels. *Br J Pharmacol*. 2005; 146(7): 1027-39.
271. Wen Y.R., Tan P.H., Cheng J.K., Liu Y.C., Ji R.R. (2011). Role of microglia in neuropathic pain, postoperative pain, and morphine tolerance. *J Formos Med Assoc*. 2011 Aug; 110(8): 487–494.
272. West, S. J., Bannister, K., Dickenson, a H., and Bennett, D. L. (2015). Circuitry and plasticity of the dorsal horn - Toward a better understanding of neuropathic pain. *Neuroscience*, 300(May), 254–275.
273. Whalley, K. (2015). Neural circuits: Pain or pleasure? *Nat Rev Neurosci*. 2015 Jun;16(6):316.
274. Wilcock C. and C. J. Bailey (1994). Accumulation of metformin by tissues of the normal and diabetic mouse. *XENOBIOTICA*, 1994, Vol. 24, No. 1, 49-57
275. Williams A.C and Craig K.D. Updating the definition of pain. *Pain*. (2016). Nov;157(11):2420-2423.
276. Wolf, S., Barton, D., Kottschade, L., Grothey, A., and Loprinzi, C. (2008). Chemotherapy-induced peripheral neuropathy: Prevention and treatment strategies. *European Journal of Cancer*, 44(11), 1507–1515.
277. Woolf C.J. and Ma Q. (2007). Nociceptors--noxious stimulus detectors.

- Neuron. 2007 Aug 2;55(3):353-64.
278. Woolf C.J. Evidence for a central component of post-injury pain hypersensitivity. (1983). *Nature*. 1983 Dec 15-21;306(5944):686-8.
279. Wu, K.C., Lu, Y.H., Peng, Y.H., Tsai, T.F., Kao, Y.H., Yang, H.T., Lin, C.J. Decreased expression of organic cation transporters, Oct1 and Oct2, in brain micro vessels and its implication to MPTP-induced dopaminergic toxicity in aged mice. (2015). *J Cereb Blood Flow Metab*. 2015; 35(1): 37-47.
280. Y. M. Cho and T. J. Kieffer (2011). New aspects of an old drug: metformin as a glucagon-like peptide 1 (GLP-1) enhancer and sensitizer. *Diabetologia* (2011) 54:219–222.
281. Yamamoto, S., Ono, H., Kume, K., Ohsawa, M. Oxaliplatin treatment changes the function of sensory nerves in rats. (2016). *J Pharmacol Sci*. 2016 Apr;130(4):189-93.
282. Yao Y., Echeverry S., Shi X.Q., Yang M., Yang Q.Z., Wang G.Y., Chambon J., Wu Y.C., Fu K.Y., De Koninck Y., Zhang J. (2016). Dynamics of spinal microglia repopulation following an acute depletion. *Sci Rep*. 2016 Mar 10; 6:22839.
283. Yong-Jing Gao and Ru-Rong J. (2010). Targeting astrocyte signaling for chronic pain. *Neurotherapeutics*. 2010 oct; 7(4): 482–493.
284. Yothers, G., Connell, M. J. O., Allegra, C. J., Kuebler, J. P., Colangelo, L. H., Petrelli, N. J., and Wolmark, N. (2011). Oxaliplatin As Adjuvant Therapy for Colon Cancer: Updated Results of NSABP C-07 Trial,

- Including Survival and Subset Analyses Patients and Methods. *Journal of Clinical Oncology*. 29(28).
285. Yu, G., Fang, W., Xia, T., Chen, Y., and Gao, Y. (2015). Metformin potentiates rapamycin and cisplatin in gastric cancer in mice. *Oncotarget, Advanced Publications*, 6, 1–15.
286. Yu, Z., Zhao, G., Xie, G., Zhao, L., Chen, Y., and Yu, H. (2015). Metformin and Temozolomide act synergistically to inhibit growth of glioma cells and glioma stem cells *in vitro* and *in vivo*. *Oncotarget*, 6(32), 32930-43.
287. Yudin D., Hanz S., Yoo S., Iavnilovitch E., Willis D. Localized regulation of axonal RanGTPase controls retrograde injury signaling in peripheral nerve. *Neuron*. 2008; 59:241–52.
288. Zaafar, D. K., Zaitone, S. A., and Moustafa, Y. M. (2014). Role of Metformin in Suppressing 1, 2- Dimethylhydrazine-Induced Colon Cancer in Diabetic and Non-Diabetic Mice: Effect on Tumor Angiogenesis and Cell Proliferation. *PLoS One*. 2014 Jun 27; 9(6): e100562.
289. Zamboni, W.C., Gervais, A.C., Egorin, M.J., Schellens, J.H., Hamburger, D.R., Delauter, B.J., Grim, A., Zuhowski, E.G., Joseph, E., Pluim, D., Potter, D.M., Eiseman, J.L. (2002). Inter- and intratumoral disposition of platinum in solid tumors after administration of cisplatin. *Clin Cancer Res*. 2002; 8: 2992–2999.
290. Zhang J.M., MSc, M.D. An J. (2007). Cytokines, Inflammation and Pain. *Int Anesthesiol Clin*. 2007 Spring; 45(2): 27–37.

291. Zhang, S., Lovejoy, K.S., Shima, J.E., Lagpacan, L.L., Shu, Y., Lapuk, A., Chen, Y., Komori, T., Gray, J.W., Chen, X., Lippard, S.J., Giacomini, K.M. (2006). Organic cation transporters are determinants of oxaliplatin cytotoxicity. *Cancer Res.* 2006; 66(17): 8847-57.
292. Zheng, H., Xiao, W. H., and Bennett, G. J. (2011). Functional deficits in peripheral nerve mitochondria in rats with paclitaxel- and oxaliplatin-evoked painful peripheral neuropathy. *Experimental Neurology*, 232(2), 154–161.
293. Zhi-Jiang Zhang, et. al. (2011). Reduced Risk of Colorectal Cancer with Metformin Therapy in Patients with Type 2 Diabetes. *Diabetes Care*, Volume 34, October 2011.
294. Zhou W., Kavelaars A., Heijnen C.J. Metformin Prevents Cisplatin-Induced Cognitive Impairment and Brain Damage in Mice. *PLoS One*. 2016 Mar 28;11(3): e0151890.
295. Zhou, C., Ji, J. U. N., Shi, M. I. N., Yang, L. I. U., Yu, Y., Liu, B., Zhang, J. U. N. (2014). Suberoylanilide hydroxamic acid enhances the antitumor activity of oxaliplatin by reversing the oxaliplatin - induced Src activation in gastric cancer cells. *Mol Med Rep.* 2014 Nov; 10(5):2729-35.
296. Zhu W., Oxford G.S. Phosphoinositide-3-kinase and mitogen activated protein kinase signaling pathways mediate acute NGF sensitization of TRPV1. *Mol. Cell Neurosci.* 2007; 34:689–700.
297. Zhu, M., Zhang, Q., Wang, X., Kang, L., and Yang, Y. (2016). Metformin potentiates anti-tumor effect of resveratrol on pancreatic cancer

- by down-regulation of VEGF-B signaling pathway. *Oncotarget* October 01, 2016:1-11.
298. Zündorf, G., and Reiser, G. (2011). Calcium dysregulation and homeostasis of neural calcium in the molecular mechanisms of neurodegenerative diseases provide multiple targets for neuroprotection. *Antioxid Redox Signal*. 2011 Apr 1;14(7):1275-88.
299. Zylka, M.J., Rice, F.L., and Anderson, D.J. (2005). Topographically distinct epidermal nociceptive circuits revealed by axonal tracers targeted to Mrgprd. *Neuron* 45, 17–25.

17. ADDENDUM PREFACE.

DIFFERENCES IN LOCAL DYNAMICS OF GLUCOSE BETWEEN SOMATIC AND AXONAL REGIONS OF SINGLE NEURONS.

IN ADDITION TO THE MAIN THEORETICAL AND EMPIRICAL BODY OF THIS THESIS, BELOW WE PRESENT AN ADDEMDUM SECTION WITH DISCUSSION OF INTRIGUING PRELIMINARY RESULTS REGARDING POTENTIAL DIFFERENCES IN LOCAL DYNAMICS OF GLUCOSE BETWEEN SOMA AND AXONAL REGIONS OF SINGLE NEURONS, OBTAINED DURING A DOCTORAL INTERNSHIP IN THE SCIENTIFICAL STUDIES CENTER OF VALDIVIA.

18. RESUMEN DEL ADDENDUM

(tr. ADDENDUM ABSTRACT)

La resolutiveidad experimental actual permite la exploración en neuronas de las dinámicas de producción y consumo de metabolitos energéticos específicos a nivel celular en tiempo real. En este contexto, una descripción detallada del metabolismo energético neuronal ha sido extensivamente reportada. Sin embargo, poco se sabe acerca de la homogeneidad del metabolismo energético en distintas áreas de la misma célula. Es por ello por lo que nos propusimos explorar el metabolismo energético en distintas áreas de las neuronas, midiendo el metabolismo energético en somas y axones de neuronas aisladas.

Para esto, usando nanosensores metabólicos genéticamente codificados, exploramos la tasa glicolítica y la tasa de consumo mitocondrial de piruvato en neuronas del ganglio de la raíz dorsal (DRG) *in vitro*, y comparamos los resultados obtenidos en somas y axones de la población de neuronas.

De nuestro conocimiento, nosotros reportamos acá por primera vez tasas glicolíticas y tasa de consumo mitocondrial de piruvato en axones de neuronas aisladas. Aún más, por primera vez, se presentan resultados preliminares que indican diferencias significativas en la tasa glicolítica de soma y axones. Esto sugiere un nuevo nivel de complejidad en la energética neuronal más allá de lo celular, hasta las distintas regiones de las neuronas, y apunta a la existencia de heterogeneidad en la ejecución de la glicólisis entre somas y axones de una misma neurona. Es necesaria evidencia adicional para respaldar estos resultados preliminares y explorar el rol potencial de la heterogeneidad del metabolismo energético en somas y axones en el contexto de la fisiología y fisiopatología neuronal.

19. ADDENDUM ABSTRACT

Current experimental resolutivity allows the exploration of neuronal production and consumption dynamics of specific energetic metabolites at the cellular level in real time. In this context, detailed description of neuronal energetic metabolism has been extensively reported. However, little is known about the homogeneity of energetic metabolism in different areas of the same cell. Thus, to explore the energetic metabolism in different areas of neurons, we proposed to measure energetic metabolism fluxes in soma and axons of isolated neurons.

To this goal, using genetically codified metabolic nanosensors we explored glycolytic rate and mitochondrial pyruvate consumption rate in *in vitro* neurons of dorsal root ganglia and compared outcomes between soma and axons of the neurons population.

To our knowledge, for the first time, here we report glycolytic rate and mitochondrial pyruvate consumption rates in axons of isolated neurons. More importantly, for the first time, we report preliminary results indicating significant differences between soma and axon glycolytic rates in neurons. This suggest a novel level of complexity on neuronal energetics beyond cellular to local regions of neurons and points the existence of heterogeneity in glycolysis execution between soma and axons in the same neuron. Further evidence is needed to support these preliminary results and explore the potential role of metabolic heterogeneity between soma and axons in neuronal physiology and pathology.

20. ADDENDUM INTRODUCTION

Nervous system energetic metabolism has been extensively investigated, and textbook biochemistry indicates that brain energy demands comprehend around 20% of the total energy consumption of the body (Magistretti and Allaman, 2015). In this context, during the last century, imaging techniques such as fMRI (Functional Magnetic Resonance Imaging) and PET (Positron Emission Tomography) scan have allowed the characterization of energy delivery and use during synaptic activity in regions of the nervous system under physiological and pathological conditions (Tomasi *et al.*, 2017; Sonnay *et al.*, 2017). As its widely known, the main conclusions of this characterization show that synaptic activity and neuronal energy metabolism are coupled through glial energy metabolism (neuro-glial metabolic coupling) (Sonnay *et al.*, 2017; Magistretti and Pellerin, 1999; Nehlig and Coles, 2007; Fernandez-Fernandez *et al.*, 2012).

More recently, the development of experimental models to report the expression and activity of metabolic pathways enzymes and to measure specific energetic metabolites fluxes in cells of the nervous system has allowed to dissect the dynamics of glycolysis and oxidative phosphorylation in neurons and glia (Barros *et al.*, 2017; Bittner *et al.*, 2010; Takanaga *et al.*, 2008; Sotelo-Hitschfeld *et al.*, 2012; Barros *et al.*, 2013; San Martín *et al.*, 2014; Rodriguez-Rodriguez *et al.*, 2012; Rodriguez-Rodriguez *et al.*, 2013). In this context, genetically encoded

Förster Resonance Energy Transfer (FRET) nanosensors have been developed for measuring the dynamic changes in concentration of metabolic energetic substrates (e.g.: glucose, pyruvate, lactate, and others) (Barros *et al.*, 2017; Magistretti and Allaman, 2015; Bittner *et al.*, 2010; San Martín *et al.*, 2014; Barros *et al.*, 2013; Mohsin *et al.*, 2015) with improved spatiotemporal resolution. FRET sensors are fusion proteins composed of a ligand binding moiety, the recognition element, and a fluorescent pair with overlapping emission and excitation spectra. Binding of the target metabolic intermediary causes a conformational change that affects the relative distance and/or orientation between the fluorescent proteins, causing an increase or a decrease in FRET efficiency and thus changing fluorescence intensity of proteins. Using this technology, Dr. Felipe Barros group has reported successful measurement of glycolytic rate (Bittner *et al.*, 2010), mitochondrial pyruvate consumption rate (San Martín *et al.*, 2014) and changes in Warburg state of single cells (San Martín *et al.*, 2014) in astrocytes. Dr. Felipe Barros group development and setting of metabolic fluxes measurements in single cells have allowed the exploration of energetic metabolism fluxes in different areas of a single neuron reported in this thesis addendum.

Altogether, there is current consensus that experimental evidence in single cells of the central nervous system indicates astrocytes predominantly use glucose to produce lactate and pyruvate through glycolysis (Magistretti and Allaman, 2015; Fernandez-Fernandez *et al.*, 2012; Bouzier-Sore *et al.*, 2006; Nehlig and Coles, 2007). Complementarily, neurons utilize pyruvate and lactate through tricarboxylic acid cycle (TCA) to produce ATP during phosphorylate oxidation (Magistretti and Allaman, 2015; Fernandez-Fernandez *et al.*, 2012; Bouzier-Sore *et al.*, 2006; Nehlig and Coles, 2007).

However, this *status quo* underlies an unintentional assumption of homogeneity in the dynamics of energy production and consumption between regions of a single neuron.

Interestingly, several authors have described or proposed significant differences in anatomical and physiological characteristics of soma and axons of neurons, either in a physiological context or as isolated cells (Brittis *et al.*, 2002; MacAskill and Kittler, 2010; Baas *et al.*, 1988; Tahirovic and Bradke, 2009; Neukirchen and Bradke, 2011; Arimura and Kaibuchi, 2007; Rasband, 2010; Fohlmeister, 2010; Szu-Yu Ho and Rasband, 2011; Rolls *et al.*, 2007; Kole and Stuart, 2008) . In this context, Dr. Felipe Court, Jaime Álvarez and collaborators have been long describing a local regulation of axonal phenotype based on functionally soma independent synthesis of axonal proteins supported by Schwann cells (Court, F. A., and Álvarez, J., 2005; Lopez-Leal R., *et al.*, 2016; Court F.A., *et al.*, 2016). Dr. Court's findings and proposal of axon as an emerging soma independent functional unit have been a fundamental framework to propose the rationale of this thesis addendum.

Furthermore, seminal mathematical biology work of physicist Nicolas Rashevsky had described a mathematical modeling of the diffusion and metabolic differences between soma and axon of a neuron (Rashevsky, 1972; Rashevsky, 1973; Cull, 2007). In his work, Rashevsky establishes that neuronal diffusion patterns and metabolism is influenced by neuron's geometry (Rashevsky, 1973). Specifically, Rashevsky's models predict that in a single neuron -at a constant diffusion coefficient- consumption and production dynamics of glucose or pyruvate differences would arise and correlate with size differences between soma and axons (Rashevsky, 1973). Consequently, this geometrical related heterogeneity in

energetic dynamics between soma and axons could be present in large neurons such as giant brain neurons and dorsal root ganglia neurons and potentially to play a role in physiology or pathology of the nervous system.

Notably, Kadekaro and Sokoloff (1985) have reported that electrical stimulation of the proximal stump of the transected sciatic nerve produces a frequency-dependent activation of glucose utilization, measured with the autoradiographic deoxy[¹⁴C] glucose method, in the dorsal horn of the spinal cord but produces no change in glucose utilization in the dorsal root ganglion cells (Kadekaro *et al.*, 1985). These results suggest that axon terminals and not the cell bodies are the sites of enhanced metabolic activity during increased functional activity of this nerve pathway. Furthermore, Sokoloff (1993) also described that functional activation of the hypothalamo-hypophysial pathway by salt-loading increases glucose utilization in the pituitary neural lobe, where the terminal axons of the pathway reside, but not in the paraventricular and supraoptic nuclei, the sites of the cell bodies of origin of the pathway (Sokoloff L., 1993). This experimental set of data suggest that regions of the nervous system predominantly composed by neuronal soma have significant differences in glucose utilization in comparison to regions with axons. However, the experimental conditions mentioned before did not allow to elucidate the role of physiological context and differentiate the role of different cell types in this phenomenon.

Particularly interesting would be to elucidate whether significant differences in pyruvate and glucose consumption do exist in isolated neurons. This would suggest that potential heterogeneity in the dynamics of energy production and consumption between regions of a single neuron could be an endogenous characteristic of certain neurons.

To give some light about this, we investigated potential differences between mitochondrial pyruvate consumption rate and glycolytic rate between disaggregated DRG neurons soma and axons *in vitro*. To this goal, we induced the expression of genetically encoded protein metabolic FRET nanosensors pyronic (pyruvate reporter) and FLII12Pglu600 m Δ 6 (glucose reporter) in disaggregated DRG neurons and performed pyruvate and glucose consumption assays.

21.ADDENDUM MATERIALS.

21.1 addendum Culture Media and General Reactives.

- 5-Fluoro-2'-deoxyuridine $\geq 98\%$ (Sigma-Aldrich Cat. No. 856657).
- Acetone for analysis, ACS standard (Merck-Millipore Cat. No. 100014).
- Aphidicolin from *Nigrospora sphaerica* $\geq 98\%$ (HPLC) (Sigma-Aldrich Cat. No. A0781).
- B27 Supplement 50X, serum free, cell culture grade (Thermo-Fisher Cat. No. 17504044).
- Cold Water Fish Skin Gelatin (Sigma-Aldrich, Cat. No. G704).
- Collagen I Rat Protein, Tail (Thermo-Fisher, Cat. No. A1048301).
- D-Glucose, $C_6H_{12}O_6$, cell culture tested (Sigma-Aldrich, Cat. No. G7021).
- EDTA; Ethylenediaminetetraacetic acid anhydrous, crystalline, BioReagent, suitable for cell culture (Sigma-Aldrich, Cat. No. E6758).

- Ethanol, ACS, ISO, and Reag. Ph. Eur standards (Merck-Millipore, Cat. No. 1009832500).
- Fetal Bovine Serum (FBS), ISO13485 standard (Thermo-Fisher, Cat. No. 10437-028).
- Fluoromont G (Electron Microscopy Sciences, Cat. No. 17984-25).
- Glycine, for electrophoresis, $\geq 99\%$ (Sigma-Aldrich, Cat. No. G8898).
- Hydrochloric acid 37%, ACS, ISO, and Reag. Ph. Eur standards (Merck-Millipore, Cat. No. 100317).
- Isopropanolol, ACS, ISO, and Reag. Ph. Eur standards (Merck-Millipore, Cat. No.109634).
- L-glutamine 200 mM, animal origin free, ISO13485 standard (Thermo-Fisher, Cat. No. 25030-081).
- Manganese Chloride Tetrahydrate ($\text{MnCl}_2 \times 4\text{H}_2\text{O}$) 99, 99% trace metal basis (Sigma-Aldrich, Cat. No. 203734).
- Methanol, ACS standard. (Merck-Millipore, Cat. No. 1070182511).
- Neurobasal Medium (NBS) Serum Free (Thermo-Fisher, Cat. No. 21203049).
- OCT (Sakura Finetek, Cat. No. 4583).

- Paraformaldehyde Powder 95% (Sigma-Aldrich, Cat. No. 158127).
- Penicillin-Streptomycin 100X 10,000 U/mL (Thermo-Fisher, Cat. No. 15140-122).
- Poly-L-lysine hydrobromide (PLL) molecular weight 30,000-70,000 (Sigma-Aldrich, Cat. No. P2636).
- K⁺ chloride Molecular Biology Grade (Merck Millipore Cat. No. 7447407).
- Sodium bicarbonate (NaHCO₃), ACS, ISO, and Reag. Ph. Eur standards (Merck-Millipore, Cat. No. 1063290500).
- Sodium chloride (NaCl) ACS, ISO, and Reag. Ph. Eur standards (Merck-Millipore, Cat. No. 1064041000).
- Sodium hydroxide (NaOH) (Sigma-Aldrich, Cat. No. S5881).
- Sodium phosphate dibasic 99.95% trace metals basis (Sigma-Aldrich, Cat. No. 255793).
- Sodium phosphate monobasic BioReagent, for molecular biology, anhydrous, ≥98% (Sigma-Aldrich, Cat. No S3139).
- Sodium Pyruvate 100 mM, ISO13485 standard (Gibco Cat. No. 11-360-070).
- Sucrose for molecular biology, ≥99.5% (GC) (Sigma-Aldrich S0389).

- Triton-X-100 laboratory grade (Sigma-Aldrich, Cat. No. 234729).
- Trizma[®] base Primary Standard and Buffer, $\geq 99.9\%$ (titration), crystalline (Sigma-Aldrich Cat. No. T1503).
- Trypsin 2, 5 % 10X (Thermo-Fisher, Cat. No. 15090046).
- Vectashield antifade mounting medium (Vector Laboratories Cat. No.H-1000).
- Dimethyl sulfoxide ACS reagent $\geq 99.9\%$ (Sigma-Aldrich Cat. No. 472301).

21.2 Addendum Plastic Materials, Surgical Instruments and Medical Supplies.

- 1, 5 mL Microcentrifuge tubes (SSI, Inc.).
- 12 mm coverslips (Marienfeld, Cat. No. 0111520).
- 15 mL FALCON conical centrifuge tube (Genexpress Cat. No. FC.352097).
- 24-well multiwell dishes (TrueLine, Cat. No. TR5002).
- 50 mL FALCON conical centrifuge tube (Genexpress Cat. No. FC.352098).

- Bacteriologic culture plastic dishes (ISOLAB, Cat. No. 081.02.091).
- Economy Tweezers #5, 11cm, 0.4x0.45 (WPI, Cat. No. 501979).
- Falcon™ Cell strainer (Fisher Scientific, Cat. No. 08-771-2).
- Gillies Dissecting Forceps, 15.5cm, Straight, 1x2 teeth (WPI, Cat. No. 501266).
- Mini Dissecting Scissors, 8.5cm, Curved, Blunt Tips (WPI, Cat. No. 503668).
- Spring Scissors, 14cm, Round Hand les, straight, 6.5mm Blades (WPI, Cat. No. 14111).
- Syringe, 1mL with 25G 5/8 tuberculin needle, disposables (TCL Cat. No. JD-01T2516-SB by Nipro).
- Syringe, 5mL with 21X 1 ½ l/lock tip needle, disposable (TCL Cat. No. JD-05L2138-SB by Nipro).

21.3 Addendum Drugs and Treatments.

- AR-C155858 (TOCRIS, Cat. No. 4960).
- Cytochalasin B from *Drechslera dematioidea* $\geq 98\%$ (HPLC), powder (Sigma-Aldrich Cat. No. C6762)

21.4 Addendum Markers, Reporters and Antibodies.

- DAPI; 4', 6-Diamidino-2-Phenylindole, Dihydrochloride (Thermo-Fisher, Cat. No. D1303).
- Rat Anti-Neurofilament 200 (NF-H), suitable for IHC, microarray and WB (Sigma-Aldrich, Cat. No. N4142).
- Goat Anti-Monocarboxylate Transporter 1 (MCT1; T-19) (Santa Cruz Biotechnologies, Cat. No. sc-14917)
- Goat Anti-Monocarboxylate Transporter 2 (MCT2; M-17) (Santa Cruz Biotechnologies, Cat. No. sc-14926)
- Goat Anti-Glucose Transporter 2 (Glut2; C-19) (Santa Cruz Biotechnologies, Cat. No. sc-7580)
- Donkey anti-Rabbit IgG (H+L) Highly Cross-Adsorbed Secondary Antibody, Alexa Fluor 546 (Thermo Fischer, Cat. No. A10040)
- Donkey anti-Rabbit IgG (H+L) Cross-Adsorbed Secondary Antibody, Alexa Fluor 488 (Thermo Fischer, Cat. No. A11055)
- fluo-4 acetoxymethyl (AM), cell permeant (Invitrogen, Cat. No. F14201)

21.5 Addendum Energetic Metabolism Nanosensors (Adenoviral Vectors).

- Adenoviral vector Ad FLII12Pglu600 μ Δ 6 (Vector BioLabs, custom made).
- Adenoviral vector Ad Pyronic (all serotype 5) (Vector BioLabs, custom made).

21.6 Addendum Specialized Hardware, Devices and Equipment:

- Olympus IX70 inverted microscope (Olympus).
- Basic CO₂ Water Jacketed Incubator, Infrared (IR) Sensor, 6, 7 Cu. Ft. 220V (SHELL LAB, Cat. No. 2406-2).
- Hamamatsu Orca camera (Hamamatsu, Japan).

21.7 Addendum Software:

- Graphpad Prism 6 (Graphpad Software)
- Fiji (NIH).

22. ADDENDUM METHODS.

22.1 Addendum Animal Housing.

Animals used were mixed F1 male mice (C57BL/6J x CBA/J), kept in an animal room under SPF conditions at a room temperature of 20 ± 2 °C, in a 12/12 h light/dark cycle with free access to food and water. Experiments were approved by the Center for Scientific Studies of Valdivia Animal Care and Use Committee.

22.2 Addendum Dorsal Root Ganglia Culture and Infection.

E12 C57BL/6J mice embryos were decapitated, and the vertebral column was removed. Spinal cord with dorsal root ganglia (DRG) were dissected and placed in a Petri dish containing L-15 medium. Immediately after, DRG were treated with 1X Trypsin-EDTA for 15 min at 37°C and then centrifuged at RT in the same solution by 10 min at 0,7 rcf. Finally, DRG were disaggregated mechanically by resuspension with a Pasteur pipette in Neurobasal medium and centrifuged again at RT by 10 min at 0,7 rcf. Disaggregated DRG debris was removed filtering through 70µm cell strainer

Disaggregated DRG neurons were seeded over 12mm coverslip and cultured by seven days in 24-well dishes containing 400 mL of Neurobasal medium, 2% B27, 0,3% L-glutamine, 1% streptomycin/penicillin, and 50 ng/ml Neural Growth Factor 2,5S (NGF). Also, a mixture of aphidicolin and fluoro-2-deoxyuridine was added to disaggregated DRG neurons to inhibit proliferation of Schwann cells by inhibition of DNA polymerase. Culture media was replaced every other day.

We identified and distinguished the existence of soma and axons in disaggregated DRG neurons qualitatively by morphology under bright field, cytoskeleton stain or cytosolic homogeneous distribution of calcium stain and FRET sensors in all the studies here mentioned.

Disaggregated DRG neurons were exposed to Adenoviral vector AdPyronic 1:10000 (San Martín A, *et al.*, 2014) or Adenoviral vector Ad FLII12Pglu600 $\mu\Delta 6$ (serotype 5) 1:10000 (Fehr *et al.*, 2003; Deuschle *et al.*, 2005; Takanaga *et al.*, 2008) and studied after 24 h. Expression of AdPyronic or Ad FLII12Pglu600 $\mu\Delta 6$ (serotype 5) was determined by observation of FRET pairs fluorescence under microscope. Cultures with qualitatively homogeneous fluorescence in cytoplasm and nuclei exclusion were studied and cultures with different traits were dismissed.

22.3 Addendum Immunofluorescence.

Disaggregated DRG neurons were fixed by immersion in 4% paraformaldehyde (PFA) in 0.1 M phosphate buffer (PB) for 1 h, followed by three 10 min washes in 1× PB, sucrose gradient (5%, 10%, 20% in 1× PBS). After, disaggregated DRG neurons were washed in 1x PBS for 10 min and then blocked/permeabilized in 0.1% Triton X-100, 2% cold water fish skin in 1X PBS for 1h at RT. Finally, disaggregated DRG neurons were incubated in primary antibodies in blocking/permeabilizing solution overnight at 4°C, washed in 1XPBS 3x10 min, and incubated in secondary antibodies for 2h at RT. Disaggregated DRG neurons were washed 3x10 min in 1XPBS and mounted in Vectashield.

22.4 Glut2 and MCT1 or MCT2 Qualitative Expression and Distribution in DRG Neurons.

Qualitative expression and distribution of glucose and pyruvate transporters was studied by observation of immunofluorescences of disaggregated DRG neurons stained against Glut2, MCT1 or MCT2. NF-H (cytoskeleton) was used as counterstain and nucleus were stained with DAPI. These assays were performed in uninfected disaggregated DRG neurons.

22.5 Addendum Table 1. Addendum Primary and Secondary Antibodies Dilutions.

Species Reactivity in this thesis	Primary Antibody or Secondary Antibody	Host	Immunofluorescence Dilution
Mouse	Anti-Monocarboxylate Transporter 1 (MCT1-T19)	Goat	1:500
Mouse	Anti-Monocarboxylate Transporter 2 (MCT1-T17)	Goat	1:500
Mouse	Anti-Glucose Transporter 2 (Glut2-C19)	Goat	1:500
Mouse	Anti-Neurofilament 200 (Heavy chain); NF-H.	Rabbit	1:1000
-	Anti-Rabbit Alexa 546	Donkey	1:1000
-	Anti-Goat Alexa 488	Donkey	1:1000

22.6 *In Vitro* Determination of Depolarization Induced Cytosolic Calcium Dynamics.

Cytosolic calcium dynamics were measured using the fluorescent indicator fluo-4 acetoxymethyl (AM) and laser scanning confocal microscopy. These measurements were performed in uninfected disaggregated DRG neurons.

Disaggregated DRG neurons were incubated with 4 μ M fluo-4 acetoxymethyl (AM) by 30 min at RT in Krebs Ringer Hepes Buffer of the following composition: 136 mM NaCl, 3mM KCl, 10 mM HEPES, 1,25 mM MgSO₄ and 1,25 mM CaCl₂, pH 7,4, 300mOsm/L.

After, disaggregated DRG neurons were washed three times with KRH/HEPES Buffer.

Disaggregated DRG neurons cytosolic calcium dynamics measurements were imaged at 490 excitation/530 nm emission with an Olympus IX70 inverted microscope equipped with a 60 \times water-immersion objective, a Cairn monochromator with Optosplit, and a Hamamatsu Orca camera controlled by Kinetics software.

Before cytosolic calcium dynamic measurements, disaggregated DRG neurons were incubated until steady state at RT in 95% O₂/5% CO₂-gassed working buffer of the following composition: 112 mM NaCl, 3mM KCl, 10 mM HEPES, 24 mM NaHCO₃, 1,25 mM MgSO₄ and 1,25 mM CaCl₂, pH 7,4, 300mOsm/L.

Cytosolic calcium dynamics were measured simultaneously in soma and axons of the same disaggregated DRG neurons.

Depolarization was induced by high K^+ in disaggregated DRG neurons by 3s superfusion of 95% O_2 /5% CO_2 -gassed buffer of the following composition: 65 mM NaCl, 50mM KCl, 10 mM HEPES, 24 mM $NaHCO_3$, 1,25 mM $MgSO_4$ and 1,25 mM $CaCl_2$, pH 7,4, 300mOsm/L. After, disaggregated neurons were superfused again with working buffer until steady state.

Alternatively, disaggregated DRG neurons calcium dynamics were registered until steady state and then depolarization was induced by electrical field stimulation with a single square-wave DC pulse, at 150V, 25Hz of 3ms duration. Finally, registration was ended when disaggregated DRG neurons calcium dynamics were at steady state again.

Fluo-4 fluorescence at each point was normalized with initial fluorescence (F/F_0). Also, maximal delta of normalized Fluo-4 was determined (maximal $\Delta(F/F_0)$) in high K^+ stimulation and electrical field stimulation treatments. Paired t-test was performed to compare between cytosolic calcium dynamics of soma and axons in high K^+ stimulation or electrical field stimulation treatments.

22.7 *In Vitro* Determination of Mitochondrial Pyruvate Consumption Rate in Neurons.

Pyruvate dynamics were measured in disaggregated DRG neurons expressing FRET pyruvate nanosensor pyronic protein (San Martín *et al.*, 2014) during a mitochondrial pyruvate consumption protocol.

All experiments were carried out at room temperature (22–25°C). Disaggregated DRG

neurons cells were imaged in 95% O₂/5% CO₂-gassed buffer (working buffer) of the following composition 112 mM NaCl, 3mM KCl, 1,25 mM CaCl₂, 1,25 mM MgCl₂, 10 mM HEPES, 24 mM NaHCO₃, pH 7,4. Superfusion was performed at 1 mL/min.

Disaggregated DRG neurons expressing pyronic protein were excited at 430nm and registered at 485nm for mTFP and 528nm for Venus with an Olympus IX70 inverted microscope equipped with a 60× water-immersion objective, a Cairn monochromator with Optosplit and a Hamamatsu Orca camera controlled by Kinetics software. Data were encoded in 14 bits and the camera was shown to behave linearly in the range of 200–10,000 gray units. Due to variations in sensor expression, exposure times were adjusted for each experiment so that in a typical ROI average intensity was between 1,000 and 4,000.

Mitochondrial pyruvate consumption rate protocol treatments were superfused sequentially as follows: (1) pyruvate concentration was zero until steady state; (2) 1mM pyruvate until steady state; (3) pyruvate concentration was dropped to zero again until steady state; (4) 0,4 mM pyruvate until steady state; (5) 0,4 mM pyruvate and MCTs inhibition with 1 μM AR-C155858.

Pyruvate dynamics were measured in soma and axons of different disaggregated DRG neurons.

To assess Mitochondrial pyruvate consumption rate, disaggregated DRG neurons expressing pyronic were previously depleted of glucose and lactate for 30 min. Importantly, working buffer also did not contained pyruvate.

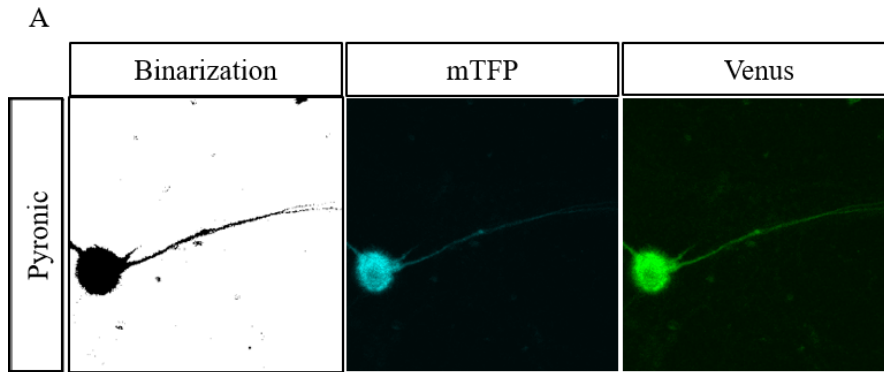
First, mTFP and Venus fluorescence intensity was registered until basal steady state. Then, to determine pyronic functionality in this preparation, mTFP and Venus fluorescence intensity was registered in disaggregated DRG neurons while superfused with working buffer supplemented with 1mM pyruvate until steady state. After, pyruvate concentration was dropped to zero until basal steady state. Finally, disaggregated DRG neurons were superfused with 0,4 mM pyruvate until steady state and MCTs were consequently inhibited by superfusion with 1 μ M AR-C155858.

mTFP or Venus fluorescence was normalized by background mTFP or Venus channels fluorescence. Subsequently, background normalized mTFP or Venus fluorescence was normalized by mTFP or Venus fluorescence values in the first 3s of registration (control fluorescence).

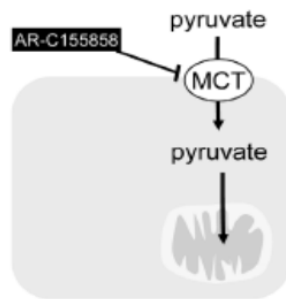
mTFP/ Venus fluorescence ratio (R_x) was determined after normalizations. R_0 is the ratio in the absence of pyruvate and ΔR_{\max} is the difference between R_0 and the maximum ratio estimated in 1 mM pyruvate. The value of the mTFP/ Venus ratio at each time point minus R_0 . Pyruvate concentration dynamics during mitochondrial pyruvate consumption protocol was estimated from mTFP/Venus ratio (ΔR) data using maximal mTFP/Venus ratio delta (ΔR_{\max}) of pyronic in disaggregated DRG neurons and previously reported K_D for pyronic *in vitro*: 107 μ M (San Martín *et al.*, 2014).

Mitochondrial pyruvate consumption rate was determined as the rate of decrease in pyruvate concentration immediately after inhibition of glucose transport with 1 μ M AR-C155858, by

calculating the linear regression slope adjusted to the first 10 data points after MCTs inhibition. Unpaired student t test was performed to compare between soma and axon mitochondrial pyruvate consumption rates in disaggregated DRG neurons.



B



C

$$\Delta R = \frac{Kd_{Pyr} * [Pyr]}{\Delta R_{max} - [Pyr]}$$

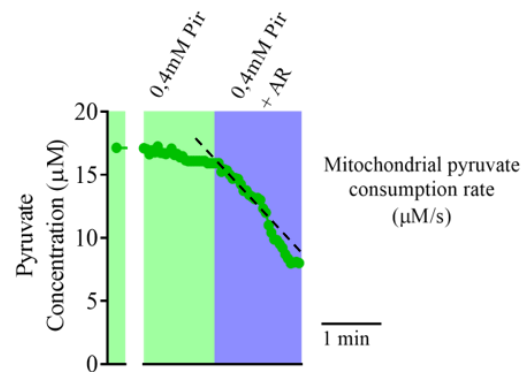
R : (mTFP/Venus)FluorescenceRatio

$Kd_{Pyr} : 0,107$

D

$$[Pyr] = \frac{Kd_{Pyr} * \Delta R}{\Delta R_{max} - \Delta R}$$

E



ADDENDUM FIGURE N°1. Measurement of Mitochondrial Pyruvate Consumption Rate. (A) 60X images of disaggregated Dorsal root ganglia neurons expressing pyruvate FRET nanosensor pyronic (binary). Disaggregated DRG neurons were exposed to Ad Pyronic1:10000 and studied after 24 h. Expression of Ad Pyronic was determined by observation of fluorescence under microscope. Cultures with qualitatively homogeneous fluorescence in cytoplasm were studied and cultures with fluorescent aggregates were dismissed. Pyronic FRET pair was composed by mTFP donor (Cyan) and Venus acceptor (Green). (B) Mitochondrial pyruvate consumption rate was measured in disaggregated dorsal root ganglia neurons using pyruvate as the exclusive fuel. MCTs were inhibited using 1 μ M AR-C155858 (Mod. from San Martín *et al.*, 2014) (C) mTFP/Venus fluorescence ratio delta formula. mTFP/ Venus fluorescence ratio (R_x) was determined after normalizations. R_0 is the ratio in the absence of pyruvate and ΔR_{max} is the difference between R_0 and the maximum ratio estimated in 1 mM pyruvate. (D) pyruvate concentration formula. The value of the ratio at each time point minus R_0 , ΔR , was transformed into pyruvate concentration in mM using the measured DR_{max} and the K_D previously reported *in vitro* (107 μ M) (San Martín *et al.*, 2014). (E) Mitochondrial pyruvate consumption rate (dashed black line) was determined as the rate of decrease in pyruvate concentration immediately after inhibition of pyruvate transport by 1 μ M AR-C155858. (cyan background), by calculating the linear regression slope adjusted to the first 10 data points after MCTs inhibition.

22.8 *In vitro* Determination of Glycolytic Rate in Neurons.

Glucose dynamics were measured in disaggregated DRG neurons expressing FRET glucose nanosensor FLII12Pglu600 $\mu\Delta 6$ protein (Fehr *et al.*, 2003; Deuschle *et al.*, 2005; Takanaga *et al.*, 2008) during a glycolysis protocol.

All experiments were carried out at room temperature (22–25°C). Disaggregated DRG neurons cells were imaged in 95% O₂/5% CO₂-gassed buffer of the following composition 112 mM NaCl, 3mM KCl, 1,25 mM CaCl₂, 1,25 mM MgCl₂, 10 mM HEPES, 24 mM NaHCO₃ and 1 mM sodium lactate, pH 7.4. This buffer was supplemented with 5mM glucose to measure glucose dynamics. Disaggregated DRG neurons expressing FLII12Pglu600 $\mu\Delta 6$ protein were imaged at 488 excitation/505-550 nm emission (for YFP/CFP) and 543 excitation/>580 nm emission (for Alexa Fluor 568) with an Olympus IX70 inverted microscope equipped with a 60× water-immersion objective, a Cairn monochromator with Optosplit, and a Hamamatsu Orca camera controlled by Kinetics software. Data were encoded in 14 bits and the camera was shown to behave linearly in the range of 200–10,000 gray units. Due to variations in sensor expression, exposure times were adjusted for each experiment so that in a typical ROI average intensity was between 1,000 and 4,000.

Glycolytic rate protocol treatments were superfused sequentially as follows: (1) 5 mM glucose and 1 mM lactate until steady state; (2) glucose and lactate concentration dropped to zero until steady state; (3) 5 mM glucose and 1 mM lactate again until steady state (white background); (4) glucose transport inhibition with 20 μ M Cytochalasin B.

Glycolytic dynamics were measured in soma and axons of different disaggregated DRG neurons.

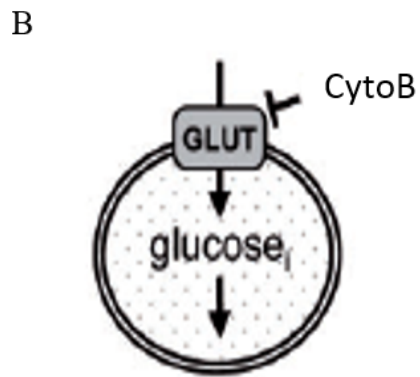
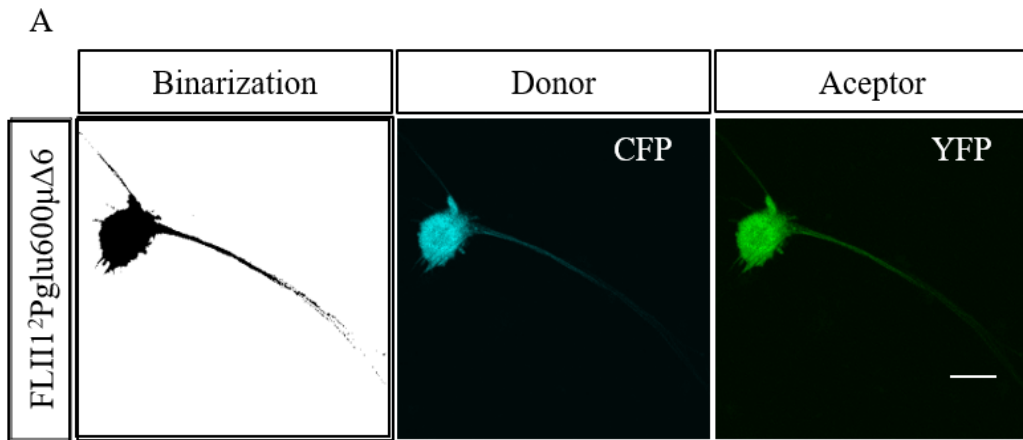
YFP and CFP fluorescence was constantly measured under permanent superfusion of buffer at 1 mL/min with different glucose concentrations. At first, control YFP and CFP fluorescence was measured under superfusion of buffer containing 5mM glucose until basal steady state. After, a YFP and CFP fluorescence was determined by dropping to zero glucose buffer superfusion in a single step until steady state. Then, YFP and CFP fluorescence was measured again under superfusion of buffer containing 5mM glucose until basal steady state. Finally, YFP and CFP fluorescence was measured under superfusion of buffer containing 5mM glucose and glucose transport inhibition with 20 μ M Cytochalasin B until steady state.

YFP or CFP fluorescence was normalized by background YFP or CFP channels fluorescence. Subsequently, background normalized YFP or CFP fluorescence was normalized by YFP or CFP fluorescence values in the first 3s of registration (control fluorescence). YFP/ CFP fluorescence ratio (R_x) was determined after normalizations [Addendum Figure N°2].

Glycolytic rate was determined as the rate of decrease in YFP/ CFP fluorescence ratio immediately after inhibition of glucose transport by 20 μ M Cytochalasin B ([Addendum Figure N°2] yellow dashed line), by calculating the linear regression slope adjusted to the first 10 data points after glucose transport inhibition. Unpaired student t test was performed to compare between soma and axon glycolytic rates of disaggregated DRG neurons [Addendum

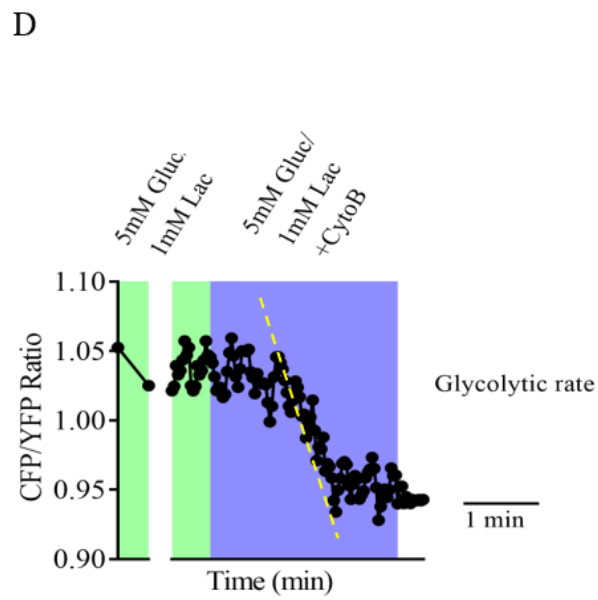
Figure N°18].

Mathematical model of glucose homeostasis has been extensively described before (Bittner *et al.*, 2010).



C

$$\Delta R = \frac{K_{d\text{Gluc}} * [\text{Gluc}]}{\Delta R_{\text{max}} [\text{Gluc}]}$$



ADDENDUM FIGURE N°2. Measurement of Glycolytic Rate. (A) 60X images of disaggregated Dorsal root ganglia neurons expressing glucose FRET nanosensor FLII12Pglu600 mΔ6 (binary). Disaggregated DRG neurons were exposed to Ad FLII12Pglu600 mΔ6 (serotype 5) 1:10000 and studied after 24 h. Expression of Ad FLII12Pglu600 mΔ6 (serotype 5) was determined by observation of fluorescence under microscope. Cultures with qualitatively homogeneous fluorescence in cytoplasm and nuclei exclusion were studied and cultures with different traits were dismissed. FLII12Pglu600 mΔ6 FRET pair was composed by CFP donor (Cyan) and YFP acceptor (Green). (B) Glycolytic rate was estimated in disaggregated dorsal root ganglia neurons under inhibition of glucose transport by 20 μM Cytochalasin B (Mod. from Bittner *et al.*, 2010). (C) YFP/CFP fluorescence ratio delta formula. YFP/CFP fluorescence ratio (R_x) was determined after normalizations. R_0 is the ratio in the absence of pyruvate and ΔR_{\max} is the difference between R_0 and the maximum ratio estimated in 1 mM pyruvate. (E) Glycolytic rate (dashed yellow line) was determined as the rate of decrease in YFP/CFP ratio immediately after inhibition of glucose transport by 20 μM Cytochalasin B (cyan background), by calculating the linear regression slope adjusted to the first 10 data points after glucose transport inhibition.

22.9 Addendum Statistical Analysis.

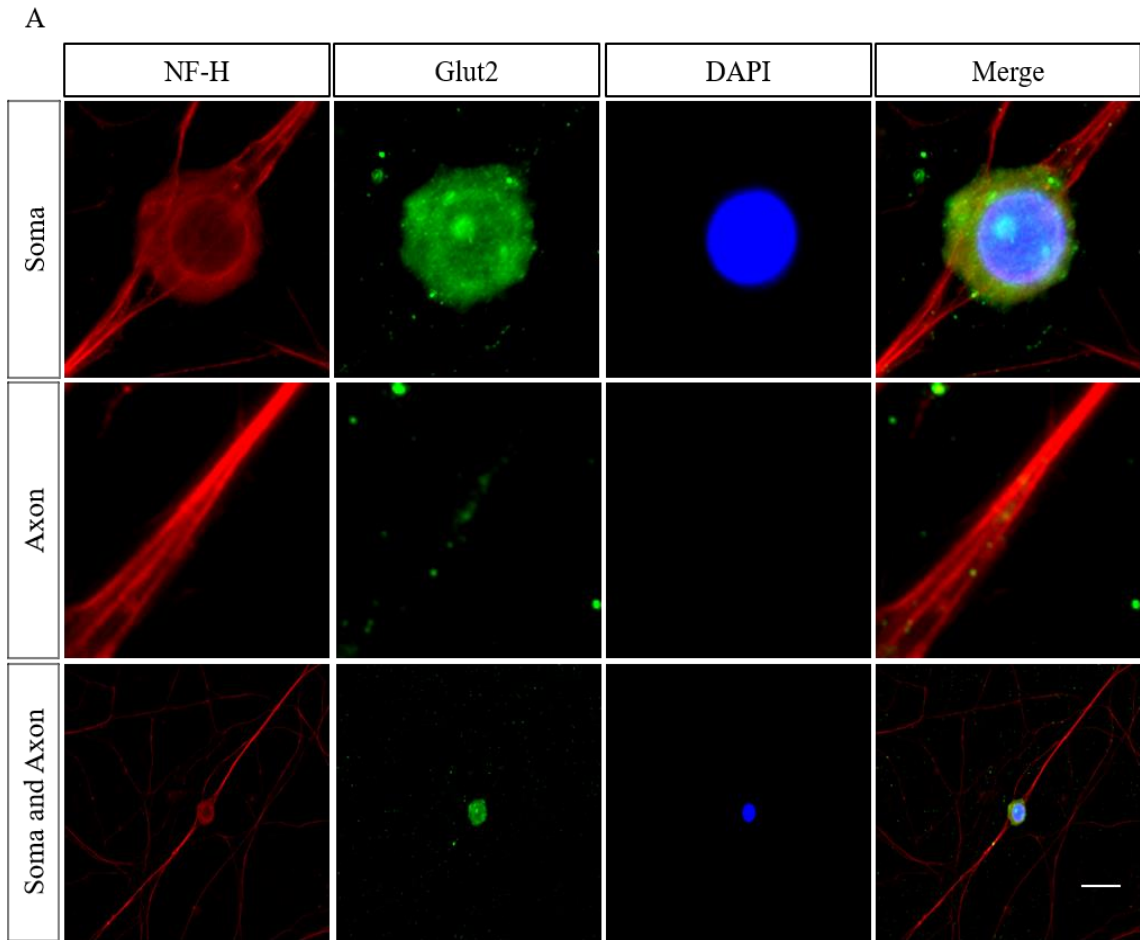
Regression analyses student t test, and Fischer test were carried out as statistical analysis. Bonferroni's test was used as *post hoc* analysis. $P < 0.05$ was considered as statistically significant. All statistics and graphs were done using *GraphpadPrism6* software.

23. ADDENDUM RESULTS.

23.1 Glucose and Pyruvate Transporters Distribution in Soma and Axons of Disaggregated DRG Neurons.

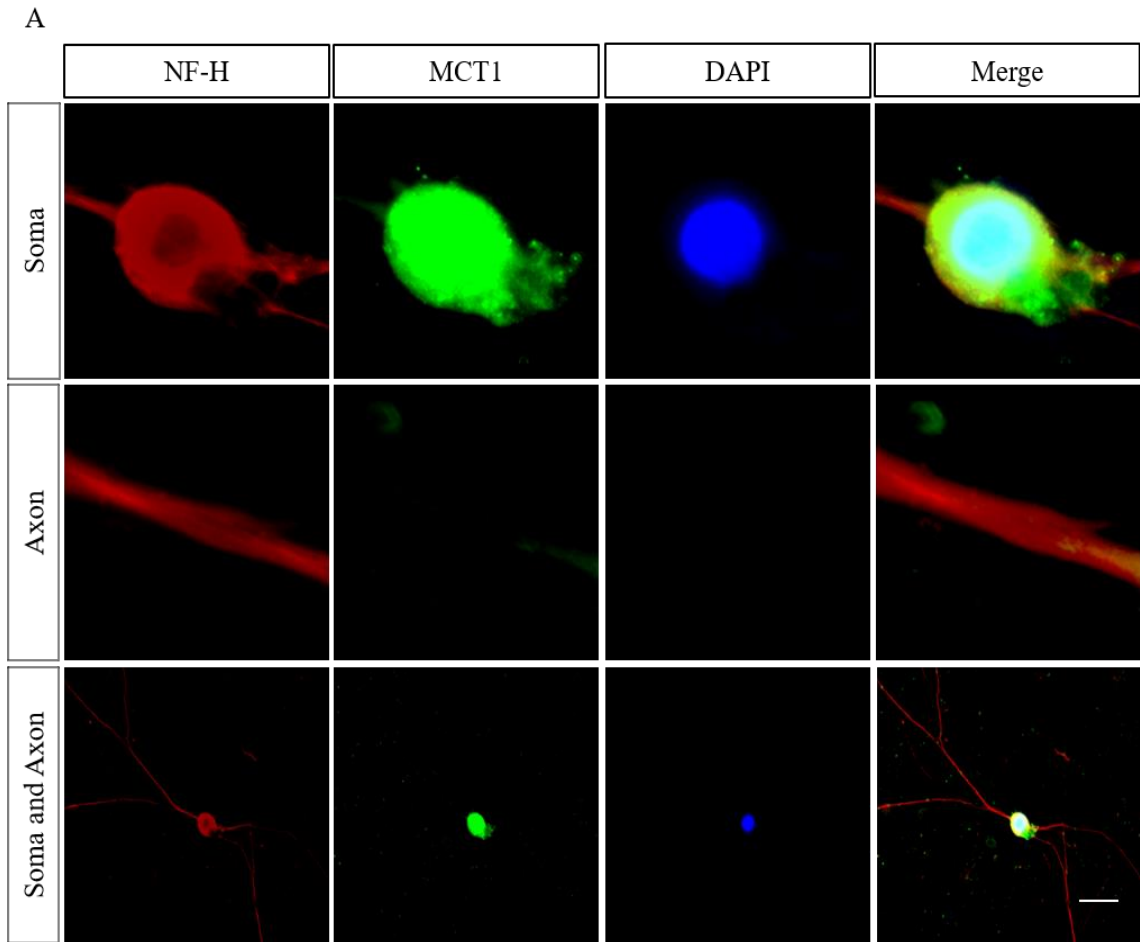
Neurons are highly dependent in a constant supply of energetic substrates (Bélanger, M., *et al.*, 2011). Specifically, glucose and pyruvate entrance to neurons is facilitated largely via the Glucose transporters (Gluts) and Monocarboxylate transporters (MCTs), respectively (Simpson *et al.*, 2007). To characterize the expression and distribution of GLUTs and MCTs in our disaggregated DRG neurons *in vitro* model, we performed immunofluorescence against Glut2, MCT1 and MCT2 after 7 days of culture.

After observation of all immunofluorescence performed, we qualitatively describe that Glut2 [Addendum Figure N°3] and MCT1 [Addendum Figure N°4] is present in soma of disaggregated DRG neurons and absent in axons. On the other hand, MCT2 is consistently distributed homogeneously along soma and axons of disaggregated DRG neurons [Addendum Figure N°5].



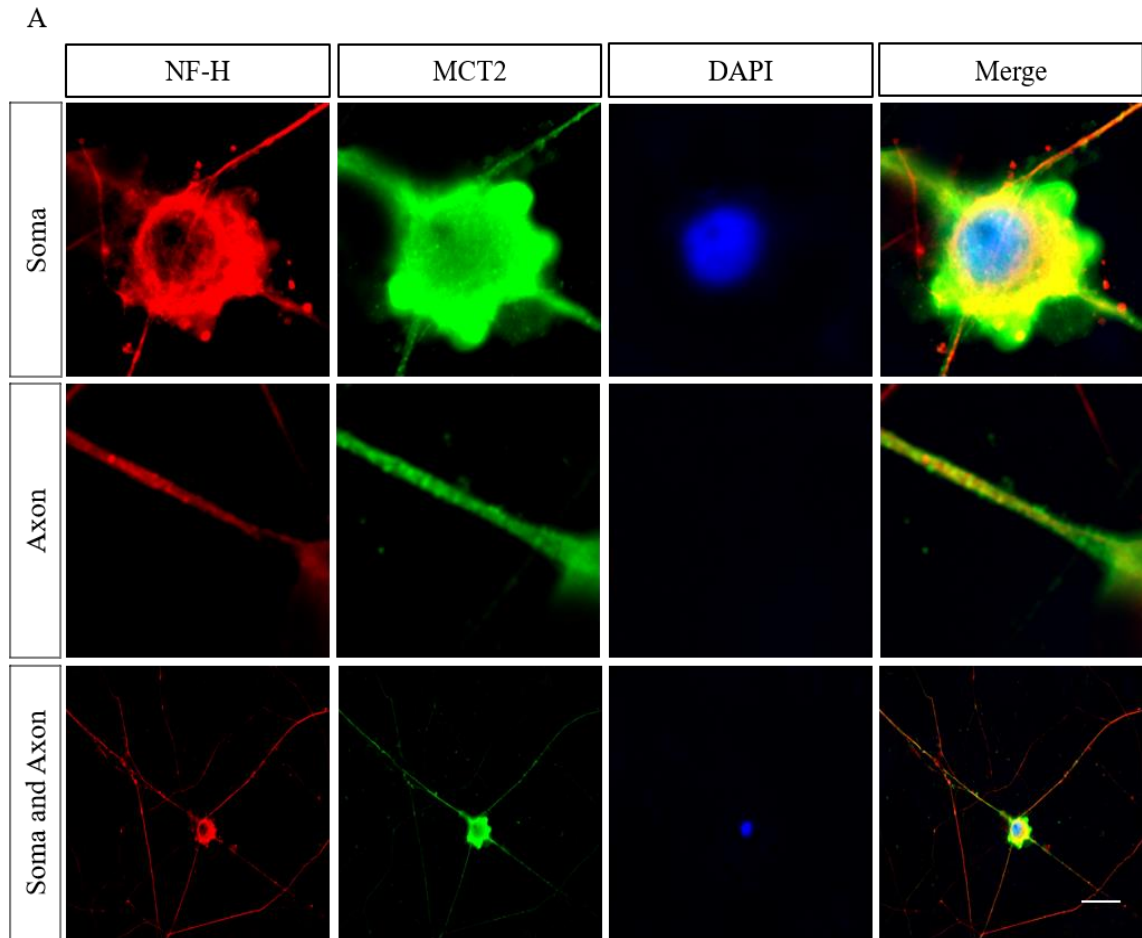
ADDENDUM FIGURE N°3. Glucose Transporter 2 (Glut2) cellular distribution in dorsal root ganglia neurons. (A) 60X and 40X images of Disaggregated DRG Neurons from E12 mouse embryo dorsal root ganglia after 7 days culture using High Neurofilament Chain (NF-H) stain for neurite cytoskeleton, anti Glut2 stain and DAPI. Scale Bar: 20 μ m.

Qualitative observation of images shows that Glut2 is present mostly in soma of disaggregated DRG neurons. This cellular distribution pattern of Glut2 was consistent along all the images obtained.



ADDENDUM FIGURE N°4. Monocarboxylate Transporter 1 (MCT1) Cellular Distribution in Dorsal Root Ganglia Neurons. (A) 60X and 40X images of Disaggregated DRG Neurons from E12 mouse embryo dorsal root ganglia after 7 days culture using heavy neurofilament chain (NF-H) stain for neurite cytoskeleton, anti MCT1 stain and DAPI. Scale Bar: 20 μm .

Qualitative observation of images shows that MCT1 is present mostly in soma of disaggregated DRG neurons. This cellular distribution pattern of MCT1 was consistent along all the images obtained.



ADDENDUM FIGURE N°5. Monocarboxylate Transporter 2 (MCT2) Cellular Distribution in Dorsal Root Ganglia Neurons. (A) 60X and 40X images of Disaggregated DRG Neurons from E12 mouse embryo dorsal root ganglia after 7 days culture using heavy neurofilament chain (NF-H) stain for neurite cytoskeleton, anti MCT2 stain and DAPI. Scale Bar: 20 μ m.

Qualitative observation of images shows that MCT2 is present in soma and axons of disaggregated DRG neurons. This cellular distribution pattern of MCT2 was consistent along all the images obtained.

23.2 Cytosolic Calcium Dynamics after High K⁺ or Electrical Stimulation Depolarization Induction in Soma and Axons of Disaggregated DRG Neurons.

In neurons, energy supply is connected to demand through calcium homeostasis (Shetty *et al.*, 2012). Depolarization induces a significant and transient increase in cytosolic calcium levels (Zündorf and Reiser, 2011; Llorente-Folch, *et al.*, 2015; Ivannikov *et al.*, 2010). Furthermore, a rise in intracellular calcium acts through multiple pathways to increase ATP synthesis, matching energy supply to demand (Llorente-Folch *et al.*, 2015). Importantly, calcium homeostasis dysregulation has been extensively related with neurodegeneration onset and progression (Zündorf and Reiser, 2011).

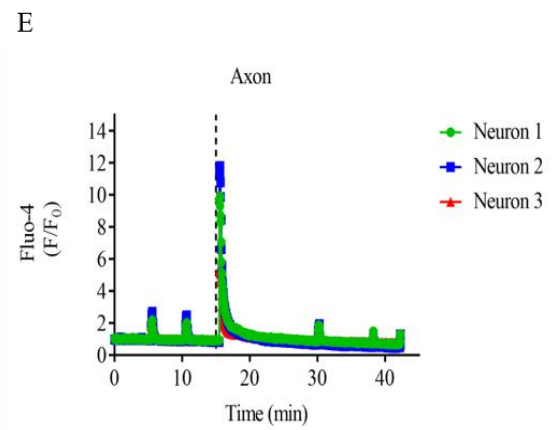
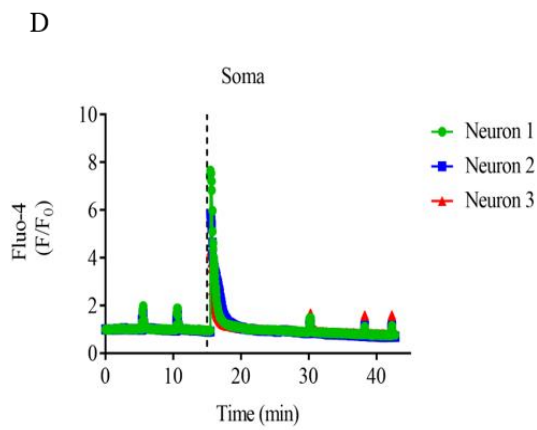
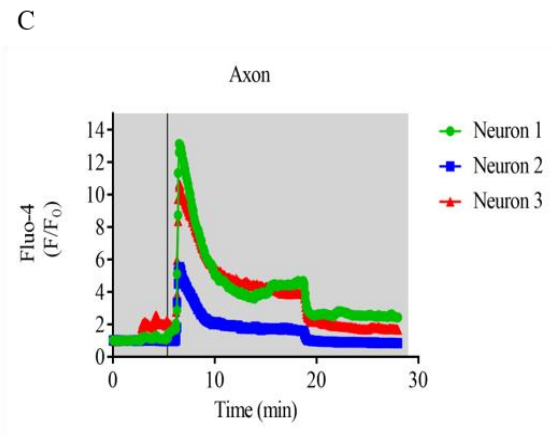
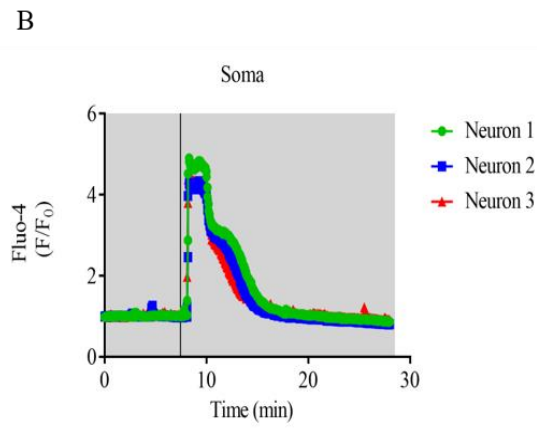
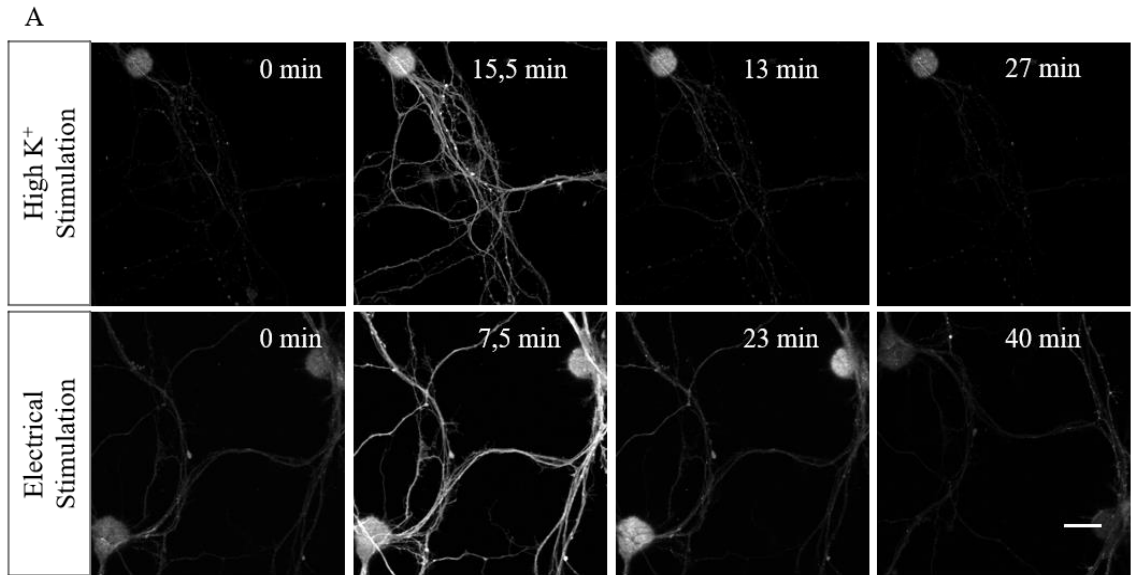
On the other hand, it has been reported that both ATP generating pathways (glycolysis and mitochondrial) participate in the calcium clearance, through ATP dependent mechanisms located in the plasma membrane, mitochondria and endoplasmic reticulum (Ivannikov *et al.*, 2010). Based on this mechanism of neuronal energetic metabolism regulation by depolarization through calcium dynamics, we used cytosolic calcium regulation capacity as a preliminary readout for the execution of energetic metabolism in our model. Also, we wanted to evaluate the cytosolic calcium regulation capacity in response to depolarization as an indicator of the general homeostasis in neurons at our experimental model.

To evaluate cytosolic calcium regulation capacity in our experimental model, disaggregated DRG neurons were cultured for 7 days and then loaded with cytosolic calcium reporter Fluo-4 acetoxymethyl (AM) (Fluo-4). After, Fluo-4 fluorescence intensity was registered until basal steady state.

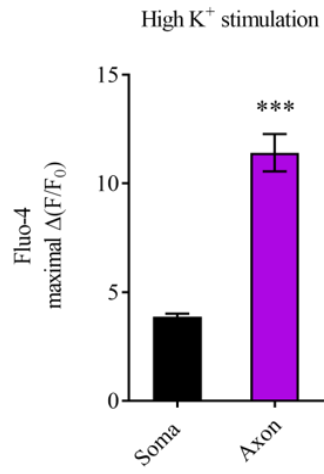
Depolarization was induced in half of Fluo-4 loaded disaggregated DRG neurons using a transient (3s) superfusion of 50 mM K⁺ and cytosolic calcium fluorescence (Fluo-4 F/F₀) was registered simultaneously in soma and axons of the same neurons [Addendum Figure N°6A]. We found that depolarization with 50 mM K⁺ immediately induced a transient significant increase of cytosolic calcium levels (Fluo-4 F/F₀) in soma and axons of disaggregated DRG neurons [Addendum Figure N°6B and N°6C]. All disaggregated DRG neurons studied returned to basal levels of steady state cytosolic calcium, indistinguishable from before K⁺ stimulation [Addendum Figure N°6B and N°6C]. Interestingly, maximal change in cytosolic calcium levels (Fluo-4 maximal $\Delta F/F_0$) was significantly higher in axons than in soma under these experimental conditions [Addendum Figure N°6F].

On the other hand, depolarization was induced by electrical field stimulation (square-wave DC pulse, 150V, 25Hz of 3ms duration) in half of Fluo-4 loaded disaggregated DRG neurons and cytosolic calcium fluorescence (Fluo-4 F/F₀) was also registered simultaneously in soma and axons [Addendum Figure N°6D and N°6E]. We found that Electrical field induced depolarization immediately triggered a transient significant increase of cytosolic calcium levels (Fluo-4 F/F₀) in soma and axons of disaggregated DRG neurons [Addendum Figure N°6D and N°6E]. All disaggregated DRG neurons studied returned to basal levels of steady state cytosolic calcium, indistinguishable from before electrical field stimulation [Addendum Figure N°6D and N°6E]. Coincidentally, maximal change in cytosolic calcium levels (Fluo-4 maximal $\Delta F/F_0$) was also significantly higher in axons than in soma under these experimental conditions [Addendum Figure N°6G].

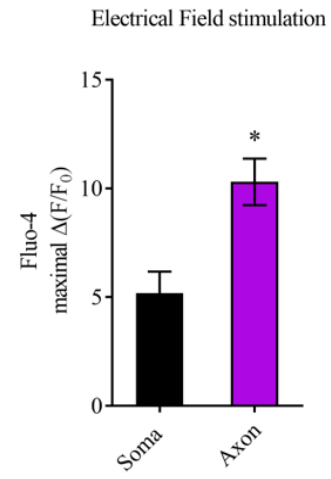
Is worth mention that we found regular spontaneous cytosolic calcium fluorescence spikes in soma and axons of disaggregated DRG neurons, consistent with spontaneous neuronal activity, before and after High K^+ or Electrical field induced depolarization [Addendum Figure N°6H and N°6I].



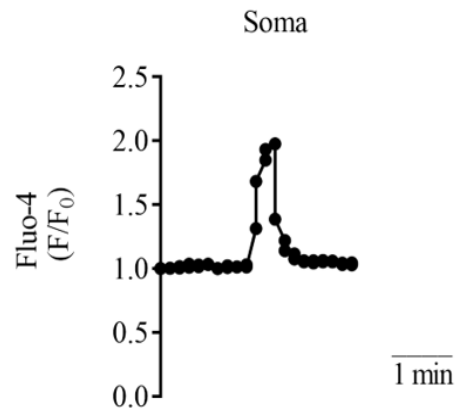
F



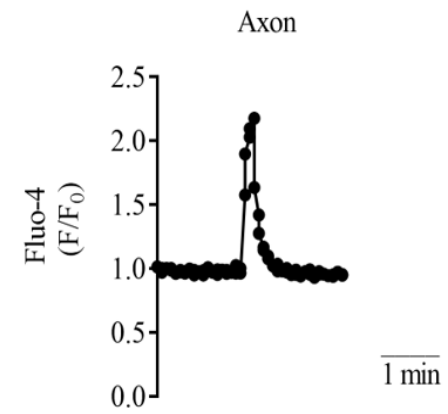
G



H



I



ADDENDUM FIGURE N°6. Calcium Dynamics after High K^+ or Electrical Field Stimulation. (A) 60X images of disaggregated dorsal root ganglia neurons calcium levels staining with Fluo-4. Registrations were performed simultaneously in soma and axon areas of the same fields under high K^+ stimulation (50mM, 3s duration) or electrical field stimulation (square-wave DC pulse, 150V, 25Hz of 3ms duration) (B) Fluo-4 normalized intensity (F/F_0) in soma under high K^+ stimulation (30mM; black line) treatment. (C) Fluo-4 normalized intensity (F/F_0) in axons under high K^+ stimulation (50mM; black line) treatment. (D) Fluo-4 normalized intensity (F/F_0) in soma during electrical field stimulation (dashed line) treatment. (E) Fluo-4 normalized intensity (F/F_0) in axons under electrical field stimulation (dashed line) treatment. (F) Mean maximal delta of normalized Fluo-4 fluorescence intensity (maximal $\Delta(F/F_0)$) in soma and axons under high K^+ stimulation treatment. (G) Mean maximal delta of normalized Fluo-4 fluorescence intensity (maximal $\Delta(F/F_0)$) in soma and axons under electrical field stimulation treatment. (H) Representative register of spontaneous spikes in Fluo-4 normalized intensity (F/F_0) in soma. (I) Representative register of spontaneous spikes in Fluo-4 normalized intensity (F/F_0) in axons.

High K^+ stimulation and electrical field stimulation treatments induce a significant increase in cytosolic calcium levels of soma in axons of disaggregated DRG neurons. Importantly, cytosolic calcium levels induced by high K^+ stimulation or electrical field stimulation treatments are significantly different between soma and axons of the same disaggregated DRG neurons.

We found regular spontaneous cytosolic calcium fluorescence spikes in disaggregated DRG neurons, consistent with spontaneous neuronal activity, before and after high K^+ or Electrical field induced depolarization.

n=3; *p<0,05 or ***p<0,001 indicates significant differences in paired t test between Mean maximal delta of normalized Fluo-4 fluorescence intensity between soma and axon. SEM.

23.3 Pyronic and FLII12Pglu600 $\mu\Delta 6$ Expression in Disaggregated DRG Neurons.

Genetically encoded FRET nanosensors have been increasingly used to measure real time metabolic fluxes (Barros, *et al.*, 2017; Magistretti and Allaman, 2015). In the context of neuronal energetic metabolism, Felipe Barros group and collaborators have reported ex vivo measurement of glycolytic rates and pyruvate mitochondrial consumption rates using genetically codified FRET nanosensors in hippocampal slices (Bittner, *et al.*, 2010; San Martín *et al.*, 2014). Furthermore, the same group has reported lactate flux measurements in somatosensory cortex neurons *in vivo* using genetically encoded FRET nanosensors (Lerchundi, *et al.*, 2015).

To evaluate the expression of glucose and pyruvate FRET nanosensors in our *in vitro* model, after 7 days in culture we infected disaggregated DRG neurons with Adenoviral pyronic pyruvate sensor [Addendum Figure N°1] or Adenoviral vector FLII12Pglu600 $\mu\Delta 6$ respectively [Addendum Figure N°2].

We found that disaggregated DRG neurons express pyronic or FLII12Pglu600 $\mu\Delta 6$ 24 hours after infection. Under these conditions, we observed a consistent homogenous distribution of both FRET nanosensors in cytoplasm of disaggregated DRG neurons with nuclei exclusion [Addendum Figure N°1] and [Addendum Figure N°2]. In this context, fluorescence intensity of both FRET nanosensors decayed from soma to distal regions of the axons [Addendum Figure N°1] and [Addendum Figure N°2]. To our knowledge, this is the first time pyronic or FLII12Pglu600 $\mu\Delta 6$ expression is reported in peripheral neurons.

23.4 Mitochondrial Pyruvate Consumption Rates in Soma and Axons of Disaggregated DRG Neurons.

To compare the mitochondrial pyruvate consumption rates between soma and axons, we induced the expression of pyronic (pyruvate sensor) in disaggregated DRG neurons after 7 days of culture [Addendum Figure N°1]. Consequently, a protocol of mitochondrial pyruvate consumption was performed in disaggregated DRG neurons measuring mTFP and Venus (pyronic FRET pair) fluorescence intensity in soma and axons under constant superfusion [Addendum Figure N°1].

We found that fluorescence intensity of mTFP and Venus was stable in absence of pyruvate in soma and axons of disaggregated DRG neurons [Addendum Figure N°7 and Addendum Figure N°10]. Consequently, mTFP/Venus ratio remained in a basal steady state in soma and axons under these treatments [Addendum Figure N°8 and Addendum Figure N°11].

Interestingly, superfusion of pyruvate induced an increase in mTFP fluorescence intensity and a decrease in Venus fluorescence intensity in soma and axons of disaggregated DRG neurons [Addendum Figure N°7 and Addendum Figure N°10], consistent with a decrease in FRET efficiency and a new steady state was established. Furthermore, we found that after pyruvate concentration was dropped to zero again, mTFP/Venus ratio reached the basal steady state again in soma and axons [Addendum Figure N°8 and Addendum Figure N°11].

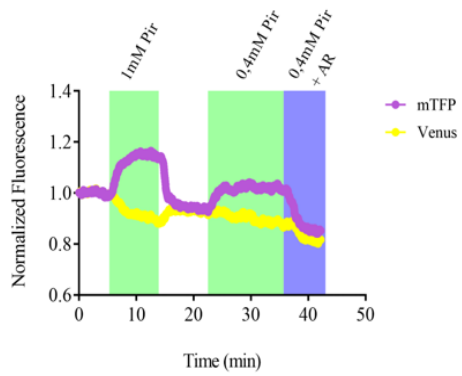
Notably, superfusion of MCTs inhibitor AR- C155858 (1 μ M) in presence of 0,4 mM pyruvate induced a decrease in mTFP fluorescence intensity and an increase in Venus

fluorescence intensity in soma and axons of disaggregated DRG neurons [Addendum Figure N°7 and Addendum Figure N°10]. Thus, mTFP/Venus ratio decreased, consistent with a decrease in FRET efficiency [Addendum Figure N°8 and Addendum Figure N°11]. Interestingly, decrease in mTFP/Venus ratio induced by MCTs inhibition reached basal steady state in soma of disaggregated DRG neurons [Addendum Figure N°8]. However, mTFP/Venus ratio in axons of disaggregated DRG neurons after MCTs inhibition decreased and then increased alternately and never reached a steady state during the registration time [Addendum Figure N°11].

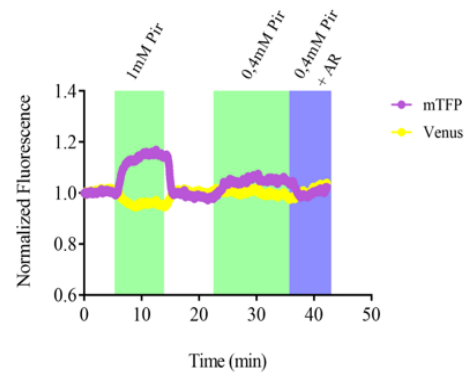
Pyruvate concentration dynamics during mitochondrial pyruvate consumption protocol was estimated from mTFP/Venus ratio data using maximal mTFP/Venus ratio delta of pyronic in disaggregated DRG neurons and previously reported K_D for pyronic (San Martín *et al.*, 2014) [Addendum Figure N°1C]. In this context, mitochondrial pyruvate consumption rate was calculated using the slope of mTFP/Venus ratio decrease immediately after MCTs inhibition in soma and axons of disaggregated DRG neurons [Addendum Figure N°1E].

We found that soma of disaggregated DRG neurons have a mean mitochondrial pyruvate consumption rate of $0,07 \mu\text{M/s}$ ($n= 35$) and axons have a mean mitochondrial pyruvate consumption rate of $0,08 \mu\text{M/s}$ ($n=12$) that are not significantly different under these treatments [Addendum Figure N°13A].

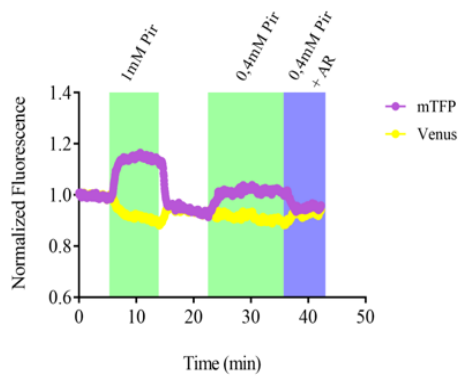
A



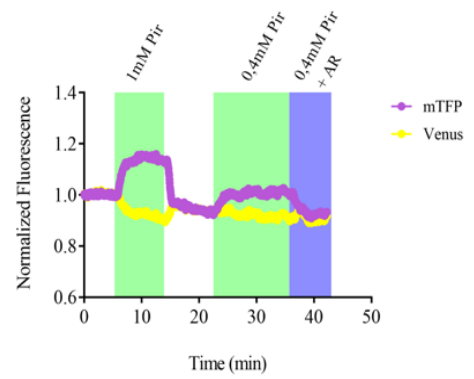
B



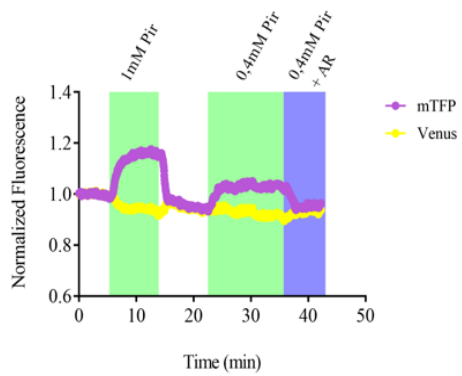
C



D



E

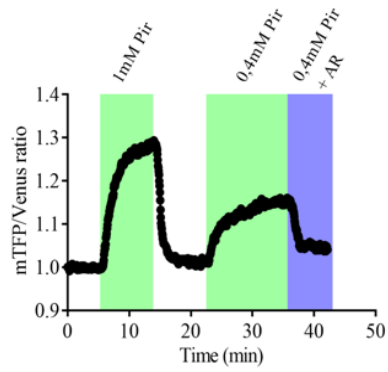


ADDENDUM FIGURE N°7. Pyronic Fluorescence Intensity in Disaggregated DRG Neurons Soma during MCTs Inhibition. (A), (B), (C), (D), (E): Examples of time lapse registration of mTFP (violet) and Venus (yellow) fluorescence intensity in soma of disaggregated DRG neurons in presence of pyruvate and/or MCTs inhibitor. mTFP and Venus were excited at 430nm and registered at 485nm and 528nm respectively in soma of disaggregated DRG neurons expressing pyronic.

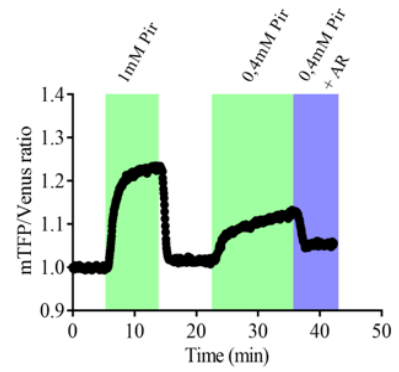
mTFP and Venus fluorescence intensities were registered continuously in soma of disaggregated DRG neurons while treatments were superfused sequentially as follows: (1) pyruvate concentration was zero until steady state (white background); (2) 1mM pyruvate until steady state (green background); (3) pyruvate concentration was dropped to zero again until steady state (white background); (4) 0,4 mM pyruvate until steady state; (5) 0,4 mM pyruvate and MCTs inhibition with 1 μ M AR-C155858 (cyan background). mTFP or Venus fluorescence was normalized by background mTFP or Venus channels fluorescence. Subsequently, background normalized mTFP or Venus fluorescence was normalized by mTFP or Venus fluorescence values in the first 3s of registration (control fluorescence).

Exposure of pyronic to pyruvate in soma of disaggregated DRG neurons caused an increase in mTFP fluorescence intensity and a decrease in Venus fluorescence intensity, consistent with a decrease in FRET efficiency. Furthermore, MCTs inhibition in presence of pyruvate, caused a decrease in mTFP fluorescence intensity and an increase in Venus fluorescence intensity, consistent with an increase in FRET efficiency due to mitochondrial pyruvate consumption.

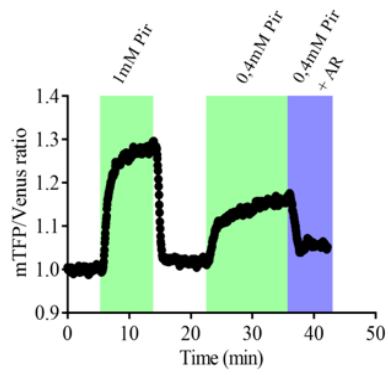
A



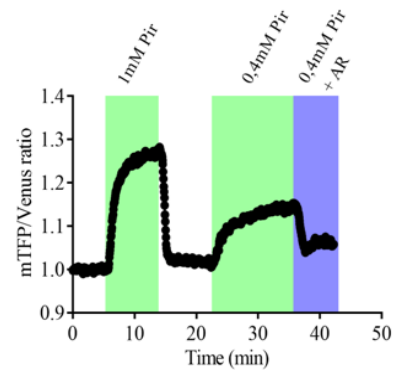
B



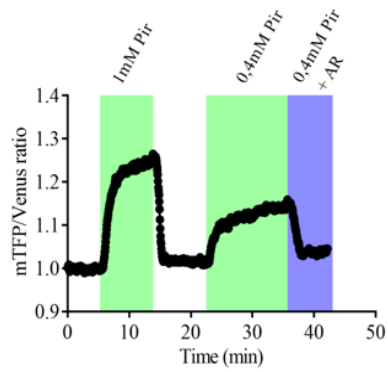
C



D



E

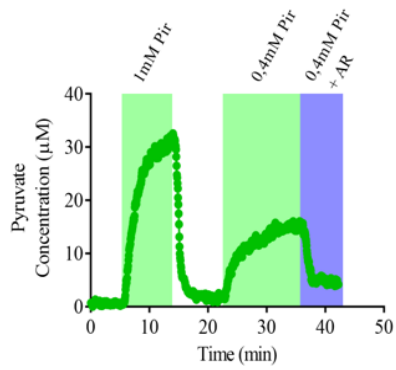


ADDENDUM FIGURE N°8. Pyronic FRET Efficiency in Disaggregated DRG Neurons Soma during MCTs Inhibition. (A), (B), (C), (D), (E): Examples of time lapse of mTFP (violet) and Venus (yellow) estimated fluorescence ratio in soma of disaggregated DRG neurons in presence of pyruvate and/or MCTs inhibitor. mTFP/Venus fluorescence ratio (R_x) was estimated after normalizations. mTFP or Venus fluorescence was normalized by background mTFP or Venus channels fluorescence. Subsequently, background normalized mTFP or Venus fluorescence was normalized by mTFP or Venus fluorescence values in the first 3s of registration (control fluorescence). R_0 is the ratio in the absence of pyruvate and ΔR_{\max} is the difference between R_0 and the maximum ratio estimated in 1 mM pyruvate.

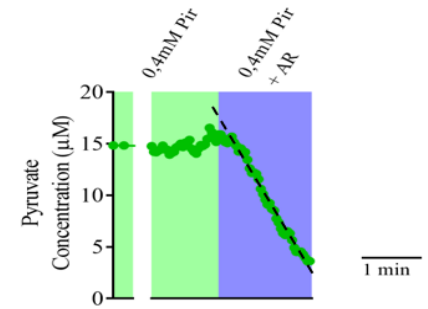
mTFP/ Venus ratio was estimated from data of disaggregated DRG neurons soma while treatments were superfused sequentially as follows: (1) pyruvate concentration was zero until steady state (white background); (2) 1mM pyruvate until steady state (green background); (3) pyruvate concentration was dropped to zero again until steady state (white background); (4) 0,4 mM pyruvate until steady state; (5) 0,4 mM pyruvate and MCTs inhibition with 1 μ M AR-C155858 (cyan background).

Exposure of pyronic to pyruvate in soma of disaggregated DRG neurons caused an increase in mTFP/Venus ratio consistent with a decrease in FRET efficiency, suggesting pyronic is functional in our experimental model. Furthermore, MCTs inhibition in presence of pyruvate, caused a decrease in mTFP/Venus ratio consistent with an increase in FRET efficiency due to mitochondrial pyruvate consumption.

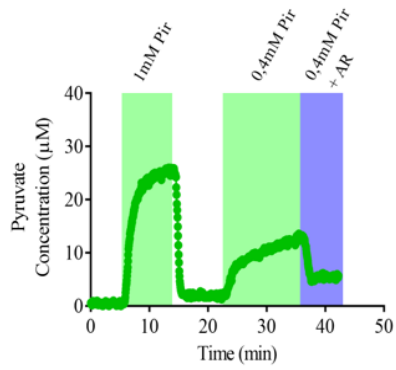
A



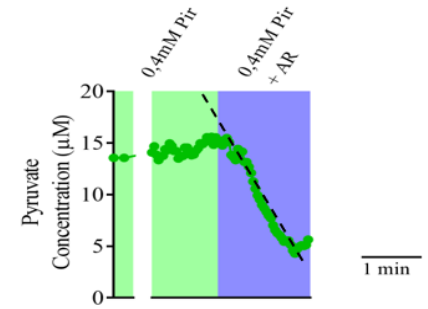
A'



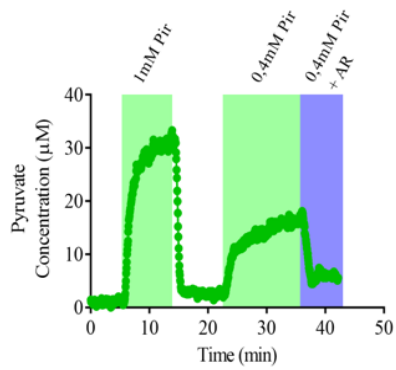
B



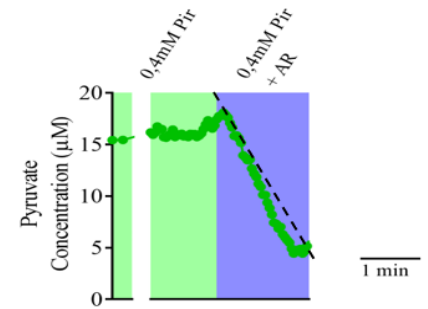
B'



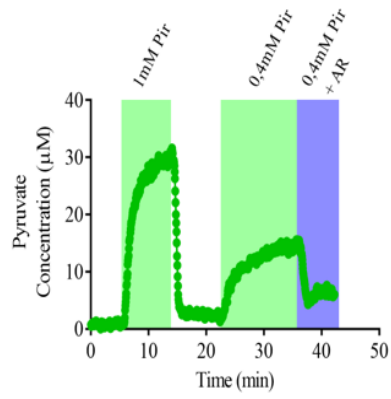
C



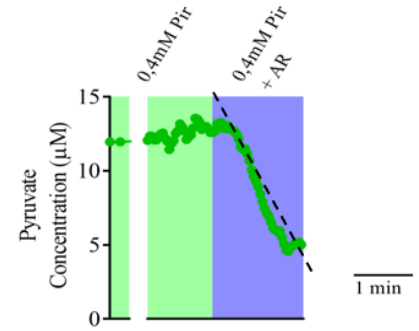
C'



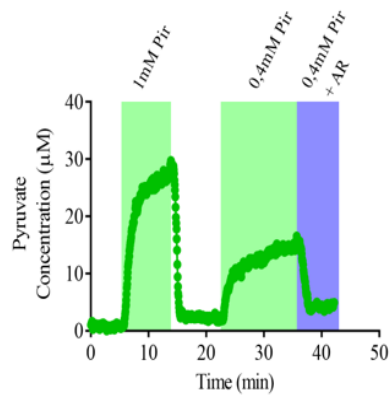
D



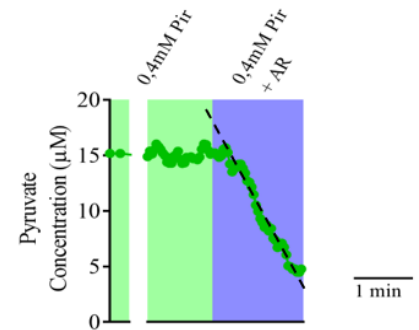
D'



E



E'



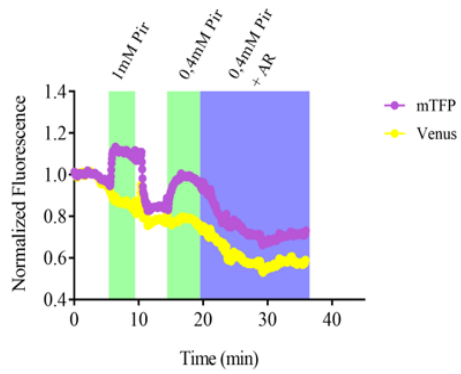
ADDENDUM FIGURE N°9. Mitochondrial Pyruvate Consumption Rate in Soma of Disaggregated DRG Neurons. (A), (B), (C), (D), (E): Examples of pyruvate concentration estimated in soma of disaggregated DRG neurons in presence of pyruvate and/or MCTs inhibitor. The value of the mTFP/ Venus ratio at each time point minus R_0 , ΔR , was transformed into pyruvate concentration in mM using the measured ΔR_{\max} and the K_D previously reported *in vitro* (107 μM) (San Martín *et al.*, 2014).

Pyruvate concentration was estimated from data of disaggregated DRG neurons soma while treatments were superfused sequentially as follows: (1) pyruvate concentration was zero until steady state (white background); (2) 1mM pyruvate until steady state (green background); (3) pyruvate concentration was dropped to zero again until steady state (white background); (4) 0,4 mM pyruvate until steady state; (5) 0,4 mM pyruvate and MCTs inhibition with 1 μM AR-C155858 (cyan background).

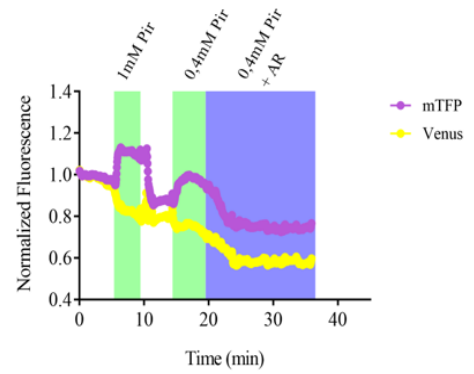
Exposure of pyronic to pyruvate in soma of disaggregated DRG neurons caused an increase in estimated pyruvate concentration suggesting pyronic senses changes in the concentration of pyruvate in the range of μM under our experimental conditions. Furthermore, MCTs inhibition in presence of pyruvate, caused a decrease estimated pyruvate concentration consistent with sensibility to pyruvate concentration changes produced by mitochondrial pyruvate consumption.

(A'), (B'), (C'), (D'), (E'): Mitochondrial pyruvate consumption rate in (A), (B), (C), (D), (E), respectively. Mitochondrial pyruvate consumption rate (dashed black line) in disaggregated DRG neurons soma was determined as the rate of decrease in pyruvate concentration immediately after inhibition of pyruvate transport by 1 μM AR-C155858 (cyan background), by calculating the linear regression slope adjusted to the first 10 data points after MCTs inhibition.

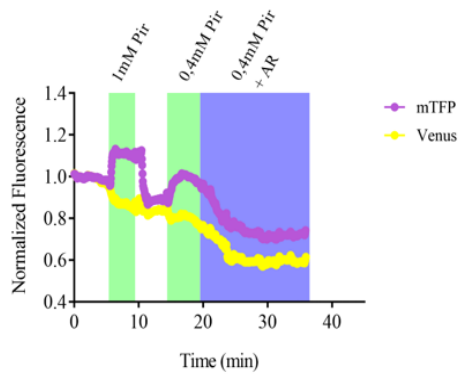
A



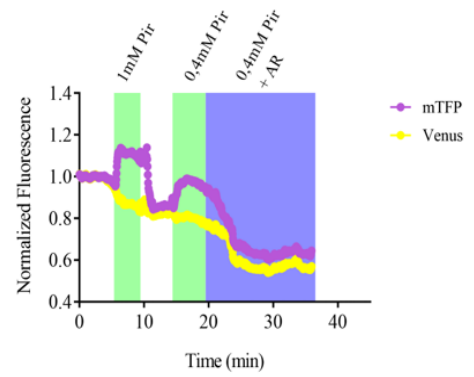
B



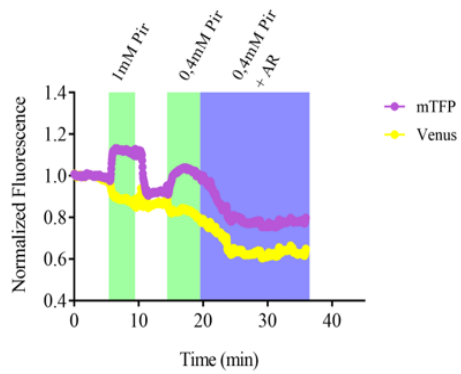
C



D



E

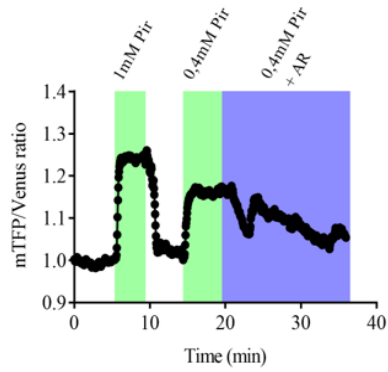


ADDENDUM FIGURE N°10. Pyronic Fluorescence Intensity in Disaggregated DRG Neurons Axons during MCTs Inhibition. (A), (B), (C), (D), (E): Examples of time lapse registration of mTFP (violet) and Venus (yellow) fluorescence intensity in axons of disaggregated DRG neurons in presence of pyruvate and/or MCT inhibitor.

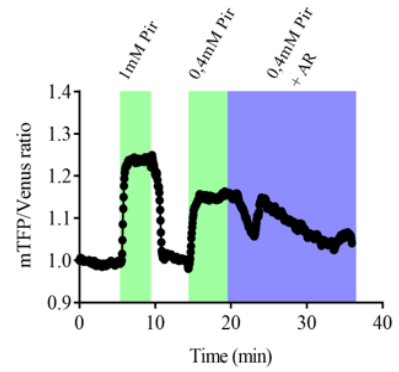
mTFP and Venus were excited at 430nm and registered at 485nm and 528nm respectively in axons of disaggregated DRG neurons expressing pyronic. mTFP and Venus fluorescence intensities were registered continuously in axons of disaggregated DRG neurons while treatments were superfused sequentially as follows: (1) pyruvate concentration was zero until steady state (white background); (2) 1mM pyruvate until steady state (green background); (3) pyruvate concentration was dropped to zero again until steady state (white background); (4) 0,4 mM pyruvate until steady state; (5) 0,4 mM pyruvate and MCTs inhibition with 1 μ M AR-C155858 (cyan background). mTFP or Venus fluorescence was normalized by background mTFP or Venus channels fluorescence. Subsequently, background normalized mTFP or Venus fluorescence was normalized by mTFP or Venus fluorescence values in the first 3s of registration (control fluorescence).

Exposure of pyronic to pyruvate in axons of disaggregated DRG neurons caused an increase in mTFP fluorescence intensity and a decrease in Venus fluorescence intensity, consistent with a decrease in FRET efficiency. Furthermore, MCTs inhibition in presence of pyruvate, caused a decrease in mTFP fluorescence intensity and an increase in Venus fluorescence intensity, consistent with an increase in FRET efficiency due to mitochondrial pyruvate consumption.

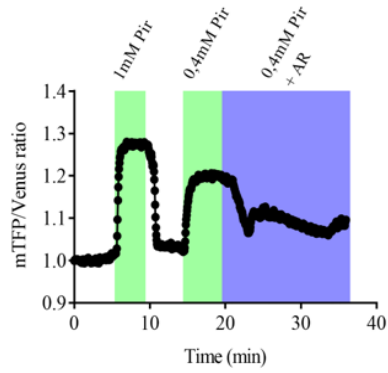
A



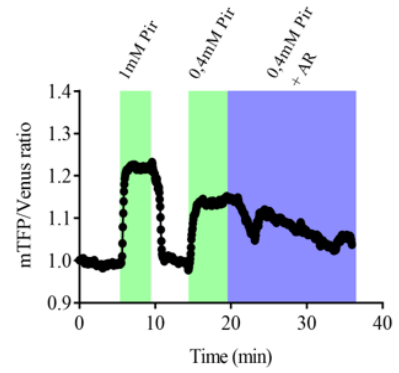
B



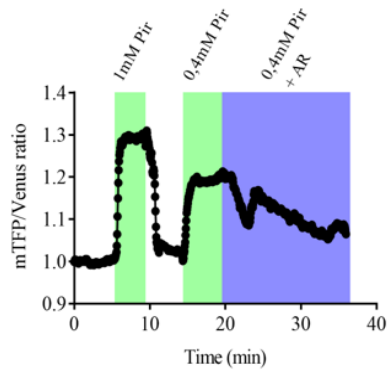
C



D



E

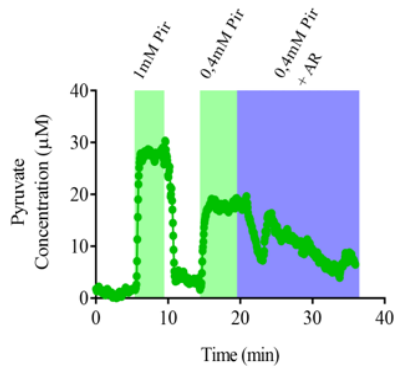


ADDENDUM FIGURE N°11. Pyronic FRET Efficiency in Disaggregated DRG Neurons Axons during MCTs Inhibition. (A), (B), (C), (D), (E): Examples of time lapse of mTFP (violet) and Venus (yellow) estimated ratio in axons of disaggregated DRG neurons in presence of pyruvate and/or MCTs inhibitor. mTFP/ Venus fluorescence ratio (R_x) was determined after normalizations. mTFP or Venus fluorescence was normalized by background mTFP or Venus channels fluorescence. Subsequently, background normalized mTFP or Venus fluorescence was normalized by mTFP or Venus fluorescence values in the first 3s of registration (control fluorescence). R_0 is the ratio in the absence of pyruvate and ΔR_{\max} is the difference between R_0 and the maximum ratio estimated in 1 mM pyruvate.

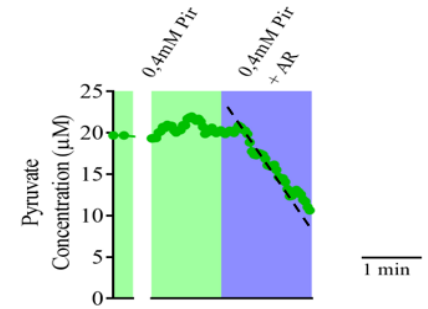
mTFP/ Venus ratio was estimated from data of disaggregated DRG neurons axons while treatments were superfused sequentially as follows: (1) pyruvate concentration was zero until steady state (white background); (2) 1mM pyruvate until steady state (green background); (3) pyruvate concentration was dropped to zero again until steady state (white background); (4) 0,4 mM pyruvate until steady state; (5) 0,4 mM pyruvate and MCTs inhibition with 1 μ M AR-C155858 (cyan background).

Exposure of pyronic to pyruvate in axons of disaggregated DRG neurons caused an increase in mTFP/Venus estimated ratio consistent with a decrease in FRET efficiency, suggesting pyronic is functional in our experimental model. Furthermore, MCTs inhibition in presence of pyruvate, caused a decrease in mTFP/Venus estimated ratio consistent with an increase in FRET efficiency due to mitochondrial pyruvate consumption.

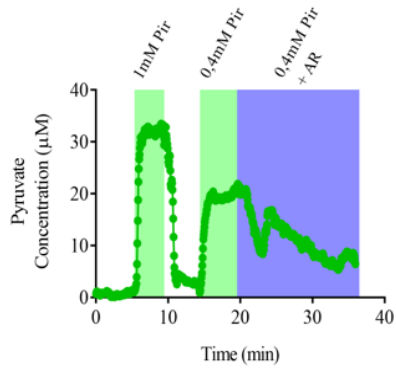
A



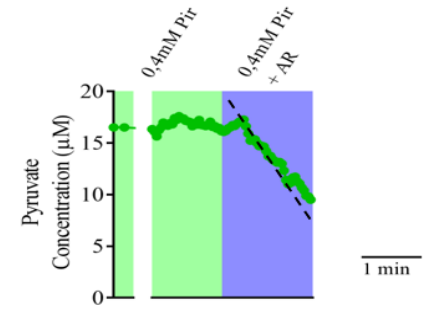
A'



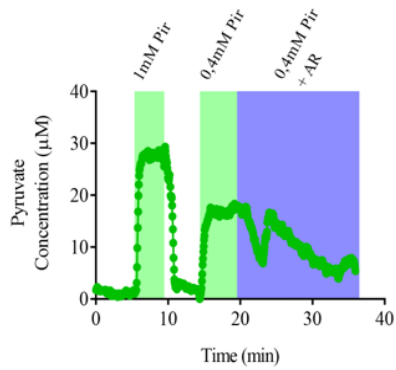
B



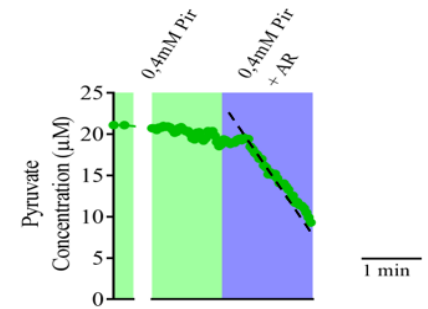
B'



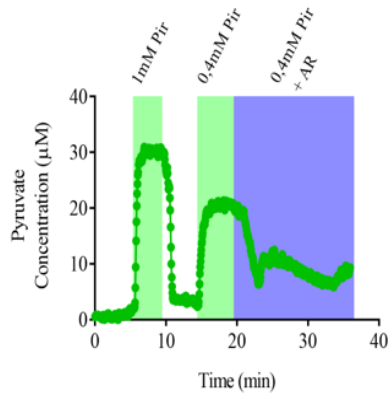
C



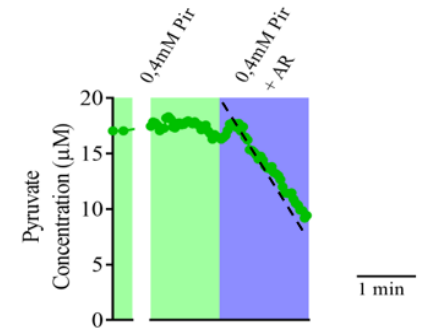
C'



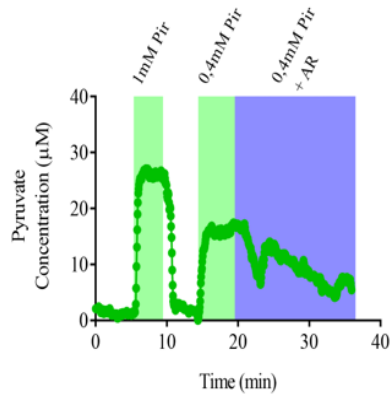
D



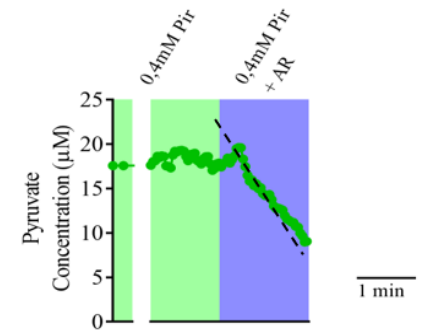
D'



E



E'

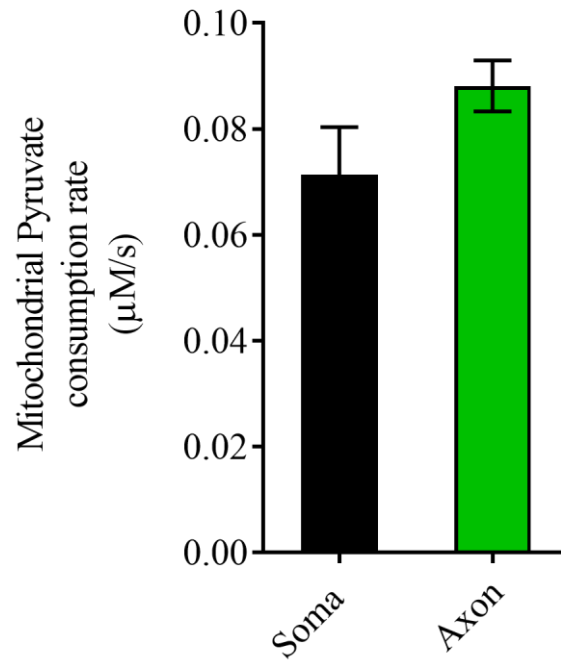


ADDENDUM FIGURE N°12. Mitochondrial Pyruvate Consumption Rate in Axons of Disaggregated DRG Neurons. (A), (B), (C), (D), (E): Examples of pyruvate concentration estimated in axons of disaggregated DRG neurons in presence of pyruvate and/or MCTs inhibitor. The value of the mTFP/ Venus ratio at each time point minus R_0 , ΔR , was transformed into pyruvate concentration in mM using the measured ΔR_{max} and the K_D previously reported *in vitro* (107 μ M) (San Martín *et al.*, 2014).

Pyruvate concentration was estimated from data of disaggregated DRG neurons axons while treatments were superfused sequentially as follows: (1) pyruvate concentration was zero until steady state (white background); (2) 1mM pyruvate until steady state (green background); (3) pyruvate concentration was dropped to zero again until steady state (white background); (4) 0,4 mM pyruvate until steady state; (5) 0,4 mM pyruvate and MCTs inhibition with 1 μ M AR-C155858 (cyan background).

Exposure of pyronic to pyruvate in axons of disaggregated DRG neurons caused an increase in estimated pyruvate concentration suggesting pyronic senses changes in the concentration of pyruvate in the range of μ M under our experimental conditions. Furthermore, MCTs inhibition in presence of pyruvate, caused a decrease estimated pyruvate concentration consistent with sensibility to pyruvate concentration changes produced by mitochondrial pyruvate consumption.

(A'), (B'), (C'), (D'), (E'): Mitochondrial pyruvate consumption rate in (A), (B), (C), (D), (E), respectively. Mitochondrial pyruvate consumption rate (dashed black line) in disaggregated DRG neurons axons was determined as the rate of decrease in pyruvate concentration immediately after inhibition of pyruvate transport by 1 μ M AR-C155858 (cyan background), by calculating the linear regression slope adjusted to the first 10 data points after MCTs inhibition.



ADDENDUM FIGURE N°13. Mitochondrial Pyruvate Consumption Rate in Soma and Axons of Disaggregated DRG Neurons. (A) Mitochondrial pyruvate consumption mean rate in 35 soma (black bar) and 12 axons (green bar) of disaggregated DRG neurons was determined as the rate of decrease in pyruvate concentration immediately after inhibition of pyruvate transport by 1 μM AR-C155858 (cyan background), by calculating the linear regression slope adjusted to the first 10 data points after MCTs inhibition.

There were no significant differences between mitochondrial pyruvate consumption rate in soma and axons of disaggregated DRG neurons.

n soma= 35; n axons =17; unpaired t test between mean mitochondrial pyruvate consumption rate in soma and axons. SEM.

23.5 Glycolytic Rates in Soma and Axons of Disaggregated DRG Neurons.

To compare the glycolytic rates between soma and axons, we induced the expression of FLII12Pglu600 $\mu\Delta 6$ protein (glucose sensor) in disaggregated DRG neurons after 7 days of culture [Addendum Figure N°2A]. Consequently, a protocol of glycolytic dynamics was performed in disaggregated DRG neurons measuring CFP and YFP (FLII12Pglu600 $\mu\Delta 6$ protein FRET pair) fluorescence intensity in soma and axons under constant superfusion [Addendum Figure N°2B].

We found that fluorescence intensity of CFP and YFP was stable in presence of 5 mM glucose and 1 mM lactate in soma and axons of disaggregated DRG neurons [Addendum Figure N°14 and Addendum Figure N°16]. Consequently, YFP/CFP ratio remained in a basal steady state in soma and axons under these treatments [Addendum Figure N°14 and Addendum Figure N°17].

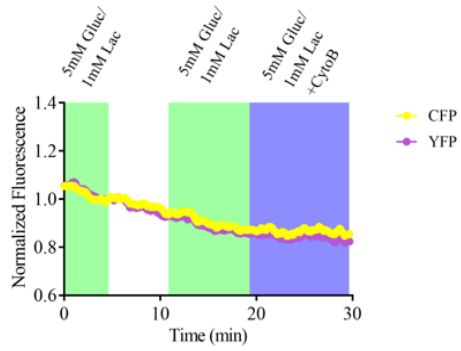
Interestingly, we found that when glucose and lactate concentration was dropped to zero, CFP or YFP fluorescence intensity remained stable in soma of disaggregated DRG neurons [Addendum Figure N°14]. Thus YFP/CFP ratio remained in basal steady state, in absence of glucose and lactate [Addendum Figure N°15]. After, disaggregated DRG neurons were superfused with 5mM glucose and 1 mM lactate again, and CFP or YFP fluorescence intensity remained stable in somas [Addendum Figure N°14]. Finally, CFP or YFP fluorescence intensity remained at basal levels after inhibition of glucose transport by superfusion of 20 μ M Cytochalasin B in soma of dissaggregated DRG neurons [Addendum Figure N°14].

Consequently, YFP/CFP ratio was unaffected in soma under glucose transport inhibition [Addendum Figure N°15].

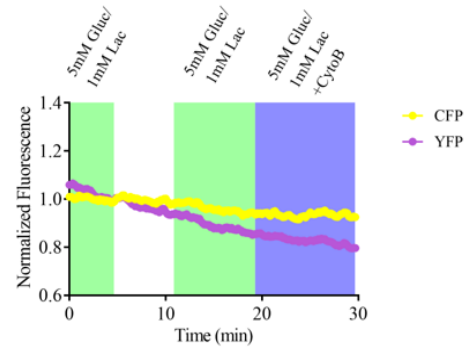
Notably, we found that when glucose and lactate concentration was dropped to zero, there was a decrease in CFP fluorescence intensity and an increase in YFP fluorescence intensity in axons of disaggregated DRG neurons [Addendum Figure N°16]. Consequently, YFP/CFP ratio decreased until a new steady state was established (below the basal steady state) in axons [Addendum Figure N°17]. After, superfusion of 5 mM glucose and 1 mM lactate again induced an increase in CFP fluorescence intensity and a decrease in YFP fluorescence intensity in axons of disaggregated DRG neurons [Addendum Figure N°16]. Thus, YFP/CFP ratio increased, and basal steady state was reached again in axons [Addendum Figure N°17]. Finally, inhibition of glucose transport in axons by superfusion of 20 μ M Cytochalasin B induced a significant decrease in CFP fluorescence intensity and an increase in YFP fluorescence intensity [Addendum Figure N°16]. Consequently, YFP/CFP ratio decreased until a new steady state was established (below the basal steady state) [Addendum Figure N°17].

Glycolytic rate was calculated from YFP/CFP ratio of disaggregated DRG neurons soma and axons as the slope of YFP/CFP ratio decrease immediately after glucose transport inhibition [Addendum Figure N°2D]. We found significant differences between glycolytic rates of soma (n=9) and axons (n=5) in disaggregated DRG neurons under that treatment [Addendum Figure N°18].

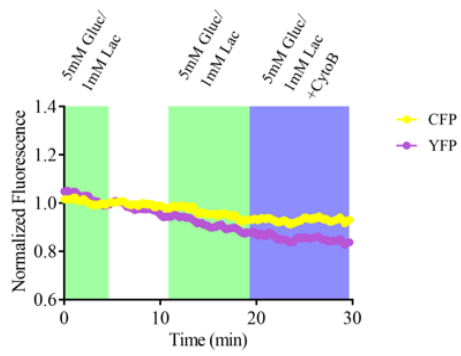
A



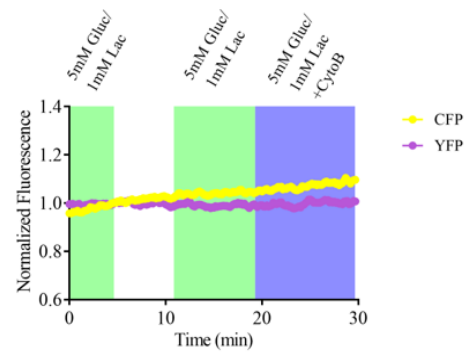
B



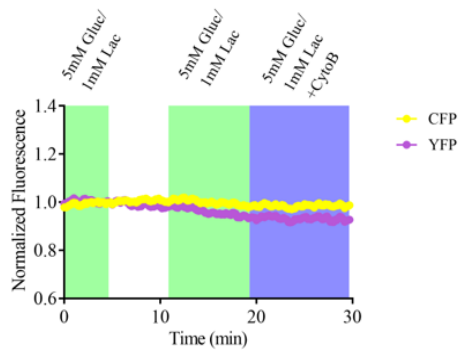
C



D



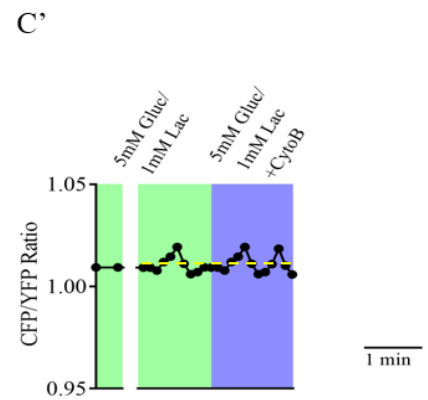
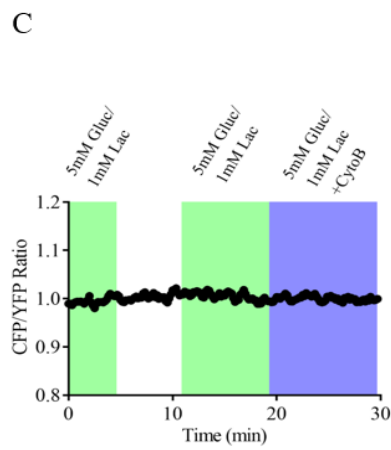
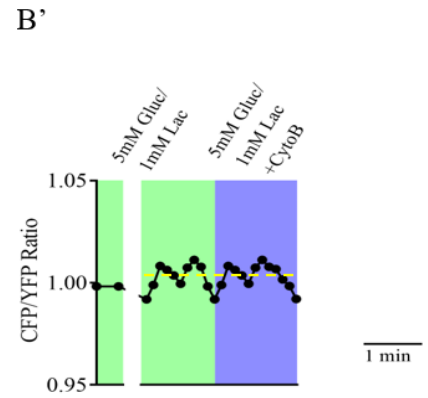
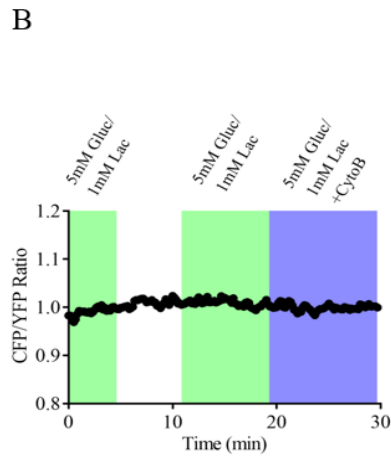
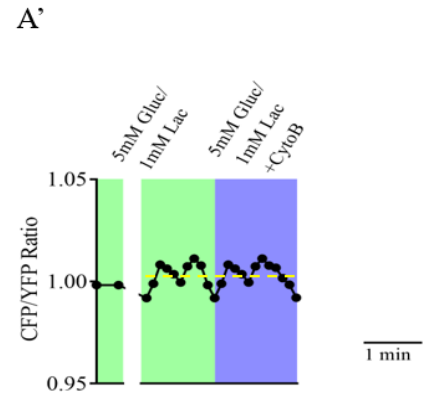
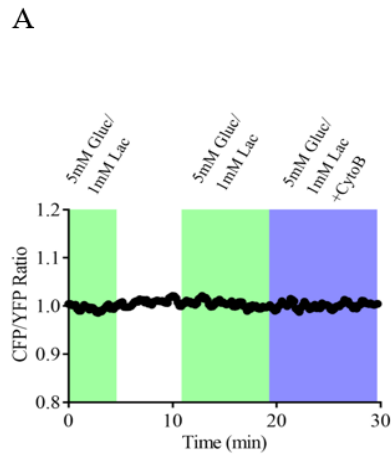
E



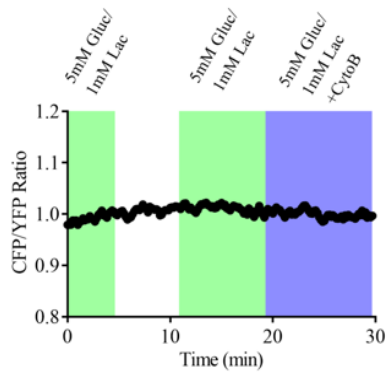
ADDENDUM FIGURE N°14. FLII12Pglu600 mΔ6 Fluorescence Intensity in Disaggregated DRG Neurons Soma during Glucose Transport Inhibition. (A), (B), (C), (D), (E): Examples of time lapse registration of YFP (violet) and CFP (yellow) fluorescence intensity in soma of disaggregated DRG neurons in presence of glucose and/or glucose transport inhibitor. YFP and CFP were imaged at 488 excitation/505-550 nm emission (for YFP/CFP) and 543 excitation/>580 nm emission (for Alexa Fluor 568) in soma of disaggregated DRG neurons expressing FLII12Pglu600 mΔ6.

YFP and CFP fluorescence intensities were registered continuously in soma of disaggregated DRG neurons while treatments were superfused sequentially as follows: (1) 5 mM glucose and 1 mM lactate until steady state (white background); (2) glucose and lactate concentration dropped to zero until steady state (green background); (3) 5 mM glucose and 1 mM lactate again until steady state (white background); (4) glucose transport inhibition with 20 μM Cytochalasin B (cyan background). YFP or CFP fluorescence was normalized by background YFP or CFP channels fluorescence. Subsequently, background normalized YFP or CFP fluorescence was normalized by YFP or CFP fluorescence values in the first 3s of registration (control fluorescence).

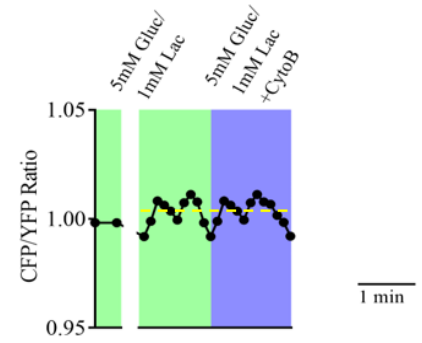
YFP or CFP fluorescence intensity remained steady during exposure of FLII12Pglu600 mΔ6 to glucose or glucose transport inhibition in soma of disaggregated DRG neurons.



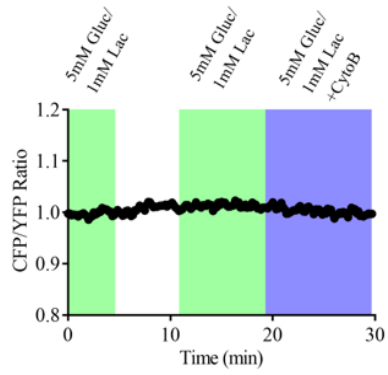
D



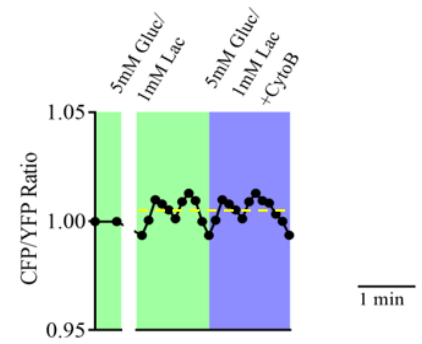
D'



E



E'



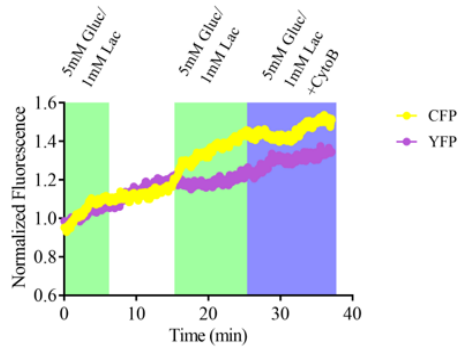
ADDENDUM FIGURE N°15. Glycolytic Rate in Soma of Disaggregated DRG Neurons. (A), (B), (C), (D), (E): Examples of time lapse of YFP (violet) and CFP (yellow) estimated ratio in soma of disaggregated DRG neurons in presence of glucose and/or glucose transport inhibitor. YFP/ CFP fluorescence ratio (R_x) was determined after normalizations. YFP or CFP fluorescence was normalized by background YFP or CFP channels fluorescence. Subsequently, background normalized YFP or CFP fluorescence was normalized by YFP or CFP fluorescence values in the first 3s of registration (control fluorescence). R_0 is the ratio in the absence of glucose and ΔR_{\max} is the difference between R_0 and the maximum ratio estimated in 5 mM glucose and 1 mM lactate.

YFP/ CFP ratio was estimated from data of disaggregated DRG neurons axons while treatments were superfused sequentially as follows: (1) 5 mM glucose and 1 mM lactate until steady state (white background); (2) glucose and lactate concentration dropped to zero until steady state (green background); (3) 5 mM glucose and 1 mM lactate again until steady state (white background); (4) glucose transport inhibition with 20 μ M Cytochalasin B (cyan background).

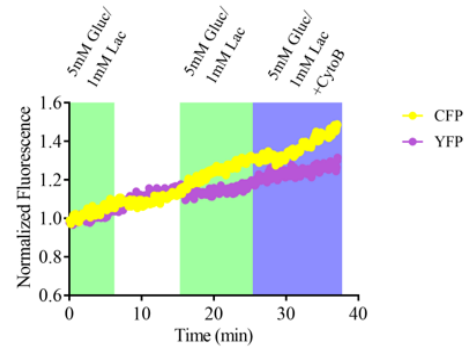
(A'), (B'), (C'), (D'), (E'): Glycolytic rate in (A), (B), (C), (D), (E), respectively. Glycolytic rate (dashed yellow line) in disaggregated DRG neurons soma was determined as the rate of decrease in YFP/CFP ratio immediately after inhibition of glucose transport by 20 μ M Cytochalasin B (cyan background), by calculating the linear regression slope adjusted to the first 10 data points after glucose transport inhibition.

YFP/CFP estimated ratio remained steady during exposure of FLII12Pglu600 m Δ 6 to glucose or glucose transport inhibition in soma of disaggregated DRG neurons.

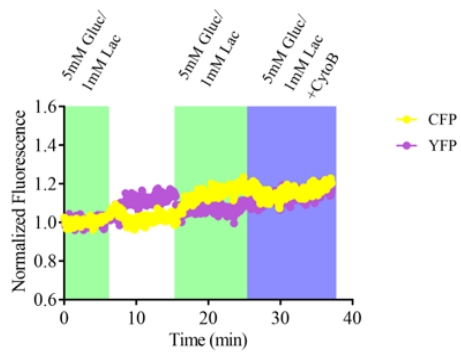
A



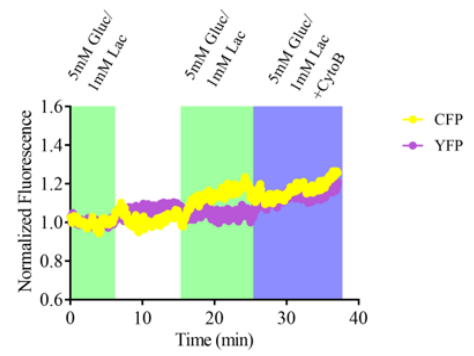
B



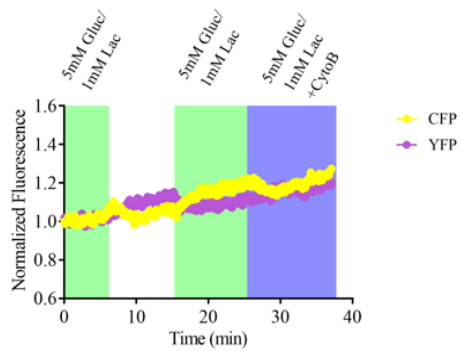
C



D



E



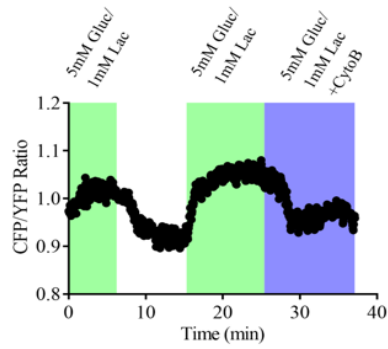
ADDENDUM FIGURE N°16. FLII12Pglu600 mΔ6 Fluorescence Intensity in Disaggregated DRG Neurons Axons during Glucose Transport Inhibition. (A), (B), (C), (D), (E): Examples of time lapse registration of YFP (violet) and CFP (yellow) fluorescence intensity in axons of disaggregated DRG neurons in presence of glucose and/or glucose transport inhibitor. YFP and CFP were imaged at 488 excitation/505-550 nm emission (for YFP/CFP) and 543 excitation/>580 nm emission (for Alexa Fluor 568) in axons of disaggregated DRG neurons expressing FLII12Pglu600 mΔ6.

YFP and CFP fluorescence intensities were registered continuously in axons of disaggregated DRG neurons while treatments were superfused sequentially as follows: (1) 5 mM glucose and 1 mM lactate until steady state (white background); (2) glucose and lactate concentration dropped to zero until steady state (green background); (3) 5 mM glucose and 1 mM lactate again until steady state (white background); (4) glucose transport inhibition with 20 μM Cytochalasin B (cyan background). YFP or CFP fluorescence was normalized by background YFP or CFP channels fluorescence. Subsequently, background normalized YFP or CFP fluorescence was normalized by YFP or CFP fluorescence values in the first 3s of registration (control fluorescence).

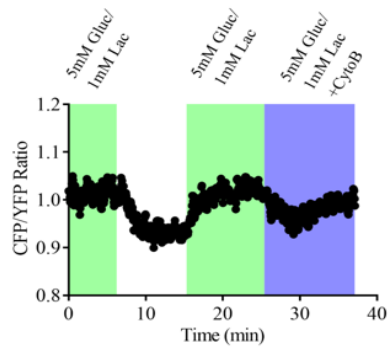
FLII12Pglu600 mD6 exposure to zero glucose caused a decrease in CFP fluorescence intensity and an increase in YFP fluorescence intensity, consistent with an increase in FRET efficiency. After This, superfusion 5mM glucose and 1 mM lactate caused an increase in CFP fluorescence intensity and a decrease in YFP fluorescence intensity, consistent with a decrease in FRET efficiency.

Furthermore, glucose transport inhibition, caused a decrease in CFP fluorescence intensity and an increase in YFP fluorescence intensity, consistent with an increase in FRET efficiency due to glucose consumption in axons.

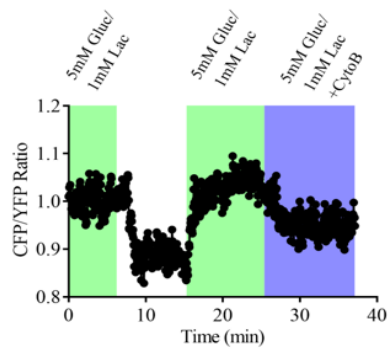
A



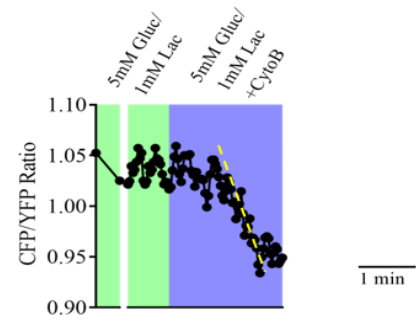
B



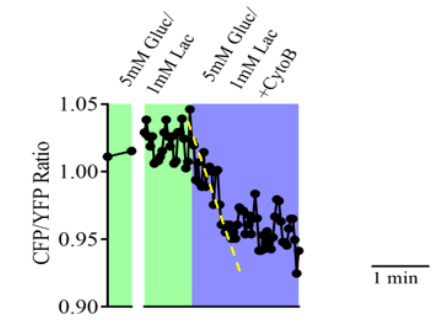
C



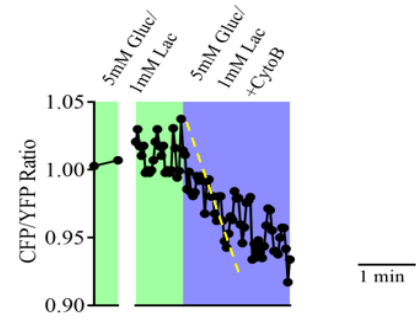
A'



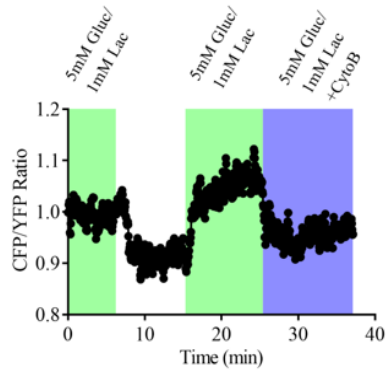
B'



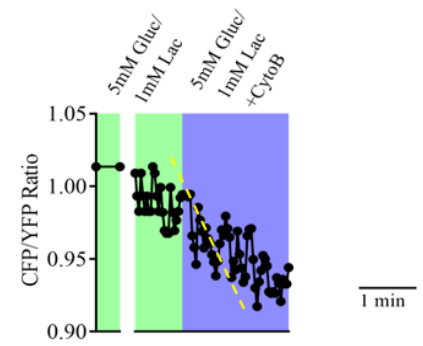
C'



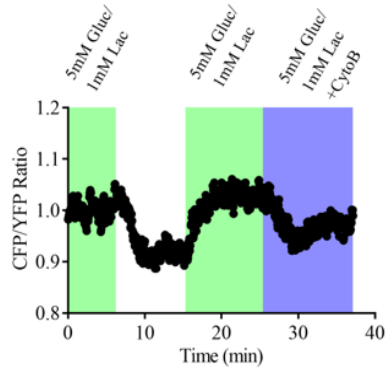
D



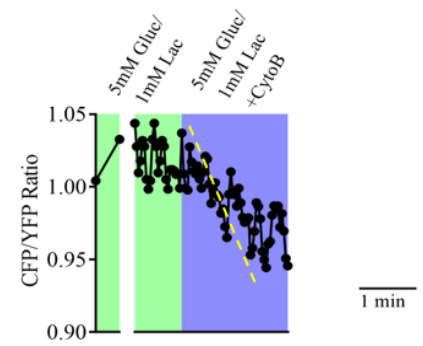
D'



E



E'

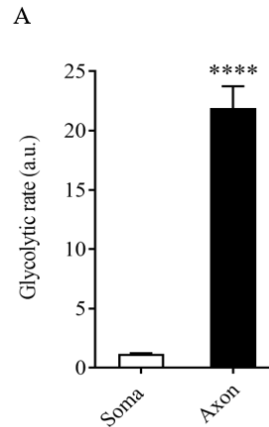


ADDENDUM FIGURE N°17. Glycolytic Rate in Axons of Disaggregated DRG Neurons. (A), (B), (C), (D), (E): Examples of time lapse of YFP (violet) and CFP (yellow) estimated ratio in axons of disaggregated DRG neurons in presence of glucose and/or glucose transport inhibitor. YFP/ CFP fluorescence ratio (R_x) was determined after normalizations. YFP or CFP fluorescence was normalized by background YFP or CFP channels fluorescence. Subsequently, background normalized YFP or CFP fluorescence was normalized by YFP or CFP fluorescence values in the first 3s of registration (control fluorescence). R_0 is the ratio in the absence of glucose and ΔR_{\max} is the difference between R_0 and the maximum ratio estimated in 5 mM glucose and 1 mM lactate.

YFP/ CFP ratio was estimated from data of disaggregated DRG neurons axons while treatments were superfused sequentially as follows: (1) 5 mM glucose and 1 mM lactate until steady state (white background); (2) glucose and lactate concentration dropped to zero until steady state (green background); (3) 5 mM glucose and 1 mM lactate again until steady state (white background); (4) glucose transport inhibition with 20 μ M Cytochalasin B (cyan background).

(A'), (B'), (C'), (D'), (E'): Glycolytic rate in (A), (B), (C), (D), (E), respectively. Glycolytic rate (dashed yellow line) in disaggregated DRG neurons axons was determined as the rate of decrease in YFP/CFP ratio immediately after inhibition of glucose transport by 20 μ M Cytochalasin B (cyan background), by calculating the linear regression slope adjusted to the first 10 data points after glucose transport inhibition.

FLII12Pglu600 mD6 exposure to zero glucose transport inhibition caused a decrease in YFP/CFP ratio, consistent with a decrease in FRET efficiency. After This, superfusion of 5mM glucose and 1 mM lactate caused an increase in YFP/CFP ratio consistent with an increase in FRET efficiency due to crescent levels of glucose in axons. Furthermore, glucose transport inhibition, caused a decrease YFP/CFP ratio, consistent with an increase in FRET efficiency due to glucose consumption in axons.



ADDENDUM FIGURE N°18. Glycolytic Rate in Soma and Axons of Disaggregated DRG Neurons. (A) Glycolytic mean rate in 9 soma (white bar) and 5 axons (black bar) disaggregated DRG neurons was determined as the rate of decrease in YFP/CFP immediately after inhibition of glucose transport by 20 μ M Cytochalasin B (cyan background), by calculating the linear regression slope adjusted to the first 10 data points after glucose transport inhibition. Glycolytic rate was significantly higher in axons than in soma of disaggregated DRG neurons.

n soma= 9; n axons =5; unpaired t test between mean glycolytic rate in soma and axons. SEM.

24. ADDENDUM DISCUSSION.

In this thesis addendum, we explored potential differences between the physiology of soma and axons of DRG neurons, with a special focus on metabolic fluxes. Specifically, we compared: cytosolic calcium levels during activity, glucose and pyruvate transporters distribution, glycolytic rates and mitochondrial pyruvate consumption rates, in soma and axons of disaggregated DRG neurons.

The preliminary results of this thesis addendum suggest that there are significant differences in the cytosolic calcium levels during activity, the distribution of glucose and pyruvate transporters and glycolytic rates between soma and axons of disaggregated DRG neurons *in vitro*.

24.1 Glucose and Pyruvate Transporters Distribution in Soma and Axons of Disaggregated DRG Neurons.

Glucose transport is facilitated largely via the Glucose transporters (Gluts), and sodium-driven sugar cotransporters (Nijland *et al.*, 2014; Szablewski, 2017). In this context, it has been reported that mammal's sensory neurons express Gluts *in vivo* (Szablewski, 2017). Specifically, soma of rat dorsal root ganglia (DRGs) neurons express Glut1 and axons at the spinal nerve express Glut1 and Glut3 (Nijland *et al.*, 2014; Szablewski, 2017). Glut2 has been reported in soma and axons at different areas of the brain, but its distribution has not been explored in dorsal root ganglia (Arluison, *et al.*, 2004; Szablewski, 2017).

As a preliminary result, we focused on the general exploration of presence or absence of glucose transporters in soma or axons of disaggregated DRG neurons, beside the potential role of each specific transporter and its kinetics on DRG neurons energetic metabolism, which is beyond the scope of this thesis addendum. Based on this, we considered the references about the *in vitro* and *in vivo* presence of glucose transporters in DRG neurons (Domenech-Estevez *et al.*, 2015; Nijland *et al.*, 2014; Szablewski, 2017; Arluison *et al.*, 2004) in relationship with our technical availability at the time these preliminary results were generated.

Considering this, we characterized for the first time, the distribution of Glut2 in disaggregated DRG neurons, we performed immunofluorescence against this glucose transporter and qualitatively evaluated its presence in soma and axons after 7 days of culture [Addendum Figure N°3]. We found that Glut2 is expressed in disaggregated DRG neurons and distributed

mostly in soma [Addendum Figure N°3]. Under these conditions, Glut2 was absent in axons of disaggregated DRG neurons [Addendum Figure N°3]. This suggests that glucose transport into soma of disaggregated DRG neurons is facilitated by Glut2. Further evidence is needed to confirm *in vivo* reported distribution of Glut1 and Glut3 in *in vitro* DRG neurons. Exploration of this would be relevant to elucidate the mechanism of delivery of glucose into soma of DRG neurons *in vitro* and thus, potential differences in the availability of glucose between soma and axons in this experimental model.

On the other hand, pyruvate transport is facilitated by Monocarboxylate transporters (MCTs) and sodium coupled Monocarboxylate transporters (SCMTs) in the central nervous system of mammals (Nijland *et al.*, 2014). In this context, MCTs facilitate the transport of lactate and pyruvate with a higher affinity for lactate (Nijland *et al.*, 2014). Specifically, in the peripheral nervous system, it has been reported that a subset of mice sensory neurons express MCT1 at ganglia (soma) and nodes of myelinated nerve fibers (axons) (Domenech-Estevéz *et al.*, 2015).

To characterize, for the first time, the distribution of MCT1 and MCT2 in disaggregated DRG neurons *in vitro*, we performed immunofluorescence against these Monocarboxylate transporters and qualitatively evaluated their presence in soma and axons after 7 days of culture [Addendum Figure N°4 and Addendum Figure N°5]. We found that MCT1 was present mostly in soma of disaggregated DRG neurons [Addendum Figure N°4]. Considering this, distribution of MCT1 could be different in *in vivo* and *in vitro* models of DRG neurons. Furthermore, as we mentioned before, MCT1 has been reported in axons of myelinated DRG neurons. Consequently, absence of Schwann Cells in our *in vitro* model of disaggregated DRG

neurons could influence the distribution of MCT1.

Moreover, we found that MCT2 was distributed along soma and axons of disaggregated DRG neurons [Addendum Figure N°5]. To our knowledge, this is the first time MCT2 is reported in neurons of the peripheral nervous system. Further evidence is needed to elucidate the expression and distribution of MCT2 in dorsal root ganglia neurons *in vivo*.

Beyond this, it is worth to mention that our exploration on the distribution of Gluts and MCTs was performed in disaggregated DRG neurons that were extracted from mouse embryo and reports of its distribution have been performed in tissues from adult rats and mice (Domenech-Estevez *et al.*, 2015). Concomitantly, changes in the expression of MCT1, MCT2 and MCT4 have been previously reported during development have been reported in mice. However, distribution of those Monocarboxylate transporters during the development remains unexplored.

Altogether, exploration in the distribution of Gluts and MCTs in our experimental model suggest that glucose and pyruvate transport could be facilitated both in soma and axons of disaggregated DRG neurons. Considering this, potential differences in metabolic fluxes between soma and axons could arise either by differential energetic demand (e.g. energy demand for cytosolic calcium clearance explored in [Addendum Figure N°6]), or consumption and production dynamics differences as we discussed in the introduction of this thesis addendum and unlikely by differences in the transport of this metabolites.

24.2 Spontaneous Cytosolic Calcium Spikes and Regulation of Cytosolic Calcium after Depolarization in Soma and Axons of Disaggregated DRG Neurons.

Cytosolic calcium increase in response to activity is largely removed via energy dependent mechanisms located in the plasma membrane and the endoplasmic reticulum (ER) (Szabadkai and Duchen, 2008; Brini *et al.*, 2014). Therefore, cytosolic calcium clearance depends critically on the adequate supply of ATP, which may come from either glycolysis or mitochondria, or both (Pfeiffer-Guglielmi *et al.*, 2007; Rueda *et al.*, 2015). Additionally, it has been widely reported that dysregulation of cytosolic calcium levels participates in the induction and the execution of cell death programs in soma and axons of disaggregated DRG neurons (Villegas, *et al.*, 2014; Barrientos *et al.*, 2011; Uguz and Nazıroglu, 2012).

Considering this, healthy neurons would have a cytosolic calcium clearance under homeostasis of energetic metabolism. Thus, to evaluate the suitability of our cultures for the exploration of metabolic fluxes, we wanted to evaluate the healthiness of our disaggregated DRG neurons using cytosolic calcium clearance as an indicator.

We incubated disaggregated DRG neurons with fluorescent cytosolic calcium reporter fluo-4 acetoxymethyl (AM) and registered calcium dynamics before and after high K^+ or electrical field induced depolarization [Addendum Figure N°6]. We found that our disaggregated DRG neurons had spontaneous spikes of cytosolic calcium that return to basal steady state, before and after depolarization induction by high K^+ or electrical field stimulation [Addendum Figure N°6]. This suggest that our disaggregated DRG neurons have the adequate energy supply to

clear cytosolic calcium increments in the range of the spontaneous spikes in soma and axons.

Furthermore, depolarization was induced by high K^+ (50 mM) superfusion to disaggregated DRG neurons. Under these conditions, we found a significant increase in disaggregated DRG soma and axons cytosolic calcium in response to high K^+ [Addendum Figure N°6B and Addendum Figure N°6C]. Interestingly, mean maximal delta of cytosolic calcium induced by high K^+ was significantly higher in axons than in soma of disaggregated DRG neurons [Addendum Figure N°6B and Addendum Figure N°6C]. Immediately after the peak in cytosolic calcium induced by high K^+ stimulation, cytosolic calcium levels in both soma and axons of disaggregated DRG neurons decreased until basal steady state [Addendum Figure N°6B and Addendum Figure N°6C]. This suggest that our *in vitro* neurons have the adequate energy supply to clear cytosolic calcium increments in the range induced by the high K^+ stimulation.

Alternatively, depolarization was induced in disaggregated DRG neurons by electrical field stimulation (square-wave DC pulse, 150V, 25Hz of 3ms duration). We found a significant increase in disaggregated DRG soma and axons cytosolic calcium after Electrical field stimulation [Addendum Figure N°6D and Addendum Figure N°6E]. Interestingly, mean maximal delta of cytosolic calcium induced by Electrical field stimulation also was significantly higher in axons than in soma of disaggregated DRG neurons [Addendum Figure N°6D and Addendum Figure N°6E]. Further research is needed to explain the differences in mean maximal delta of cytosolic calcium between soma and axons after depolarization. This differences in cytosolic calcium peaks between soma and axons during activity, has been

previously reported in layer V pyramidal neurons in an *ex vivo* model (Schiller *et al.*, 1995). In this context, based on previous reports on the differences in morpho physiology between soma and axons (Study and Kral, 1996), we suggest that factors as differences in the surface/volume ratio, distribution, density or properties of voltage dependent calcium channels (VDCCs) or endogenous buffering capacity between soma and axons could generate this phenomenon.

Furthermore, immediately after the peak in cytosolic calcium induced by electrical field stimulation, cytosolic calcium levels in both soma and axons of disaggregated DRG neurons decreased until basal steady state [Addendum Figure N°6D and Addendum Figure N°6E]. This suggest that our *in vitro* neurons have the adequate energy supply to clear cytosolic calcium increments in the range induced by electrical field stimulation. Considering that we found that our disaggregated DRG neurons were able to clear cytosolic calcium increases induced by high K⁺ or Electrical field stimulation that are 5 time larger than those induced by spontaneous activity, we suggest that in our experimental model, neurons have a reserve capacity in the activation of energy expenditure.

Altogether, further evidence is needed to relate cytosolic calcium clearance capacity in our disaggregated DRG neurons with ATP consumption. Consequently, further evidence is also needed to elucidate whether cytosolic calcium clearance after high K⁺ or electrical field stimulation induces an activation of glycolysis and/or mitochondrial pyruvate consumption.

However, the here reported difference between the cytosolic calcium levels between soma and axons in response to depolarization could lead to differences in energetic demand between those regions of a neuron.

24.3 Mitochondrial Pyruvate Consumption Rates in Disaggregated DRG Neurons.

Pyruvate is the product of glycolysis that enters mitochondria where its metabolized through the tricarboxylic acid cycle (TCA) and oxidative phosphorylation in the electron transport chain (ETC). This process generates 3 adenosine triphosphate (ATP) molecules and carbon dioxide (CO₂) while consumes oxygen (O₂), using 2 pyruvate molecules as a fuel (Camandola and Mattson, 2017; Barros and Martínez, 2007; Barros, 2013). Alternatively, pyruvate can also be generated from lactate through lactate dehydrogenase (LDH) enzymatic activity (Castro, 2009).

In neurons, it has been reported that energetic metabolism is predominantly oxidative (Bélanger *et al.*, 2011). In this context, it has been proposed that neuronal energetic demands by activity are supported majorly by mitochondrial ATP production generated from lactate (Trevisiol *et al.*, 2017; Ferguson *et al.*, 2018). Furthermore, several authors have proposed that astrocytes produce lactate through glycolysis and supply it to neurons through MCTs in response to activity (Astrocyte Neuron Lactate Shuttle; ANLS) (Nave and Trapp, 2008; Mächler *et al.*, 2016; Barros, 2013; Ferguson *et al.*, 2018). Regardless of its cellular origin, major energetic fuel for ATP production in neurons will likely enter to TCA as pyruvate. In this context, ATP would take over 1 h to diffuse between soma and a needy dendrite located 1 mm away, far too long compared with the ATP turnover, which occurs in seconds (Barros and Martínez, 2007; Barros, 2013). Thus, pyruvate supply and ATP production must colocalize. Furthermore, pyruvate production or consumption could correlate with differences in local demands for ATP.

Importantly, as we explained in the addendum introduction, axonal glycolytic and oxidative energetic metabolism is poorly understood in isolated neurons and mathematical models predict differences in energy production or consumption in distant region of larger neurons (Rashevsky, 1972; Rashevsky, 1973; Barros and Martínez, 2007).

Considering this, we explored mitochondrial pyruvate consumption rates in soma and axons of isolated DRG neurons. To this goal, we measured the rate of decrease in pyruvate concentration (mitochondrial pyruvate consumption rate) at soma and axons of disaggregated DRG neurons using genetically encoded FRET pyruvate nanosensor pyronic [Addendum Figure N°1].

First, we found that disaggregated DRG neurons express genetically modified pyruvate FRET nanosensor pyronic distributed along soma and axons [Addendum Figure N°1]. Furthermore, superfusion of 1mM or 0,4 mM of pyruvate caused an increase in mTFP fluorescence intensity and a decrease in Venus fluorescence intensity in soma and axons of disaggregated DRG neurons, consistent with a decrease in FRET efficiency [Addendum Figure N°7 and Addendum Figure N°8]. Thus, changes in pyruvate concentration we estimated from mTFP/Venus ratio correlated with changes in concentrations of pyruvate superfused in soma and axons of disaggregated DRG neurons [Addendum Figure N°9 and Addendum Figure N°12].

All the ups and downs in the pyruvate concentration during our assays were followed by the establishment of a steady state, both in soma and axons of disaggregated DRG neurons [Addendum Figure N°9 and Addendum Figure N°12]. Altogether, this suggest that our

method allows the measurement of pyruvate dynamics in disaggregated DRG neurons and reproduces the time and concentration resolution previously reported in other cell types (San Martín *et al.*, 2014). Considering this, to our knowledge, here we report for the first time, fluxes of pyruvate (concentration) in peripheral neurons [Addendum Figure N°9] measured with genetically encoded FRET nanosensors. Importantly, this is the first report of measurement of pyruvate fluxes in axons of single neurons [Addendum Figure N°12].

Furthermore, we assayed mitochondrial pyruvate consumption rate in soma and axons of disaggregated DRG neurons, by inhibition of MCTs in presence of 0,4 mM pyruvate [Addendum Figure N°9 and Addendum Figure N° 12]. It's worth to mention that mTFP/Venus ratio in axons of disaggregated DRG neurons after MCTs inhibition decreased and then increased alternately and never reached a steady state during the registration time [Addendum Figure N°11]. This phenomenon remains unexplained. We calculated axonal mitochondrial pyruvate consumption rate in the first negative slope after MCT inhibition.

At this respect, we found that soma of disaggregated DRG neurons have a mean mitochondrial pyruvate consumption rate of 0,07 $\mu\text{M/s}$ (n= 35) and axons have a mean mitochondrial pyruvate consumption rate of 0,08 $\mu\text{M/s}$ (n=12) that are not significantly different [Addendum Figure N°13]. This suggest that consumption of pyruvate is equivalent between soma and axons of disaggregated DRG neurons under these conditions. Notably, our mitochondrial pyruvate consumption rates in soma and axons of disaggregated DRG neurons are in the range of the only one previously reported mitochondrial pyruvate consumption rate in hippocampal neurons (in presence of astrocytes) (San Martin, *et al.*, 2014).

We discuss that further evidence is needed to explain our results regarding not significantly different mitochondrial pyruvate consumption rates in soma and axons of disaggregated DRG neurons, considering previous reports that suggest differential energetic demand between those areas of a neuron and dependence of neuronal activity in ATP produced from pyruvate through TCA in mitochondria. It would be interesting to perform mitochondrial pyruvate consumption assays in soma and axons of disaggregated DRG neurons during depolarization protocols as in [Addendum Figure N°6].

Finally, one of the main difficulties during this experimental procedure, was that pyronic FRET pair fluorescence intensity decayed from soma to distal axons [Addendum Figure N°1]. Thus, our experimental design did not allow to register pyronic FRET efficiency in soma and axon of the same single disaggregated DRG neuron without saturation or background noise. Thus, we performed the measurements in soma or axons from different samples of the same cultures. Considering this, we suggest further experiments should be performed in compartmentalized disaggregated DRG cultures to (1) select the optimal number of neurons per lane and consequently, (2) measure mitochondrial pyruvate consumption rate in the same neuron simultaneously and obtain paired data, (3) selectively inhibit MCTs either in soma or axons and finally (4) control the distance between the areas at soma and axons where registration is performed, and thus (5) evaluate potential correlations between neurons size and mitochondrial pyruvate consumption rates heterogeneity.

24.4 Glycolytic Rates in Soma and Axons of Disaggregated DRG Neurons.

Glucose metabolism in the Central Nervous System (CNS) has been extensively studied and competing theories have been presented. In one hand, ANLS hypothesis suggest that glycolysis is outsourced to astrocytes, and thus glucose is primarily converted to lactate in astrocytes (Lundgaard *et al.*, 2015). On the other hand, parsimonious hypothesis proposes that neurons take up glucose directly and synthesize ATP via glycolysis and oxidative metabolism (Lundgaard *et al.*, 2015). Furthermore, glycolytic rates are comparatively lower in neurons than in astrocytes (Bélanger *et al.*, 2011; Bolaños and Almeida, 2010; Herrero-Mendez *et al.*, 2009).

Importantly, Bolaños JP., Moncada S., and collaborators have described the molecular mechanism through which neurons cannot upregulate glycolysis (Almeida *et al.*, 2001; Almeida *et al.*, 2004). In this context, the same group has shown that neurons downregulate glycolysis to maintain antioxidant status through Pentose Phosphate Pathway (PPP) as the expense of its utilization for glycolytic ATP production (Herrero-Mendez *et al.*, 2009). All these characterizations of neuronal glycolysis have been performed under conditions that do not allow to differentiate between dynamics in soma and axons.

Beyond the bioenergetic or antioxidant role of glucose in neurons, glycolytic rates have been poorly explored in isolated neurons, mostly due to lack of technical resolution in the past. However, development of genetically encoded FRET nanosensors has allowed to explore metabolic fluxes at this scale, with improved temporal resolution (Barros *et al.*, 2017;

Magistretti and Allaman, 2015; Bittner *et al.*, 2010; San Martín *et al.*, 2014; Barros *et al.*, 2013; Mohsin *et al.*, 2015). In this context, there is only one previous report of glycolytic rates using FRET nanosensors in isolated cortical neurons (Bittner *et al.*, 2010). Other *ex vivo* reports have been reported in hippocampal slices (Bittner *et al.*, 2010; San Martín *et al.*, 2014). However, these measurements have been performed in the somatodendritic area, and thus, axonal glycolytic rates have remained unexplored. Interestingly, radioactive glucose uptake significantly increases in central and peripheral nerve tracts after stimulation, but not in cell bodies areas (Kadekaro *et al.*, 1985; Sokoloff, 1993). However, as we mentioned in the introduction of this thesis addendum, these findings did not allow to establish whether those differences in glucose utilization are an endogenous property of neurons.

Considering this, we explored glycolytic rates in soma and axons of isolated DRG neurons in absence of glial cells. To this goal, we measured the rate of decrease in YFP/CFP ratio (glycolytic rate) at soma and axons of disaggregated DRG neurons using genetically encoded FRET pyruvate nanosensor FLII12Pglu600 m Δ 6 [Addendum Figure N°2].

First, we found that disaggregated DRG neurons express genetically modified glucose FRET nanosensor FLII12Pglu600 m Δ 6 distributed along soma and axons [Addendum Figure N°2]. Furthermore, in presence of 5mM glucose and 1mM lactate fluorescence intensity of CFP and YFP was stable in soma and axons of disaggregated DRG neurons [Addendum Figure N°14 and Addendum Figure N°16]. Consistently, YFP/CFP ratio remained in a basal steady state during those treatments in soma and axons [Addendum Figure N°15 and Addendum Figure N°17]. However, after glucose Concentration was dropped to zero, response of soma and axons

of disaggregated DRG neurons were surprisingly different.

In one hand, absence of glucose did not induce a change in YFP or CFP fluorescence intensity in soma [Addendum Figure N°14], and consequently YFP/CFP ratio remained in basal steady state under those conditions [Addendum Figure N°15].

It's worth to mention that disaggregated DRG neurons were superfused with 5mM glucose and 1mM lactate by 30 mins before assays. Furthermore, as we mentioned earlier, YFP/CFP ratio remained steady during the first several minutes of the assay in presence of glucose. We expected that, during these treatments, transport and consumption of glucose are operating in soma of disaggregated DRG neurons in presence of 5mM glucose and 1mM lactate. Importantly, some authors have proposed that lactate inhibits glycolysis execution in neurons (Cerdán et al., 2006). Beyond this, we expected that soma of disaggregated DRG neurons would have transported glucose. However, steady state in YFP/CFP ratio after glucose concentration was dropped to zero, strongly suggest that soma of disaggregated DRG neurons were completely depleted of glucose before this step. In other words, we discuss that soma of disaggregated DRG neurons did not transport glucose during incubation and thus, CFP/CFP ratio cannot be lowered with the drop to zero glucose step. Interestingly, it has been reported that soma of DRG neurons express glucose transporters (Simpson *et al.*, 2007) and we found expression of Glut2 in soma of our disaggregated DRG neurons [Addendum Figure N°3].

Importantly, we found that under our culture conditions soma of disaggregated DRG neurons have spontaneous activity, using calcium as a reporter [Addendum Figure N°6]. Absence of glucose transport in those conditions of spontaneous activity and lactate presence suggest that

energy production from oxidative metabolism and not glycolysis supports calcium clearance in soma of disaggregated DRG neurons. Furthermore, it's worth to remember that we found mitochondrial pyruvate consumption rates in soma of disaggregated DRG neurons under the same conditions [Addendum Figure N°9]. Considering all of this, we assume soma of disaggregated DRG neurons are healthy.

Altogether, further evidence is needed to elucidate this suggested absence of glucose transport in soma of disaggregated DRG neurons.

Consequently, CFP and YFP fluorescence intensity remained stable when 5mM glucose and 1mM lactate were superfused again after the drop to zero step in soma of disaggregated DRG neurons [Addendum Figure N°14]. Thus, YFP/CFP ratio also remained in basal steady state [Addendum Figure N°15]. We discuss that maintenance of YFP/CFP ratio after 5mM glucose and 1mM lactate superfusion, post drop to zero step, suggest that soma of our disaggregated DRG neurons do not transport glucose up to this point of the treatment.

Finally, we assayed glycolytic rate in soma of disaggregated DRG neurons by inhibition of glucose transport using 20 μ M Cytochalasin B in presence of 5 mM glucose and 1 mM lactate [Addendum Figure N°2]. We found that, CFP and YFP fluorescence intensity remained stable during that treatment in soma of disaggregated DRG neurons [Addendum Figure N°14]. Thus, YFP/CFP ratio also remained in basal steady state [Addendum Figure N°15]. Glycolytic rates during these treatments were almost undetectable [Addendum Figure N°15]. This suggest that soma of disaggregated DRG neurons have an extremely low glucose transport and minimal

glycolytic activity under these conditions. We discuss that further evidence is needed to evaluate the scope of this results, considering glycolytic rates have never been explored in soma of peripheral sensory neurons. Beyond this, mean glycolytic rates that we report here in soma of disaggregated DRG neurons ($0,001 \mu\text{M/s}$), are considerably lower than mean somatodendritic glycolytic rates previously reported in isolated cortical neurons ($0,5 \mu\text{M}$) (Bittner *et al.*, 2010).

Furthermore, considering that we found spontaneous or post stimulation calcium clearance capacity [Addendum Figure N°6] and mitochondrial pyruvate consumption [Addendum Figure N°9], we suggest that ATP demand is supplied by oxidative metabolism in these conditions in soma of disaggregated DRG neurons. Altogether, we discuss that our results showing minimal glycolytic rates in soma of isolated DRG neurons under these conditions are consistent with the ANLS hypothesis. We will comment on this later again, after discussion of glucose dynamics in axons of disaggregated DRG neurons.

It's worth to mention that, one of the main difficulties during this experimental procedure, was that FLII12Pglu600 m Δ 6 FRET pair fluorescence intensity decayed from soma to distal axons [Addendum Figure N°2]. Thus, our experimental design did not allow to register FLII12Pglu600 m Δ 6 FRET efficiency in soma and axon of the same single disaggregated DRG neuron without saturation or background noise. Thus, we performed the measurements in soma or axons from different samples of the same cultures. Considering this, further experiments are also needed to measure here shown mitochondrial pyruvate consumption rates and glycolytic rates simultaneously in soma or axons of disaggregated DRG neurons.

On the other hand, glucose dynamics in axons of disaggregated DRG neurons were completely different than in soma during the same treatments [Addendum Figure N°15 and Addendum Figure N°17]. As we mentioned before, both soma and axons of disaggregated DRG neurons were assayed after 30 min incubation with 5 mM glucose and 1 mM lactate and registration started when CFP and YFP fluorescence intensities remained stable [Addendum Figure N°14 and Addendum Figure N°16]. It is worth to remember that YFP and CFP fluorescence remained in soma of disaggregated DRG neurons during all the treatments, so soma were mostly unresponsive [Addendum Figure N°14]. However, when glucose concentration was dropped to zero, we found a decrease in CFP fluorescence intensity and an increase in YFP fluorescence intensity in axons of disaggregated DRG neurons [Addendum Figure N°16]. Consequently, YFP/CFP ratio decreased until a new steady state was established (below the basal steady state) in axons [Addendum Figure N°17]. This result suggests that axons of our disaggregated DRG neurons incorporated glucose during the incubation before our measurements and consequently, YFP/CFP ratio decrease is consistent with a decrease in glucose inside the axons after glucose concentration was dropped to zero. Further evidence is needed to establish whether this decrease of glucose in axons of disaggregated DRG neurons after the drop to zero step is due to glucose transport and/or glycolysis. However, we discuss that the fact that YFP/CFP ratio reaches a lower than the basal steady state after glucose concentration was dropped to zero, suggest that glucose was transported outside axons after this treatment.

After this drop to zero glucose step, superfusion of 5 mM glucose and 1 mM lactate again induced an increase in CFP fluorescence intensity and a decrease in YFP fluorescence

intensity in axons of disaggregated DRG neurons [Addendum Figure N°16]. Thus, YFP/CFP ratio increased, and basal steady state was reached again in axons [Addendum Figure N°17].

We discuss that reestablishment of basal steady state in YFP/CFP ratio, indicates that glucose was transported inside axons of disaggregated DRG neurons after this treatment. Beyond this, dynamics of glucose transport and consumption was reestablished when glucose was superfused after the depletion step in axons of disaggregated DRG neurons [Addendum Figure N°17]. This suggest that axons of dissaggregated DRG neurons are healthy after the drop to zero glucose step.

Additionally, changes in FLII12Pglu600 $m\Delta 6$ FRET efficiency after glucose superfusion or drop to zero glucose suggest that the sensor is functional in axons of dissaggregated DRG neurons during our experiments. We discuss that this indicates that flat CFP and YFP fluorescence intensity signals registered in soma of disaggregated DRG neurons under the same conditions are not artifacts.

Finally, glycolytic rates were measured in axons of dissaggregated DRG neurons after inhibition of glucose transport using 20 μM Cytochalasin B [Addendum Figure N°2]. We found that glucose transport inhibition induced a significant decrease in in CFP fluorescence intensity and an increase in YFP fluorescence intensity [Addendum Figure N°16]. Consequently, YFP/CFP ratio decreased until a new steady state was established (below the basal steady state) [Addendum Figure N°17]. We discuss that this decrease in YFP/CFP ratio after glucose transport inhibition is consistent with glycolysis in axons of disaggregated DRG neurons. However, further evidence is needed to reproduce these results beyond

pharmacological inhibition of glucose transport.

We discuss that further evidence is also needed to establish whether glycolysis here reported in axons of disaggregated DRG neurons leads to pyruvate or lactate synthesis. Consequently, further evidence is also needed to establish whether axonal glycolysis here reported leads to glycolytic and/or oxidative ATP production. Additionally, considering past reports on the glucose consumption to support antioxidant status through Pentose Phosphate Pathway in neurons (Herrero-Mendez *et al.*, 2009) it would be very interesting to determine whether axonal glycolysis is supporting antioxidant capacity in our disaggregated DRG neurons. Exploration of this would be particularly relevant to elucidate potential intrinsic antioxidant capacity supported by glycolysis during neurodegeneration.

Notably, it has been recently proposed that axonal glycolysis exclusively provides ATP for fast axonal transport in *Drosophila melanogaster* cultured cortical neurons (Zala *et al.*, 2013). Considering this, further evidence is needed to elucidate the potential role of here reported axonal glycolysis in axonal transport at disaggregated DRG neurons.

Ultimately, we determined mean glycolytic rate in axons of disaggregated DRG neurons. In this context, we found that mean glycolytic rate in axons of disaggregated DRG neurons (0,02 $\mu\text{M/s}$) [Addendum Figure N°18] is lower than the only previously reported mean glycolytic rate in isolated neurons (0,5 $\mu\text{M/s}$) using genetically encoded glucose FRET nanosensors (Bittner *et al.*, 2010). However, it's worth to mention that glycolytic rates have never been explored in axons of isolated neurons before. Considering this, the cytosolic calcium clearance

capacity and the consumption of pyruvate at mitochondria under the same conditions, the mean glycolytic rate we found in axons of our disaggregated DRG neurons could be in the physiological range for this type of neurons.

We discuss that here reported glycolysis execution in axons of disaggregated DRG neurons is consistent with the parsimonious hypothesis. Furthermore, we found that mean glycolytic rate is significantly higher in axons (0,02 $\mu\text{M/s}$) than in soma (0,001 $\mu\text{M/s}$) of disaggregated DRG neurons [Addendum Figure N°18].

Altogether, our result suggests that disaggregated DRG neurons have remarkable differences in the glucose dynamics assayed under our experimental conditions. Specifically, we discuss that soma and axons of disaggregated DRG neurons differ in their glucose transport dynamics. More importantly, soma and axons of disaggregated DRG neurons present significant differences in the dynamics of glucose consumption.

We discuss that this heterogeneity in glucose consumption along the same neuronal cell here presented is relatable to the differences in glucose metabolism at soma and axons predicted by mathematical modelling of glucose metabolism for large neurons by Rashevsky (1972; 1973). Furthermore, we discuss that our results support the Kadekaro M. and Sokoloff L. findings of significant increase in glucose uptake in nerves but not in cell bodies during retrograde electrical stimulation in sensory tracts (DRG tracts) *in vivo* (Kadekaro *et al.*, 1985; Sokoloff, 1993).

The fact that our assays were performed in isolated neurons suggest that heterogeneity in glucose consumption along the same cell could be an endogenous characteristic of neurons.

Considering the above mentioned, our results suggest a simplified scenario where the same neuronal cell simultaneously executes glycolysis in axons but not in soma. We discuss that multiple further experiments are needed to support this scenario.

25. ADDENDUM CONCLUSION.

In this thesis addendum we report significant differences in glucose dynamics between soma and axons of disaggregated DRG neurons.

Based on this, we strongly suggest the systematization of measurements in different regions (soma and axons) of the same neuron simultaneously when energetic metabolism is being explored. This simple praxis will potentially allow a deeper understanding in energetic metabolism regulation of local physiological and pathophysiological mechanisms of neurons.

26. ADDENDUM BIBLIOGRAPHY.

1. Uguz A.C. and Nazıroglu M. (2012). Effects of Selenium on Calcium Signaling and Apoptosis in Rat Dorsal Root Ganglion Neurons Induced by Oxidative Stress. *Neurochem Res* (2012) 37:1631–1638.
2. Almeida, A., Almeida, J., Bolaños, J. P. and Moncada, S. (2001). Different responses of astrocytes and neurons to nitric oxide: the role of glycolytically-generated ATP in astrocyte protection. *Proc. Natl Acad. Sci. USA* 98, 15294–15299 (2001).
3. Almeida, A., Moncada, S. and Bolaños, J. P. (2004). Nitric oxide switches on glycolysis through the AMP protein kinase and 6-phosphofructo-2-kinase pathway. *Nature Cell Biol.* 6, 45–51 (2004).
4. Trevisiol A., Saab A.S., Winkler U. , Marx G., Imamura H. , Möbius W., Kusch K., Nave K-A., and Hirrlinger J. (2017). Monitoring ATP dynamics in electrically active white matter tracts. *eLife.* 2017; 6: e24241.
5. Arimura, N., and Kaibuchi, K. (2007). Neuronal polarity: from extracellular signals to intracellular mechanisms. *Nature reviews. Neuroscience*, 8(3), 194–205. doi:10.1038/nrn2056

6. Arluison, M., Quignon, M., Nguyen, P., Thorens, B., Leloup, C., and Penicaud, L. (2004). Distribution and anatomical localization of the glucose transporter 2 (GLUT2) in the adult rat brain — an immunohistochemical study, 28, 117–136.
7. Baas, P. W., Deitch, J. S., Black, M. M., and Banker, G. A. (1988). Polarity orientation of microtubules in hippocampal neurons: uniformity in the axon and nonuniformity in the dendrite. *Proceedings of the National Academy of Sciences*, 85(21), 8335–8339.
8. Barrientos, S. A., Martinez, N. W., Yoo, S., Jara, J. S., Zamorano, S., Hetz, C., Twiss J. F., Court, F. A. (2011). Axonal degeneration is mediated by the mitochondrial permeability transition pore. *The Journal of Neuroscience: The Official Journal of the Society for Neuroscience*, 31(3), 966–78.
9. Barros, L. F. and Martínez C. (2007). An Enquiry into Metabolite Domains, 92(June), 3878–3884.
10. Barros, L. F. (2013). Metabolic signaling by lactate in the brain. *Trends in Neurosciences*, 36(7), 396–404.
11. Barros, L. F., Bolaños, J. P., Bonvento, G., Bouzier-Sore, A.-K., Brown, A., Hirrlinger, J., Kasparov, S., Kirchoff, F., Murphy, A.N., Pellerin, L., Robinson, M.B., Weber, B. (2017). Current technical approaches to brain energy metabolism. *Glia*, 2017; 1-22.
12. Barros, L. F., San Martín, A., Sotelo-Hitschfeld, T., Lerchundi, R., Fernández-Moncada, I., Ruminot, I., Gutierrez R., Valdebenito R., Ceballo S., Alegría K., Baeza-Lehnert F., and Espinoza, D. (2013). Small is fast: astrocytic

glucose and lactate metabolism at cellular resolution. *Frontiers in Cellular Neuroscience*, 7(March), 1–8.

13. Bélanger, M., Allaman, I., and Magistretti, P. J. (2011). Brain energy metabolism: Focus on Astrocyte-neuron metabolic cooperation. *Cell Metabolism*, 14(6), 724–738.

14. Bélanger, M., Allaman, I., and Magistretti, P.J. (2011). Brain energy metabolism: focus on astrocyte-neuron metabolic cooperation. *Cell Metab.*

15. Bittner, C. X., Loaiza, A., Ruminot, I., Larenas, V., Sotelo-Hitschfeld, T., Gutiérrez, R., Córdova A., Valdebenito R., Frommer Wolf B., Barros, L. F. (2010). High resolution measurement of the glycolytic rate. *Frontiers in Neuroenergetics*, 2(September), 1–11.

16. Bolaños J.P and Almeida A. (2010) The pentose-phosphate pathway in neuronal survival against nitrosative stress. *IUBMB Life* 62:14–8

17. Bouzier-Sore, A.-K., Voisin, P., Bouchaud, V., Bezancon, E., Franconi, J.-M., and Pellerin, L. (2006). Competition between glucose and lactate as oxidative energy substrates in both neurons and astrocytes: a comparative NMR study. *The European Journal of Neuroscience*, 24(6), 1687–94.

18. Brini, M., Cali, T., and Ottolini, D. (2014). Neuronal calcium signaling: function and dysfunction.

19. Brittis, P. A., Lu, Q., and Flanagan, J. G. (2002). Axonal protein synthesis provides a mechanism for localized regulation at an intermediate target. *Cell*, 110(2), 223–235.

20. Camandola, S., and Mattson, M. P. (2017). Brain metabolism in health, aging, and neurodegeneration. *The EMBO Journal*, 36(11), 1474–1492.
21. Castro, M. A, Beltrán, F. A, Brauchi, S., and Concha, I. I. (2009). A metabolic switch in brain: glucose and lactate metabolism modulation by ascorbic acid. *Journal of Neurochemistry*, 110(2), 423–40.
22. Cerdán, S., Rodríguez, T. B., Sierra, A., Benito, M., Fonseca, L. L., Fonseca, C. P., and García-Martín, M. L. (2006). The redox switch/redox coupling hypothesis. *Neurochemistry International*, 48(6–7), 523–30.
23. Court F.A., and Álvarez J. (2016). Schwann Cell and Axon: An Interlaced Unit-From Action Potential to Phenotype Expression. *Adv Exp Med Biol*. 2016; 949:183-201.
24. Court, F. A., and Álvarez, J. (2005). Local regulation of the axonal phenotype, a case of merotrophism, 365–374.
25. Cull, P. (2007). The mathematical biophysics of Nicolas Rashevsky. *Bio Systems*, 88(3), 178–84.
26. Domenech-Estevez E., Baloui, H., Repond, X. C., Rosafio, K., Me, J., Tricaud, N., Pellerin, L., and Chrast, R. (2015). Distribution of Monocarboxylate Transporters in the Peripheral Nervous System Suggests Putative Roles in Lactate Shuttling and Myelination, 35(10), 4151–4156.
27. Ferguson, B. S., Rogatzki, M. J., Goodwin, M. L., Kane, D. A., Rightmire, Z., and Gladden, L. B. (2018). Lactate metabolism: historical context, prior misinterpretations, and current understanding. *European Journal of Applied Physiology* (Vol. 0). Springer Berlin Heidelberg.

28. Fernandez-Fernandez, S., Almeida, A., and Bolaños, J. P. (2012). Antioxidant and bioenergetic coupling between neurons and astrocytes. *The Biochemical Journal*, 443(1), 3–11.
29. Fohlmeister J., Cohen E., Newman E. (2010). Mechanisms and distribution of ion channels in retinal ganglion cells: using temperature as an independent variable. *J Neurophysiol*. 2010 Mar;103(3):1357-74.
30. Gjedde, A., Marrett, S., and Vafae, M. (2002). Oxidative and nonoxidative metabolism of excited neurons and astrocytes. *Journal of Cerebral Blood Flow and Metabolism: Official Journal of the International Society of Cerebral Blood Flow and Metabolism*, 22(1), 1–14.
31. Herrero-Mendez A., Almeida A., Fernandez E., Maestre C., Moncada S. and Bolaños J. P. (2009) The bioenergetic and antioxidant status of neurons is controlled by continuous degradation of a key glycolytic enzyme by APC/C-Cdh1. *Nat. Cell Biol.* 11, 747–752.
32. Kadekaro M, Crane AM, Sokoloff L. (1985). Differential effects of electrical stimulation of sciatic nerve on metabolic activity in spinal cord and dorsal root ganglion in the rat. *Proc Natl Acad Sci USA*, 82(September), 6010–13.
33. Kole M., Stuart G. (2008). Is action potential threshold lowest in the axon? *Nat Neurosci.* 2008 Nov; 11(11):1253- 5.
34. Lerchundi, R., Fernández-Moncada, I., Contreras-Baeza, Y., Sotelo-Hitschfeld, T., Mächler, P., Wyss, M. T., Stobart J., Baeza-Lehnert F., Alegría K., Weber B., Barros, L. F. (2015). NH₄⁺ triggers the release of astrocytic

lactate via mitochondrial pyruvate shunting. *Proceedings of the National Academy of Sciences*, 112(35), 11090–11095.

35. Lopez-Leal R., Alvarez, J., Court F.A. (2016). Origin of Axonal Proteins: is the axon-Schwann cell unit a functional syncytium? *Cytoskeleton* (Hoboken). 2016 Oct;73(10):629-639.

36. Lundgaard, I., Li, B., Xie, L., Kang, H., Sanggaard, S., Sun, W., Goldman, S., Blekot, S., Nielsen, M., Takano, T., Deane, Rashid., Nedergaard, M. (2015). Direct neuronal glucose uptake heralds activity-dependent Increases in Cerebral Metabolism, *Nat Commun.* 2015; 6: 6807.

37. MacAskill, A. F., and Kittler, J. T. (2010). Control of mitochondrial transport and localization in neurons. *Trends in Cell Biology*, 20(2), 102–12.

38. Mächler, P., Wyss, M. T., Elsayed, M., Stobart, J., Gutierrez, R., Von Faber-Castell, A., Kaelin, V., Zuend, M., San Martín, A., Romero-Gomez, I., Baeza-Lehnert, F., Lengacher. S., Schneider, B.L., Aebischer. P., Magistretti, J.P., Barros, L.F., Weber, B. (2016). In Vivo Evidence for a Lactate Gradient from Astrocytes to Neurons. *Cell Metabolism*, 23(1), 94–102.

39. Magistretti, P. J., and Allaman, I. (2015). A Cellular Perspective on Brain Energy Metabolism and Functional Imaging. *Neuron*, 86(4), 883–901.

40. Magistretti, P. J., and Pellerin, L. (1999). Cellular mechanisms of brain energy metabolism and their relevance to functional brain imaging. *Philosophical Transactions of the Royal Society of London. Series B, Biological Sciences*, 354(1387), 1155–63.

41. Mohsin, M., Ahmad, A., and Iqbal, M. (2015). FRET-based genetically-

encoded sensors for quantitative monitoring of metabolites. *Biotechnology Letters*, 37(10), 1919–1928.

42. Nave, K.-A., and Trapp, B. D. (2008). Axon-glia signaling and the glial support of axon function. *Annual Review of Neuroscience*, 31, 535–61.

43. Nehlig, A., and Coles, J. A. (2007). Cellular Pathways of Energy Metabolism in the Brain: Is Glucose Used by Neurons or Astrocytes? *1250(May 2006)*, 1238–1250.

44. Nehlig, A., and Coles, J. A. (2007). Cellular Pathways of Energy Metabolism in the Brain: Is Glucose Used by Neurons or Astrocytes? *Glia (May 2006)*, 55: 1238–1250.

45. Neukirchen, D., and Bradke, F. (2011). Neuronal polarization and the cytoskeleton. *Seminars in cell and developmental biology*, 22(8), 825–33.

46. Nijland, P. G., Michailidou, I., Witte, M. E., Mizee, M. R., Pol, S. M. A. Van Der, Hof, B. Van., Reijerkerk A., Pellerin L., Valk P. Van., de Vries, H.E. Horsen, J. Van. (2014). Cellular Distribution of Glucose and Monocarboxylate Transporters in Human Brain White Matter and multiple sclerosis Lesions, 1125–1141.

47. Pfeiffer-Guglielmi, B., Francke, M., Reichenbach, A., and Hamprecht, B. (2007). Glycogen phosphorylase isozymes and energy metabolism in the rat peripheral nervous system-An immunocytochemical study. *Brain Research*, 1136(1), 20–27.

48. Rasband, M. (2010). The axon initial segment and the maintenance of neuronal polarity. *Nature reviews. Neuroscience*, 11(8), 552–62.

49. Rashevsky N. (1972) Suggestions for a mathematical model of a pathological neuron with spontaneous repetitive discharges. *Bull Math Biophys.* 1972 jun;34(2):223-30.
50. Rashevsky, N. (1973). The diffusion and metabolic differences between soma and axon of a neuron. *Bull Math Biol.* 1973 Aug;35(4):421-9.
51. Rodriguez-Rodriguez, P., Fernandez, E., and Bolaños, J. P. (2013). Underestimation of the pentose-phosphate pathway in intact primary neurons as revealed by metabolic flux analysis. *Journal of Cerebral Blood Flow and Metabolism*, 33(12), 1843–1845.
52. Rodriguez-Rodriguez, P., Fernandez, E., Almeida, a, and Bolaños, J. P. (2012). Excitotoxic stimulus stabilizes PFKFB3 causing pentose-phosphate pathway to glycolysis switch and neurodegeneration. *Cell Death and Differentiation*, 1–8.
53. Rolls, M. M., Satoh, D., Clyne, P. J., Henner, A. L., Uemura, T., and Doe, C. Q. (2007). Polarity and intracellular compartmentalization of *Drosophila* neurons. *Neural development*, 2(April), 7.
54. Rueda, C. B., Pardo, B., Szabadkai, G., Duchen, M. R., and Satrustegui, J. (2015). The regulation of neuronal mitochondrial metabolism by calcium, 16(July 2014), 3447–3462.
55. San Martín A., Ceballo S., Baeza-Lehnert F., Lerchundi R., Valdebenito R., Contreras Baeza Y., Alegria K., Barros L.F. (2014). Imaging mitochondrial flux in single cells with a FRET sensor for pyruvate. *PLoS One* 9(1): e85780.

56. San Martín, A., Ceballo, S., Ruminot, I., Lerchundi, R., Frommer, W. B., and Barros, L. F. (2013). A Genetically Encoded FRET Lactate Sensor and Its Use to Detect the Warburg Effect in Single Cancer Cells. *PloS One*, 8(2), e57712.
57. Schiller, J., Helmchen, F., Sakmann, B., Forschung, M. M., Zellphysiologie, A., and Heidelberg, D. (1995). Spatial profile of dendritic calcium transients evoked by action potentials in rat neocortical pyramidal neurones, 583–600.
58. Shetty, P. K., Galeffi, F., and Turner, D. A. (2012). Cellular links between neuronal activity and energy homeostasis. *Frontiers in Pharmacology*, 3 MAR(March), 1–14.
59. Simpson, I., Carruthers, A., and Vannucci, S. J. (2007). Supply and Demand in Cerebral Energy Metabolism: The Role of Nutrient Transporters. *J Cereb Blood Flow Metab.*, 27(11), 1766–1791.
60. Sokoloff, L. (1993). Function-related changes in energy metabolism in the nervous system: localization and mechanisms. *The Keio Journal of Medicine*, 42(3), 95–103.
61. Sonnay, S., Gruetter, R., and Duarte, J. M. N. (2017). How energy metabolism supports cerebral function: Insights from ¹³C magnetic resonance studies *in vivo*. *Frontiers in Neuroscience*, 11(MAY), 1–20.
62. Sonnay, S., Gruetter, R., and Duarte, J. M. N. (2017). How energy metabolism supports cerebral function: Insights from ¹³C magnetic resonance studies *in vivo*. *Frontiers in Neuroscience*, 11(MAY), 1–20.

63. Sotelo-Hitschfeld, T., Fernández-Moncada, I., and Barros, L. F. (2012). Acute feedback control of astrocytic glycolysis by lactate. *Glia*, 60(4), 674–80.
64. Study, E., and Kral, M. G. (1996). Spontaneous action potential activity in isolated dorsal root ganglion neurons from rats with a painful neuropathy, *Pain* 65, 235–242.
65. Szabadkai, G., and Duchen, M. R. (2008). Mitochondria: the hub of cellular Ca²⁺ signaling. *Physiology (Bethesda, Md.)*, 23, 84–94.
66. Szablewski, L. (2017). Glucose Transporters in Brain: In Health and in Alzheimer's Disease. *Journal of Alzheimer's Disease*, 55(4), 1307–1320.
67. Szu-Yu Ho, T., and Rasband, M. N. (2011). Maintenance of neuronal polarity. *Developmental neurobiology*, 71(6), 474–82.
68. Tahirovic, S., and Bradke, F. (2009). Neuronal polarity. *Cold Spring Harbor perspectives in biology*, 2009 Sept 1(3), a001644.
69. Takanaga, H., Chaudhuri, B., and Frommer, W. B. (2008). GLUT1 and GLUT9 as major contributors to glucose influx in HepG2 cells identified by a high sensitivity intramolecular FRET glucose sensor. *Biochimica et Biophysica Acta*, 1778(4), 1091–9.
70. Tomasi, D. G., Shokri-Kojori, E., Wiers, C. E., Kim, S. W., Demiral, Ş. B., Cabrera, E. A., Lindgren E., Miller G., Wang G-J., and Volkow, N. D. (2017). Dynamic brain glucose metabolism identifies anti-correlated cortical-cerebellar networks at rest. *Journal of Cerebral Blood Flow and Metabolism*, Dec;37(12):3659-3670.
71. Villegas, R., Martinez, N. W., Lillo, J., Pihan, P., Hernandez, D., Twiss, J.

L., and Court, F. A. (2014). Calcium Release from Intra-Axonal Endoplasmic Reticulum Leads to Axon Degeneration through Mitochondrial Dysfunction. *The Journal of Neuroscience: The Official Journal of the Society for Neuroscience*, 34(21), 7179–89.

72. Winckler, B., Forscher, P., and Mellman, I. (1999). A diffusion barrier maintains distribution of membrane proteins in polarized neurons. *Nature*, 397(6721), 698–701.

73. Zala, D., Hinckelmann, M.V., Yu, H., Lyra da Cunha, M. M., Liot, G., Cordelières, F. P., Marco S., Saudou, F. (2013). Vesicular glycolysis provides on-board energy for fast axonal transport. *Cell*, 152(3), 479–91.